SAND2000–8662
Unlimited Release
Printed March 2001

From Atoms to Autos
A New Design Paradigm Using Microstructure-Property Modeling Part 1: Monotonic Loading Conditions

M.F. Horstemeyer

Prepared by
Sandia National Laboratories
Albuquerque, New Mexico 87185 and Livermore, California 94550

Sandia is a multiprogram laboratory operated by Sandia Corporation, a Lockheed Martin Company, for the United States Department of Energy under Contract DE-AC04-94AL85000.

Issued by Sandia National Laboratories, operated for the United States Department of Energy by Sandia Corporation.

Available to DOE and DOE contractors from
Office of Scientific and Technical Information
P.O. Box 62
Oak Ridge, TN 37831

Prices available from (703) 605-6000
Web site: http://www.ntis.gov/ordering.htm

Available to the public from
National Technical Information Service
U.S. Department of Commerce
5285 Port Royal Rd
Springfield, VA 22161

NTIS price codes
Printed copy: A12
Microfiche copy: A01

SAND2000-8662
Unlimited Release
Printed March 2001

From Atoms to Autos
A New Design Paradigm Using Microstructure-Property Modeling
Part 1: Monotonic Loading Conditions

Mark F. Horstemeyer
Sandia National Laboratories
P.O. Box 969
Livermore, CA 94551-0969

Abstract

A multiscale analysis was performed to develop a macroscale microstructure-mechanical property model that includes several types of microstructural inclusions found in an A356-T6 cast aluminum alloy for use in automotive chassis component design. This microstructure-property model can be used for finite element analysis in which the deformation history, temperature dependence, and strain rate dependence vary. To capture the history effects from the boundary conditions and load histories, the microstructural defects and progression of damage from these defects and microstructural features such as casting porosity, silicon particles, and intermetallics must be reflected in the model. Internal state variables are used in the material model to reflect void/crack nucleation, void growth, and void coalescence from the casting microstructural features under different temperatures, strain rates, and deformation paths. Furthermore, internal state variables are used to reflect the dislocation density evolution that affects the work hardening rate and thus stress state under different temperatures and strain rates. In order to determine the pertinent effects of the microstructural features, several different length scale analyses were performed. Once the pertinent microstructural features were determined and included in the microstructure-mechanical property model, tests were performed on a control arm to validate its precision. Very encouraging results were demonstrated when using the model for optimizing structural components in a predictive fashion.

This page intentionally blank

From Atoms to Autos
A New Design Paradigm Using Microstructure-Property Modeling
Part 1: Monotonic Loading Conditions

EXECUTIVE SUMMARY

In designing a structural component, a failure analysis will typically include a finite element analysis and microstructural evalutation. Sometimes the microstructural evalution will quantify the inclusion content (source of damage in a component) in a prioritized fashion differently than the finite element analysis. Let us consider the hypothetical situation exemplified in Figure 1. Here we have an automotive control arm that shows that has undergone certain boundary conditions in a finite element analysis. The finite element analysis revealed that the highest Mises stress occurred at point D. For the different regions of interest, microstructural analysis using optical imaging revealed the largest defect occurred at point B. Both camps would argue about the location of final failure. However, in our hypothetical example, both are wrong, because the final failure state is both a function of the initial inclusion state and boundary conditions. As such, point A failed first. The key is the development of the microstructure-property model that can be included in a finite element analysis, which includes the inclusion content (or the sources of damage progression).

Stress (from highest to lowest)	Inclusion (from most severe to less severe)	Damage (from most severe to less severe)
D	B	A
A	E	D
C	A	E
E	D	C
B	C	B

Figure 1. Stress and inclusion analysis studies can be done independently on this control arm, but both would give an erroneous location of failure because damage accumulation is dependent upon both entities.s

In order to accomplish such a task, a multiscale analysis was performed with a focus on a macroscale microstructure-mechanical property model that includes several types of microstructural inclusions found in an A356-T6 cast aluminum alloy for use in automotive chassis component design. This microstructure-property model can be used for finite element analysis in which the deformation history, temperature dependence, and strain rate dependence vary. To capture the history effects from the boundary conditions and load histories, the microstructural defects and progression of damage from these defects and microstructural features such as casting porosity, silicon particles, and intermetallics must be reflected in the model. Internal state variables are used in the material model to reflect void/crack nucleation, void growth, and void coalescence from the casting microstructural features under different temperatures, strain rates, and deformation paths. Furthermore, internal state variables are used to reflect the dislocation density evolution that affects the work hardening rate and thus stress state under different temperatures and strain rates. In order to determine the pertinent effects of the microstructural features, several different length scale analyses were performed. Once the pertinent microstructural features were determined and included in the microstructure-mechanical property model, tests were performed on a control arm to validate its precision. Very encouraging results were demonstrated when using the model for optimizing structural components in a predictive fashion.

Optimization in the context of this study has to do with weight reduction. In order to reduce weight from structural components, the influence of the microstructures/defects needs to be quantified. In the absence of the microstructure-property model, optimization can be relegated to a fruitless exercise. To quantify the microstructures/defects and their influence on the mechanical properties, we performed a multiscale hierarchy of numerical simulations coupled with experiments to determine the internal state variable equations of macroscale plasticity and damage progression. The microstructures/defects observed in the cast A356 aluminum alloy in descending order of deleterious effect are large oxides/pores, smaller oxides/pores, silicon particles, dendrite cells size, and intermetallics. The attributes of these features that are included in the model are the size distributions, volume fractions, and nearest neighbor distances.

The modeling philosophy is illustrated in Figure 2, which shows experiments, modeling, and analysis at each size scale. Figure 3 shows the important features and size scales that were pertinent at each size scale.

At the atomic scale (nanometers), simulations were performed using Modified Embedded Atom Method (MEAM) potentials to determine the conditions when silicon fracture would occur versus silicon-interface debonding. Atomistic simulations showed that a material with a pristine interface, would incur interface debonding before silicon fracture. However, if a sufficient number of defects were present within the silicon, it would fracture before the interface would debond. Microstructural analysis of larger scale interrupted strain tests under tension revealed that both silicon fracture and debonding of the silicon-aluminum interface in the eutectic region would occur.

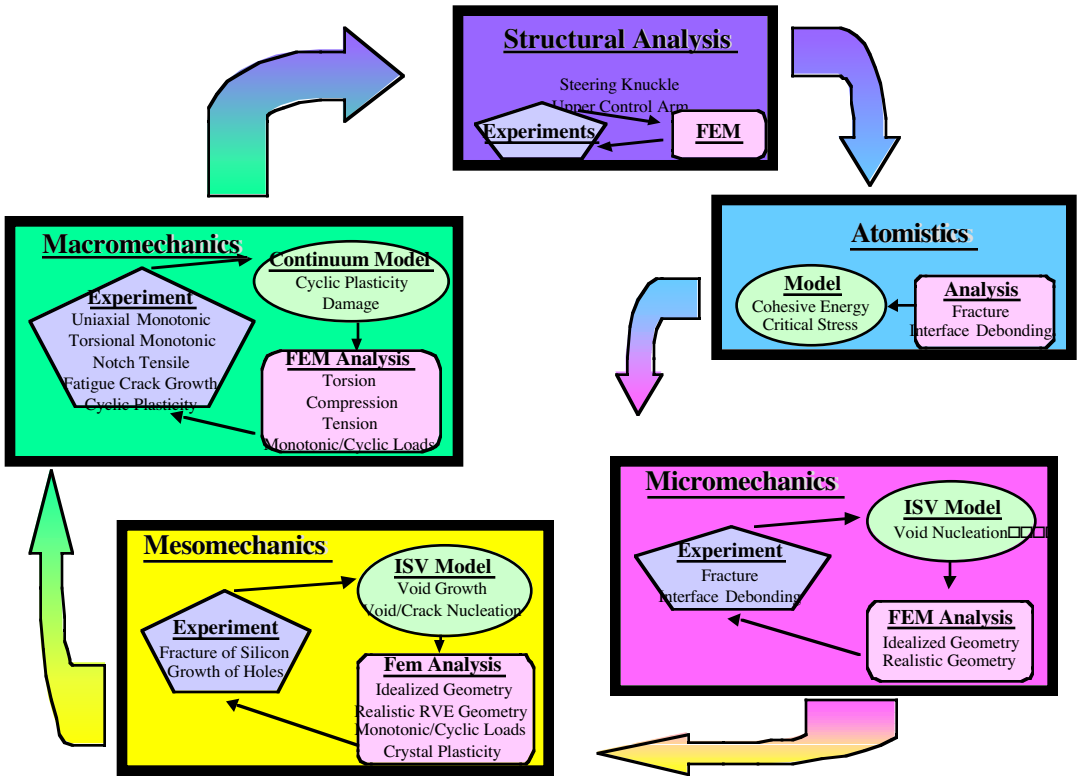

Figure 2. Microstructure-property modeling philosophy using a multiscale analysis.

Another important result from the atomistic simulations was that the stress-strain response of a region of material around an interface that was debonding could be represented by an elastic fracture analysis at the next higher size scale if the interface were assumed to be larger than 40 Å. Hence, an elastic fracture criterion was used in the microscale (1-20 microns) finite element analysis, which focused on void-crack nucleation, and mesoscale (1-200 micron) finite element analyses, which focused on silicon-pore coalescence.

In the micron size scale finite element analyses, we focused on the void-crack nucleation progression by examining the parameters that influenced silicon fracture and silicon-aluminum interface debonding. In particular, we included temperature, shape, size, nearest neighbor distance, number density, prestrain history, and loading direction as parameters for the silicon in the finite element analyses. The parametric study clearly showed that the temperature dependence on void nucleation from silicon fracture and interface debonding was the most dominant influence parameter. To verify this result, we performed notch tensile tests at ambient temperature and the two extreme limits of temperatures that a control arm would experience: 222 K and 600 K. From examining the fracture surfaces and cross-sections of deformed samples and counting the number of void nucleation sites, it was clear that at the coldest temperature, the largest voids nucleated and at the hottest temperature, the least amount of voids nucleated. Essentially, the colder temperatures induce a higher local stress state. The higher stresses fuse

damage at an increased rate. These results corroborate the microscale finite element analyses and thus a temperature dependence on the void nucleation rate was included in the macroscale microstructure-mechanical property model. As a follow-on, strain rate tests were also performed in which the strain rate effect on void nucleation was quantified for the model.

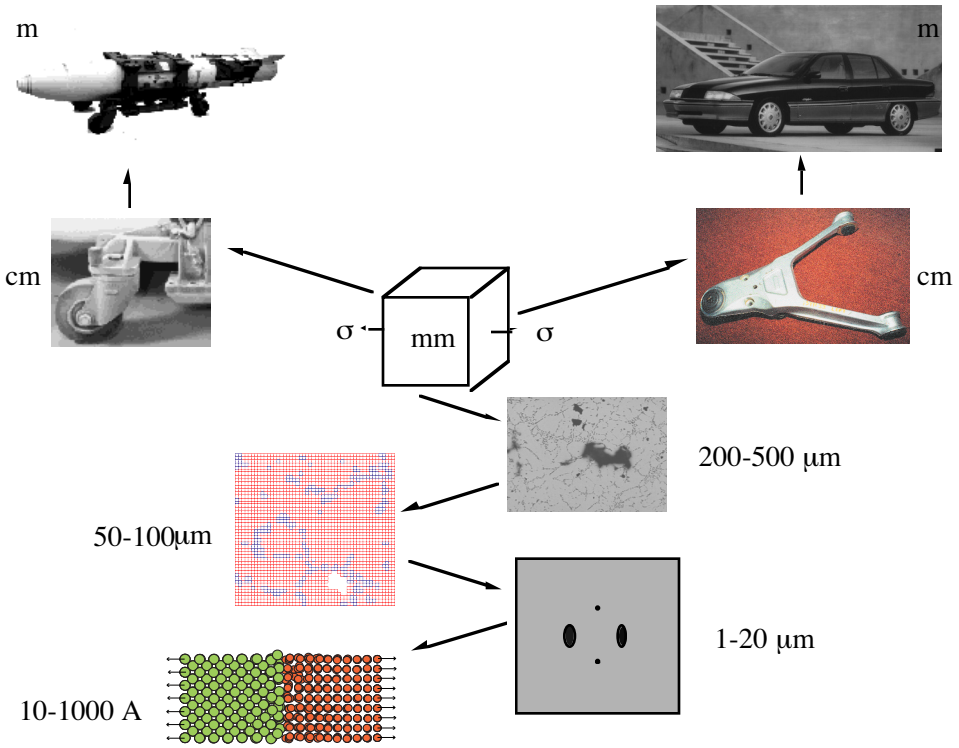

Figure 3. Schematic of important modeling aspects at each size scale.

An important set of experiments was performed to determine the void nucleation rate under different stress states and strain levels. Interrupted equivalent strain tests performed in tension, compression, and torsion were examined via optical imaging and the number densities were quantified. The experimental data showed that the void nucleation rate under torsion was the highest followed by tension and then by compression. Interestingly, the highest work hardening rate was exhibited in compression followed by tension and then by torsion. Note that the work hardening rate was in reverse order of the void nucleation rate thus revealing a coupling between the stress state and damage progression. The void nucleation rate and work hardening rate differences were included in the macroscale void nucleation model.

In the Mesoscale I analysis (1-200 microns), we focused on pores arising from silicon fracture and interface debonding that interacted with pores from the casting process. In performing these finite element analyses, we first constructed finite element meshes on real A356 micrographs. Hence, the sizes, distributions, and volume fractions of silicon, casting porosity, and dendrite cells were inherently imbedded in the simulations. We performed indenter tests on the particular second phases to determine the elastic moduli of the silicon, intermetallics, and matrix aluminum.

We also performed compression tests on the eutectic aluminum at different temperatures to obtain the stress-strain responses for the mesoscale analyses. We used those values for the finite element simulations. We then matched the progression of silicon fracture and interface debonding from the interrupted strain experiments described earlier by a trial-and-error method for the local elastic fracture silicon stresses. We further varied the applied stress state, temperature, and strain rate. The results gave insight into the functional form of the equation needed for the macroscale coalescence equation. Furthermore, temperature dependence was deemed as very important here. In fact, the influence of temperature on void coalescence was the opposite trend as that of void nucleation. For void nucleation, as the temperature decreased (increasing the stress level), the void nucleation rate increased. For void coalescence, as the temperature increased (increasing the plastic strain), the void coalescence rate increased. This temperature dependence was included in the macroscale coalescence equation.

The Mesoscale II finite element simulations (100-500 microns), focused on pore-pore interactions to give insight into coalescence from casting porosity. First we performed a parametric study by varying temperature, shape, size, nearest neighbor distance, number density, prestrain history, and loading direction and monitored the total void growth and strain at localization. The results showed that temperature, again, was a first order influence parameter on void coalescence because it increases the local plastic strains, but the size of pore and type of loading (triaxial state of stress) were first order influence parameters on strain localization. Furthermore, microporosity, prestrain history, and number density were first order influences, along with temperature, on the total void growth. Hence, these attributes were placed in the macroscale coalescence equation.

Another important result from this study showed that if a pore were within eight diameters of another pore, the void growth rates would be enhanced. Alternatively, if a casting can have nearest neighbor distances of greater than eight pore diameters, then the strain to failure will be increased.

Tension experiments on flat bars were performed to analyze void growth from surface pores under different temperatures (222K, 297K, 600K). The surface pores were first measured in the virgin state and then the specimens were tested to a certain strain level. The identical voids were then measured again. This process occurred until the specimens fractured. The voids were further than eight diameters apart; hence, the results could be used to determine the single void growth equation for the macroscale microstructure-mechanical property model. As it turns out, little void growth was measured from these surface pores until the final fracture occurred indicating that void nucleation is probably more important than void growth and coalescence in this cast A356 aluminum alloy under uniaxial monotonic loads. Furthermore, little difference was observed from the temperature changes indicating that macroscale void growth equation does not need to include the temperature dependence.

Given the lower size scale information, the macroscale total void volume fraction (cm) is a function of the void nucleation rate, void growth rate, and coalescence rate. The coalescence rate

arises from two sources: pores from silicon fracture and interface debonding interacting with casting pores and two or more casting pores interacting. Once the macroscale equations and the corresponding material constants were determined from the aforementioned analyses, we performed compression tests at different strain rates and temperatures to determine the plasticity parameters. Included in the compression tests were high strain rate Hopkinson bar analyses (~4000/sec).

Several types of macroscale tests (cm) were then performed to verify our methodology. First, reverse uniaxial tests (Bauschinger effect tests) were performed in which tension was followed by compression and compression was followed by tension up to 2%, 3%, and 5% strain levels. Because the work hardening rate is different in compression than tension due to the preferred damage, the stress state at the end of the reverse test would be different depending on the path history. Indeed, this occurred and the microstructure-mechanical property model was able to accurately capture this coupling of damage and plasticity. Typical power law plasticity formulations would not be able to capture this. The second set of experiments included interrupted notch tests in which the specimens were analyzed nondestructively by x-ray tomography and analyzed via optical imaging analysis. Void volume fractions, sizes, and distributions were quantified at failure, 90% of failure, 95% of failure, and 98% of failure. The finite element analyses, which included the macroscale microstructure-mechanical property model, gave very close results (to within 1%) to the x-ray tomography and optical imaging data.

Once the verification of the physics and validation of numerical implementation was completed, control arm simulations (m) were performed with two goals in mind: first, to finally judge the predictive capability of the model for a control arm, and second, use the model to optimize the control arm by adding mass to certain "weak" regions and taking away mass from "strong" regions. As it turned out, the simulations accurately predicted the final failure locations of the control arm as demonstrated by control arm experiments (Figure 4), and the control arm weight was reduced approximately 26% of the original weight with an increase in load-bearing capacity of 40%.

As another validation comparison, we used the microstructure-mechanical property model for a failure analysis that was of importance to the Department of Energy (DOE). A DOE weapons carrier that had failed in a cast A356 aluminum alloy component required a redesign. The microstructure-mechanical property model described in this report accurately matched the three failure sites (Figure 5) on the component and was used to successfully redesign the component.

In summary, a math-based microstructure-property model was developed based on a multiscale analysis that is implemented in a UMAT routine for (ABAQUS) finite element analysis. This model was used to determine maps of failure strains as a function of silicon particle size and void volume fraction. Hence, a designer/caster can determine the strain at failure given the average silicon particle size and casting porosity fraction as a function of various temperatures, strain rates, dendrite cell sizes, and applied stress states. This information is imperative for designing castings where processing and microstructure are invariably linked.

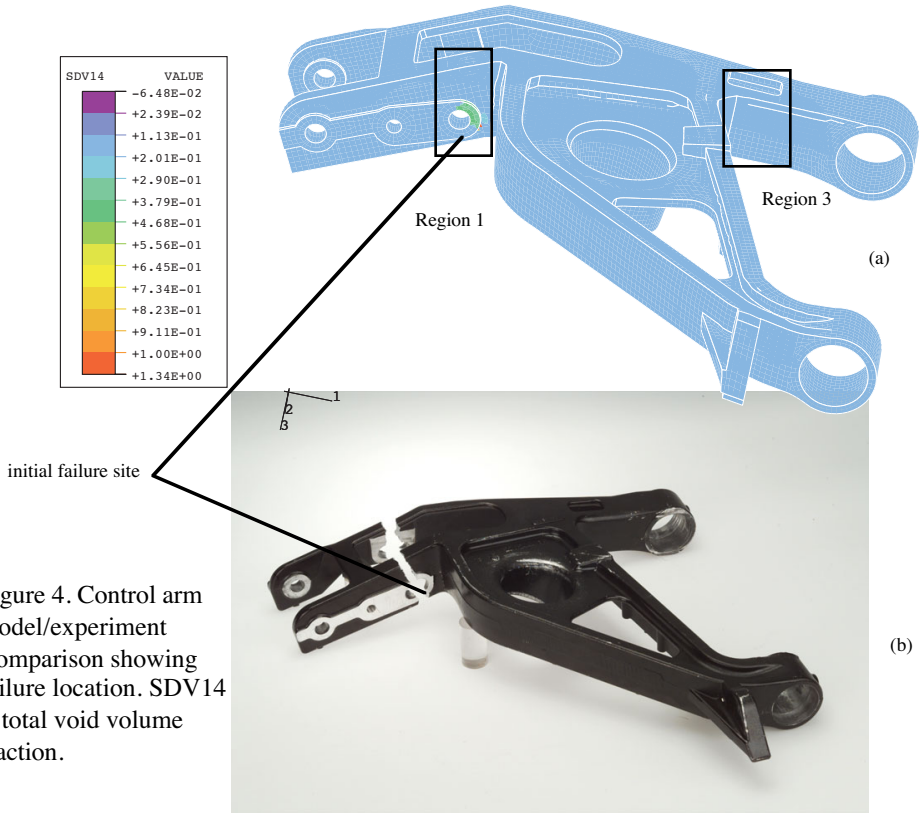

Figure 4. Control arm model/experiment Comparison showing failure location. SDV14 is total void volume fraction.

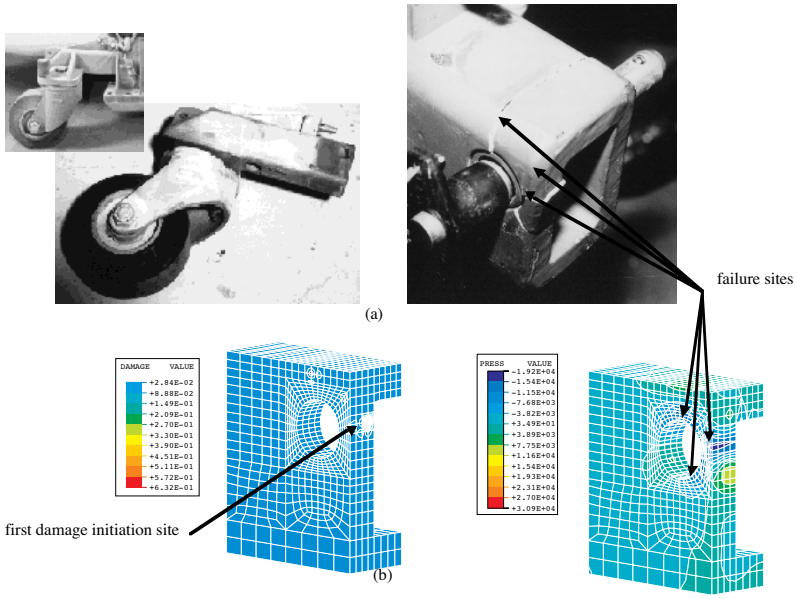

Figure 5. Comparison of (a) experiment and (b) microstructure-property model failure prediction (damage=SDV14) for weapons carrier analysis.

This five year effort was performed under the DOE USCAR-USAMP CRADA including collaborations with LLNL, ORNL, and Georgia Tech. An American Foundrymen's Society award for technical excellence and an R&D 100 award were received as a result of this work.

ACKNOWLEDGMENTS

For the work represented in this report, I certainly cannot take all the credit. First, I recognize that my work was sponsored by the U.S. Department of Energy, Sandia National Laboratories under contract DE-AC04-94AL85000 that has included a CRADA with several industrial partners who also need to be acknowledged for their support, encouragement, and advice. The leadership of Dick Osborne (GM) and Don Penrod (AFS) representing the USCAR Lightweight Metals Group is greatly appreciated along with their encouragement. Gerry Shulke (Chrysler) provided many cast A356 aluminum plates. Discussions with Doug Bammann (Sandia National Labs), David McDowell (Georgia Tech), Jinghong Fan (Georgia Tech), and Ken Gall (Sandia post-doc) were instrumental in developing the model. Nancy Yang (Sandia National Labs) and Arun Gokhale (Georgia Tech) were instrumental in performing microstructural/stereological analyses on many different specimens to help provide the motivation for the modeling effort. Ken Dolan (Lawrence Livermore National Lab) provided x-ray tomography results for the control arm specimens and the notch tensile tests. Paul Nielan (Sandia National Labs) provided the management oversight of the CRADA for Sandia. Jim Sudy and Michele Rhody at Westmoreland Mechanical Testing and Research are to be commended for their oversight of machining and testing all the specimens for the modeling effort. Dan Mosher (Sandia National Labs) performed the high strain rate Hopkinson Bar tests. Michele Matalanis (Cornell Univ.) and Ganesh Ramaswamy (Sandia post-doc) were helpful in performing the void-void coalescence finite element simulations. Matt Botos (Cornell Univ.), Matt Negrete (UC Davis), and Doug Bahr (Cornell Univ.) were helpful in performing the mesoscale finite element simulations. Brett Degner (UC Berkeley) helped by performing finite element analyses of the control arm and helped reduce the weight of the control arm. Fruitful discussions with Srinath Viswanathan (Oak Ridge National Labs) were necessary in understanding the mechanisms involved in the casting process that bring about the microstructural state. Technical reviews and encouragement throughout the program from Vijey Shende (AMCAST), James Burg (ALCOA), Fred Major (ALCAN), and Yi-shin Sheu (GM) are also greatly appreciated. Jeff Crowell, Sam Graham, and Karrolynne Tumacder graciously helped in finalizing this report by their careful reviews and attention to detail. Finally, the sacrifices of my family during my travels of the many meetings required for this program cannot be ignored as they always have been very gracious and supportive of my work.

CONTENTS

FIGURES

TABLES

1. INTRODUCTION

The Partnership for New Generation Vehicles (PNGV) has mandated that a mass produced mid-size automobile be developed in order to achieve greater gas mileage (80 mpg). This is motivated by greater emission requirements and less reliance on foreign oil sources. To achieve this unprecedented milestone in an automobile, weight reduction is a necessity. Of particular interest are the chassis components that have been chosen to be a focal point of weight reduction by the USCAR-USAMP Lightweight Metals Group. This group has identified the cast A356 aluminum alloy to be the material of choice for the chassis components.

Different methods exist to manufacture cast A356 components, and each of the methods introduces a different level of casting porosity and microstructural fineness. The modeling effort described in this report must account for all the possible scenarios of microstructure/inclusion sizes, distributions, and nearest neighbor distances. As such, it is worth briefly describing the different casting processes for context. Castings with the least amount of porosity typically come from squeeze casting. Like all the other casting processes considered here, squeeze casting uses fully liquid metal as the feed material. Squeeze casting is characterized by slow filling rates, minimum turbulence, and high pressure throughout solidification thus lowering the amount of shrinkage porosity. High pressure die casting is popular because it can produce thin walls, great detail, and good dimensional control at a fairly low cost. High pressure die casting is characterized by high pressure during casting compacting trapped pores to small sizes. In vacuum die casting, the dies are evacuated and sealed before the gate is opened. The molten metal is forced in by atmospheric pressure. Shrinkage porosity generally occurs in isolated regions of the casting. In semi-solid metal castings, a partially solidified alloy is introduced into the die and is agitated during flow to produce a rounded, global microstructure. It is used to produce thin sections and high integrity structural components, although this method is a bit expensive. Tilt Pour mold castings are characterized by a gravity pour into a permanent (or semi-permanent sand core). Vacuum riserless castings is a low pressure casting process that has been used for automotive chassis and suspension components. Lost foam castings come from another low pressure method that uses foam for the mold. This inexpensive process can give significantly larger porosity levels than the others. All of these processes are used depending on the design requirements and cost constraints.

Aluminum castings have a rich history of successful use in the automotive and aircraft industry because they are lightweight, fairly inexpensive, and well tested. However, because of their complex microstructure, understanding the mechanical response has been elusive and thus large safety factors in design are needed. Unfortunately, increased safety factors mean increased weight. Finite element analyses are typically performed to determine the highly stressed regions and microstructure analysis and experiments are performed in those regions. However, other regions that have more damaging inclusions could fail sooner than the expected higher stressed region. Alternatively, if only the worst microstructural regions were analyzed, the critical failure location could also be missed since the stresses from the finite element analyses are not considered. Hence the goal of this work is to develop the cause-and-effect understanding of the microstructure-mechanical property relationships. Moreover, our task was to develop a material model that can be used in conjunction with a finite element code. Hence, a chassis designer could

use the microstructure-property model to more precisely design components without such large safety factors. Consequently, a lighter, yet structurally safe component could be designed.

1.1 **MATERIAL: CAST A356 ALUMINUM ALLOY**

In recent years there has been a strong research initiative by the automotive industry to improve the performance of cast aluminum components. One critical aspect of optimizing design is to better understand and quantify damage progression. Developing the ability to predict damage progression is imperative for the design of components that will experience overloads during service due to impacts, rough ground, and crash environments. The progression of damage in nearly all ductile materials subjected to monotonic loading is due to the nucleation, growth, and coalescence of voids (Cocks and Ashby, 1982; Garrison and Moody, 1987). In metallic alloys, the nucleation and subsequent growth of voids occurs primarily at second phase inclusions or precipitates (Palmer and Smith, 1967; Gurland, 1972; Cox and Low, 1974; Hahn and Rosenfield, 1975). Due to their heterogeneous microstructure, cast aluminum alloys are particularly vulnerable to void-crack nucleation, growth and coalescence from Si, Mg, and Fe particles. In addition, cast aluminum alloys contain pre-existing voids (porosity) due to local feeding obstruction through dendritic solidification fronts, trapped gases, or temperature gradient driven solidification shrinkage (Pan *et al.,* 1990, 1991). Notably, pores can form at different material length scales ranging from the sub-micron size to several hundred microns, depending on the solidification process. The size, shape and distribution of the pores will have a strong influence on damage evolution, localization, and mechanical properties of aluminum castings (Pan *et al.,* 1991; Samuel and Samuel, 1995; Horstemeyer and Ramaswamy, 1999).

The microstructure of hypoeutectic cast A356-T6 Al consists of proeutectic (Al-1.6wt%Si) and eutectic (Al-12.6wt%Si) phases. In the eutectic regions, large silicon particles and clusters form a dendritic substructure while the Si remains solutionized in the proeutectic phase. Solidification rate, modification, and heat treatment all dictate the morphology and size of the Si substructures. Faster solidification rates decrease the average dendrite arm spacing (DAS) or equivalently the dendrite cell size (DCS) (Spear, 1963). The controlled addition of modifiers such as pure strontium has little effect on dendrite arm spacing, but can spheroidize elongated Si particles (Hess and Blackman, 1975). Prolonged exposure to a solutionizing temperature (~ 800 K) after casting has a similar effect as modifiers on the Si particle morphology (Meyers, 1986). The aforementioned microstructural alterations have a strong influence on the mechanical properties of Al castings through changes in void nucleation, growth, and coalescence characteristics. Under monotonic loading, cast aluminum alloys with a smaller DAS and/or spheroidized Si particles generally demonstrate more macroscopic ductility and higher ultimate tensile strengths (Harris *et al.,* 1956; Frederick and Bailey, 1968; Closset and Gruzleski, 1982; Vorren *et al.,* 1984; Caceres *et al.,* 1995; Samuel and Samuel, 1995; Yeh and Liu, 1996).

The cast A356 aluminum alloy considered in this study has a work hardenable aluminum matrix with the major second phase being silicon particles in the eutectic region. The aluminum alloy comprises 7% Si, 0.4% Mg, 0.01% Fe, 0.01% Cu, 0.01% Mn, 0.01% Sr, 0.01% Ti, and 0.01% Zn. The material used for this study was retrieved mainly from cast horizontal plates, although we also used data from actual automotive cast components and data from the literature. All of these A356 castings had a T6 annealing.

2. MACROSCALE MICROSTRUCTURE-MECHANICAL PROPERTY MODEL

In this section, we describe the macroscale model which includes the kinematics, damage progression equations, and the elastic-plastic framework. The motivations for the macroscale model equations described in this chapter are given in this chapter but are elucidated in subsequent chapters.

Standard notation is used throughout. Boldface symbols denote tensors the orders of which are indicated by the context. All tensor components are written with respect to a fixed Cartesian coordinate system, and the summation convention is used for repeated Latin indices, unless otherwise indicated. A superposed dot indicates the material time derivative, and a prime ‘ the deviatoric part of a tensor. Let **a** and **b** be vectors, **A** and **B** second order tensors, and **C** a fourth order tensor; the following definitions are used in the text $(\mathbf{A}\cdot\mathbf{B})_{ij}=A_{ik}B_{kj}$, $\mathbf{A}:\mathbf{B}=A_{ij}B_{ij}$, $(\partial A/\partial B)_{ijkl}=\partial A_{ij}/\partial B_{kl}$, $(\mathbf{C}:\mathbf{A})_{ij}=C_{ijkl}A_{kl}$, and $|\mathbf{A}|=(A_{ij}A_{ij})^{1/2}$.

2.1. KINEMATICS OF THE MACROSCALE MODEL

The formulation of the kinematics development follows closely that of Davison et al. (1977) and Bammann and Aifantis (1989). The kinematics of motion combine elastic straining, inelastic flow, and formation and growth of damage and is illustrated by the multiplicative decomposition of the deformation gradient shown in Figure 2.1. The deformation gradient, $\underline{F}$, is decomposed into the isochoric inelastic, or plastic, $\left(\underline{F}_d^p\right)$, dilational inelastic $\left(\underline{F}_v^p\right)$, and elastic parts $\left(\underline{F}^e\right)$ given by

$$\underline{F} = \underline{F}^e \underline{F}_v^p \underline{F}_d^p . \qquad \text{Equation 2.1}$$

Equation 2.1 assumes that the motion of the body is described by a smooth displacement function. This precludes the initiation of discrete failure surfaces but still allows a continuum description of damage. The elastic deformation gradient, $\underline{F}^e$, represents lattice displacements from equilibrium. The inelastic deformation gradient, $\underline{F}_d^p$, represents a continuous distribution of dislocations whose volume preserving motion produces permanent shape changes. The volumetric inelastic deformation gradient, $\underline{F}_v^p$, represents a continuous distribution of voids causing the volume change of the material from that arises from inelastic deformation. It is assumed to have the form $\underline{F}_v^p = \Phi \underline{I}$, where Φ is a function to be determined from kinematics (or conservation of mass).

The Jacobian of equation (2.1) is related to the change in volume or change in density for constant mass as

$$J = \det \underline{F}_v^p = \frac{V_2}{V_0} = \frac{\rho_0}{\rho_2} \qquad \text{Equation 2.2}$$

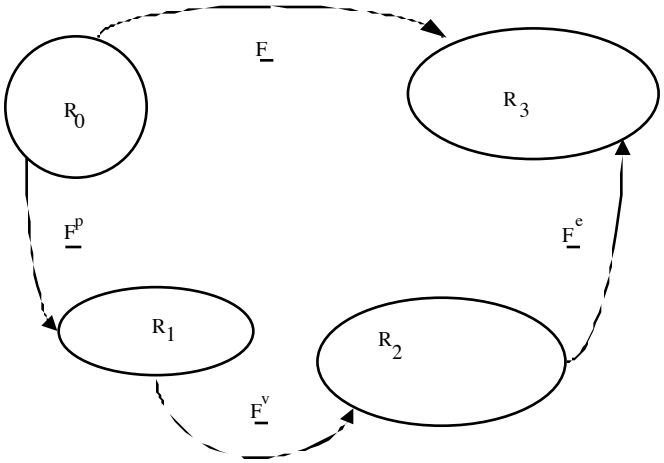

Figure 2.1. Multiplicative decomposition of the deformation gradient into the deviatoric plastic, dilational plastic, and elastic parts.

and must be positive. The change in volume from the reference configuration (State 0) to the intermediate configuration (State 2) is $V_2 = V_0 + V_v$ assuming that the volume in State 0 equals that in State 1 because of inelastic incompressibility. The volume and density in the reference configuration are given by V_0 and ρ_0, respectively. In transforming the configuration from State 0 to State 2, an added volume from the voids, V_v, is introduced to the total volume, but the volume of the solid matter remains unchanged at its reference value, because the material is unstressed in this configuration. The intermediate configuration in State 2 then designates when elastic unloading has occurred. Damage, ϕ, can be defined as the ratio of the change in volume of an element in the elastically unloaded state (State 2) from its volume in the initial reference state to its volume in the elastically unloaded state,

$$\phi = \frac{V_v}{V_2}. \qquad \text{Equation 2.3}$$

From this definition, we get

$$V_0 = (1-\phi)V_2 \qquad \text{Equation 2.4}$$

where now the Jacobian is determined by the damage parameter, ϕ, as

$$J = \det \underline{F}_v^p = \frac{1}{1-\phi}. \qquad \text{Equation 2.5}$$

Consequently, the restriction that damage is assumed to produce isotropic dilatation gives the volumetric part of the deformation gradient as

$$\underline{F}_v^p = \frac{1}{(1-\phi)^{1/3}} \underline{I}, \qquad \text{Equation 2.6}$$

where $\Phi = (1-\phi)^{-1/3}$. The velocity gradient associated with the deformation gradient, $\underline{L} = \dot{\underline{F}}\underline{F}^{-1}$, from Equation 2.1 is given by

$$\underline{L} = \underline{L}^e + \underline{L}_v^p + \underline{L}_d^p \qquad \text{Equation 2.7}$$

where $\underline{D} = \frac{1}{2}\left(\underline{L} + \underline{L}^T\right)$ and $\underline{W} = \frac{1}{2}\left(\underline{L} - \underline{L}^T\right)$ with analogous formulas holding for the elastic, volumetric plastic, and deviatoric plastic parts of the velocity gradients expressed as $\underline{L} = \dot{\underline{F}}\underline{F}^{-1}$. The volumetric part of the velocity gradient is then given by

$$\dot{\underline{F}}_v^p \underline{F}_v^{p\,-1} = \frac{\dot{\phi}}{3(1-\phi)} \underline{I} \qquad \text{Equation 2.8}$$

which defines the plastic volumetric rate of deformation as

$$\underline{D}_v^p = \frac{\dot{\phi}}{3(1-\phi)} \underline{I}. \qquad \text{Equation 2.9}$$

Also note here that $\underline{W}_v^p$ vanishes. The trace of the volumetric part, Equation 2.9, is given as

$$tr\left(\underline{D}_v^p\right) = \frac{\dot{\phi}}{(1-\phi)}, \qquad \text{Equation 2.10}$$

so the damage parameter, ϕ, directly relates to the volumetric rate of deformation. The elastic rate of deformation relates to the volumetric rate of deformation by the additive decomposition of the deformation rates similar to Equation 2.7,

$$\underline{D}^e = \underline{D} - \underline{D}_v^p - \underline{D}_d^p. \qquad \text{Equation 2.11}$$

Similarly, the elastic velocity gradient can be decomposed into components like Equations 2.7 and 2.11, where the elastic spin equals the total spin when no plastic spin is prescribed. Recall that no volumetric component exists for the spin tensor, that is, $\underline{W}_v^p = \underline{0}$.

Now that the rate of deformation related to the damaged state is defined, we can describe damage in terms of void nucleation and void growth in the unstressed intermediate configuration. First, we let N equal the total number of voids in a representative continuum volume V_0 of material in the reference configuration (State 0) and let η^* be the number of voids per unit volume in the reference configuration; hence, $\eta^* = N/V_0$. The average void volume then is $v_v = 1/N\sum_{i=1}^{N} v_i$, where v_i is the void volume from each particle that has nucleated a void. As such the volume of voids is given by

$$V_v = \eta^* V_o v_v \qquad \text{Equation 2.12}$$

By combining this definition and inserting them into Equation 2.3, the damage parameter, ϕ, can be written as

$$\phi = \frac{\eta^* V_0 v_v}{V_0 + \eta^* V_0 v_v} = \frac{\eta^* v_v}{1 + \eta^* v_v}. \qquad \text{Equation 2.13}$$

This formulation for damage was employed by Davison et al. (1977). If the number of voids per unit volume is defined in the intermediate configuration, we can write

$$\phi = \frac{V_v}{V_2} = \frac{V_v}{N}\frac{N}{V_2} = v_v \eta. \qquad \text{Equation 2.14}$$

where

$$\eta = \frac{N}{V_2} = \frac{N}{V_0}\frac{V_0}{V_2} = \eta^* \frac{V_0}{V_2}. \qquad \text{Equation 2.15}$$

Recalling that the unstressed intermediate configuration has the volume $V_2 = V_0 - V_v$ and employing Equation 2.3, we get the relation

$$\eta^* = \eta/(1-\phi). \qquad \text{Equation 2.16}$$

The density of voids is counted after the specimen is loaded to a certain strain level and then unloaded. From this point, the specimen is machined and the number counting of voids nucleated is performed representing the elastically unloaded intermediate configuration; hence, η is experimentally determined.

The damage formulation is shown conceptually in Figure 2.2. The number density of voids can change and growth of voids can occur independently or simultaneously. This framework is illustrated by the schematic in Figure 2.3 when examining the limiting cases. One void growing can exist or many voids can nucleate without void growth. A typical void growth model is

assumed to have an initial void embryo of a size determined by optical micrographs or some other method. As such, the growth rule applies to both voids that are already present and those that are nucleating. These two types of voids would experience the same void growth rule in the damage analysis. Because the void growth rule is initialized with a positive volume, the nucleated void volume is assumed to incur this same initialization volume. Perhaps the most realistic embryo size for the newly nucleated site is the size of the second phase particle. The framework conceivably allows for this initialization as well. For materials with second phases and pre-existing voids, one would anticipate that the average size of the second phase and average size of the pre-existing voids would be different owing to solidification mechanisms. Finally, nucleation is assumed to occur by decohesion of the particle/matrix interface or by particle fracture, and more than one void can be nucleated at a given particle at different sides of the particle.

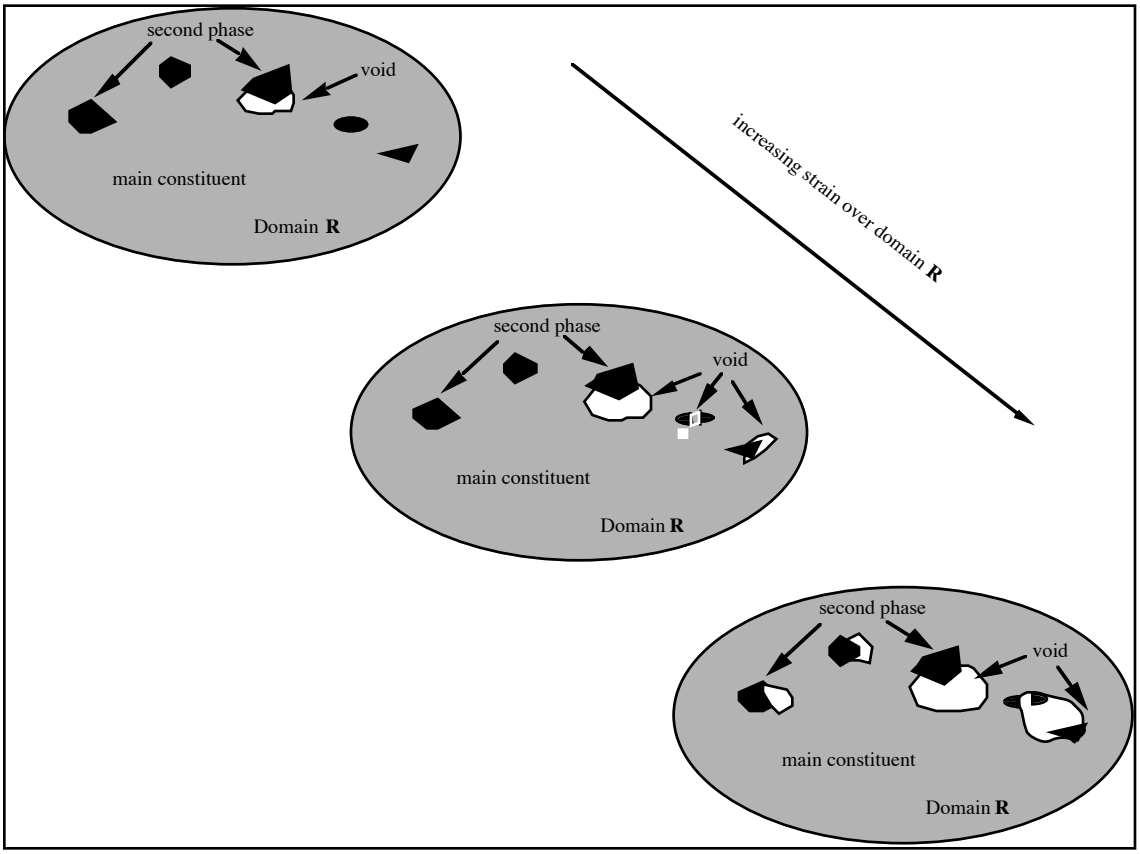

Figure 2.2. Schematic of fictitious material with increasing void nucleation density and void growth in which the model conceptually comprises.

2.2. VOID NUCLEATION, GROWTH, AND COALESCENCE ASPECTS OF MACROSCALE MODEL

In this section, the parameters for the void nucleation, growth, and coalescence terms are determined and explained. We first start with void nucleation.

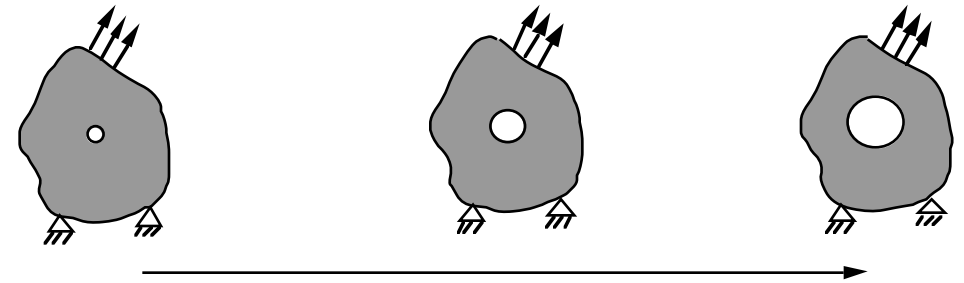

(a) increasing void growth

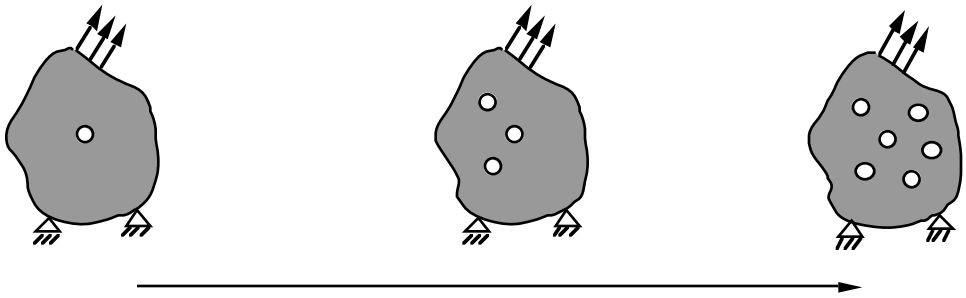

(b) increasing nucleation sites

Figure 2.3. The damage model encompasses the limiting cases shown by (a) a single void growing in and (b) just void nucleation.

The void nucleation rule of Horstemeyer and Gokhale (1998) is used to model the results from the cast A356 aluminum data under compression, tension, and torsion. The integrated form of the void nucleation rate equation is given by

$$\eta(t) = C_{coeff} \exp\left(\frac{\varepsilon(t) d^{1/2}}{K_{IC} f^{1/3}} \left\{ a\left[\frac{4}{27} - \frac{J_3^{\,2}}{J_2^{\,3}} \right] + b \frac{J_3}{J_2^{\,3/2}} + c \left\| \frac{I_1}{\sqrt{J_2}} \right\| \right\} \right) \exp\left(C_{T\eta} T \right), \qquad \text{Equation 2.17}$$

where $\eta(t)$ is the void nucleation density, $\varepsilon(t)$ is the strain at time t, C_{coeff} is a material constant. T is temperature in the absolute scale, and C_{T_η} is the temperature dependent material constant determined from experiments (Figure 3.19). The material parameters a, b, and c relate to the volume fraction of nucleation events arising from local microstresses in the material. These constants are determined experimentally from tension, compression, and torsion tests in which the number density of void sites is measured at different strain levels. The stress state dependence on damage evolution is captured in Equation 2.17 by using the stress invariants denoted by I_1, J_2, and J_3, respectively. I_1 is the first invariant of stress ($I_1 = \sigma_{kk}$). J_2 is the second invariant of deviatoric stress ($J_2 = \frac{1}{2} S_{ij} S_{ij}$), where $S_{ij} = \sigma_{ij} - \frac{1}{3}\delta_{ij}\sigma_{kk}$. J_3 is the third invariant of deviatoric stress ($J_3 = S_{ij} S_{jk} S_{ki}$), The rationale and motivation for using these three invariants of stress is discussed in Horstemeyer and Gokhale (1998). The volume fraction of the second phase material is f, the average silicon particle size is d, and the bulk fracture toughness is K_{IC}.

For the cast A356 aluminum alloy in our study, K_{1C}=17.3 MPa-m^0.5, d=6 μm, and f=0.07. The volume fraction and average size were determined from optical images of the sectioned test specimens. Fracture toughness tests were performed to determine K_{1C}. The stress state parameters were determined to be a=615.46 GPa, b=58.64 GPa, c=30.011 GPa, and C_{coeff} =90. In tension, compression, and torsion, specimens were strained to various levels and then unloaded. Samples from the specimens were extracted for image analysis, and the number of damaged sites were then counted.

A crucial feature in determining the damage state, besides nucleation of voids, is void growth. Many void growth rules have been developed and studied (Garrison and Moody, 1987; Tvergaard, 1990) but none can comprehensively capture different levels of stress triaxialities, different hardening rates, different strain rates, and different temperature regimes. The damage framework allows for different void growth rules to be included and evaluated. We considered several void growth models. The first one by McClintock (1968) is given in terms of the void radius as ,

$$\dot{r} = \frac{\sqrt{3}R_0}{2(1-n)}\left[\sinh\left(\sqrt{3}(1-n)\frac{\sqrt{2}I_1}{3\sqrt{J_2}}\right)\right]\dot{\varepsilon}. \qquad \text{Equation 2.18}$$

In Equation 2.18 the void volume grows as the strain and/or stress triaxiality increases. The material constant n is related to the strain hardening exponent and is determined from the tension tests. R_0 is taken to be the initial radius of the voids. As with most void growth models, the McClintock model allows voids to grow in tension, but not in compression or torsion. This complies with physical observations from measurements of this cast Al-Si-Mg aluminum alloy. Another void growth model in terms of void radius is given by Rice and Tracey (1969) is given by,

$$\dot{r} = 0.283R_0\exp\left(\frac{3}{2}\frac{\sqrt{2}I_1}{3\sqrt{J_2}}\right)\dot{\varepsilon} \qquad \text{Equation 2.19}$$

Another void growth model by Budiansky et al. (1982) in terms of void volume rate is given by,

$$\dot{v} = \frac{3}{2}v\left[\frac{3m}{2}\frac{\sqrt{2}I_1}{3\sqrt{J_2}} + (1+m)(1+0.4319m)\right]^{1/m}\dot{\varepsilon} \qquad \text{Equation 2.20}$$

The last one worth mentioning in this context is that by Cocks and Ashby (1981) given in terms of the void volume fraction rate,

$$\dot{\phi} = \left[\frac{1}{(1-\phi)^{1/m}} - (1-\phi)\right]\sinh\left[\frac{2(2-m)}{2+m}\frac{\sqrt{2}I_1}{3\sqrt{J_2}}\right]\dot{\varepsilon} \qquad \text{Equation 2.21}$$

As it turns out, all of these void growth rules give very similar results as will demonstrated later. In practice, the McCintock (1968) model was used for the silicon particles and the Cocks and Ashby (1982) model was used for the casting pores.

Another item related to damage is the phenomenon of void coalescence. Coalescence is the joining of voids either at the microscale or macroscale and has been observed to occur by two main mechanisms. The first mechanism (Garber et al., 1976) occurs when two neighboring voids grow together until they join as one, that is, as the ligament between them necks down to a point as illustrated in Figure 2.4. Another mechanism occurs when a localized shear band occurs between neighboring voids (Cox and Low, 1974; Rogers, 1960), often referred to as the "void sheet" mechanism also shown in Figure 2.4.

Coalescence can be added to the damage framework described in Equations 2.14. It arises naturally with the multiplicative relation between the nucleation and growth terms. As Figure 2.4 demonstrates, we start with two voids that are nucleated and each independently grows until they join together. Then, one void emerges as they coalesce together. The coalescence event causes a discontinuous jump in the nucleation evolution and growth evolution but allows for continuous growth of total damage evolution, ϕ. Although discontinuities occur in discrete regions for the nucleation and growth rules, the rate equations evolve as internal state variables at a higher length scale in the continuum where their effects are observed on macroscale effective quantities and thus are continuous functions.

In a phenomenological manner, we include a coalescence term as

$$C = \left[C_{D1} + C_{D2}\eta v\right]\left(\frac{DCS_0}{DCS}\right)^z \left(TC_{TC}\right), \qquad \text{Equation 2.26}$$

to get

$$\phi = (\eta v + \phi_{pore})C \qquad \text{Equation 2.27}$$

In the limiting case when the function $C_{D2} = 0$ in Equation 2.26 equals zero, simple coalescence occurs. In this case, the model reflects the growing of two voids into one. When $C_{D2} \neq 0$, microvoid linking is reflected and the rate of damage is increased. Garrison and Moody [1987] and Magnusen et al. [1988] observed that the microvoid sheet mechanism is related to particles initiating small voids in between two larger voids as the larger voids impose their influence on the surrounding region. As such, coalescence is a function of both nucleation and void growth. Actually, both forms of coalescence occur in this material and hence both constants C_{D1} and C_{D2} are nonzero.

From Equation 2.27, we see that the void nucleation and growth arise from the η and v, which relate to the silicon particles. The ϕ_{pore} term is related to the casting porosity and its growth is given by the Cocks and Ashby (1981) void growth form (Equation 2.21). Here, the coalescence operates on the both the silicon fracturing/debonding into voids and the initial porosity that

grows. Results from the mesomechanical finite element simulations motivated this phenomenological form.

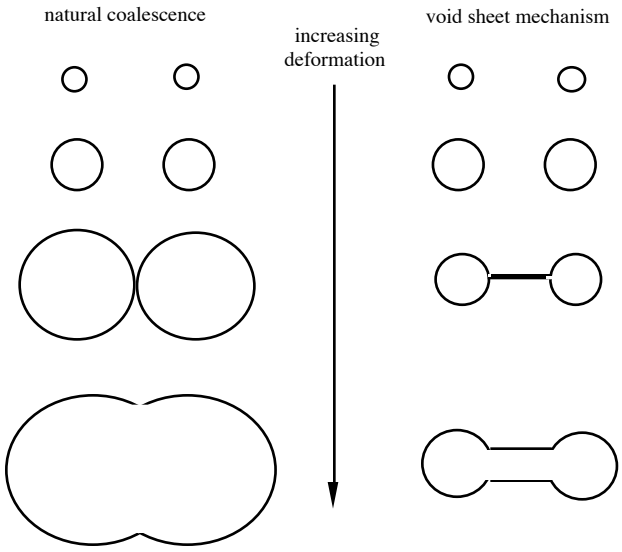

Figure 2.4. Two different coalescence mechanisms observed in various materials.

The dependence on DCS comes in based on the work of Major et al. (1994). They noted a dependence of the elongation to failure with the DCS. Since the elongation to failure is directly a result of the damage progression, we can assert that the DCS influences the damage progression. But in what way? It may be that the DCS really scales with the casting pore size and that would directly influence the damage progression. If that is true, then there would be no need to include the DCS in the coalescence model because the initial void size is already included in the model via the void growth model; however, the DCS may come into play as it reveals a length scale by which the nearest neighbor voids are represented in some, at this point, unquantifiable fashion. If the DCS reflects a quasi-nearest neighbor distance, then dislocation interaction around voids would be enhanced by a smaller DCS as described by the mesomechanical finite element simulations show in Chapter 4. In this case, the DCS would need to be included in the coalescence term. The parameter z comes in to normalize the effect of the DCS and also plays a role in the work hardening rate as will be shown in the next section. The effect of the DCS is minor compared to the other features in the model.

The temperature dependence of the coalescence term was determined from the multitude of mesomechanical simulations discussed in Chapter 4. A general trend was determined from the mesomechanical simulations, and the constant C_{TC} was determined. More work related to the coalescence needs to be done, but to first order this form captures most of the features observed from microstructure/inclusion behavior.

2.3. ELASTIC-PLASTIC ASPECTS OF MACROSCALE MODEL

The internal state variable (ISV) plasticity model (Bammann et al., 1993) is modified to account for stress state dependent damage evolution. The pertinent equations in this model are denoted by the rate of change of the observable and internal state variables. The equations used within the context of the finite element method are given by,

$$\overset{\circ}{\underline{\sigma}} = \dot{\underline{\sigma}} - \underline{W}^{e}\underline{\sigma} - \underline{\sigma}\underline{W}^{e} = \lambda(1-D)tr\left(\underline{D}^{e}\right)\underline{I} + 2\mu(1-D)\underline{D}^{e} - \frac{\dot{D}}{1-D}\underline{\sigma} \qquad \text{Equation 2.28}$$

$$\underline{D}^{e} = \underline{D} - \underline{D}^{in} \qquad \text{Equation 2.29}$$

$$\underline{D}^{in} = f(T)\sinh\left[\frac{\left\|\underline{\sigma}'-\underline{\alpha}\right\| - \left\{R+Y(T)\right\}\left\{1-D\right\}}{V(T)\left\{1-D\right\}}\right]\frac{\underline{\sigma}'-\underline{\alpha}}{\left\|\underline{\sigma}'-\underline{\alpha}\right\|} \qquad \text{Equation 2.30}$$

$$\overset{o}{\underline{\alpha}} = \dot{\underline{\alpha}} - \underline{W}^{e}\underline{\alpha} + \underline{\alpha}\underline{W}^{e} = \left\{h(T)\underline{D}^{in} - \left[\sqrt{\frac{2}{3}}r_d(T)\left\|\underline{D}^{in}\right\| + r_s(T)\right]\|\underline{\alpha}\|\underline{\alpha}\right\}\left[\frac{DCS_0}{DCS}\right]^{z} \qquad \text{Equation 2.31}$$

$$\dot{R} = \left\{H(T)\underline{D}^{in} - \left[\sqrt{\frac{2}{3}}R_d(T)\left\|\underline{D}^{in}\right\| + R_s(T)\right]R^2\right\}\left[\frac{DCS_0}{DCS}\right]^{z} \qquad \text{Equation 2.32}$$

$$\dot{D} = \left[\dot{\phi}_{particles} + \dot{\phi}_{pores}\right]c + \left[\phi_{particles} + \phi_{pores}\right]\dot{c}\,, \qquad \text{Equation 2.33}$$

$$\dot{\phi}_{particles} = \dot{\eta}v + \eta\dot{v} \qquad \text{Equation 2.34}$$

$$\dot{\eta} = \left\|\underline{D}^{in}\right\|\frac{d^{1/2}}{K_{IC}f^{1/3}}\eta\left\{a\left[\frac{4}{27} - \frac{J_3^{\,2}}{J_2^{\,3}}\right] + b\frac{J_3}{J_2^{3/2}} + c\left\|\frac{I_1}{\sqrt{J_2}}\right\|\right\}\exp\left(-C_{\eta T}\,T\right) \qquad \text{Equation 2.35}$$

$$\dot{v} = \frac{3}{2}v\left[\frac{3}{2}\frac{V(T)}{Y(T)}\frac{\sigma_H}{\sigma_{vm}} + \left(1-\frac{V(T)}{Y(T)}\right)(1+0.4319)\right]^{Y(T)/V(T)}\underline{D}^{in} \qquad \text{Equation 2.36}$$

$$\dot{c} = C_{coal}\left[\eta\dot{v} + \dot{\eta}v\right]\exp\left(C_{CT}T\right)\left(DCS_0/DCS\right)^{z} \qquad \text{Equation 2.37}$$

$$\dot{\phi}_{pores} = \left[\frac{1}{\left(1-\phi_{pores}\right)^{m}} - \left(1-\phi_{pores}\right)\right]\sinh\left\{\frac{2\left(2^{V(T)/Y(T)}-1\right)}{\left(2^{V(T)/Y(T)}+1\right)}\frac{\sigma_H}{\sigma_{vm}}\right\}\left\|\underline{D}^{in}\right\| \qquad \text{Equation 2.38}$$

The rate equations are generally written as objective rates ($\overset{o}{\underline{\sigma}}, \overset{o}{\underline{\alpha}}$) with indifference to the continuum frame of reference assuming a Jaumann rate in which the continuum spin equals the elastic spin ($\underline{W} = \underline{W}^{e}$). The internal state variable (ISV) Equations 2.28-2.38 are functions of the observable variables (temperature, stress state, and rate of deformation). In general, the rate

equations of generalized displacements, or thermodynamics fluxes, describing the rate of change may be written as independent equations for each ISV or as derivatives of a suitably chosen potential function arising from the hypothesis of generalized normality (Rice, 1971). An advantage of assuming generalized normality, although somewhat restrictive, is unconditional satisfaction of the Kelvin inequality of the second law of thermodynamics (nonnegative intrinsic dissipation), i.e.

$$\underline{\sigma} : \underline{D}^{in} - \underline{b} : \overset{\circ}{\underline{\alpha}} - \kappa \bullet \dot{R} - \phi \bullet \dot{D} \geq 0. \qquad \text{Equation 2.39}$$

The selection of the ISVs may, in principle, be somewhat arbitrary, but the kinematic hardening, isotropic hardening, and damage rate equations are physically motivated and strongly influence the history of the material. The ISV model accounts for deviatoric inelastic deformation resulting from the presence of dislocations in crystallographic material, dilatational deformation, and ensuing failure from damage progression. Damage will reduce the material strength, enhance the inelastic flow, and soften the elastic moduli.

In Equation 2.28, the elastic Lame constants are denoted by λ and μ. The elastic rate of deformation ($\underline{D}^{e}$) results when the the flow rule as shown in Equation 2.28 is subtracted from the total deformation ($\underline{D}$), which is defined by the boundary conditions.

The independent variables for the inelastic rate of deformation are given in Equation 2.30 as the stress, temperature, and internal state variables. This is similar to power law and Garofalo equations for creep except that the ISVs are now included. The deviatoric inelastic flow rule, $\underline{D}^{in}$, encompasses the regimes of creep and plasticity and is a function of the temperature, the kinematic hardening internal state variable ($\underline{\alpha}$), the isotropic hardening internal state variable (R), the volume fraction of damaged material (D), and the functions $f(T)$, $V(T)$, and $Y(T)$, which are related to yielding with Arrhenius-type temperature dependence. The function $Y(T)$ is the rate-independent yield stress. The function $f(T)$ determines when the rate-dependence affects initial yielding. The function $V(T)$ determines the magnitude of rate-dependence on yielding. These functions are determined from simple isothermal compression tests with different strain rates and temperatures,

$$V(T) = C_1 \exp\left(-C_2 / T\right),\ Y(T) = C_3 \exp\left(C_4 / T\right),\ f(T) = C_5 \exp\left(-C_6 / T\right). \qquad \text{Equation 2.40}$$

The kinematic hardening internal state variable, $\underline{\alpha}$, reflects the effect of anisotropic dislocation density, and the isotropic hardening internal state variable R, reflects the effect of the global dislocation density. As such, the hardening Equations 2.31-2.32 are cast in a hardening-recovery format that includes dynamic and static recovery. The functions $r_s(T)$ and $R_s(T)$ are scalar in nature and describe the diffusion-controlled static or thermal recovery, while $r_d(T)$ and $R_d(T)$ are scalar functions describing dynamic recovery. Hence, the two main types of recovery that are exhibited by populations of dislocations within crystallographic materials are captured in the ISVs. The anisotropic hardening modulus is $h(T)$, and the isotropic hardening modulus is $H(T)$.

The hardening moduli and dynamic recovery functions account for deformation-induced anisotropy arising from texture and dislocation substructures by means of stress-dependent variables. Miller and McDowell (1992) showed that by using $J_3^{'}$ in the hardening equations the different hardening rates between axisymmetric compression and torsion (torsional softening) were accurately captured. Miller *et al*. (1995) and Horstemeyer *et al*. (1995) included this feature in the Bammann ISV model as

$$r_d(T) = C_7\left(1 + C_{19}\left[\frac{4}{27} - \frac{J_3^{'2}}{J_2^{'3}}\right]\right)\exp\left(-C_8/T\right), \qquad \text{Equation 2.41}$$

$$h(T) = \left\{C_9\left(1 + C_{20}\left[\frac{4}{27} - \frac{J_3^{'2}}{J_2^{'3}}\right]\right)\right\} - C_{10}T, \qquad \text{Equation 2.42}$$

$$r_s(T) = C_{11}\exp\left(-C_{12}/T\right), \qquad \text{Equation 2.43}$$

$$R_d(T) = C_{13}\left(1 + C_{21}\left[\frac{4}{27} - \frac{J_3^{'2}}{J_2^{'3}}\right]\right)\exp\left(-C_{14}/T\right), \qquad \text{Equation 2.44}$$

$$H = \left\{C_{15}\left(1 + C_{22}\left[\frac{4}{27} - \frac{J_3^{'2}}{J_2^{'3}}\right]\right)\right\} - C_{16}T, \qquad \text{Equation 2.45}$$

$$R_s(T) = C_{17}\exp\left(-C_{18}/T\right), \qquad \text{Equation 2.46}$$

where $J_2^{'} = \frac{1}{2}\left(\underline{\sigma}' - \underline{\alpha}\right)^2$ and $J_3^{'} = \frac{1}{3}\left(\underline{\sigma}' - \underline{\alpha}\right)^3$. The deviatoric stress $\underline{\sigma}'$ is expressed in indicial notation as

$$\sigma_{ij}' = \sigma_{ij} - \frac{1}{3}\sigma_{ii}. \qquad \text{Equation 2.47}$$

The damage variable D represents the damage fraction of material within a continuum element. The mechanical properties of a material depend upon the amount and type of microdefects within its structure. Deformation changes these microdefects, and when the number of microdefects accumulates, damage is said to have grown. The notion of a damaged state in continuum field theory emerged when Kachanov (1958) introduced a damage variable to describe the microdefect density locally in a creeping material. The idea was that damage could be measured by the volume fraction of voids under creep conditions. Rabotnov (1969) furthered this notion with an rate equation of void density.

Equation 2.6 introduces the void volume fraction (porosity) as damage. By including damage, D, as an ISV, different forms of damage rules can easily be incorporated into the constitutive framework. Bammann *et al*. (1993; 1996) and Horstemeyer (1992, 1993) have demonstrated the applicability of the Cocks and Ashby (1980) void growth rule used as the damage rate equation in the ISV model.

The generalized thermodynamic force conjugate, ϕ, is often referred to as the energy release rate for elastic brittle materials and the J-integral for inelasticity. In essence, an increment of damage will have associated energy released per unit damage extension as new damaged area (or volume) is developed.

In Equations 2.33-2.38, the damage progression is divided into void nucleation and growth from silicon particles and from pores. Coalescence is introduced to reflect pore-pore interactions and silicon-pore interactions as expressed in Equation 2.37. The void nucleation evolution described by Equation 2.35 is discussed in length by Horstemeyer and Gokhale (1999). The void growth related to silicon particles, Equation 2.36, is that from Budiansky *et al*. (1982). Other forms can be used and evaluated (cf., Horstemeyer *et al*., 1999), but this equation allows for a strain rate sensitivity in relation the plasticity model ($m=V(T)/Y(T)$). For the porosity evolution, the Cocks and Ashby (1981) void growth rule is used as shown in Equation 2.38.

2.4. MACROSCALE MODEL SUMMARY

A damage evolution model that incorporates separate evolving functions for void nucleation, growth, and coalescence was implemented into the modified finite strain ISV plasticity model (Bammann et al., 1993) to solve boundary value problems with the finite element method. The practicality and physical basis for the void nucleation model of Horstemeyer and Gokhale (1999) is illustrated by determining the model parameters to cast A356 aluminum experimental observations. The experiments revealed that void nucleation is a function of the stress state of the material and that void nucleation proves critical to the developing damage state of cast A356 aluminum. Finite element calculations of notch tensile bars were performed to illustrate the use of the model.

This page intentionally blank

3. VOID-CRACK NUCLEATION

In order to develop a macroscale phenomenological void-crack nucleation model for ductile metals with second phases, atomic scale and microscale physical observations are needed. The competing processes of silicon fracture and aluminum-silicon interface debonding need to be sorted out in terms of developing the critical limiting parameters. Not only with respect to a cast A356 aluminum alloy, understanding the debonding and fracture characteristics of bi-material interfaces is central to modeling the mechanical response of a broad range of engineering materials. Metal matrix composites (Everett and Arsenault, 1991), unidirectional composites (Daniel and Ishai, 1994), cast aluminum alloys (Plumtree and Schafer, 1986; Gall *et al.*, 1999), commercial grade wrought aluminum (Grosskreutz and Shaw, 1969), and wrought steel alloys (Lankford and Kusenberger, 1973) all contain bi-material interfaces via second phase particles or fibers embedded in a matrix material. An interface between two different materials is traditionally classified as coherent, semi-coherent, or incoherent based on the local atomic arrangement. Relatively strong coherent interfaces usually only exist for second phase particles (precipitates) much smaller than a micron. Coherent precipitates control, for example, the high monotonic strength levels in age-hardenable aluminum alloys (Bray, 1990). Larger second phase particles (inclusions) embedded in a matrix material usually have incoherent interfaces, unless the crystal lattice mismatch between the adjoining two materials is negligible. The local deformation characteristics within large incoherent inclusions and in the surrounding matrix material have a strong influence on the mechanical properties of a composite material. For example, under cyclic loading conditions, second phase silicon or aluminum-oxide inclusions serve as fatigue crack nucleation sites in cast (Plumtree and Schafer, 1986; Gall *et al.*, 1999) and wrought (Grosskreutz and Shaw, 1969) aluminum alloys.

Predicting the monotonic or cyclic mechanical properties of materials containing incoherent inclusions requires knowledge of the local misfit stress and strain distributions near such particles when a material is subjected to far-field boundary conditions. For pristine and perfectly bonded inclusions, an Eshelby based approach (Eshelby, 1957) can be used to obtain a relationship between local and far-field stresses and strains. However, second phase inclusions within a ductile matrix are not always pristine, but rather can be fractured or debonded (Puttick, 1959; Grosskreutz and Shaw, 1969; Broek, 1973; Lankford and Kusenberger, 1973; Hahn and Rosenfield, 1975). For example, Figure 3.1 is a duo of scanning electron microscope (SEM) images taken from a fracture surface of A356 cast Al, subjected to cyclic loading conditions (Gall *et al.*, 1999). The SEM images demonstrate that pure silicon inclusions within a ductile aluminum matrix may (a) fracture or (b) debond depending on the fatigue crack tip driving force (striation spacing) and inclusion morphology. Predicting whether an inclusion will fracture versus debond for different particle shapes and loading conditions is difficult without information on the relative strength of the particle versus its interface with the matrix material.

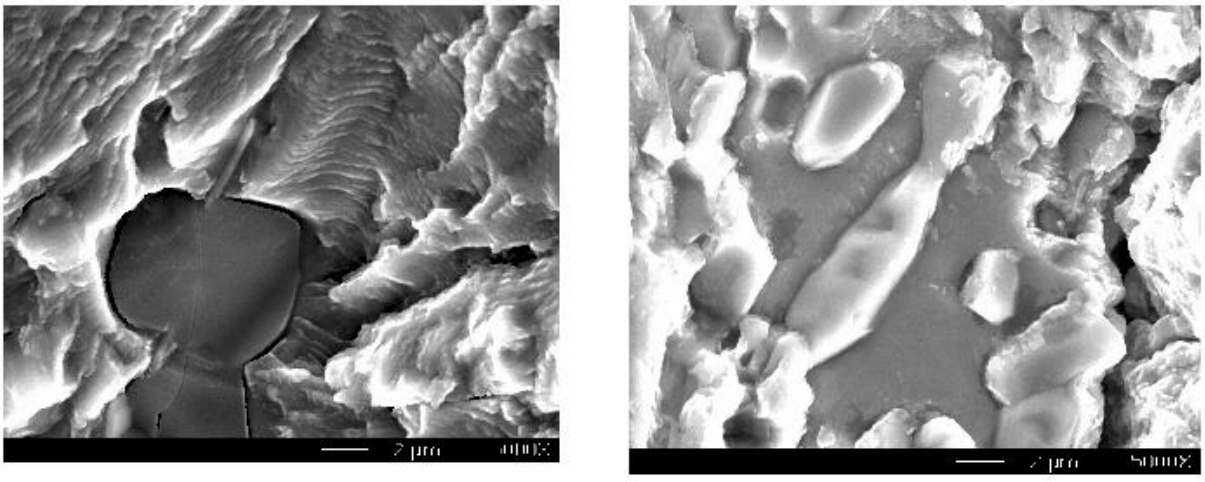

(a) (b)

Figure 3.1. Scanning electron microscope images of the fracture surface of a cast A356-al alloy subjected to cyclic loading conditions. The images demonstrate that pure silicon inclusions are observed to both (a) fracture and (b) debond.

As second phase particles fracture or debond, finite element calculations can be used to obtain the evolution of local stress and strain distributions with respect to the far-field boundary conditions (Harkegard, 1973; Gall *et al*., 1999-B). One consideration in the finite element modeling of interface debonding, and crack propagation in general, is modeling the generation of free surfaces. Previous finite element studies have used cohesive zone approaches (Dugdale, 1960; Barenblatt, 1962) to model, for example, fracture in rocks (Boone *et al*., 1986), inclusion debonding in ductile materials (Needleman, 1987; Xu and Needleman, 1993) dynamic crack propagation in brittle materials (Camacho and Ortiz, 1996), failure of adhesive joints (Tvergaard and Hutchinson 1994, 1996), and various other interfacial crack growth problems (Needleman, 1990-a, b; Suo *et al.*, 1992; Tvergaard and Hutchinson 1992; Needleman, 1992; Xu and Needleman, 1993, 1995, 1996; Needleman, 1997; Bigoni *et al.*, 1997; Siegmund *et al.*, 1997; Xu *et al.*, 1997). The mathematical forms for cohesive zone equations are motivated (Needleman, 1990-a) from metallic atomic binding energy relationships (Rose *et al.*, 1981; Rose *et al.*, 1983; Ferrante and Smith, 1985).

Given this background we proceed first with atomistic simulations to determine an understanding of silicon fracture and silicon-aluminum interface debonding. Second, we perform microscale finite element analyses to determine the parameters of interest for macroscale microstructure-mechanical property model.

3.1. ATOMISTIC STUDIES

The present atomistic study will consider the deformation characteristics of the interface between pure FCC aluminum (Al) and diamond cubic silicon (Si). Al-Si interfaces have technological importance in cast Al-Si alloys and electronics packaging applications. We will use the semi-empirical Modified Embedded Atom Method (MEAM) (Baskes, 1992) to model the Al-Si interfaces under imposed tensile boundary conditions. The MEAM (Baskes, 1992) differs from the standard EAM (Daw and Baskes, 1984) in that the angular dependence of the electron density is included in the MEAM. With exception to one MEAM simulation, which was deformed under static loading conditions at 0 K, all models were deformed in the molecular dynamics framework at high strain rates (1×10^9 1/s). The MEAM is a powerful tool for analyzing local interfacial failure mechanisms since the structure and/or strength of the interface need not be assumed *a priori*. Consequently, the predictions of the MEAM simulations provide insight into the underlying physics of interfacial decohesion and fracture.

Previous MEAM simulations on the characteristics of Ni-Si interfaces (Baskes *et al.*, 1994) have provided insightful results. In general, the work of Baskes *et al.*, (1994) determined the structure and adhesion energy of a thin layer of Ni on a Si substrate. However, such MEAM studies on Ni-Si interfaces have not considered the effects of different MEAM models on the strength of the interface. In order to draw accurate comparisons with continuum based debonding models, a more thorough study of the effects of MEAM model geometry, loading, and displacement measurement conditions should be undertaken. The current MEAM simulations consider the stress-strain and traction-displacement responses of Al and Si blocks of various size, attached at a flat interface, and subjected to tensile boundary conditions applied parallel to the interface normal. The effect of randomly dispersed point vacancy defects on the strength of the interface is investigated. In addition, the effect of crack-like vacancy defect size on the competing failure mechanisms of Al-Si interface debonding versus isolated fracture in the Al or Si is considered. Finally, different locations for measuring opening displacement are discussed in the framework of a continuum based cohesive zone approach. This preliminary study will not consider the effects of pertinent metallurgical factors such as interface misorientations (Kurtz and Hoagland, 1998), dislocations (Kurtz and Hoagland, 1998), or impurities (Rice and Wang, 1989; Olson, 1997). We attempt here to determine the overall applicability of atomistic simulations to study interfacial decohesion in the context of current continuum based modeling approaches. Once the task at hand has been accomplished, the effects of the aforementioned metallurgical factors can be more effectively studied.

The results of the present study augment the findings of different experimental techniques used to characterize the structure, strength, and fracture behavior of bi-material interfaces. For example, the properties of material interfaces have been studied using a wide range of mechanical testing methods such as: peel tests (Yoshino and Shibata, 1992), laser spallation tests (Gupta *et al.*, 1993), zero-creep tests (Josell and Spaepen, 1993-a, b), push-through tests (Warren *et al.*, 1992; Mackin *et al.*, 1992; Izawa *et al.*, 1996), pull-out tests (Lamon *et al.*, 1995), normal tension tests (He *et al.*, 1996), transverse compression tests (Turner and Evans, 1996), and bending tests (Reimanis *et al.*, 1990; Reimanis *et al.*, 1991; Bartlett and Evans, 1993; Leung *et al.*, 1995). The particular conclusions of the aforementioned collection of experimental studies are dependent on the material studied. However, the interface between two adjoining materials

almost always serves as the weak link for failure for all material systems and loading conditions considered. In addition to the experimental studies, numerous analytical approaches (Erdogan, 1963; Rice and Sih, 1965; Comninou, 1990; Loboda, 1998) have been used to study the stress and strain fields near interfacial cracks in dissimilar materials, analogous to fracture mechanics based approaches for homogeneous materials. Energy based criteria have also been utilized to study the competing modes of interface debonding versus fracture into the bulk materials (Evans *et al.,* 1989; He *et al.,* 1994).

3.1.1 ATOMISTIC SIMULATION PRELIMINARIES

Atomistic calculations, starting from atomic pair potentials or some related modification, have been used for a wide variety of materials. Brenner (1996) summarized the class of bond order formalism that has proven valuable for covalently bonded systems. Stoneham *et al.* (1996) summarized the shell model, which is a modification of a pair potential, used for ceramics. For metals, Daw and Baskes (1984) developed the MEAM, which employs a pair potential augmented by a function of another pair-wise sum based on the electron density. We use the MEAM in the atomistic simulations for the study of finite deformations of single crystal aluminum and silicon and the interface between the two materials.

The notion of embedding energy was first suggested by Friedel (1952) and further developed by Stott and Zaremba (1980). Daw and Baskes (1984) proposed a numerical method for calculating atomic energetics. Daw *et al.* (1993) summarize many applications of MEAM. Essentially, MEAM comprises a cohesive energy of an atom determined by the local electron density into which that atom is placed. A function, ρ, is viewed as the contribution to the electron density at a site due to the neighboring atoms. The embedding energy, F, is associated with placing an atom in that electron environment. The functional form of the total energy is given by

$$E = \sum_i F^i\left(\sum_{i\neq j}\rho^i\left(r^{ij}\right)\right) + \frac{1}{2}\sum_{ij}\phi^{ij}\left(r^{ij}\right), \qquad \text{Equation 3.1}$$

where i refers to the atom in question and j refers to the neighboring atom, r^{ij} is the separation distance between atoms i and j, and f^{ij} is the pair potential. Because each atom is counted, contravariant and covariant index notation is not used here. Subscripts denote the rank of the tensor, for example, one subscript denotes a vector, two subscripts denote a second rank tensor, and so on. Superscripts identify the atom of interest. In molecular dynamics, the energy is used to determine the forces on each atom. At each atom the dipole force tensor, b_{ij}, is given by

$$\beta^i_{km} = \frac{1}{\Omega^i}\sum_{j(\neq i)}^{N} f^i_k\left(r^{ij}\right) r^{ij}_m, \qquad \text{Equation 3.2}$$

where i refers to the atom in question and j refers to the neighboring atom, f_k is the force vector between atoms, r_m is a displacement vector between atoms i and j, N is the number of nearest neighbor atoms, and W^i is the atomic volume. If stress could be defined at an atom, then b_{ij}

would be the stress tensor at that point. Since stress is defined at a continuum point, we determine the stress tensor as a volume average over the block of material,

$$\sigma_{mk} = \frac{1}{N*}\sum_{i}^{N*}\beta_{mk}^{i}, \qquad \text{Equation 3.3}$$

in which the stress tensor is defined in terms of the total number of atoms, N* , in the block of material. A discussion of the atomistic stress tensor in relation to continuum based stress concepts is presented in Horstemeyer and Baskes (1999). The average uniaxial true strain for a given simulation was determined from the following relationship:

$$\varepsilon_{11} = \ln\left(1 + \frac{v_1\ t}{L}\right), \qquad \text{Equation 3.4}$$

where v_1 is the velocity of the atoms at the far end of the model (applied boundary condition), t is the simulation time, and L is the half-length of the model. In some simulations the displacement of selected atomic planes is used as a deformation metric rather than the average strain in Equation 3.4.

For the present study on Al-Si interfaces, MEAM potential functions are required for the various pair interactions between Al and Si. For the Al-Al and Si-Si interactions, we employ MEAM potentials developed previously for elemental Al and Si (Baskes, 1992). The lattice constant for the two materials were assumed to be 4.05 Å for Al and 5.4 Å for Si, to give an integer ratio of 3 for the enforcement of periodicity. The real ambient temperature lattice constants are 4.041 Å and 5.42 Å for Al and Si, respectively. For Al-Si, we compute, within the Local Density Approximation (LDA), some ground-state properties for a representative Al-Si structure, namely the B1 (NaCl) structure, and fit the MEAM potential to this data. LDA calculations were carried out using an all-electron, full-potential method (Methfessel, 1988) to obtain the cohesive energy and three cubic elastic constants for B1 Al-Si, as shown in Table 3.1. A basis set of 27 orbitals per atom ($f + 2d + 3p + 3s$), and a k mesh of 20 by 20 by 20 divisions was used to ensure that no errors arose from the basis or Brillouin zone integration.

Table 3.1: Properties of the Al-Si system in the B1 structure. The * indicates that the parameter is fitted by construction. LDA is local density approximation.

	LDA	**MEAM**
a_{AlSi}(Å)	3.64	3.64*
E_{AlSi} (eV)	3.85	3.85*
B (GPa)	85	85*
$(c_{11}-c_{12})/2$ (GPa)	89	89*
c_{44} (GPa)	19.9	13

For comparison, c_{44} was computed to be 30 GPa in Al and 76 GPa in Si. The experimental values extrapolated to 0 K are 28 GPa and 80 GPa, respectively. The lattice constant a_{AlSi} resulted in an Al-Si nearest neighbor distance of 2.576 Å which, as expected, falls between the Al-Al nearest

neighbor distance of 2.86 Å and Si-Si nearest neighbor distance of 2.35 Å. As expected from the absence of compound formation in the Al-Si phase diagram, the cohesive energy E_{AlSi} shows that the B1 structure is endothermic with respect to FCC Al and diamond cubic Si by 0.255 eV/atom. There is very little experimental data available to compare the computations at this scale. We calculate approximately the solubility of Al and Si in Al at 577C, the eutectic temperature. From the model, the heat of solution of Si in Al is 0.42 eV and for Al in Si 1.8 eV. These values lead to a solubility of 0.3% for Si in Al and essentially zero for Al in Si. The experimental values range from 1-2% and zero, respectively. Data is not available to obtain a better approximation. Shown in Table 3.1 are MEAM results. The anisotropy in the calculated shear constants is remarkably large; we were encouraged that the MEAM does a reasonable job in reproducing it. These values were used in the Universal Equation of State (UES) (Rose *et. al.,* 1984) to determine the Al-Si pair potential:

$$\Phi_{Al-Si}(r) = \frac{2}{Z}\left[E^{u}(r) - F_{Al}\left(\frac{\overline{\rho}_{Si}}{12\ \rho^{o}_{Al}}\right) - F_{Si}\left(\frac{\overline{\rho}_{Al}}{4\ \rho^{o}_{Si}}\right)\right] \qquad \text{Equation 3.5}$$

where E^{u} is the UES for Al-Si using the parameters in Table 3.1, Z=6 is the nearest neighbor coordination for the B1 structure, r^{o}_{Al} and r^{o}_{Si} are the electron densities for the aluminum and silicon. The background electron densities are given by:

$$\overline{\rho}_{Si} = Z\rho^{(0)}_{Si}(r) \qquad \text{Equation 3.6}$$

$$\overline{\rho}_{Al} = Z\rho^{(0)}_{Al}(r) \qquad \text{Equation 3.7}$$

where $\rho^{(0)}_{Al}$ and $\rho^{(0)}_{Si}$ are the s-like partial electron densities for aluminum and silicon. The scaling of the electron densities ρ^{o}_{Al} and ρ^{o}_{Si} was chosen by fitting to the shear elastic constants calculated from the LDA. The resultant shear moduli are presented in Table 3.1 for $\rho^{o}_{Si} / \rho^{o}_{Al}$ = 3.42. It was not possible to fit both shear moduli with the single electron density ratio, but the resultant shear moduli are in reasonable agreement with the LDA calculations. We note that the aforementioned procedure for estimating the bi-materials potentials is outlined in more detail by Baskes *et al.* (1994), and is only overviewed here for completeness.

3.1.2. INTERFACE STRUCTURE AND MODEL SENSITIVITY

In the present MEAM simulations, the following parameters remained fixed throughout the investigation:

1. The model is periodic in the [010] and [001] crystallographic directions, and it contains free surfaces perpendicular to the [100] direction.
2. The constant temperature molecular dynamics simulations were conducted at 300 K and the static simulations were conducted at 0 K.

3. The cubic axis for the FCC aluminum and the diamond cubic silicon blocks are aligned, i.e. $[100]_{Al}||[100]_{Si}$, $[010]_{Al}||[010]_{Si}$, $[001]_{Al}||[001]_{Si}$, and the interface normal is parallel to the [100] direction.
4. The two complimentary atomic planes farthest from, and parallel to the interface, are displaced at velocities of 1 Å/ps along the [100] and $[\bar{1}00]$ crystallographic directions. Atoms in the displaced planes were fixed from moving in the [010] and [001] directions.

The velocity of 1 Å/ps was chosen arbitrarily. Although there may be an influence of strain rate on the simulation results, we have not studied this effect systematically. Instead, we have used one extremely high strain rate (dynamic simulation with velocity of 1 Å/ps) and one extremely low strain rate (static simulation). The forthcoming results show that the influence of strain rate is small compared to other significant effects. The results of the MEAM simulations on the Al-Si interfaces are presented in Figure 3.2 through Figure 3.13. In all figures containing atomistic images, with exception to Figure 3.2b, the viewing direction is always along the [001] direction. Since the MEAM model is three-dimensional, many other viewing directions are possible, however, the images viewed from the [001] direction provided the easiest interpretation of results.

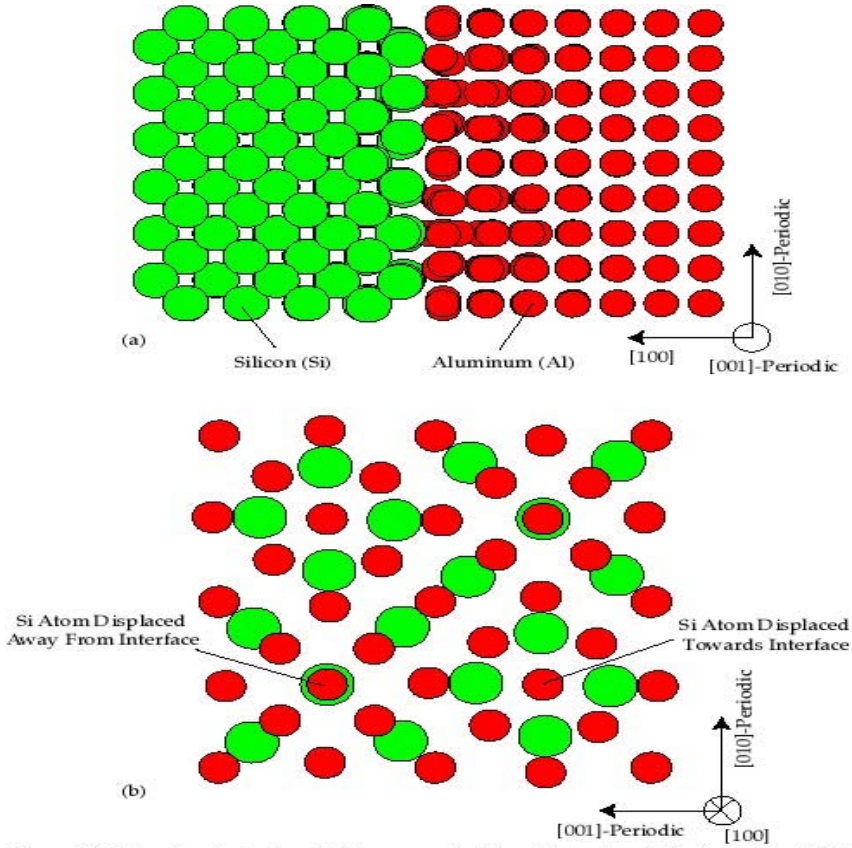

Figure 3.2. The relaxed structure (total energy minimized through a static simulation at 0 K) of the aluminum-silicon interface where [100]Si | |[100]AL The model is periodic in the [010] and [001] directions, and the viewing direction is the (a) [001] direction and the (b) [100] direction. In (b) only the two planes closest to the interface are shown.

An image of the interface viewed from the (a) [001] and (b) [100] directions is presented in Figure 3.2. The model in Figure 3.2 has been subjected to a static MEAM calculation (total

energy of the aggregate is minimized at 0 K under no external velocities) to assure that the structure of the interface is relaxed. We note that the initial distance between the atoms at the Al-Si interface was chosen by experience of modeling interfaces (Baskes et al., 1994). Although this choice is arbitrary, the interface relaxes to an equilibrium structure during the static or dynamic simulations. Thus, as long as the initial interface separation is not too small or large to cause numerical problems, the initial interface separation is not a critical issue. In Figure 3.2a, all atoms appear the same size, however, many of the atoms lie on different planes owing to the three dimensional structure of the lattice. In Figure 3.2b, all atoms are removed from the model with the exception of one Si plane and one Al plane at the interface. Although it is not trivial to identify the structure of the interface, the interface does posses a mild degree of order with some inevitable local distortions. The interface is clearly incoherent since a one-to-one correspondence between the Si and Al atoms does not exist across the junction. Similar to Ni-Si interfaces (Baskes *et al.*, 1994), the Al-Si interface posses a rippled appearance, i.e. some atoms are displaced towards a perfect interface plane and some are displaced away. The cause of the rippling is undoubtedly the strong interaction of neighboring Al and Si atoms located in the two different crystal lattice structures. If a Si or Al atom near the interface sees a void in the adjacent material, the atom will be drawn toward that void. Conversely, if a Si or Al atom near the interface is placed directly next to an atom in the adjacent material, the atom will be pushed away from that atom. Although atoms from both materials are displaced at the surface, the aluminum atoms are predicted to ripple more severely compared to the Si atoms.

Figure 3.3 is a representative example of the response of the interface model to applied far-field velocity boundary conditions. The center figure is a plot of the average uniaxial stress versus the true uniaxial strain for the aggregate shown in Figure 3.3. The average stress is calculated using Equation 3.3 for the entire aggregate of atoms, while the true strain is determined from equation 3.4. Upon initial application of the end velocities, the average axial stress in the model is compressive (negative). The initial negative stresses, which exist even in a statically relaxed model, is caused by the attempted contraction of the Al and Si due to the presence of the free surfaces. Moreover, the lattice constants of the materials are not exact (.5 % error) since their ratio must be an integer to properly enforce periodicity. During continued movement of the end atoms, the average axial stresses become tensile, and the stresses continue increasing until a critical stress level is reached. At the critical stress level, the failure of the interface between the Al and the Si atoms begins to nucleate (Figure 3.3). The nucleation of interfacial failure occurs spatially at the location where the Al and Si atoms are displaced (rippled) in the relaxed and undeformed state (Figure 3.2). In fact, aside from differences in the bonding potentials between Al and Si atoms, the rippled nature of the interface is one reason that the interface is weak compared to the pristine bulk material. The rippling facilitates local stress concentrations and failure through local damage nucleation and a subsequent unzipping of the interface atoms rather than simultaneous bond breakage. Such a failure mechanism is analogous to the severe decrease in strength for the movement of a single dislocation versus the simultaneous failure of all adjacent atomic bonds.

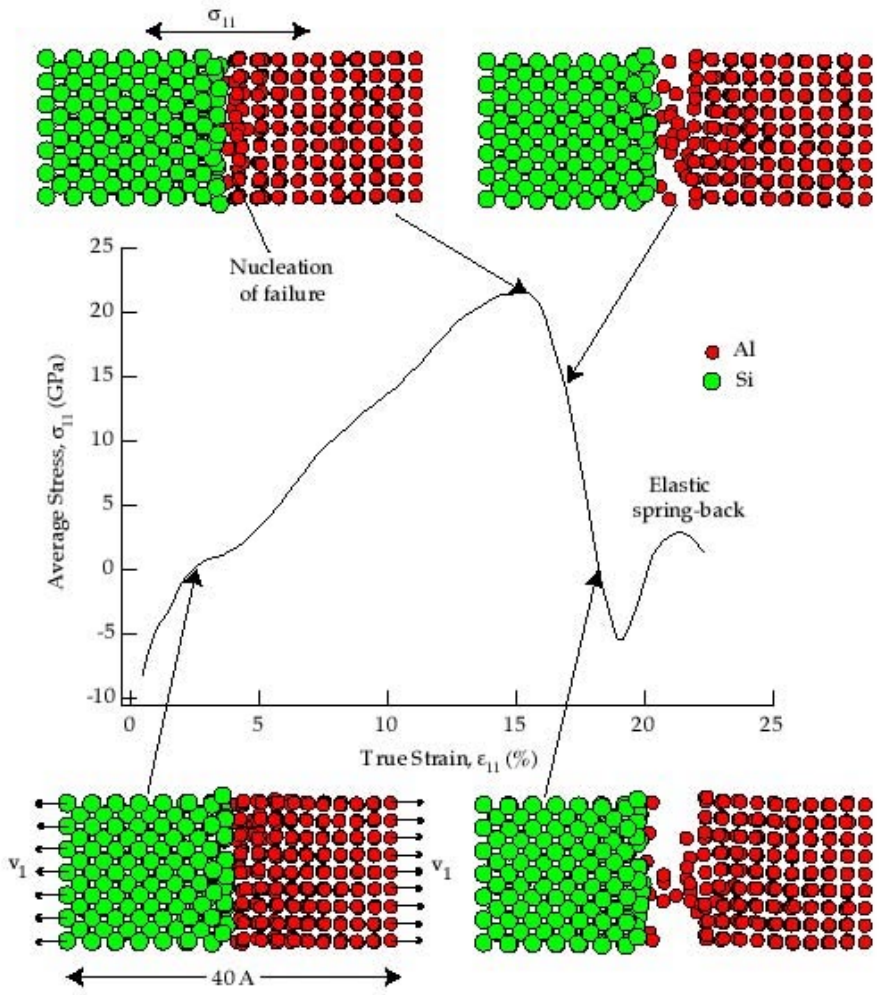

Figure 3.3. Representative average-stress versus true-strain response of the [100]Si||[100]aluminum interface model to boundary velocities, vl, at the far ends of the blocks in the [100] and [-100] directions. The model is periodic in the [010] and [001] directions.

As the interface debonds, the average stresses in the atomistic model decrease over a finite strain increment (Figure 3.3). Moreover, during interfacial debonding, the Si atoms are slightly distorted from their elastic positions, however the Al atoms undergo gross permanent changes in position, revealing that plastic dissipation occurs in the Al. Owing to the highly constrained and pristine state of the present lattice, it is difficult to envision any explicit dislocation emission or movement near the fracturing interface. When the average stress in the block reaches approximately 0 GPa, the interfacial separation is complete and several Al atoms are still attached to the Si (Figure 3.3). After separation, the two blocks experience elastic springback in an oscillatory manner as indicated in Figure 3.3. For the remaining figures, the elastic springback portion of the stress-strain curve is removed since it is not pertinent to understanding the local debonding mechanisms. We note that the predicted debonding stress levels (~20 GPa) in the present study are elevated compared to, for example, the ultimate tensile strength (~200 MPa) of cast Al-Si alloys where debonded and fractured Si particles are observed (Dighe and Gokhale, 1997; Samuel and Samuel, 1995). The high attainable stress levels are due to the pristine state of the interface (defect and impurity free), the highly constrained (relatively thin and periodic)

nature of the interface model, and the dynamic loading conditions. The periodic nature and relatively high applied strain rates are inherent to practical MEAM simulations, thus revealing a limitation of current atomistic modeling efforts. The addition of defects such as point vacancies will slightly lower the strength of the "perfect" incoherent interface, as will be demonstrated in Section 5. Interface misorientations, dislocations (Kurtz and Hoagland, 1998), and impurities (Rice and Wang, 1989; Olson, 1997) will further lower the strength of the interface as much as several orders of magnitude. We also note that under some stress states other than pure tension, a size scale effect, which is the basis of strain gradient plasticity, will also cause the local stresses to be much higher than experimental observations on large scale samples (Fleck *et al*., 1994; Horstemeyer and Baskes, 1999).

In order to assure that the results do not have a strong sensitivity to the boundary velocity conditions or periodic lengths in the transverse directions, several MEAM interface models were deformed under varying conditions. The average-stress versus true-strain response of the MEAM interface models to the selected conditions is demonstrated in Figure 3.4. It was discovered that applying a velocity at both ends versus fixing one end and moving the other has no effect on the model response. Furthermore, applying a velocity exclusively to the end atoms creates conditions for the propagation of an elastic shock wave. To eliminate the propagation of an elastic shock wave we give the atoms within the model a spatially linear *initial* velocity distribution with a zero value at the interface and the same maximum value at the displaced far-field end. However, by applying end velocities augmented by the initial velocities for the internal atoms, we demonstrate that the average stress-strains response is unchanged (Figure 3.4), thus the shock wave is not significantly affecting the debonding behavior.

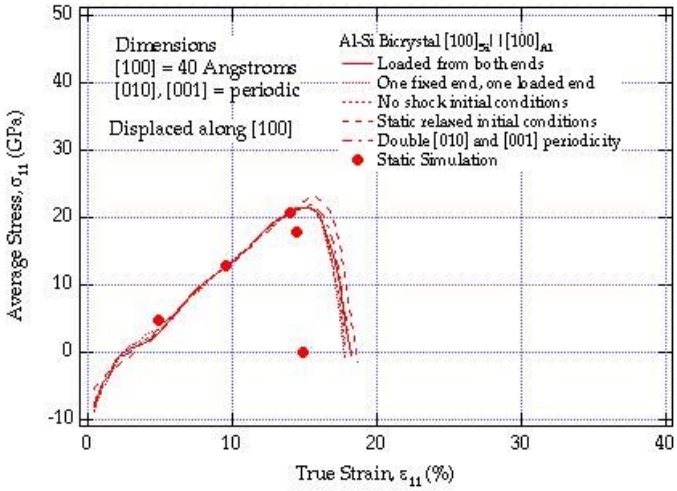

Figure 3.4. The average-stress versus true-strain response of the $[100]_{Si}||[100]_{Al}$ interface model under various conditions. The model is periodic in the [010] and [001] directions.

We also relax the interface through a static calculation at 0 K, before applying the external boundary velocities. The results show that, regardless if the interface is statically relaxed or not, the interface quickly reaches an equivalent deformed state under the imposed boundary velocities as evidenced from the similarity in the stress-strain responses in Figure 3.4. In addition, an incremental static simulation was conducted at 0 K with incrementally increased end displacement values. Upon loading, the response of the model under static and dynamic conditions is essentially the same. However, the drop-off of stresses in the static simulation occurs at a slightly smaller critical stress (strain) level. Finally, periodic lengths along the [010] and [001] directions, were initially assumed to be four aluminum unit cells and three silicon unit cells, i.e. 16.2 Å. Doubling the periodic lengths to eight unit cells for the aluminum and six unit cells for the silicon, i.e. 32.4 Å, had a negligible effect on the predicted stress strain response (Figure 4).

3.1.3. INTERFACE DEBONDING

Before investigating the interface debonding in detail, we first studied the differences between the average stress-strain response of the MEAM interface model and equivalent MEAM models containing only silicon or aluminum (Figure 3.5). Although nonlinear at such large strains, the loading slopes of the stress-strain curves for the Al and Si are on the order of the measured elastic constants for this crystallographic direction, i.e. C_{11} (Si) = 166 GPa (Suwito *et al.*, 1998) and C_{11} (Al) = 108 GPa (Meyers and Chawla, 1984). This agreement is inherent to the MEAM since the potentials are determined from the elastic properties of both materials (Table 3.1). The failure strain of all three models occurs over a finite increment, with the interface model having the lowest failure stress and strain, followed by the pure aluminum and then the pure silicon. At this atomistic size scale, the fracture of the pure silicon is more abrupt compared to the aluminum and the Al-Si interface models, i.e. less curvature at the peak and a more rapid stress drop. The brittle nature of pure silicon single crystals for large-scale mechanical testing samples has been experimentally observed (Suwito *et al.*, 1998). Most importantly, in the absence of defects, the Al-Si interface is weaker than either the pure Al or pure Si materials, however the interfacial fracture resembles failure characteristics in pure Al.

We now illustrate the dependence of the MEAM interface model response on the block size (length) in the non-periodic [100] loading direction. Figure 3.6 shows the (a) average-stress versus true strain response, (b) average-stress versus far-field displacement response, and (c) average-stress versus local displacement response of the MEAM interface model with four different block sizes. The far-field opening displacements and true strains were calculated from the velocities at the far ends of the respective MEAM models. The local opening displacements were calculated as the displacement difference during the simulation between the atomic planes initially at +/- 3 planes (approximately +/- 5 Å) from the interface. For reference, the overall length of the block shown in Figure 3.3 is 40 Å, and the other block sizes investigated are one-fourth (10 Å), one-half (20 Å), and twice (80 Å) this length in the [100] direction. We note that the sizes here indicate the entire model length, such that the Si and Al block lengths are each half of this overall length. The results in Figure 3.6a indicate that the average stress-strain response exhibits a relatively strong dependence on the block size in the [100] direction. A possible reason for the dependence is a size scale effect, however, this argument is circumvented below.

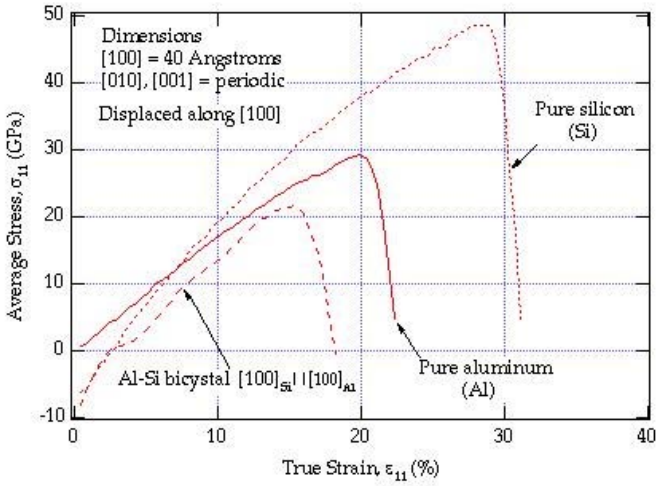

Figure 3.5. The average-stress versus true-strain response of the $[100]_{Si}\|[100]_{Al}$ interface model compared to pure silicon and aluminum MEAM models with the same dimensions loaded under identical conditions. All three models are periodic in the [010] and [001] directions.

Figure 3.7 presents four average stress-strain curves from the 80 Å Al-Si interface model. The bounds to determine the average stress-strain response were systematically decreased. For example, averaging from –40 to 40 Å encompasses the entire 80 Å model. However, averaging from –5 to 5 Å only includes six total atomic layers near the interface. The other averaging bounds are in between these two extremes. The averaging bounds for the 80 Å model in Figure 3.7 were chosen to match the different MEAM model sizes studied in Figure 3.6. Essentially, the overall shapes of the curves in Figure 3.7 are independent of the averaging volume even if the atoms exclusively near the interface are considered. As such, the postulate of locality in macroscale continuum mechanics is valid even at these size scales when developing an interfacial debonding damage criterion under pure tension. However, we note that as the averaging volume becomes very small the response demonstrates significant local fluctuations due to the smaller number of atoms sampled. In either case, owing to the results in Figure 3.7, the differences in the curves in Figure 3.6 cannot be attributed to differences in the averaging volume for different size models.

As the block size is increased, the average stress versus true strain response (Figure 3.6a) converges since the interaction of the interface atoms with the displaced surface atoms diminishes. However, due to the localization phenomenon in the present bi-material atomistic simulation, the average stress-strain response is not the most appropriate approach for studying the interface debonding. To gain further insight into the debonding mechanisms, several stress (traction) versus displacement curves were plotted from the same MEAM simulations as Figure 3.6a. As the block size is increased, the average-stress versus far-field displacement response (Figure 3.6b) diverges since the applied end displacement is dispersed over a larger MEAM

model length. However, when local displacements are measured at the same location for all model sizes, the average-stress versus local-displacement curves are far less sensitive to the block size (Figure 3.6c). Moreover, a static traction versus local-displacement curve is also shown in Figure 3.6c, and the result is similar to the molecular dynamics simulations for the different block sizes. The results in Figure 3.6c indicate that local displacement measurements provide much different results than far-field displacement measurements. The most appropriate location of the measured opening displacement reference planes for the 40 Å model.

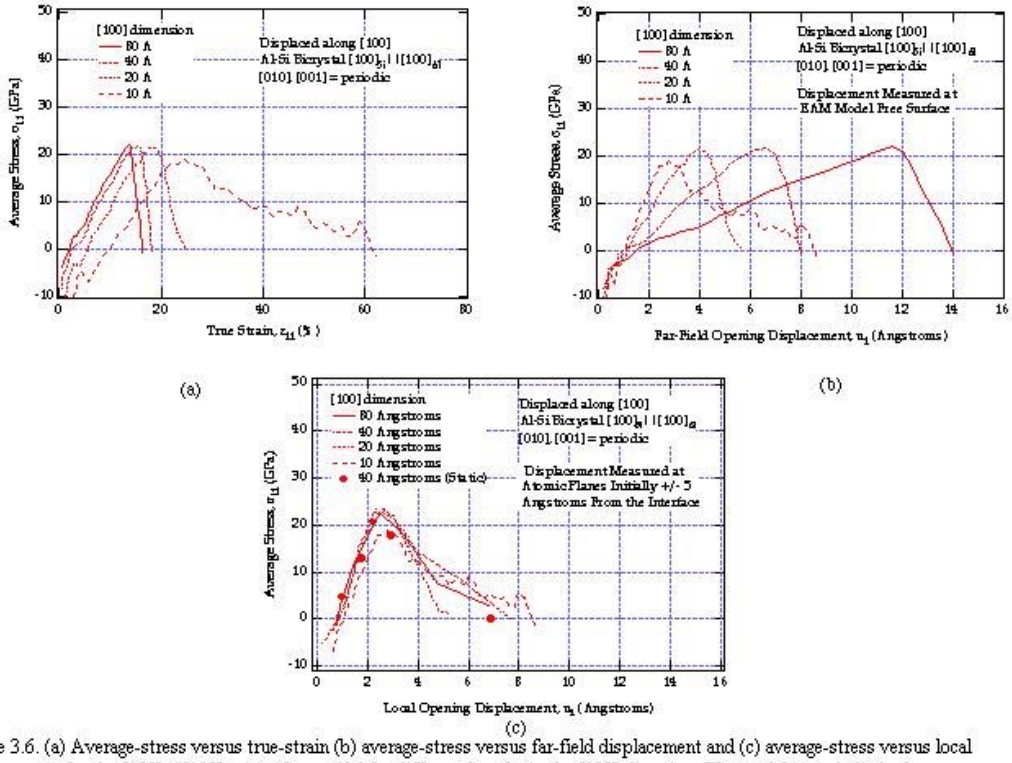

Figure 3.6. (a) Average-stress versus true-strain (b) average-stress versus far-field displacement and (c) average-stress versus local displacement for the $[100]_{Si}||[100]_{Al}$ interface model for different lengths in the [100] direction. The model is periodic in the [010] and [001] directions.

On the other hand, the most suitable block size for MEAM modeling is one that minimizes the interaction between the displaced far-field surfaces and the interface atoms. The average-stress versus true strain response is used as a measure of the interaction between the interface atoms and the displaced free surfaces. As the free surfaces are moved farther from the interface, and the block size increases, the average-stress versus true strain response converges towards a nominal response centered at the origin (Figure 3.6a). Based on the curves in Figure 3.6a, the differences in the responses of the 40 Å and 80 Å models are minimal, whereas models below 20 Å show significant deviations from the responses of the larger blocks. The aforementioned observation, coupled with the excessive computation time for the 80 Å model, render the 40 Å model the most appropriate for the MEAM simulation of interface debonding for a pristine Al-Si interface.

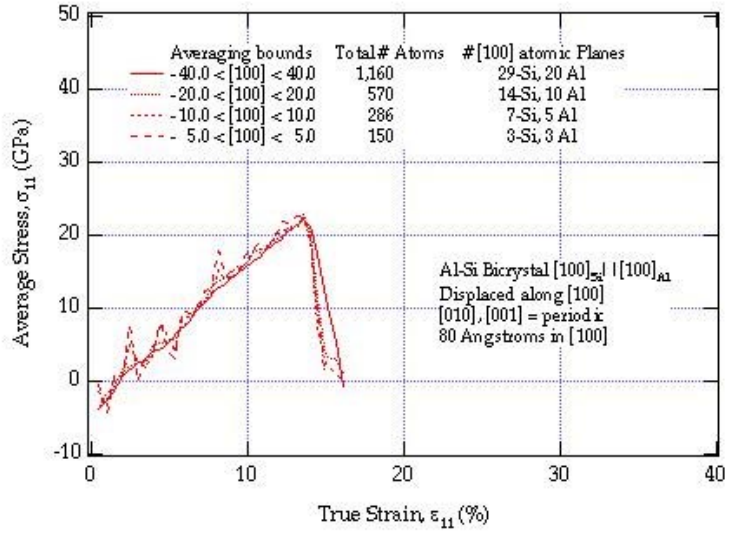

Figure 3.7. Effect of averaging volume on the average-stress versus true-strain response of the 80 Angstrom $[100]_{Si}||[100]_{Al}$ interface model. The model is periodic in the [010] and [001] directions.

The stress distributions across the interface, predicted by the MEAM simulations, provide insight into the local failure mechanisms. Figure 3.8 is a distribution of average uniaxial stresses just before interfacial failure (14 % strain in Figure 3.4). The stresses were averaged in the [010] and [001] directions, and the average stress in the entire volume is also indicated in Figure 3.8 as a straight line. The distributions predicted by both the molecular dynamics and static simulations are presented in Figure 3.8. The average stresses in the stiffer silicon material are higher for an equivalent dynamic displacement of both model ends. The different stress levels in the two materials are artifacts of the dynamic nature of the simulations. However, in the static case, the stresses away from the interface are comparable in both materials, consistent with static stress equilibrium concepts. Very close to the interface, the stresses in both materials are higher than the nominal values away from the interface, under both static and dynamic loading conditions. The magnification of stresses is due to the rippled nature of the interface and the local balance of forces. In other words, owing to the different crystal structures and lattice parameters of the two phases, some atoms cannot interact strongly with immediate neighbors across the interface. The low interaction force levels between certain atoms promotes high forces between other atoms which are attempting to keep the interface intact. Thus, extremely close to the interface, several atoms are equilibrated under relatively higher forces as evident in Figure 3.8. This microscopic disturbance of stresses near the interface facilitates the nucleation and propagation of debonding failure. We note that such a local disturbance in the stress fields is produced by the

heterogeneous nature of the interface as caused by the lattice structure of the two materials. Of course, in a homogeneous continuum based model, no stress intensification would be predicted for the given periodicities and boundary conditions.

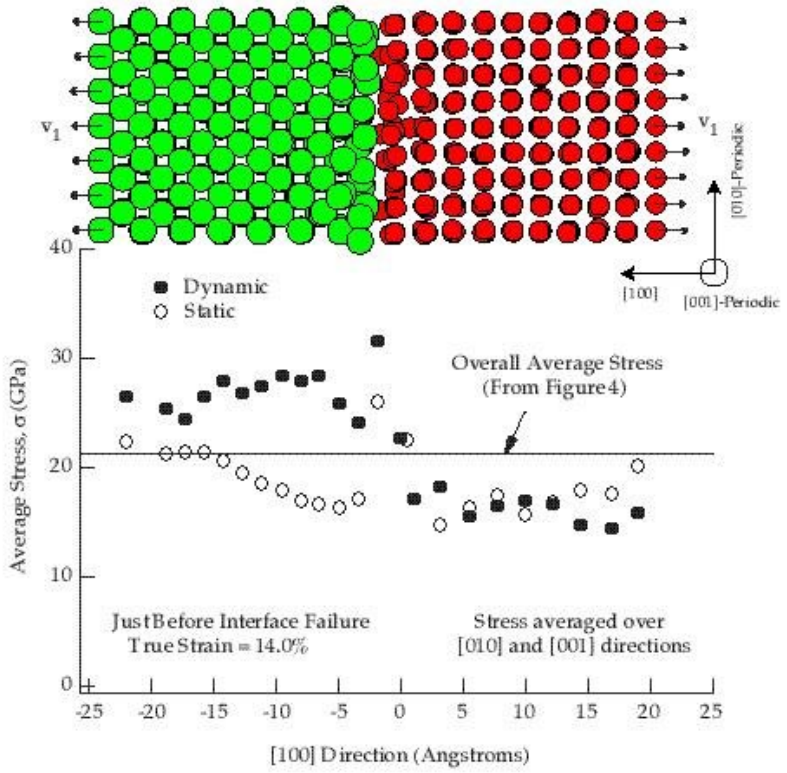

Figure 3.8. Stress distribution along the [100] direction for the [100]Si | |[100]Al interface model. The atomistic image corresponds directly to the different positions indicated along the lower axis of the plot. The model is periodic in the [010] and [001] directions, and the stresses are averaged in these directions.

3.1.4. ROLE OF VACANCY TYPE DEFECTS

The strength of material interfaces will invariably be degraded by the presence of metallurgical defects such as dislocations, vacancies, and chemical impurities. Although chemical impurities (Rice and Wang, 1989; Olson, 1997) and interface dislocations (Kurtz and Hoagland, 1998) are expected to have a significant influence on the strength of an interface, the present MEAM simulation will exclusively consider the effects of vacancy-type defects on interface debonding. The incorporation of impurity atoms in MEAM simulations requires the development of atomic potentials for such materials and is beyond the scope of the present study. Moreover, a thorough study of different interface dislocations and misorientations is a separate topic altogether and can be attacked once the present framework is set forth. Figure 3.9 illustrates the dependence of the strength of the interface on the number fraction of defects near the interface. The point vacancy defects in the simulations in Figure 3.9 were distributed randomly throughout the two atomic planes adjacent to the interface in (a) just the Al, (b) just the Si, and (c) both the Al and Si. In all three situations (Figures 3.9 a-c) the incorporation of vacancy defects at the interface lowers the fracture strength of the interface. In the range of defect number fractions considered, the decrease

in the interfacial strength scales nearly linearly with the number fraction of defects (Figure 3.9a). The small reductions in strength due to the randomly dispersed vacancies (Figures 3.9 a-c) are absolutely negligible given the small overall concentration (<< 1%) of vacancies traditionally found in metals (Meyers and Chawla, 1984).

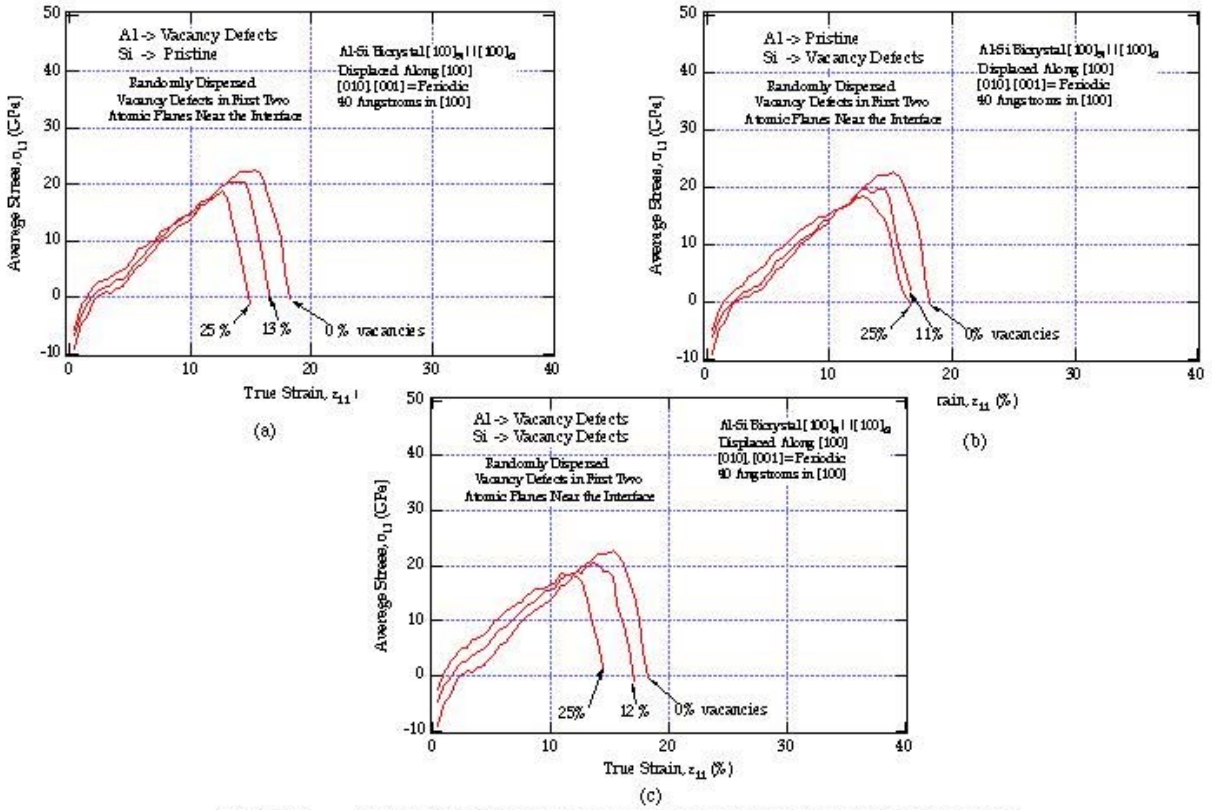

Figure 3.9. Effect of randomly distributed point vacancy defects on the stress-strain response of the 40 Angstrom $[100]_{Si}||[100]_{Al}$ interface model. The vacancy defects are distributed within the first two atomic layers near the interface in (a) the Al, (b) the Si, and (c) both the Al and Si.

We have established that the Al-Si interface with and without point vacancy defects is a weak link for failure under tensile loading parallel to the $[100]_{Al}||[100]_{Si}$ interface normal. Now we investigate the role of microscopic crack like defects in the bulk materials on the competing mechanisms of fracture in the pure Al, pure Si, or at the Al-Si interface. Figures 3.10 and 3.11 are compilations of the initial damaged state and final failure mode of four different MEAM simulations with different sized and spaced flaws in the Si or Al, respectively. Before conducting the MEAM simulations, atomic rows along the [001] direction were removed to create a crack-like vacancy defect in the silicon (Figure 3.10) or aluminum (Figure 3.11). Since the model is periodic in the [010] direction, the models in Figures 3.10 and 3.11 simulate a periodic array of evenly spaced cracks rather than a single defect. As the initial flaw size is increased (periodic flaw spacing is concurrently decreased) in both materials, failure in the pure materials is favored over interfacial failure. Flaws in the Si do not distract the failure from occurring at the interface until the flaw area projected onto a plane normal to the tensile axis is nearly 30% (Figure 3.10). Flaws in the Al are even less effective in moving the failure away from the interface since it takes a larger flaw area projected on a plane normal to the tensile axis (about 50%) to accomplish

bulk failure in the Al (Figure 3.11) versus the interface. These values are only valid for pristine materials with defects on this size scale.

Figure 3.10. Effect of initial defect size in the pure silicon material on the failure mode of the 40 Angstrom [100]Si | |[100]Al interface model. All models have equivalent geometry's, and they are periodic in the [010] and [001] directions.

Figure 3.11. Effect of initial defect size in the pure aluminum material on the failure mode of the 40 Angstrom [100]Si | |[100]Al interface model. All models have equivalent geometry's, and they are periodic in the [010] and [001] directions.

Figure 3.12 demonstrates that the periodic size scales of the model in the [010] and [001] directions have an influence on the fracture behavior of the material in the presence of defects. The lower model in Figure 3.12 has double periodicity in both directions and a flaw size that is also double compared to the model at the top of the figure. Recall that changing the transverse periodic lengths had a negligible influence on the tensile stress-strain behavior of the model without defects (Figure 3.4). However, the size of the periodic lengths has an influence when flaws within the materials are introduced. The dependence of the fracture mode of the model on the flaw size is consistent with fracture mechanics notions where the intrinsic flaw size is related to the driving force for fracture. However, in the present simulations, the larger flaw in the Si does not promote earlier fracture in the Si compared to the smaller flaw, which is not entirely consistent with static fracture mechanics concepts. One reason that the smaller flaw could promote earlier failure is due to the propagation of elastic waves in the dynamic MEAM model. Such elastic waves can promote premature fracture in the smaller model since the ligament between the cracks is smaller than in the larger model, and shorter time is required for spatial movement of the waves. As such, the probability that the local stress field that initiates fracture will be augmented by an elastic stress wave is increased in the smaller scale MEAM model. Moreover, we note that the interaction between the different flaw sizes and the interface, which is a flaw itself, may also provide some rational for the qualitative disagreement with static fracture mechanics flaw size concepts. In either case, caution must be exercised when extending static fracture mechanics based ideas to dynamic debonding problems since complex local stress states may develop due to interactions with the flaws, elastic waves, and the interface. Moreover, extending fracture mechanics based ideas to atomistic size scales is not trivial due to the small flaw and geometry size scale inherent to atomistic simulations.

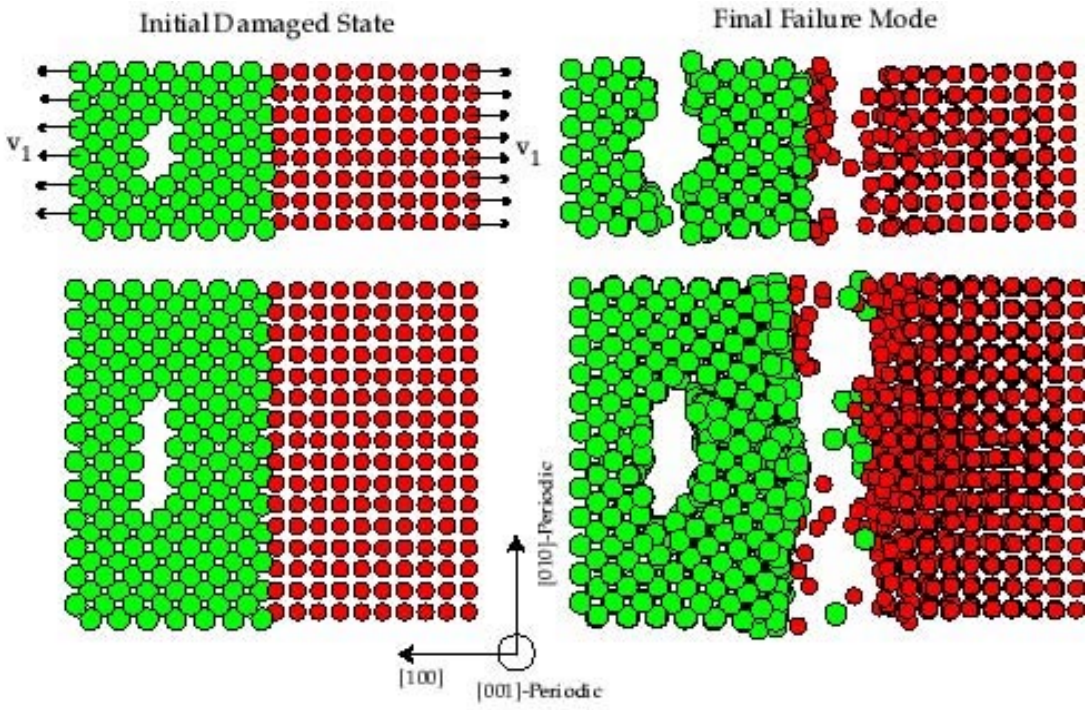

Figure 3.12. Effect of initial defect size in the pure silicon material on the failure mode of the 40 Angstrom [100]Si||[100]Al interface model. The two models are periodic in the [010] and [001] directions and have periodicity's scaled equivalently with the two different initial flaw sizes.

3.1.5. COMPARISON TO CONTINUUM DECOHESION MODELS

Continuum based decohesion models, developed for implementation into finite element codes, traditionally assume a traction versus opening-displacement relationship dictated by closed-form equations. Several different versions of the equations exist, however, we focus on the Equation 3.8 used by Needleman (1987), and Equation 3.9 by Needleman (1990a) and Tvergaard and Hutchinson (1992, 1994, 1996). The equations of Needleman (1987, 1990-a) are given below:

$$\frac{\sigma_{11}}{\sigma_{\max}} = \frac{27}{4}\frac{u_1}{u_{\max}}\left[1-\frac{u_1}{u_{\max}}\right]^2 \qquad \text{Equation 3.8}$$

or

$$\frac{\sigma_{11}}{\sigma_{\max}} = 13.136\ \frac{u_1}{u_{\max}}\exp\left[-4.833\ \frac{u_1}{u_{\max}}\right] \qquad \text{Equation 3.9}$$

Where σ_{11} and $\sigma_{\max}$ are the instantaneous traction normal to the interface and the maximum traction normal to the interface, respectively. Similarly, u_1 and $u_{\max}$ represent the instantaneous normal opening displacement and maximum normal opening displacement, respectively. Although Equations 3.8 and 3.9 usually have a coupling to shear stresses across the interface

(Needleman, 1987; Needleman, 1990-a), the pure normal traction forms are used for comparison to the present MEAM results. The separation laws are contrived such that when u_1 approaches u_{max}, σ_{11} approaches zero and the interface is considered to be separated. The model of Tvergaard and Hutchinson (1992, 1994, 1996) uses a tri-linear approximation with similar s_{max} and u_{max} parameters (Figure 3.13b). The Tvergaard and Hutchinson model (1992, 1994, 1996) includes adjustable shape parameters which alter the positions of the intercepts between the stress plateau at σ_{max} and the loading and unloading lines. The graphical versions of Equation 3.8, Equation 3.9, and the linear model are presented in Figure 3.13b. The adjustable shape parameters in the linear model have been chosen to fit one of the MEAM results.

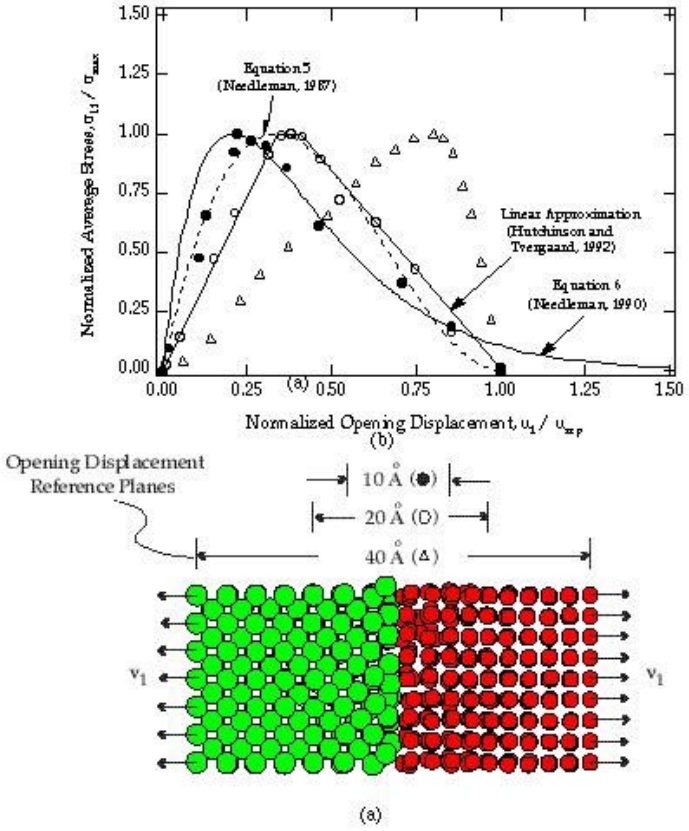

Figure 3.13. (a) Schematic of the three different reference planes used to calculate the opening displacement in the MEAM simulations. (b) Traction-displacement curves for the 40 Angstrom MEAM model and different continuum based cohesive laws.

In Figure 3.13b, three traction versus displacement relationships from the 40 Å MEAM simulation are included in addition to the predictions of the continuum based models. The locations of the different reference planes for the measurement of the model displacements are indicated in Figure 3.13a. The displacements were calculated point-wise during the simulation by averaging the difference between the positions of the atoms initially in corresponding planes indicated in Figure 3.13a. In general, the MEAM simulations predict that as the relative opening displacement is measured from reference planes farther from the interface, the location of the stress-drop is shifted to a larger normalized displacement value. Regardless of where the opening displacement is measured, the interface failure is ultimately governed by individual atomic separations through a cohesive type relationship. However, when the opening displacement is measured farther from the interface, a significant fraction of the total displacement comes from

the stretching of the bulk materials away from the interface. Consequently, the location of the stress peak on the normalized displacement axis is shifted to a larger normalized displacement as evident in Figure 3.13b. The MEAM results using opening displacements near +/- 10 Å of the interface demonstrate strong quantitative agreement with all continuum based traction-displacement relationships.

The adjustable linear model of Tvergaard and Hutchinson (1992, 1994, 1996), yields the best overall correlation with MEAM results, owing to the two adjustable parameters. Basically, the adjustable parameters in the Tvergaard and Hutchinson model (1992, 1994, 1996) control the physical rate at which the interface accumulates stresses and the rate of stress drop during decohesion. The present analysis suggests that these two rates are dependent on the measurement point of the opening displacement, i.e. the required cohesive zone size of the bi-material system considered. In the Needleman analysis these two rates are fixed as motivated by the atomic separation of paired atoms. However, complex atomic interactions due to different lattice structures and interfacial defects may require an analysis of opening a few atoms away from the interfacial plane for the sake of robustness. In this case the unloading and loading rates will be different depending on the location of the measured opening, and will require adjustable parameters. Therefore, the adjustable parameters are useful from a physical standpoint when the separation a particular material interface does not strictly obey a universal binding energy curve due to local atomic interactions.

The results in Figure 3.13b demonstrate that the predictions of current continuum based cohesive models are consistent with dynamic MEAM predictions. However, when choosing a continuum based approach it is imperative to consider the distance over which atoms from the two materials near the interface interact with one another during the debonding, i. e. the *physical* cohesive zone size. Appropriately, the cohesive model should represent the response of the entire volume of the material near the interface that is contributing to the debonding failure mechanisms in the material. In Figure 3.13b the local distortions are evident within +/- 10 Å from the interface plane. Thus, the traction-displacement MEAM results from the reference planes 20 Å apart are appropriate for the present material interface system, and Equation 3.8, Equation 3.9, and the linear model are sufficient to represent the debonding character of such an interface. It is not appropriate to measure the displacement within the bounds of the physical cohesive zone. Using planes within the cohesive zone to measure the opening displacement is inaccurate since the atoms do not remain in a planar structure, and atoms contributing to the debonding mechanism are discarded in the analysis. The physical cohesive zone size in the present material system is relatively small since an Al-Si compound does not exist. For other materials systems, applied stress states, or interface geometries, the cohesive zone may be larger, and appropriate MEAM simulations would be required to determine if the interfacial debonding behavior followed Equations 3.8 and 3.9 with equivalent accuracy.

In closing, we note that the material outside of the cohesive zone bounds may be treated with traditional elastic-plastic constitutive laws. Consequently, it is not *necessary* to measure the opening displacement outside the cohesive zone boundary. However, as the displacements are measured farther from the interface, and away from the cohesive zone, the traction versus displacement relationship of the MEAM model approaches that of a traditional elastic solid undergoing linear elastic fracture (Figure 3.13b). Improving the continuum based approaches can

be suggested based on these atomistic simulation results. Most importantly, the adjustable parameters necessary to capture the actual shape of the traction-separation curve can be obtained, owing to interactions between the different structures of the joined materials at the interface. Consideration of the cohesive zone size with a continuum based approach must also be taken. Defects at the interface can alter the actual size of the cohesive zone, and we want to make sure that we capture all interacting entities within the zone. By admittance of a cohesive zone size we have introduced a length scale to the problem, and we should recognize that this length scale may change based on the interface debonding characteristics. If we are unsure of the cohesive zone size, the present atomistic results suggest that the fracture may be modeled with a local critical stress approach. Such an approach requires that the element size be correlated to the fracture strength to avoid a severe mesh size dependence.

3.1.6. ATOMISTICS SUMMARY

The $[100]_{Al}||[100]_{Si}$ incoherent interface between pure aluminum (Al) and silicon (Si) possesses a rippled structure with respect to a perfect interface plane. If the silicon and aluminum atoms are directly adjacent then they are displaced away from the interface plane. If a silicon or aluminum atom is adjacent to a void in the corresponding material, the respective atoms are displaced towards the interface plane.

A composite aluminum and silicon block attached at a $[100]_{Al}||[100]_{Si}$ interface, subjected to far field velocities, fails through interfacial debonding before the bulk Al or Si materials fail. In the absence of vacancies, dislocations, impurities, and mechanical defects, the nucleation of interfacial fracture occurs at the atomic positions where the local displacement of interface atoms creates a rippled structure. The interfacial failure occurs over a finite strain (displacement) increment with fracture characteristics similar to the pure aluminum.

During tensile loading parallel to the interface normal, the atoms +/- 10 Å from the Al-Si interface contribute to the debonding process. The physical cohesive zone size in of an Al-Si interface is around 20 Å. The introduction of random point vacancy defects near the interface lowers the interface strength at a rate nearly linearly proportional to the number fraction of point defects.

Crack-like vacancy defects in the bulk Al or Si must reach projected areas onto the plane normal to the tensile axis of approximately 50% and 30%, respectively, before failure occurs in the bulk materials versus the interface. These area fractions are for tensile loading parallel to the interface normal along the [100] direction, and they may be lower for other loading configurations not considered in the present study. When defects are introduced into the bulk Al and Si materials near the interface, the cohesive zone size is increased.

Continuum based cohesive laws have mathematical forms consistent with the present MEAM simulation results which consider local opening displacements. However, as the displacement is measured farther from the interface, the present results show that the peak stress position is increased, and the following stress drop-off becomes more severe. As such, the MEAM predictions approach those of linear elastic fracture mechanics with elastic loading up to a far field critical stress level for bulk fracture.

3.2. MICROSCALE VOID NUCLEATION PARAMETRIC STUDY

This section describes micron scale analyses that were performed to examine the role of seven independent parameters (number of silicon particle sites, uniformity of particle sizes, shape of particles, additional microporosity, temperature, prestrain history, and loading conditions) on debonding and fracture of silicon particles in A356 aluminum by performing a series of parametric calculations using the finite element method. Owing to the wide range of parameters, an optimal matrix of finite element calculations is generated using the statistical method of design of experiments (DOE). The DOE method is also used to screen the finite element results and yield the desired parametric influences as outputs. Concerning void nucleation, we observe that temperature was the most dominant influence parameter with the other parameters not even being a close second.

No substantial effort thus far has gone into studying the individual roles played by simultaneously interacting parameters on fracture and/or interface debonding. Developing a macroscale model for void nucleation needs to include the first order influence parameters from the lower size scales. The main focus of the micromechanical analyses in the present section is to qualify and, to a certain extent, quantify the influences of the interacting set of different parameters on void nucleation.

Because we are considering seven parameters, it becomes helpful to use a statistical procedure such as the DOE technique (Fisher, 1935a,b) for efficiency's sake. The DOE approach, popularized by Taguchi (1960; 1987) in the field of quality engineering, has recently been utilized in various contexts of mechanics and design by Trinh and Gruda (1991), Horstemeyer (1993), Stutsman *et al.* (1996), Young (1996), and Horstemeyer and McDowell (1997). The DOE methodology enables an investigator to select levels for each parameter and then conduct experiments in order to evaluate the effect of each parameter in an efficient manner. Any number of parameters and levels for each parameter can be placed in an orthogonal array which lends itself to the optimal determination of parametric effects. Here, orthogonality refers to the requirement that the parameters be statistically independent. The basic terminology of orthogonal arrays $L_a(b^c)$ goes as follows: a denotes the number of calculations, b denotes the number of levels for each parameter and c denotes the number of parameters. For example, in order to examine 8 parameters at 3 levels per parameter, one would have an orthogonal array represented by $L_{18}(3^8)$ (Taguchi, 1960; 1987) which would reduce the number of calculations if done linearly in series from 6561 to 18.

Eight finite element calculations under plane strain tensile conditions were performed on a cast A356 aluminum alloy using the Sandia material model. The DOE method is then used to screen the finite element results and yield the desired parametric influences on debonding and fracture of the silicon particles.

In our study, we seek to obtain the influences of seven independent parameters on two responses, namely, fracture of silicon particles and debonding of the aluminum matrix from the

silicon particles, through micromechanical calculations. The following are the seven parameters adopted in our study: number of particles, size of particles, shape of particles, microporosity, temperature, prestain history, and loading direction.

Inclusions within metals are generally inhomogeneously present in various shapes and sizes throughout the material. The pattern of the inclusion distribution becomes important while considering nucleation in ductile metals. Some regions of the material could have heavy concentrations of particles, while other regions may be relatively free of the inclusions. The number of interacting particles in this study are either two or four.

The particle size in our study deals with the uniformity of the particle size with respect to the other sizes. We chose a uniform distribution of sizes and a non-uniform distribution of particle sizes for our study.

Two shapes were chosen for use in our study, circular and elliptical. The elliptical particles have a major-to-minor axis ratio of 2:1.

Microporosity below a void volume fraction of 10^{-4} is difficult to measure experimentally. Yet, levels of porosity lower than 10^{-4} do occur within a material thereby influencing the resulting macromechanical properties. We used initial values of microporosity of zero and 10^{-6} in this study.

Very little has been accomplished in the way of determining void nucleation at wide ranges of temperature. The temperature range chosen in this study is in the low homologous temperature range (294 K and 400K).

Prestrain effects can arise from manufacturing processes where anisotropic hardening can arise from directional deformation that is imposed upon the material or under conditions where nonmonotonic loading sequences are experienced. Mackenzie *et al.* (1997) has shown from experimental data for several steels that, under rolling conditions, notch tensile tests are sensitive to the direction of loading. Horstemeyer and Revelli (1996) have also illustrated pre-strain effects on damage accumulation in several boundary value problems. A moderate pre-strain level of 10% is chosen in this study to examine the history effects.

The loading direction is a rather obvious influence parameter that plays an important role in determining the stress state of a material which in turn has important consequences for void nucleation. In our plane strain finite element computations, the two directions of consideration are chosen to be the horizontal direction and the vertical direction.

3.2.1 Design of Experiments Description

In an effort to handle seven interacting parameters in an efficient manner, we make use of the design of experiments (DOE) technique. We use the DOE method to generate the optimal matrix

(an orthogonal array) of finite element calculations suited for the present set of parameters. Furthermore, once the necessary finite element computations have been performed and the responses obtained, the DOE method is used as a screening process to obtain the desired parametric influences.

Each of the seven parameters is allowed to occupy one of two possible states during each calculation. The appropriate orthogonal array in our case is the $L_8(2^7)$, or simply L_8, array which allows up to seven independent parameters with two levels for each parameter. Each level is characterized by a particular attribute. For example, the two levels for the temperature parameter could be the end points of the temperature range of interest in a particular application. Although a full factorial set of calculations could be performed to vary each parameter in a linear fashion (the full set of calculations with seven parameters would be 2*7 = 128), the DOE approach using an L_8 array requires only eight calculations. The advantage of DOE as a screening process for parameter influence grows exponentially as the number of parameter variations increases. Table 3.2 shows the L_8 array with the seven parameters and the two corresponding levels for each parameter.

In essence, the DOE method provides a linear system of equations that relates the responses $\{R\}$ from the finite element computations to the desired influences $\{A\}$ as

$$\{R\} = [P]\{A\}, \qquad \text{Equation 3.10}$$

where [P] is the parameter matrix corresponding to the chosen orthogonal array. The components of $\{R\}$, $\{A\}$, and [P] are denoted by (cf. Box et al., 1978)

$$\{R\} = \begin{Bmatrix} R_1 \\ R_2 \\ R_3 \\ R_4 \\ R_5 \\ R_6 \\ R_7 \\ R_8 \end{Bmatrix}, \quad \{A\} = \begin{Bmatrix} 2A_0 \\ A_1 \\ A_2 \\ A_3 \\ A_4 \\ A_5 \\ A_6 \\ A_7 \end{Bmatrix}, \quad [P] = \begin{bmatrix} +1 & +1 & -1 & -1 & -1 & -1 & +1 & +1 \\ +1 & +1 & -1 & -1 & +1 & +1 & -1 & -1 \\ +1 & +1 & +1 & +1 & -1 & -1 & -1 & -1 \\ +1 & +1 & +1 & +1 & +1 & +1 & +1 & +1 \\ +1 & -1 & -1 & +1 & -1 & +1 & -1 & +1 \\ +1 & -1 & -1 & +1 & +1 & -1 & +1 & -1 \\ +1 & -1 & +1 & -1 & -1 & +1 & +1 & +1 \\ +1 & -1 & +1 & -1 & +1 & -1 & -1 & -1 \end{bmatrix} \qquad \text{Equation 3.11}$$

The goal is to determine the values for $\{A\}$, given the DOE methodology provides [P] and the finite element calculations give the response vector $\{R\}$. This is achieved by inverting the matrix [P] in Equation 3.10 to obtain

$$\{A\} = [P]^{-1}\{R\}. \qquad \text{Equation 3.12}$$

As mentioned earlier, two sets of responses are considered in our study. They are nucleation by means of fracturing of the silicon particles and also by debonding of the aluminum from the silicon particles. The quantities A_1, A_2, A_3, A_4, A_5, A_6, and A_7 reflect the influences of particle size, number of particles, particle shape, pre-strain, temperature, additional micro-porosity, and loading direction, respectively.

The first column in the parameter matrix [P] given in Equation 3.11 relates to A_0 , a statistical average of the DOE outputs. Except for column 1 in [P], each level within any of the remaining columns occurs an equal number of times. This introduces the statistical independence, or balance, into the orthogonal array. If the response {R} associated with one level change at another level, then the parameter from one level to the other has a strong impact on the response being considered. Because different levels occur an equal number of times, an effect on the particular response of interest by each of the other parameters is canceled out. Hence, the positive and negative ones in matrix [P] are simply used to express the effect of the two different levels.

3.2.2. Design of Experiments Results

The constitutive model outlined in the previous section is implemented using the ABAQUS general purpose finite element program (Hibbitt *et al*., 1998). The code provides a general interface by which the user may introduce a constitutive model by means of a "user-material subroutine' (UMAT). One DOE analysis with eight calculations was performed under plane strain tensile loading conditions. The schematic representations of the geometries and boundary conditions for the calculations performed in the analysis are shown in Figure 3.14. The initial void fraction is kept constant at 0.001 for all calculations performed. The exterior boundaries of the undeformed configurations in each of the eight calculations are chosen to be unit squares. In our analysis we are interested in symmetric deformation modes and therefore analyze only one quadrant of the domain in calculations 1 to 6, and one half of the domain in calculations 7 and 8. Four-noded isoparametric plane strain elements with 2 x 2 Gauss integration points are used in the calculations. The determination of the material parameters C_I (I = 1,...,18) and the damage parameter m is described in detail in Bammann *et al.* (1993). The values of these parameters for A356 Aluminum are provided in Appendix A.

The criterion used to determine fracture and interface debonding included important assumptions. To determine the influence from silicon fracture we did not have a fracture stress available. As such, we ran the simulations all to the same applied strain level. Then, we determined the maximum principal stress within the silicon particle. These principal stresses for each of the simulations were used to determine the relative parametric influence on fracture. The same procedure was used to analyze debonding except that the negative pressure (tensile pressure) in the aluminum matrix adjacent to the silicon was used. Figure 3.15 illustrates the distribution of principal stresses for the fracture case for simulation #5.

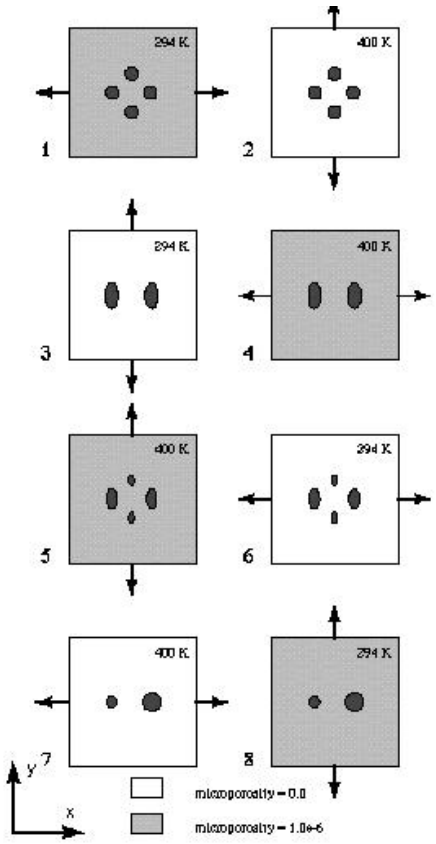

Figure 3.14. Schematic illustrating geometries and loading conditions of eight design of experiments simulations.

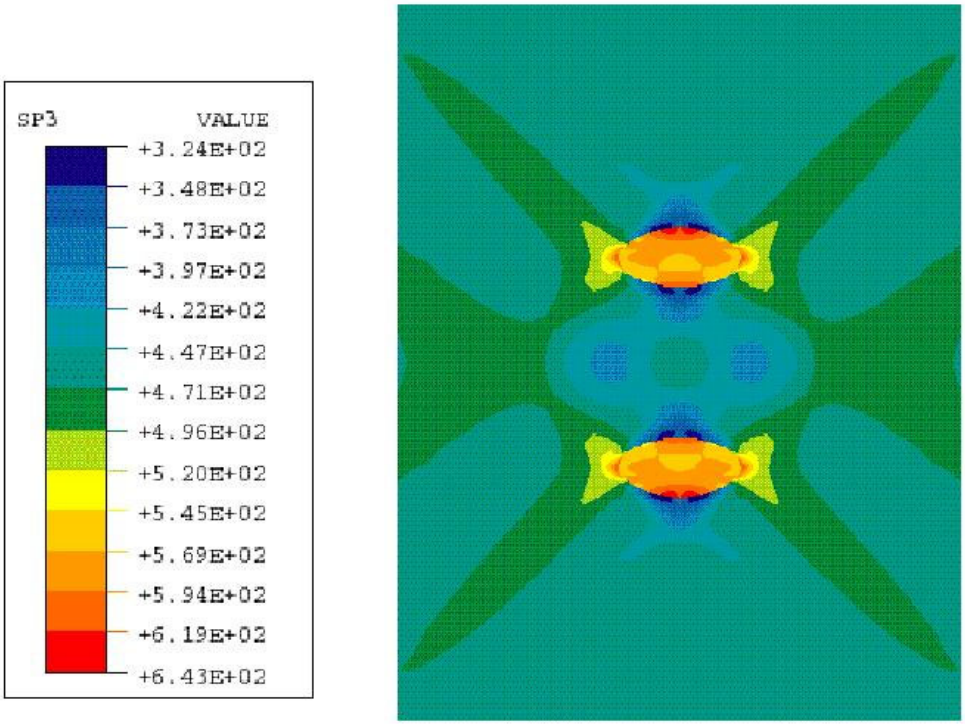

Figure 3.15. Distribution of maximum principal stresses (SP3 in MPa) illustrating location of silicon particle fracture for simulation #2.

Figures 3.16 and 3.17 show the normalized parametric influences on fracture and debonding, respectively, from the DOE analysis. It can be observed that temperature is by far the most influential parameter in both cases. Although individual studies have shown the importance of the other parameters, no studies have revealed that temperature is much more important to a macroscale model than the other parameters.

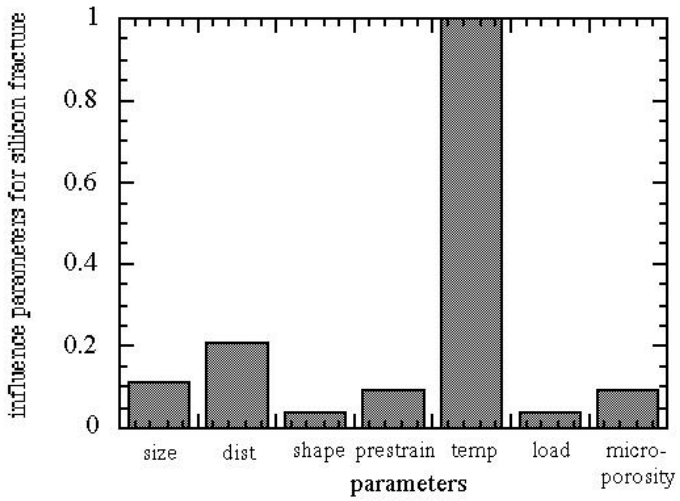

Figure 3.16. Normalized design of experiments result for void nucleation from silicon particle fracture.

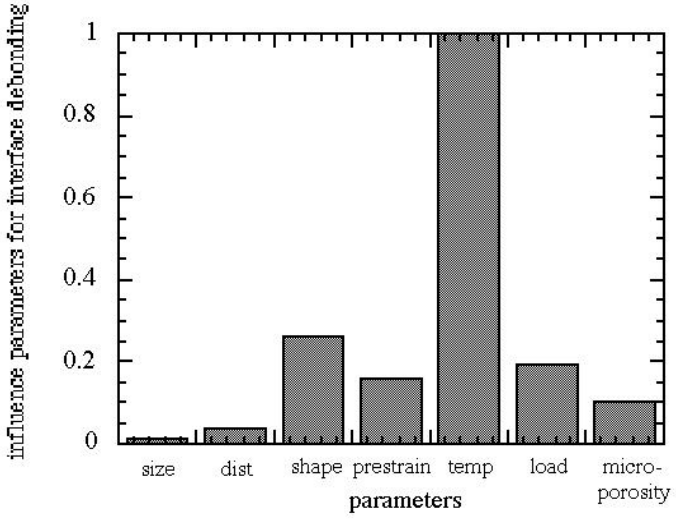

Figure 3.17. Normalized design of experiments result for void nucleation from silicon-aluminum interface debonding.

TABLE 3.2 Design of experiments simulation conditions.

Calc.	Loading	Size	Pre-strain	Temp.	Dist.	Shape	Microporosity
1	X (+)	uniform (-)	$\alpha_{xx}>0$, $\alpha_{yy}<0$ (-)	294 K (-)	4 (+)	round (-)	10e-6 (+)
2	Y (-)	uniform (-)	$\alpha_{xx}<0$, $\alpha_{yy}>0$ (+)	400 K (+)	4 (+)	round (-)	0 (-)
3	Y (-)	uniform (-)	$\alpha_{xx}>0$, $\alpha_{yy}<0$ (-)	294 K (-)	2 (-)	elliptical (+)	0 (-)
4	X (+)	uniform (-)	$\alpha_{xx}<0$, $\alpha_{yy}>0$ (+)	400 K (+)	2 (-)	elliptical (+)	10e-6 (+)
5	Y (-)	non-uniform (+)	$\alpha_{xx}>0$, $\alpha_{yy}<0$ (-)	400 K (+)	4 (+)	elliptical (+)	10e-6 (+)
6	X (+)	non-uniform (+)	$\alpha_{xx}<0$, $\alpha_{yy}>0$ (+)	294 K (-)	4 (+)	elliptical (+)	0 (-)
7	Y (-)	non-uniform (+)	$\alpha_{xx}>0$, $\alpha_{yy}<0$ (-)	400 K (+)	2 (-)	round (-)	0 (-)
8	X (+)	non-uniform (+)	$\alpha_{xx}<0$, $\alpha_{yy}>0$ (+)	294 K (-)	2 (-)	round (-)	10e-6 (+)

3.3. Temperature Effects

The micromechanical parametric study indicated that temperature was the most dominant influence behavior for silicon fracture and aluminum-silicon interface debonding. We performed notch tensile experiments at different temperatures to measure the number density of fractured particles and debonds on the fracture surfaces. Figure 3.18 shows that as the temperature is increased, the number density of total fractured and debonded particles decreases. The same trend is observed when the area fraction (number fractured and debonded over the total number of particles) is used in the figure as well. The reason that the number density of fracture/debond sites increases at a lower temperature is that the stress level and work hardening rate are higher. These observations are in agreement with those of Yeh and Lih (1996), who varied the strength of an A357 alloy through heat treatment and measured the fraction of broken silicon particles in the failed tensile test specimens. They observed at room temperature that the rate of fracture of silicon particles increases with the strength of the alloy.

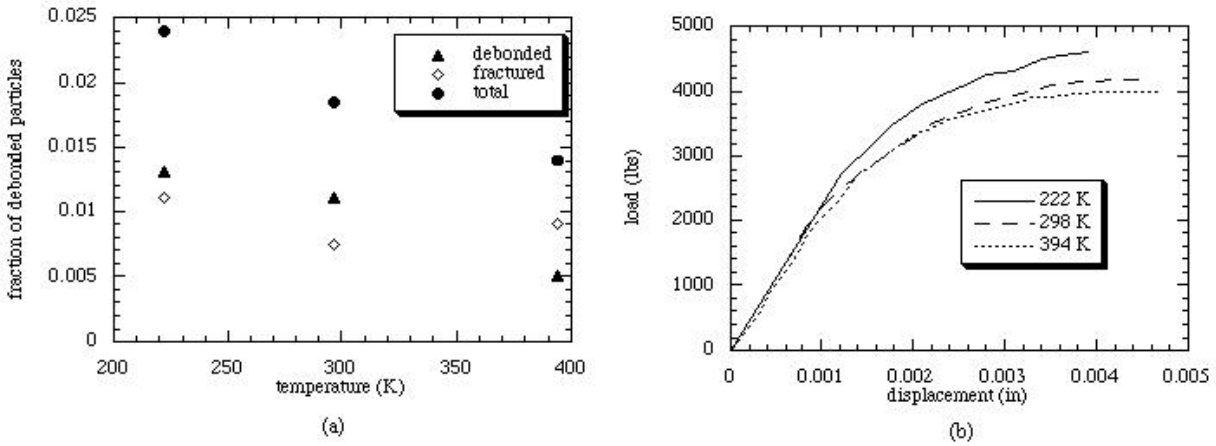

Figure 3.18. (a) Number of damaged particles versus temperature and (b) corrosponding load-displacement curves from notch tensile data.

An exponential function is used to fit to the data, which is shown in Figure 3.18a. This function was used to determine the temperature dependence needed for macroscale void nucleation rate equation.

3.4. Strain Rate Effects

Because the macroscale microstructure-property model includes both temperature and strain rate effects, we now focus on strain rate effects for the cast A356 aluminum alloy. Compression tests were performed at two extreme strain rates (0.0001/sec and 4900/sec) in which microstructural damage from silicon fracture was observed by optical methods. The number of fractured particles is quantified as a function of strain rate for constant uniaxial compression tests at approximately the same strain (20%-25%). The results indicate that the fraction of damaged particles, their average size, and size distribution do not vary significantly with the strain rate range chosen here. Figure 3.19 shows optical images of a specimen that has undergone compression at the low strain rate. Here, the cracks align themselves with the compression axis. This behavior was observed at the high strain rate as well. Figure 3.20 shows the number density of damage particles as a function of strain rate. At first glance, the results suggest that the damage level is invariant to the applied strain rate. However, this may not be true.

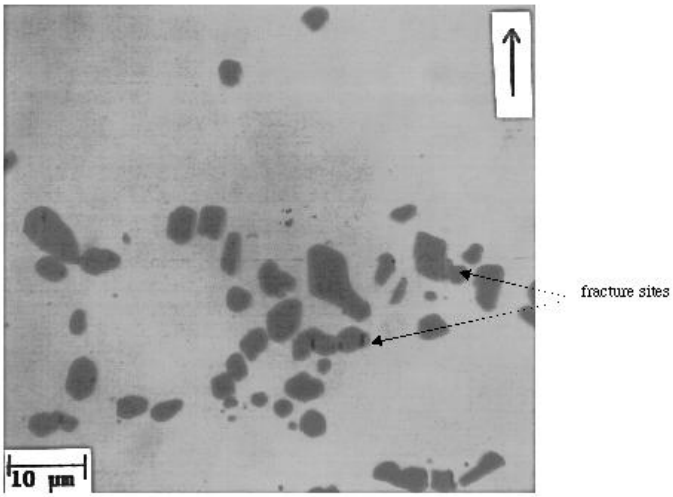

Figure 3.19. Damaged silicon particles in compression specimen at a low strain rate.

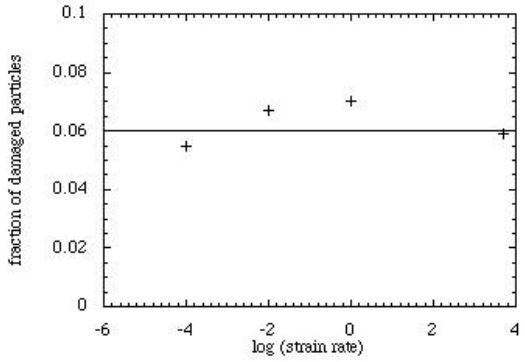

Figure 3.20. Plot of number fraction of damaged silicon particles as a function of strain rate.

The stress-strain histories change as a function of strain rate. Figure 3.21 shows the stress-strain responses of the low and high strain rate tests. One can see that the stress-strain response for the high strain rate tests incur a higher yield than the lower strain rate tests; however, the work hardening rate is lower for the high strain rate tests and at about 7% strain, the total stress levels are approximately equal. After 7% strain, the lower strain rate specimen stress levels were higher than the high strain rate specimen stress levels. Several things are occurring which complicate matters. First, because we observed stress dependent fracture as a function of temperature in the previous section, we would anticipate a strain rate dependence on silicon fracture as well, but Figure 3.20 does not show the strain rate dependence. Unfortunately, that was the level chosen for the experiments. Based on arguments of dislocation motion at temperatures and strain rates, we would anticipate that as the strain rate increased the stress state, the silicon fracture level would increase. Much like as the temperature decreased, thus increasing the stress state, the silicon fracture level increased. The high strain rate test is more than likely not a constant temperature test because of the local increases in plastic work that would raise the temperature in an adiabatic fashion. More tests are warranted at different strain levels to sort out the ambiguities. Surely one possibility is that the Hopkinson bar is creating a complex dynamic stress state in a non-isothermal condition compared with the traditional tests. In Figure 3.20, the damage sites do slightly increase with strain rate until the experimental method is switched.

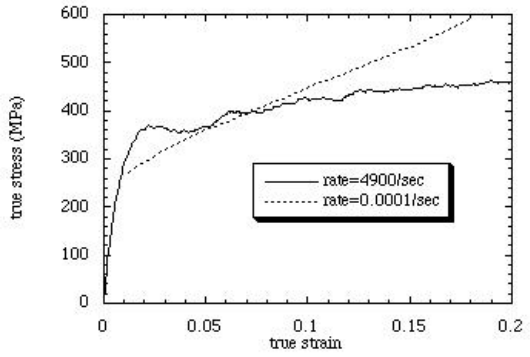

Figure 3.21. True stress-strain curves for compression performed at the lowest (0.0001/s) and highest (4900/s) strain rates.

3.5. MACROSCALE VOID NUCLEATION MODEL

In this section, the macroscale model derivation for void nucleation will be explained. As observed in the atomistic study, the microscale finite element study, and data in the literature, voids nucleate at sites of local microscale stress/strain raisers. The majority of voids nucleate at inclusions, precipitates, and other second phases of ductile metals (Palmer and Smith, 1967; Gurland, 1972; Cox and Low, 1974; Hahn and Rosenfield, 1975). Voids can also nucleate at the intersection of slip bands (Gysler *et al.*, 1974; Asaro, 1979), at grain boundaries (Nieh and Nix, 1980), at twin boundaries (Lu *et al.*, 1998), and at vacancy clusters (Wilsdorf, 1983). In this writing, a void nucleation model is introduced based from microstructural analysis related to second phase particles since they are the most numerous and the weakest links compared to the other defects.

The formulation presented in this paper is consistent with the thermodynamic framework that constrains internal state damage parameters (Coleman and Gurtin, 1967). Because this development is cast in a macroscale continuum damage mechanics formulation, phenomenological notions are recognized to play a role; however lower length scale physical observations are used to motivate the void nucleation evolution equation. The thermodynamic restrictions are elucidated further in Horstemeyer *et al.* (1998).

The void nucleation evolution equation is a function of a length scale parameter (chosen to be the mean size of inclusions for this study), volume fraction of second phase materials, stress state (invariants of stress), strain rate, and fracture toughness. Nucleation models have been proposed in the past in trying to address some of these attributes (cf. Gurland and Plateau, 1963; Ashby, 1966; Rosenfield, 1968; Barbee *et al.*, 1972; Argon *et al.*, 1975; Raj and Ashby, 1975; Gurson, 1977a,b; Needleman and Rice, 1978; Goods and Brown, 1979; Tvergaard, 1982a; Saje *et al.*, 1982; Hirth and Nix, 1985), but none include all of the features mentioned above that have been shown to influence the damage state.

In short, the void nucleation model will be motivated from fracture toughness and extended into a rate form in a phenomenological manner. A complicated stress function will be added to supplant the yield stress. A length scale parameter is added to incorporate a size effect within the model. Finally the volume fraction of the second phase is added in a manner that reflects experimental observations.

Void-crack nucleation truly starts at the atomic level where dislocations are emitted from the crack tip. The void-crack then grows to a point where it can be empirically observed by microscopy methods. In the present phenomenological formulation, a void-crack is observed empirically by optical methods and the atomistic level of void-crack is not considered. Because of this assumption for the initial embryo size, we first consider the Irwin (1958) fracture mechanics equation, which accounts for a small amount of plasticity near an already formed void-crack. The stress intensity from the Irwin equation is given by

$$K_I = \sigma_y \sqrt{2r_p}\,\lambda(w) \qquad \text{Equation 3.13}$$

where σ_y is the yield stress, r_p is the plastic zone size, and $\lambda(w)$ is a function based on the geometry of a specimen. When the stress intensity reaches a critical value, the fracture toughness is defined. In generalizing Equation 3.13 for the dynamic fracture case, we get

$$K_I = K_{IC} = f(\sigma)g(d)\lambda(w)h(rate) \qquad \text{Equation 3.14}$$

where $f(\sigma)$ is not just dependent upon a scalar yield strength but can be a flow stress function that distinguishes stress state behavior based upon the three stress invariants. Instead of r_p, we propose $g(d)$ a function related to size scale parameter. And for $\lambda(w)$, material constants will be introduced that will account for fracture arising from the geometry. $h(rate)$ is a function related to strain rate. Cox and Low (1974) and Maloney and Garrison (1989) observed that a resistance to void nucleation promotes higher fracture toughness. Hence, the more nucleation that occurs, the less tough the material. No mathematical form was given for this relation, but a simple function such as that following can be inferred from the qualitative statements made in those papers,

$$h(rate) = \frac{\eta\|\underline{\dot{\varepsilon}}\|}{\dot{\eta}} \qquad \text{Equation 3.15}$$

By introducing this function, the strain rate, $\underline{\dot{\varepsilon}}$, would be included into the fracture criterion. Kanninen and Popelar (1985) summarized several works describing a nonlinear rate effect on fracture that were dependent on assumptions related to elasticity and the geometry of the specimen. Brickstad (1983) employed Perzyna's viscoplastic model with experimental data that eliminated the geometry effects and the nonlinear effects. Research to quantify fracture rate effects as a function of void nucleation is still an open area. Nevertheless, we assume the form expressed by Equation 3.15 with an openness to modification when more data is available.

The simplest representation for the flow stress function is a rate independent yield function. The J_2 theory yield function is probably the most widely used form for inelasticity, where J_2 is the second invariant of deviatoric stress defined by

$$J_2 = \frac{1}{2}S_{ij}S_{ij}. \qquad \text{Equation 3.16}$$

The second rank stress deviator is defined by $S_{ij} = \sigma_{ij} - \sigma_{hydro}\delta_{ij}$, where $\sigma_{hydro} = \frac{1}{3}\sigma_{kk}$. The stress function that we will employ in Equation 3.14 is introduced as

$$f(\sigma) = z(I_1, J_2, J_3), \qquad \text{Equation 3.17}$$

where

$$z(I_1, J_2, J_3) = a\left[\frac{4}{27} - \frac{J_3^{\,2}}{J_2^{\,3}}\right] + b\frac{J_3}{J_2^{\,3/2}} + c\left\|\frac{I_1}{\sqrt{J_2}}\right\|, \qquad \text{Equation 3.18}$$

and

$$I_1 = \sigma_{ii},\ J_3 = \frac{1}{3} S_{ij} S_{ij} S_{ij}. \qquad \text{Equation 3.19}$$

The material constants a, b, and c are determined from different stress states. This complicated form is elucidated further in the next section, but the reader should know that the motivation for including these particular stress invariant forms in Equation 3.18 is to allow for the void nucleation model to distinguish between tension, compression, and torsion (cf. Miller and McDowell, 1992).

The size-related parameter is given by

$$g(d) = \sqrt{d}\,, \qquad \text{Equation 3.20}$$

where d is a length scale parameter determined by the most important length scale feature that drives the void nucleation. For example, it can be assumed to be the average particle size of the second phase or the distance between particles.

We can now solve for the void nucleation rate as a function of fracture toughness by substituting Equations 3.15, 3.17, 3.18, and 3.20 into Equation 3.14 and then solving for the void nucleation rate,

$$\dot{\eta} = \frac{\|\dot{\underline{\varepsilon}}\| d^{1/2}}{K_{IC}} \eta \left\{ a \left[\frac{4}{27} - \frac{J_3^{\,2}}{J_2^{\,3}} \right] + b \frac{J_3}{J_2^{\,3/2}} + c \left\| \frac{I_1}{\sqrt{J_2}} \right\| \right\}, \qquad \text{Equation 3.21}$$

yielding a nondimensionalized function.

Fracture toughness can be influenced by the initial volume fraction of inclusions as Gangalee and Gurland (1967) observed for aluminum alloys, Hahn *et al.* (1968) for several steel and aluminum alloys, and Moody *et al.* (1993) for powder-processed titanium alloys. Hence, the initial volume fraction of inclusions is included in the nucleation rate from Gangalee and Gurland (1967) form as

$$\dot{\eta} = \frac{\|\dot{\underline{\varepsilon}}\| d^{1/2}}{K_{IC} f^{1/3}} \eta \left\{ a \left[\frac{4}{27} - \frac{J_3^{\,2}}{J_2^{\,3}} \right] + b \frac{J_3}{J_2^{\,3/2}} + c \left\| \frac{I_1}{\sqrt{J_2}} \right\| \right\}, \qquad \text{Equation 3.22}$$

Gangalee and Gurland (1967) showed that the $d^{1/2}/f^{1/3}$ ratio is useful over a broad range of particle volume fractions and sizes for aluminum-silicon alloys. As a particle is fractured or debonded from the matrix material, its capacity to hold strength is reduced and hence it would probably not fracture or debond again as the energy is being released to drive void growth. Because of this local stress redistribution, this particle is probably not capable of creating a void

again, hence the volume fraction of the second phase that is capable of creating a void would be reduced. This change would probably be negligible though in practical applications, so the volume fraction of second phase particles, *f*, can be approximated by the initial volume fraction of second phases. Regardless of whether one or more voids can start from a second phase material, the model described in this section can accommodate either case.

The inclusion of the volume fraction in the denominator is counter intuitive at first glance. One might think that the more volume of a second phase present, the more chances exist of nucleating particles. However, the opposite has been experimentally observed (cf. Gangalee and Gurland, 1967; Hahn *et al.*, 1968; Moody *et al.*, 1993). This is due to the fact that the distribution of particle spacing is inherently included in the diameter over volume ratio.

The void nucleation rate, denoted by Equation 3.22, is a function of stress state, strain rate, fracture toughness, average size of second phase particles (which are assumed to be round), and initial volume fraction of second phase particles. Rice and Johnson (1970) showed that for small second phase particles, the fracture toughness scales linearly with particle spacing; hence, particle spacing effects are effectively included in this model.

Equation 3.22 readily yields the following qualitative trends for the void nucleation rate. As the fracture toughness and initial void volume fraction increase, the nucleation rate decreases. As the stress, strain rate, and particle size increase, the void nucleation rate increases.

When integrating this evolution equation over time, a constant strain rate, fracture toughness, particle size, and particle volume is assumed resulting in the following form,

$$\eta(t) = C_{coeff} \exp\left(\frac{\varepsilon(t) d^{1/2}}{K_{IC} f^{1/3}} \left\{ a\left[\frac{4}{27} - \frac{J_3^{\,2}}{J_2^{\,3}} \right] + b \frac{J_3}{J_2^{\,3/2}} + c \left\| \frac{I_1}{\sqrt{J_2}} \right\| \right\} \right), \qquad \text{Equation 3.23}$$

where $\varepsilon(t)$ is the strain magnitude at time, t, and C_{coeff} is material constant that scales the response as a function of initial conditions since it is equal to a constant times η_0, in which η_0 is the lower limit of the integration signifying an initial void nucleation level.

3.5.1. MACROSCALE VOID NUCLEATION PARAMETRIC STUDY

In the next section, we elucidate each of the void nucleation parameters employed in equation (3.23) by examining ranges of the parameters. Table 3.3 summarizes the parameters used except where the parameter was examined for its sensitivity. The strain rate, $\underline{\dot{\varepsilon}}$, is given by the only prescribed component for uniaxial tension as $\dot{\varepsilon}_{11}$.

Table 3.3. The parameters used for various loading conditions.

parameters	nominal values
d (μm)	4
f	0.07
K_{1C} (MPa-m^0.5)	46.0
C_{coeff}	5.0
a (MPa)	3e5
b (MPa)	0
c (MPa)	5e4
$\dot{\varepsilon}_{11}(sec^{-1})$	0.1

The length scale parameter chosen for this initial study is that of the average size of the second phase particles. The average particle size of second phases can vary significantly depending on the material and processing method. For materials such as powder processed titanium alloys (cf. Moody *et al.*, 1993), the second phase particle sizes can range from 1 to 3 μm in diameter. For A356 cast aluminum the second phase silicon can range from 3 to 10 μm (cf. Gangalee and Gurland, 1967). For the cast Al-Si-Mg alloy used in this study to analyze the different loading conditions, the silicon particle size ranged from 4 to 70 μm with an average of 6 μm.

Figure 3.22a shows the density of voids nucleated per unit volume versus strain level for varying particle size. The trends agree with the observations that void nucleation occurs first at larger particles for a number of different materials (cf. Gurland, 1972; Cox and Low, 1974; Hahn and Rosenfield, 1975). Figure 3.22a illustrates a nonlinear behavior for the nucleation rate. Figure 3.22b shows the increased accumulation of total damage from void nucleation and growth with the increases in particle size as a function of strain.

Volume fractions of second phases in composites can be widespread depending on the material and processing method. For materials such as powder processed titanium alloys (cf. Moody *et al.*, 1993), the second phase can range from 0.2% to 7% by volume. For A356 cast aluminum the second phase silicon can range from 1% to 13% (cf. Gangalee and Gurland, 1967) by volume. Some metal matrix composites can have up to 50% by volume fraction of second phases.

The initial volume fraction of second phase is included in the void nucleation rate equation with a power to the one-third because of observations made by Gangalee and Gurland (1967). For silicon particles embedded in aluminum, Gangalee and Gurland observed that the fraction of broken silicon particles and particles debonded from the aluminum increased in proportion to the parameter $d^{1/2} / f^{1/3}$.

We have shown the trends related to the changes in the particle size, d. Now we show the trends for changes in the particle volume fraction. Figure 3.23a presents the number density of voids nucleated per unit volume versus strain level for increasing volume size.

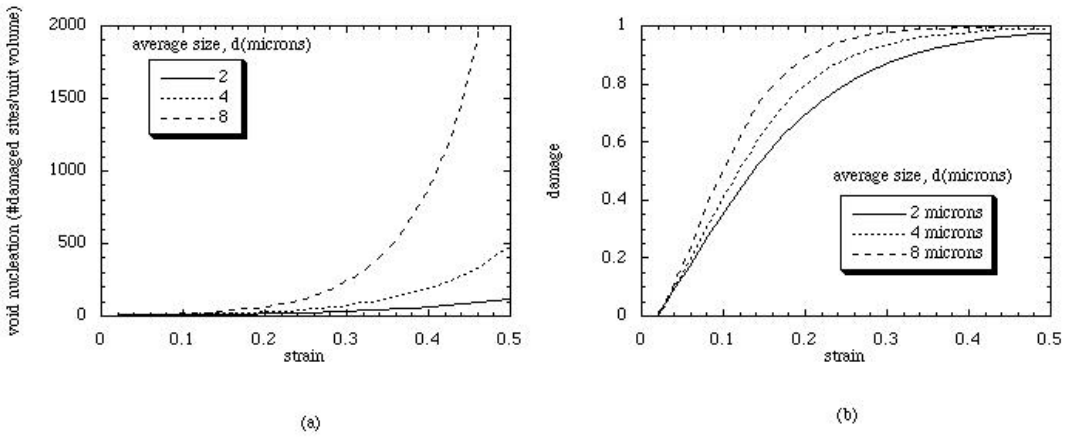

Figure 3.22. (a) Nucleation per unit volume versus strain and (b) damage versus strain under uniaxial tension showing the increase in number of voids and total damage as the particle size increases.

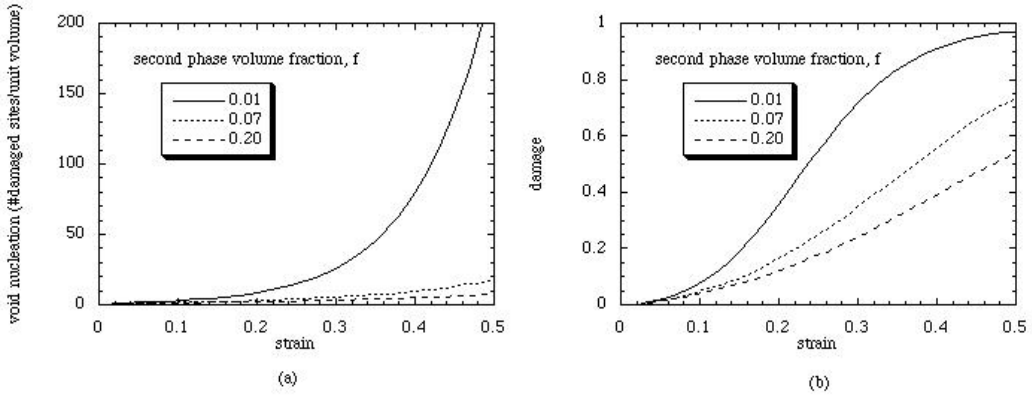

Figure 3.23. (a) Nucleation per unit volume versus strain and (b) damage versus strain under uniaxial tension showing the decrease in number of voids and total damage as the particle volume fraction increases.

As the volume of second phase particles increases, the nucleation rate decreases. Similarly Figure 3.23b shows the decreased accumulation of total damage as the volume fraction increases. As expected, these trends follow closely with those of Gangalee and Gurland (1967).

Spacing of particles is inherently incorporated into the nucleation evolution equation presented in Equation 3.22 in a phenomenological manner by employing the fracture toughness (Green and Knott, 1976; Rice and Johnson, 1970). This has been shown for small particles but not for large particles (Lee *et al.*, 1985; Wojcieszynski, 1993). A range of fracture toughness is given here to illustrate the trends of the nucleation and damage rates. The fracture toughness for A356 cast aluminum ranges from 16.7-18.0 MPa-m^0.5 (Koh and Stephens, 1988), for titanium alloys (Ti-10V-2Fe-3Al, Ti-6Al-4V, and Ti-6Al-6V-2Sn) from 39.1 to 46.0 MPa-m^0.5, and for high purity 4340 steel up to 474 MPa-m^0.5 (Cox and Low, 1974). Figure 3.24a shows the trends for nucleation when the fracture toughness is varied over the ranges listed above as a function of strain. Figure 3.24b shows the decreased accumulation of total damage as a function of strain as the fracture toughness increases. In these strain regimes, when the fracture toughness is fairly large (>46 MPa-m^0.5), nucleation occurs in a linear fashion with respect to strain but is more nonlinear as the fracture toughness decreases.

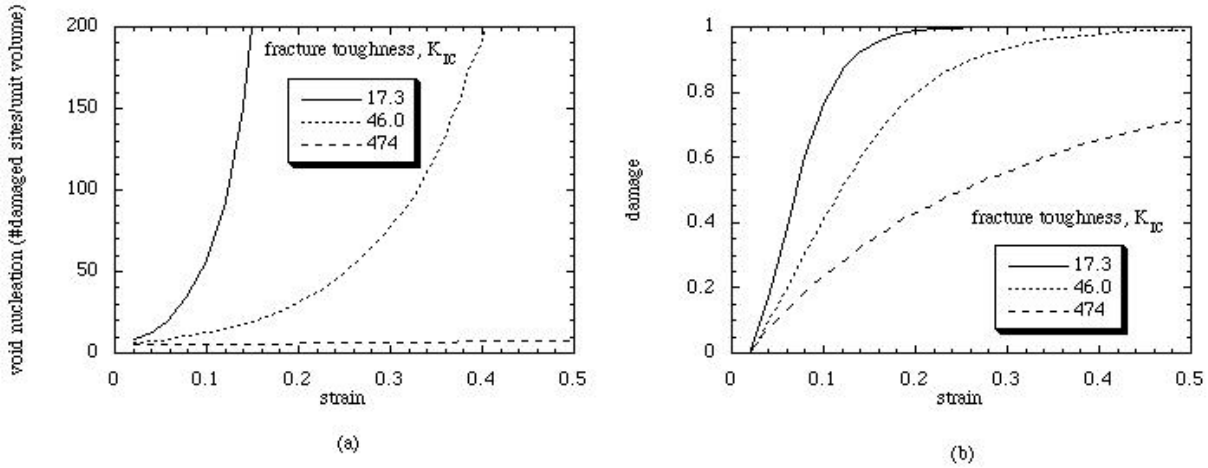

Figure 3.24. (a) Nucleation per unit volume versus strain and (b) damage versus strain under uniaxial tension showing the decrease in number of voids and total damage as the fracture toughness increases.

The onset of nucleation can occur at various strains depending on the material. The material constant C_{coeff} is used to reflect this initial nucleation strain. It is essentially used to linearly scale

the void nucleation equation to cover a wide range of materials. Figure 3.25a shows the trends for the void nucleation rate and damage rate as functions of strain. Note in Figure 3.25b the different types of nonlinearities that can be modeled for damage when C_{coeff} is changed an order of magnitude.

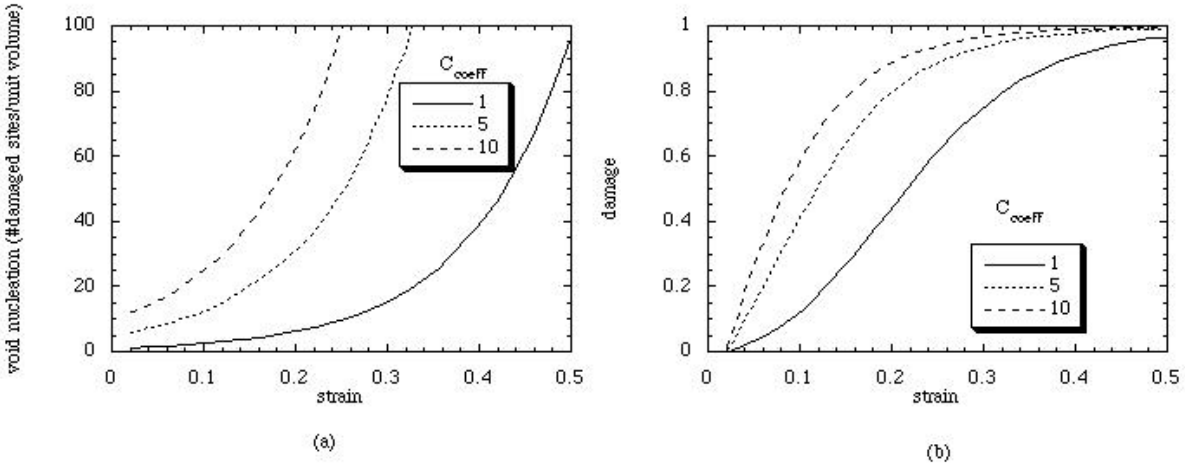

Figure 3.25. (a) Nucleation per unit volume versus strain and (b) damage versus strain under uniaxial tension showing the decrease in number of voids and total damage as the coefficient constant increases.

The motivation for including the stress invariants in Equation 3.22 is to allow for the void nucleation model to account for other stress states besides tension. The three deviatoric stress invariants used in Equation 3.22 have been used as yield "type" functions before. Perzyna (1985) has introduced a general constitutive framework that uses a viscoplastic flow rule three invariants of overstress and a failure criterion. Before this, McClintock (1968), Rice and Tracey (1969), Gurson (1977a,b), Rousselier (1981), Tvergaard (1981, 1982a,b), Becker and Needleman (1986), Kim and Carroll (1987), Lee (1988), Cocks (1989), Mear (1990), Eftis and Nemes (1991), and Lee (1991) included the first two invariants in the yield function to analyze metallic behavior. Rudnicki and Rice (1975) used the first two invariants in determining localization effects in pressure-sensitive materials. Dorris and Nemat-Nasser (1980) and Nemat-Nasser and Shokooh (1980) used the first two invariants with isotropic hardening for compressible frictional geomaterials.

Edelman (1950) showed that the three independent stress invariants I_1, J_2, and J_3 represent a minimal integrity basis for a yield criterion. Adding J_3 has had some practical advantages in

material modeling. Goldman *et al.* (1983) used J_3 in the yield function for determining the strength of polymers. Weng (1987) developed a micromechanical theory for high temperature creep of polycrystals that included J_3 in the yield function and showed that the climb force weakly depended on J_3. Takeda et. al. (1987) showed by experiments on thin-walled cylindrical specimens of a fully annealed mild steel under combined loadings of tension, internal pressure and torsion that the effect of J_3 on the yield behavior of material was larger than that of initial anisotropy. Papadopoulos (1988, 1989) employed J_3 to determine the crack propagation direction in polycrystalline metals. Kearsley (1989) showed the stretch effects within a single cube of using the three invariants. Gupta (1989) generalized Drucker's (1949) inclusion of J_3 into the yield function as a series function. Ohtaki (1988) used a seventh-degree yield function containing J_3 in a two dimensional finite element method for elasto-plasticity to get yield surfaces other than the von Mises yield function.

Over the years, J_3 has been included for modeling certain geomaterials by Desai *et al.* (1984, 1986), for sand by Poorooshasb (1989), and for concrete and soils by Schreyer (1984). Schreyer (1983a, 1983b) also used J_3 to examine strain hardening, strain softening, dilatation, and compaction for frictional materials. De Boer and Dresenkamp (1989) used the three invariants with a non-associative flow rule to determine failure in concrete. Simo and Meschke (1993) added the first invariant to Desai's *et al.* (1986) formulation along with the second and third invariants to arrive at new computational algorithms for finite strain plasticity but the approach was limited to rate independent, isotropic behavior.

Miller and McDowell (1992) were the first to employ stress invariants in internal state variable hardening equations. Drucker (1949) explained that J_3 enabled the proper weighting of the shearing stresses acting on the various slip planes. Miller and McDowell (1992) asserted that J_3 reflects a change of constraint on slip as a function of stress state and thus should be used in the hardening equations in addition to the yield function. Horstemeyer *et al.* (1995) slightly modified the Miller and McDowell (1992) form of the hardening equations of Bammann (1988) to illustrate localization and shear bands related to forming limits.

To the authors' knowledge, employing the three stress invariants to distinguish various stress states has not been applied to modeling void nucleation. Hence, Equation 3.18 allows nucleation to be a function of stress triaxiality and also distinguishes between tension, compression, and torsion.

The material constants a, b, and c in Equation 3.18 relate to the volume fraction of nucleation events arising from local microstresses in the material and as such have dimensions of stress (MPa). These constants are determined experimentally from compression, torsion, and tension tests whereby the density of voids nucleated is measured at different strain levels.

The use of stress invariants in nondimensional form as shown in Equation 3.18 allows for robust determination of the nucleation constants from the various stress state effects. If a, b, and c are zero, the damage evolution form reduces to just void growth. In torsion, the constant a is determined. The constants b and c are determined from tension and compression tests. For

future reference, the constant a is referred to as the torsional constant, b as the tension/compression constant, and c as the triaxiality constant. Table 3.4 shows the delineation of effects from the stress state dependence.

Table 3.4. The stress invariant expressions under different stress states.

	tension	compression	torsion
$\frac{4}{27}-\frac{J_3^{\,2}}{J_2^{\,3}}$	0	0	$\frac{4}{27}$
$\frac{J_3}{J_2^{\,3/2}}$	$\frac{2}{3\sqrt{3}}$	$-\frac{2}{3\sqrt{3}}$	0
$\left\|\frac{I_1}{J_2^{\,1/2}}\right\|$	1	1	0

The influence of the stress triaxiality has been observed for nucleation of voids related to second phases in the works of Cox and Low (1974) and French and Weinrich (1974). Park and Thompson (1988) for 1520 steel, observed that voids started at both sides of the tensile pole of the particle. Because tensile states exist for even compression loadings, some nucleation events are expected to occur even under compression loads. The model allows for this capability. Figures 3.26a and 3.26b show the increase in density of voids nucleated per unit volume and damage, respectively, as a function of strain for an increase in the triaxiality constant, c.

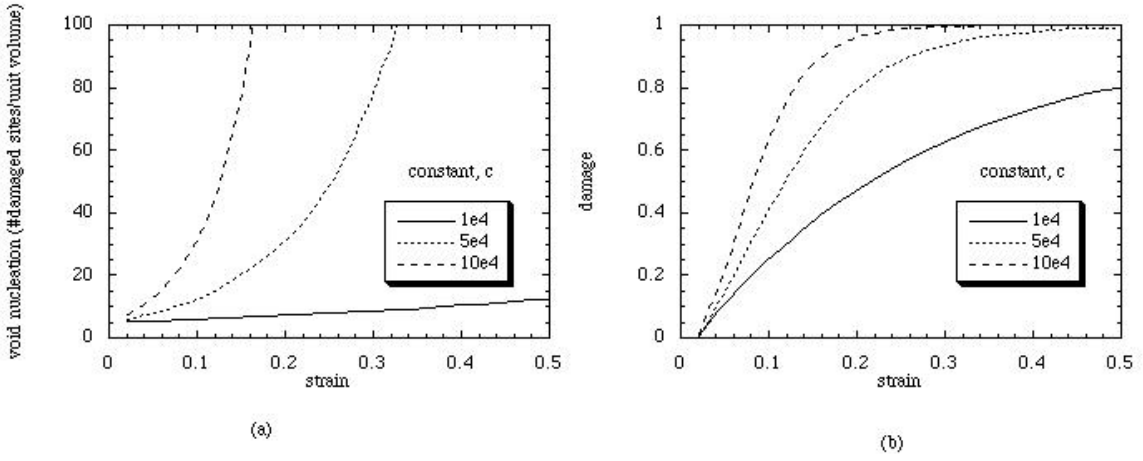

Figure 3.26. (a) Nucleation per unit volume versus strain and (b) damage versus strain under uniaxial tension showing the increase in number of voids and total damage as the triaxiality constant, c, increases.

Figure 3.27a and 3.27b show the increase in voids nucleated per unit volume and damage, respectively, as a function of strain for an increase in the tension/compression constant, b. Note that the trends are nonlinear in a similar manner as when the triaxiality constant, c, is used. Also, note that nucleation occurs more rapidly in tension than compression which concurs with intuition.

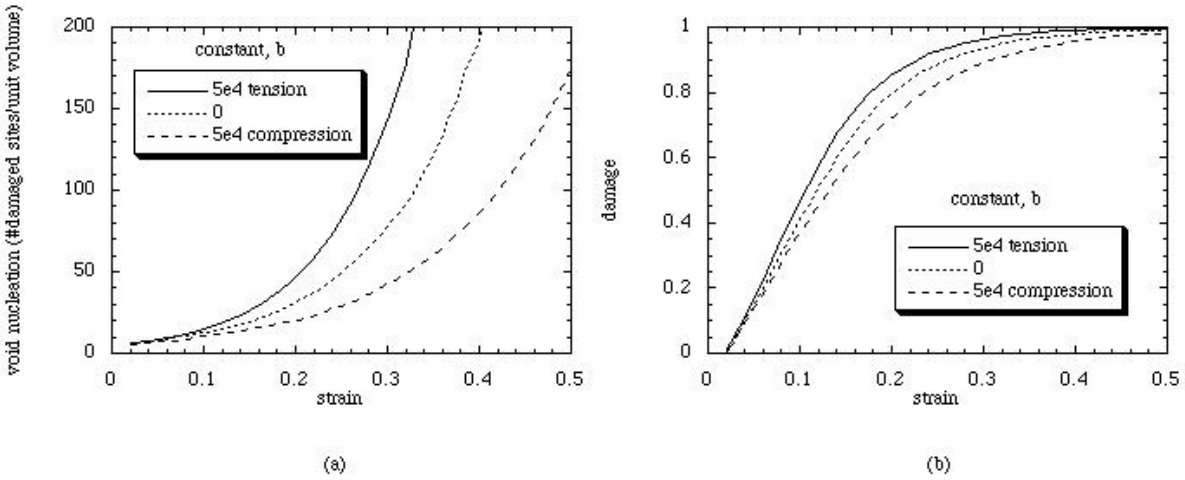

Figure 3.27. (a) Nucleation per unit volume versus strain and (b) damage versus strain showing the change in number of voids and total damage as the tension/compression constant, b, changes

Figure 3.28a and 3.28b show the increase in voids nucleated per unit volume and damage, respectively, as a function of strain for an increase in the torsional constant, a. Figure 3.28 illustrates that much more torsional straining is needed to achieve the same amount of damage as under tension. This arises because the void growth is based on the stress triaxiality which is zero for torsion. Hence the damage purely accumulates due to nucleation events.

The void nucleation model can be used for multiaxial stress states as shown in Figure 3.29. The nucleation model parameters were chosen such that the lowest void nucleation rate arises for simple shear (torsion) and the next lower rate arises for compression. The upper limit of void nucleation occurs when the multiaxial condition of tension plus torsion is applied giving just a slightly higher nucleation rate than tension alone. The constants in Table 3.5 were employed for illustrative purposes, but different values for the constants would obviously place a different level of influence from the stress state on the nucleation behavior. As such, any material can be accommodated given that experimental data is available.

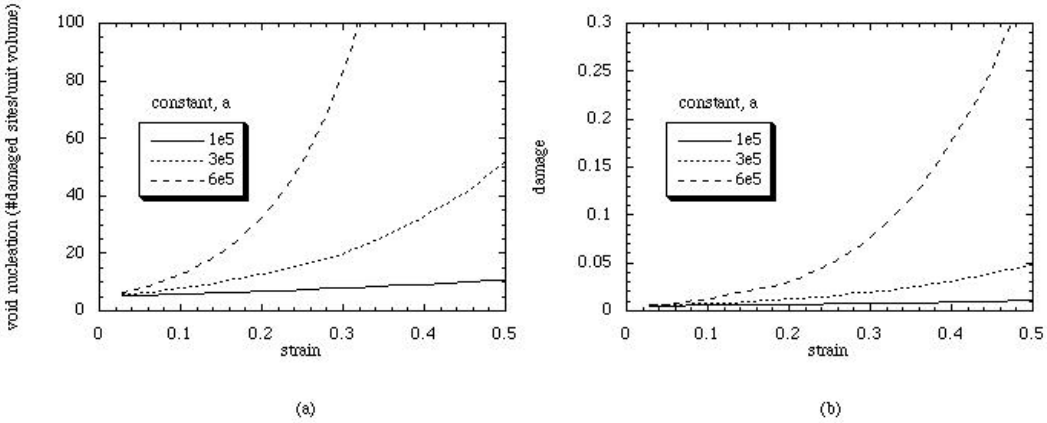

Figure 3.28. (a) Nucleation per unit volume versus strain and (b) damage versus strain under torsion showing the increase in number of voids and total damage as the torsional constant, a, increases.

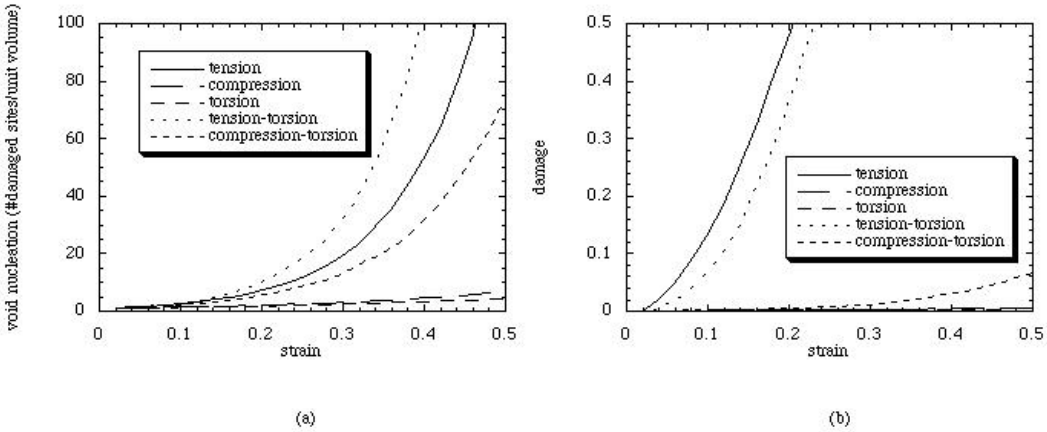

Figure 3.29. (a) Nucleation per unit volume versus strain and (b) damage versus strain under various loading conditions.

Figure 3.29b shows the damage level versus strain for the same multiaxial loading conditions in Figure 3.29a. In these calculations the initial porosity level was assumed to be 0.001. The damage trends are different than the nucleation trends because of the stress state dependence on the void growth rule (Equation 3.22). Void growth would dominate over void nucleation when tensile triaxialities are present. Under compression and torsion void growth is typically less.

Table 3.5. The parameters for a cast Al-Si-Mg alloy under various loading conditions.

parameters	Multiaxial values
d (μm)	8
f	0.07
K_{IC} (MPa-m^0.5)	17.3
C_{coeff}	0.01
a (MPa)	6.16e5
b (MPa)	5.86e4
c (MPa)	5.20e4

3.5.2. SUMMARY

A void nucleation evolution model is presented that is a function the fracture toughness of the aggregate material, a length scale parameter (taken to be the average size of the second phase particles in the examples shown in this writing), the volume fraction of the second phase, strain rate, and stress state. Different loading tests were performed for this study for a cast Al-Si-Mg aluminum alloy to analyze the stress state dependence of void nucleation. The void nucleation model was then correlated to the void nucleation data under different stress states.

This page intentionally blank.

4. VOID GROWTH AND COALESCENCE

Void nucleation, growth, and coalescence often characterize damage progression in ductile metals. Of the three components, void growth has been studied the most. A wealth of researchers have focused on different aspects of void growth, for example, strain rate effects (Cocks and Ashby, 1980; 1982; Budiansky *et al.*, 1960), work hardening effects (McClintock, 1968), and yield function effects (Gurson, 1977). However, the least amount of research has been performed on understanding void coalescence, which is typically associated with the last step of the idealized three stage damage process. Void coalescence realistically occurs at different spatial size scales throughout the deformation and is not just limited to final failure. Understanding coalescence throughout deformation is key for macroscale prediction of failure in finite element codes. As such, numerical and physical micromechanical studies can provide important information for constructing phenomenological equations that are necessary at higher spatial size scales.

Within the last 20 years, different aspects of void coalescence have been examined. Garrison and Moody (1987) provide a thorough review of studies before 1987. Since that time, some work has focused on quantifying void coalescence. Faleskog and Shih (1997) recently performed planar micromechanical calculations based upon the constitutive model and numerical implementation of Cuitino and Ortiz (1992) and Moran *et al.* (1990). In the Faleskog and Shih (1997) study, different initial void volume fractions and different stress triaxialities were examined. Tvergaard and Needleman (1995, 1997) and Ramaswamy and Aravas (1998) have discussed void coalescence from a macroscale continuum perspective using an intrinsic spatial size scale parameter. Pardoen *et al.* (1998) compared four different coalescence criteria in finite element simulations and compared these results to experimental data for copper. Nagaki *et al.* (1993) examined void growth by coalescence from using different nearest neighbor distances in a numerical setting. Benson (1993) has numerically analyzed different void configurations (coalescence) for high strain rate shock environments. Eftis *et al.* (1991) examined void growth under high rate spall conditions and quantified void growth influences on the final damage state. Chan (1988) has analyzed void growth under high temperature creep environments. Recent physical experiments from studies in the materials science literature reveal a strong influence of coalescence on final failure of metals (cf. Jun, 1991; Worswick *et al.* 1994; 1995; Geltmacher *et al.*, 1996; 1998; Zurek *et al.*, 1997; Tonks *et al.*, 1997; Al-Ostaz *et al.*, 1997; Bandstra *et al.*, 1998; Lu *et al.*, 1998).

Coalescence of voids has typically been categorized into either void impingement or void sheeting (Figure 2.4). During void impingement, the material ligament between two voids necks to a point as the two neighboring voids grow together (Cottrell, 1959). The void sheet mechanism occurs by the following process. Primary voids can nucleate from second phase particles, and these voids grow as the material is plastically deformed. At a higher strain/stress level, neighboring particles will nucleate secondary voids. These particles tend to be smaller and have stronger bonds with the matrix. Then, voids from the larger particle distributions will link to the smaller void distribution through the ligament over a small interval of strain. The material path between the void distributions looks sheet-like, hence, the name “void sheet” mechanism.

In the following sections, we focus on two types of coalescence operating at different length scales. The first type occurs when silicon particles either fracture and/or debond from the

aluminum matrix. Here the new pores will interact with casting pores. This type of coalescence is a void sheet form. The second type includes void coalescence from void-void interactions from casting pores, and this is the void impingement form of coalescence. Hence, both forms are included in the macroscale model. In this section, we first proceed with the interaction from the silicon and casting pores.

4.1. MESOSCALE I: SILICON-POROSITY COALESCENCE STUDY

Void growth and coalescence is a complicated mechanism in this cast A356-T6 aluminum alloy. In order to understand the mechanisms related to voids growing from silicon and how they interact with casting pores, we placed finite element meshes on actual micrographs. The parameters we examined were the number of boundary elements, applied loading conditions, and temperature. The microstructure-property model was used with constants that were determined from dendritic aluminum (1% Si in solution) compression stress-strain curves at different temperatures.

Figure 4.1 illustrates how we determined the finite element mesh from a micrograph. Because the silicon particles were on average 4 μm and the dendrite cell size on average were 20 μm, the mesh was made about 100 μm square. The mesh included 50 elements on a side, so each element was 2 μm in size. The region in Figure 4.1 was chosen because the pore was an averaged size pore in the large micrograph (not shown). The maximum dimension of initial size of the pore was about 16 μm and was fairly equiaxed. The initial void area fraction used in the simulation from the initial casting pore equaled the overall initial void volume fraction (~1.4%), and the initial silicon area fraction equaled the overall silicon volume fraction (7%).

Recall that the total damage comprises three components: void nucleation, void growth, and void coalescence. From these simulations, we can determine the total void volume fraction. We know the void nucleation rate from experiments. We also know the void growth rate from McClintock (1968), for example. Hence, the only unknown is the coalescence. As such, we tune the void nucleation rate, by trial-and-error, in the simulations to the experimental void nucleation rate data for tension. Then, we quantify the total void volume fraction as a function of strain. Before we get into the results, let us first explore the effects from various boundary layers.

Because we are examining local responses at the scale of microns, we must consider the representative volume in the midst of the aggregate casting. To accomplish this, we used microstructure-property model constants for the aggregate cast A356-T6 aluminum alloy in the boundary elements analogous to a self-consistent approach. Figure 4.2 shows that a boundary is indeed desired because when the local uniaxial true stress is examined in the boundary elements, a difference arises from zero to two boundary elements. However, when more than two boundary elements are used, the same results arise as the two element boundary layer. We examined just the boundary elements because when the boundary element stresses start to drop that reflects internal weakening of the representative volume chosen. From these simulations we conclude that two boundary elements are the optimal choice to represent the aggregate response of the cast A356-T6 aluminum alloy. The rest of the discussion in this section will include only two boundary element layers.

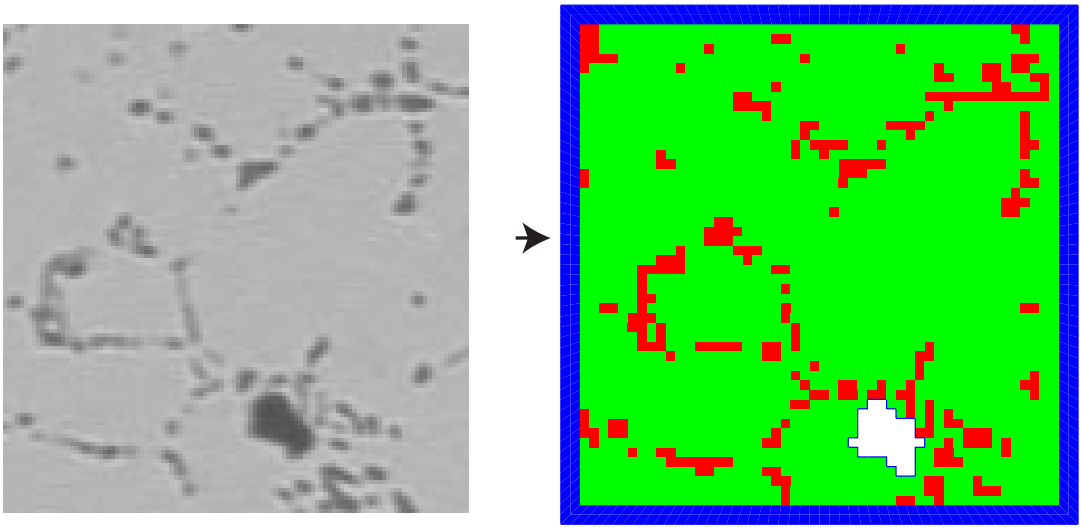

Figure 4.1. Conversion of micrograph into finite element mesh.

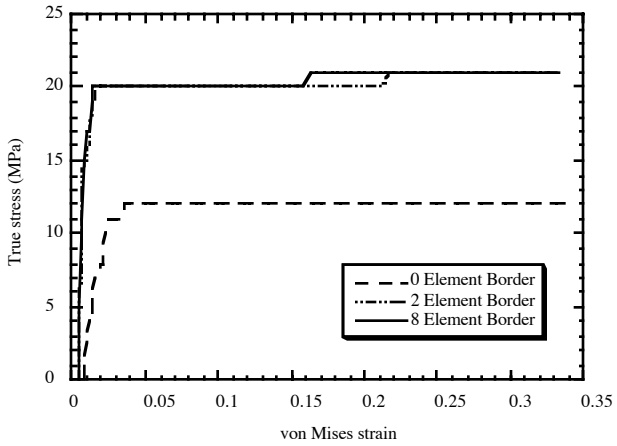

Figure 4.2. Stress-strain curves with varying number of boundary layer elements.

We ran simulations that were correlated with the tensile void nucleation data. By examining cases when only debonding occurred, when only silicon fracture occurred, and when both occurred (like the actual material), we were able to ascertain the different failure mechanisms relation to the global response. Practically though, the cast A356-T6 aluminum alloy experienced both silicon fracture and silicon-aluminum interface debonding. Figure 4.3 shows a comparison of the simulations to the experimental data when the void nucleation for both silicon fracture and interface debonding were used. An elastic maximum critical principal stress was used for the silicon fracture criterion. Two methods were used for the interface debonding. The first method was using the Cocks and Ashby (1980) void growth rule that is driven from the local stress triaxiality, which plays a major role in interface debonding. The second method included a local maximum critical stress similar to the silicon fracture criterion. We employed this method after running the atomistic simulations. The atomistic simulations showed that when the interface debonding stress was determined approximately 40 Å from the interface, an elastic fracture criterion could model the debonding fairly accurately. Although both methods for the interface debonding gave similar results, we mostly used the linear elastic debonding criterion. The silicon fracture stress was determined to be 310 MPa, and the elastic debonding stress was determined to be 1.5 GPa. From the atomistic simulations, we determined the elastic debonding stress to be approximately 20 GPa. Higher atomistic simulation results are expected because no nearest neighbors were included, idealized shapes were used, only uniaxial tension was used, only one crystal orientation was used, and no initial dislocations were included. Hence, the micromechanical simulation results give the correct order of magnitude of the fracture stress levels.

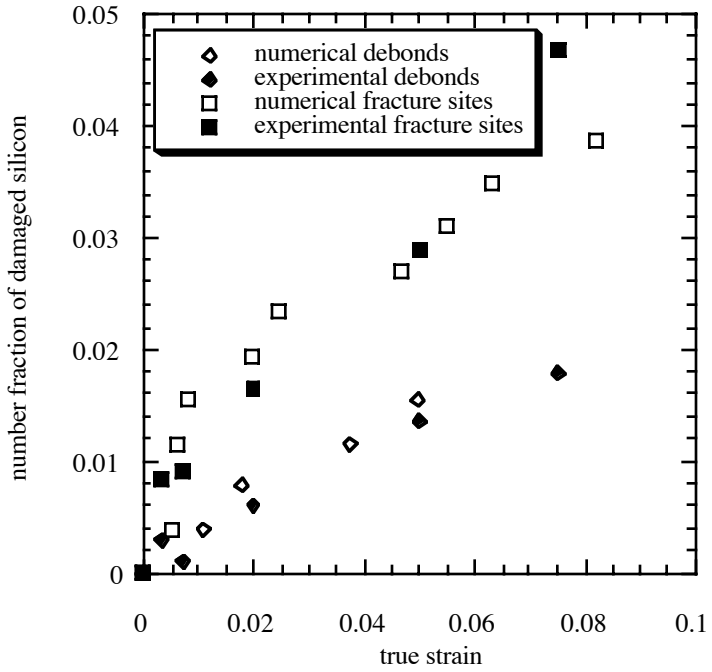

Figure 4.3. Comparing Mesoscale I simulation and experimental void nucleation data as a function of strain.

When only silicon fracture was assumed, the elastic fracture stress level changed in order to match the experimental void nucleation data. Alternatively, when only interface debonding was assumed, the elastic debonding stress level also changed in order to match the experimental void nucleation data. These two simulations gave insight into how the material is dissipating energy upon deformation. Also, one can anticipate that the stress level criteria would change as material without pre-existing defects within the silicon or oxides at the aluminum-silicon interface would change. Interestingly, when evaluating the total void volume fraction for the three cases: (1) just debonding, (2) just silicon fracture, and (3) both fracture and debonding, the total void volume fraction as a function of uniaxial strain is not much different between the three cases. Figure 4.4 shows the comparison.

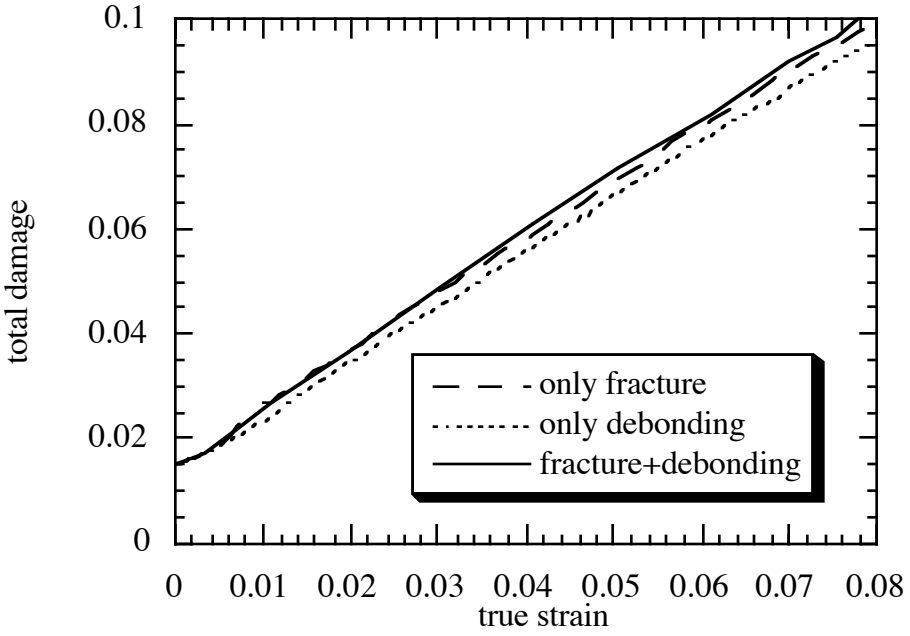

Figure 4.4. Comparison of total damage prgression from initial casting porosity growing under deformation and from cases when (i) fracture of silicon occurs, (ii) debonding of the silicon-aluminum interface occurs, and (iii) when both occur.

Now let us discuss the results from the actual case in which both silicon fracture and aluminum-silicon interface debonding occurs. Figure 4.5 shows a contour plot of total damage at failure of the representative volume under uniaxial tension. One can see that the original casting pore grew along with new voids that have nucleated from silicon particles. By examining the equivalent (von Mises) plastic strain in Figure 4.6 one can see that the local plastic strain from the pore strongly affects the nearby region that includes the silicon particles. Other simulations, not shown here, show that the casting pore comprises most of the damage early on in deformation but gradually lessens its influence as more voids are nucleated and grown from silicon particles.

Under biaxial tension, one can see when comparing Figure 4.7 and Figure 4.8 that the total void volume growth rate is higher for the biaxial tension case. One can expect biaxial and even triaxial stress states to exist in a complex geometry such as a control arm. As such, caution needs to be present when extrapolating uniaxial data to real 3D complex geometries that may incur stress biaxialities or triaxialities.

Next we examine the micromechanical simulations at different temperatures in the context of the biaxial and uniaxial loadings. Table 4.1 summarizes the results. Clearly, the final porosity level at failure is different when considering different loading states and temperatures. The failure strain was determined from the drop-off of the stress-strain response of the boundary elements and correlating saturation of the total porosity level. Both of these indicators suggest that the representative volume has failed since the load bearing capacity has been lost and no more void growth occurs. Interestingly some patterns arise from the simulations. As temperature increases, the strain at failure increases. This concurs with observations made from the notch tensile data shown in Figure 3.19b. Another observation is that as the temperature increases, the porosity at failure increases, at least for the uniaxial case. Clearly, the biaxial case had more influence than temperature on these simulations. As far as macroscale modeling of coalescence, temperature dependence and stress state dependence are critical for a coalescence model.

Table 4.1 Summary of % porosity and strain at failure for the micromechanical simulations.

	%porosity at failure	% strain at failure
Uniaxial (T=294 K)	7.8	14.0
Biaxial (T=294 K)	59.0	13.5
Uniaxial (T=400 K)	12.1	22.1
Biaxial (T=400 K)	58.5	15.0

4.2. MESOSCALE II: PORE-PORE COALESCENCE STUDY

Now that we have an idea of the void coalescence from the silicon-pore interactions, we must consider the size scale from 10-500 μm in which pore-pore interactions will occur. We attempt to quantify pore-pore interactions in this section by first performing a Design of Experiments (DOE) study similar to the one described in Section 3.2 for void nucleation. We then perform more simulations to examine further parametric trends.

4.2.1. VOID COALESCENCE PARAMETRIC STUDY

Although void volume fraction has been the most examined quantity for void growth (cf., McClintock, 1968; Rice and Tracey, 1969; Gurson, 1977; Cocks and Ashby, 1980), a large number of factors besides void volume fraction are known to play significant roles on influencing void growth and strain localization. The works that have considered the void volume fraction and void growth studies, for the most part, have neglected coalescence. Here, we examine the role of seven parameters by performing a series of design of experiments (DOE) finite element simulations to determine the most important parameters relative to each other. The DOE, as described in Section 3.2.1., is used to screen the parametric effects related to the total void growth and strain localization within the aggregate.

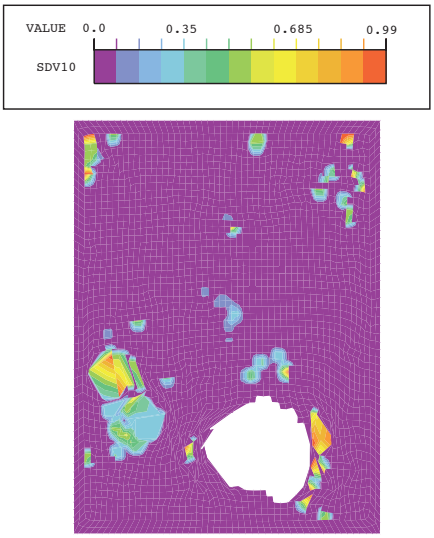

Figure 4.5. Contour plot of total damage (sdv10) at failure (approximately 12% strain) under uniaxial tension at 294 K.

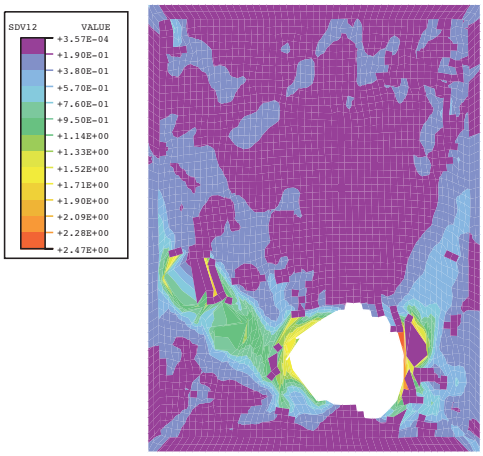

Figure 4.6. Contour plot of equivalent plastic strain (sdv12) at failure (approximately 12% strain) under uniaxial tension at 294 K.

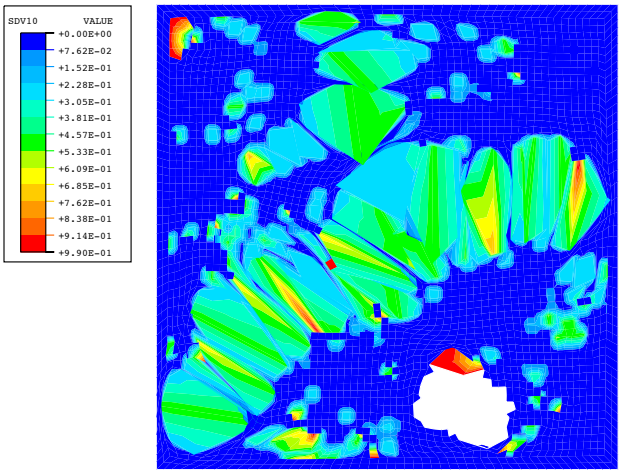

Figure 4.7. Contour plot of total damage (sdv10) at failure under biaxial tension at 294 K.

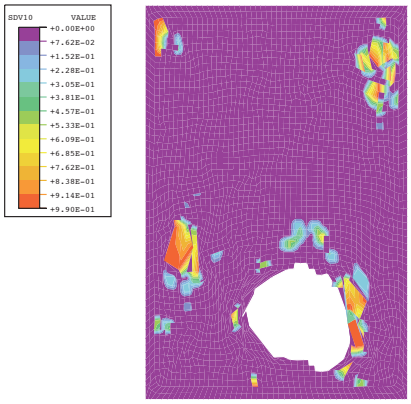

Figure 4.8. Contour plot of total damage (sdv10) at failure (approximately 14% strain) under uniaxial tension at 400 K.

For the seven parameters, we used two limits to determine the responses. The seven parameters include: (1) number of pores, (2) size of pores, (3) shape of pores, (4) additional microporosity, (5) temperature, (6) prestrain history, and (7) loading direction. These parameters have been studied independently but not in the context of the others. Incidentally, each investigator showed that all of these parameters are important. Although this may be true, for a macroscale model, one must consider the first order effects and then if (1) it is simple or (2) time is allocated, then further modeling to include the second order effects is warranted.

Voids within a casting are generally inhomogeneously present in various shapes and sizes. In fact, many materials exhibit this behavior, and as a consequence the number of pores has been examined by several investigators. Needleman (1972) has presented a numerical investigation that accounts for interaction between neighboring voids. Becher (1987) has employed finite element analyses to examine the effects of different distributions on final failure. Melander and Stahlberg (1980) have analyzed void distribution effects on localization. All of these studies indicate that the number of voids plays a role in void growth. In our micromechanical study, we chose either two or four voids while keeping the void volume fraction the same.

Needleman *et al.* (1995) studied the evolution of pore sizes as a function of loading using micromechanical simulations. Recently, Faleskog and Shih (1997) have also used micromechanical simulations to analyze multi-size effects on void growth. These studies have indicated the important role that size has on the total void growth of the material. In our study, the pore size deals with the uniformity of pore size with respect to the other sizes; hence, we chose a uniform distribution and nonuniform distribution.

Gologanu *et al.* (1993; 1994) have developed formulations to study effects of prolate and oblong voids. Needleman (1972) performed micromechanical finite element simulations to analyze the evolution of pore shape on initially equiaxed pores. These studies indicate that the shape of the pores give rise to a pattern of void growth that is not typically captured using simple scalar void growth equations. The shape is somewhat related to the pore size, but for the sake of quantifying the relative influence effects on void growth and localization, we use round pores and elliptical pores. The elliptical pores are chosen with a major-to-minor axis ratio of 2:1.

Microporosity below a void volume fraction of 10^{-4} is tedious and impractical and as such is difficult to measure. Yet, levels of porosity below 10^{-4} can occur with a material. Tvergaard (1982a) through micromechanical simulations concluded that microporosity can introduce highly localized straining and voids can grow in bands between larger voids arise from the microporosity present between the larger holes. Horstemeyer and Revelli (1997) have also shown that microporosity can change the void growth and localization behavior in wrought 6061-T6 aluminum. In this study, we chose the initial levels of microporosity as identically zero and 10^{-6}.

Except for small temperature changes Bridgman (1923) and Espey *et al.* (1959) imposed on notch tests, very little has been accomplished in the way of determining void growth phenomena at wider ranges of temperatures. Since plasticity is temperature dependent, void growth is too. In

this study, we chose 294 K and 400 K as the two temperature levels. This is a typical range experienced by automotive chassis components.

Prestrain effects can arise from manufacturing processes where directional deformation is imposed upon the material or under conditions where nonmonotonic loading sequences are experienced. Mackenzie *et al.* (1977) showed experimentally that for several steels, notch tensile tests are sensitive to prestraining loading direction. Horstemeyer and Revelli (1997) also showed the prestrain effects on damage accumulation in several boundary value problems. A moderate prestrain level of 10% was chosen for this study.

The loading direction is an obvious influence parameter that plays an important role in determining the stress state of the material. Bourcier and Koss (1981) have shown that, in regions where pairs of holes occur, different stress states and void growth rates arise depending on the orientation of the holes with respect to each other and with the loading path. In this study, we impose uniaxial conditions in the horizontal and vertical directions.

For the DOE study, eight simulations, shown in Figure 4.9, were performed using the microstructure-property model with the constants determined from the cast A356-T6 aluminum compression data at different temperatures. Two outputs were desired: total void volume fraction and strain at localization. The total void volume fraction was determined from directly measuring the total void area. To approximate the strain at localization, we examined the stress drop-off from the stress-strain curve. Figure 4.10 shows the total void volume fraction versus the applied strain, and Figure 4.11 shows the load versus applied strain for the related simulations. Clearly, because of the various parameter levels, the void growth rates are different. The simulations were terminated upon the onset of strain localization (or strain softening). The total void volume fraction and strain at localization were then placed into the DOE array to get the relative influences.

Figure 4.12 and 4.13 are histograms of the DOE results from the finite element simulations for the strain localization and total void volume fraction, respectively. The results were normalized to the peak value to illustrate the relative influence.

Unlike the DOE void nucleation study in Chapter 3 which showed one dominant influence parameter (temperature), there were several first order influence parameters related to strain localization (pore size, temperature, loading direction, and prestrain) and void growth (microporosity, pore size, and temperature). Clearly, the macroscale model should have these first order characteristics represented in order to determine realistic damage levels to determine final failure. Fortunately, the macroscale plasticity model captures the prestrain effects and the boundary conditions for the macroscale finite element simulations captures the loading direction effects. The important parameters to include in the coalescence model are temperature and pore size.

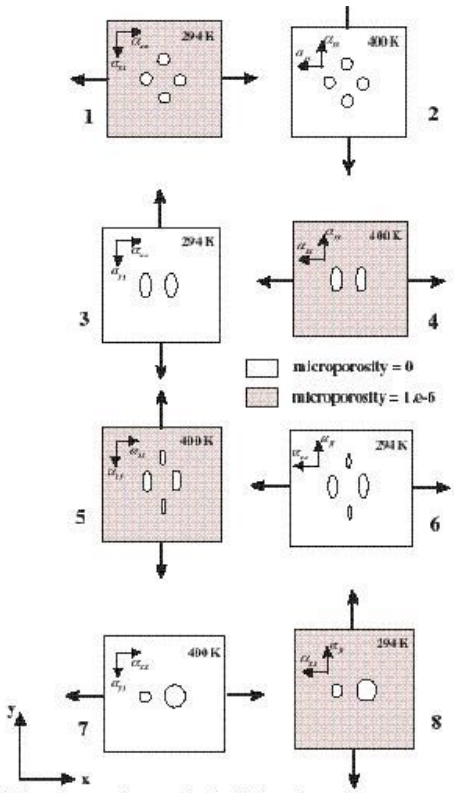

Figure 4.9. Various geometries used in the design of experiments parametric study.

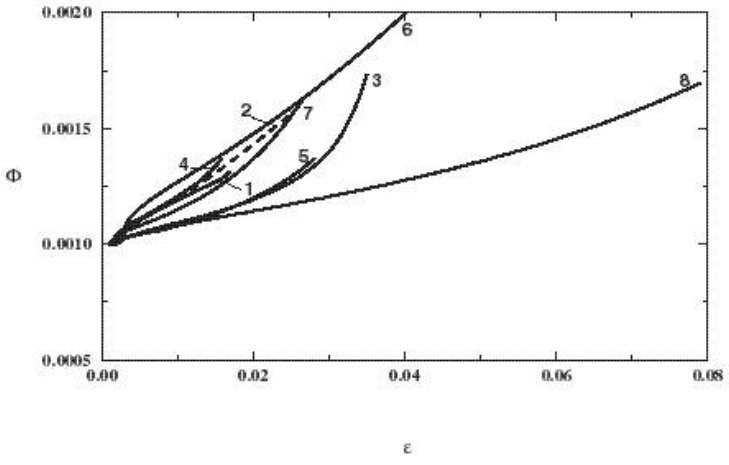

Figure 4.10. Damage versus applied strain for eight design of experiments simulations.

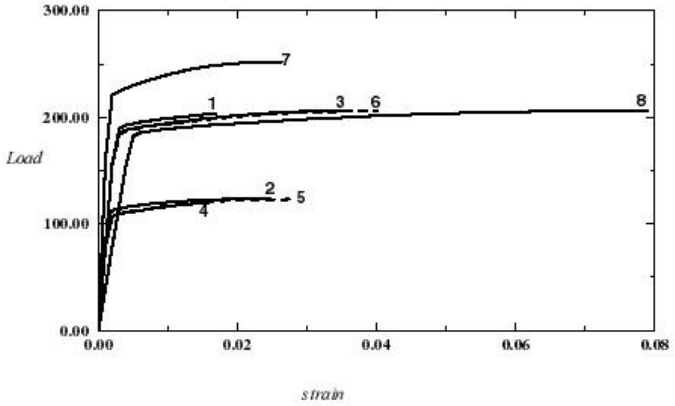

Figure 4.11. Load versus applied strain for eight design of experiment simulations.

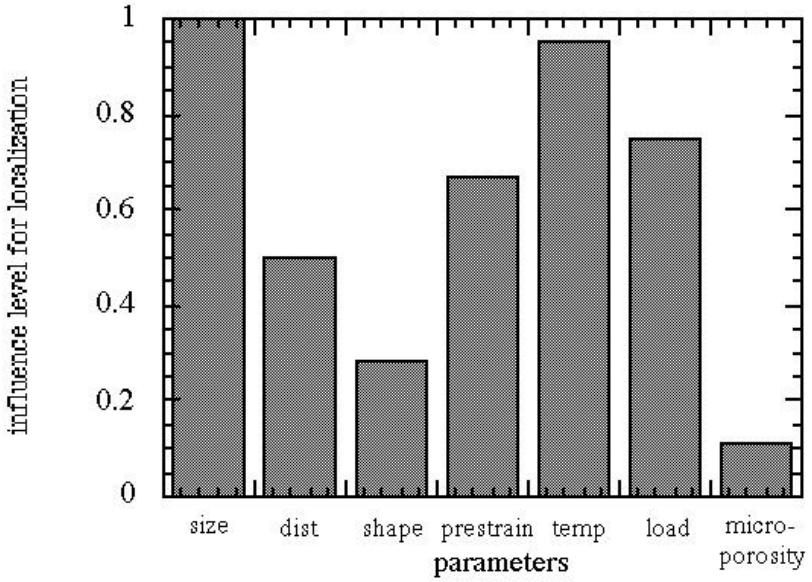

Figure 4.12. Normalized design of experiments results when examining strain localization from pore-pore interactions.

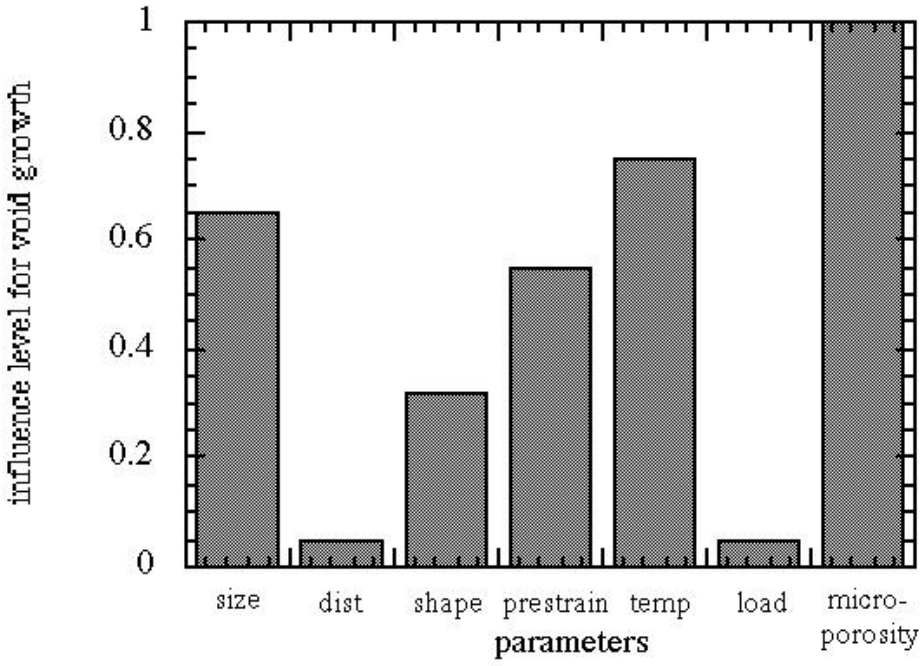

Figure 4.13. Normalized design of experiments results when examining void growth from pore-pore interactions

The effects of the hydrostatic stress and equivalent plastic strain on the responses are critical. Clearly, these two quantities influence single voids growing (e.g., Cocks and Ashby, 1980). We would assume then that these two quantities would also drive void growth as related to coalescence. Figure 4.14 shows a contour plot of the hydrostatic stress for simulation #5. Here, the relative influence of the various parameters affects the magnitude of the hydrostatic stress and the distribution. Figure 4.15 shows a contour plot of the equivalent plastic strain for simulation #5. One can see the band between the two voids of large strains indicating its influence on coalescence as well.

4.2.2. TEMPERATURE EFFECTS ON COALESCENCE

Now that we understand that temperature and pore size are crucial to void growth and coalescence, we further examine these quantities in addition to the intervoid ligament distance. We quantify the temperature effects by varying several parameters related to pore-pore coalescence in a micromechanical setting (100-500 μm) using the microstructure-property model. In doing so, we varied the following characteristics:

1. number of voids (one void and various two void configurations),
2. three different temperatures (297 K, 400 K, and 600 K), and
3. intervoid ligament distance (ILD).

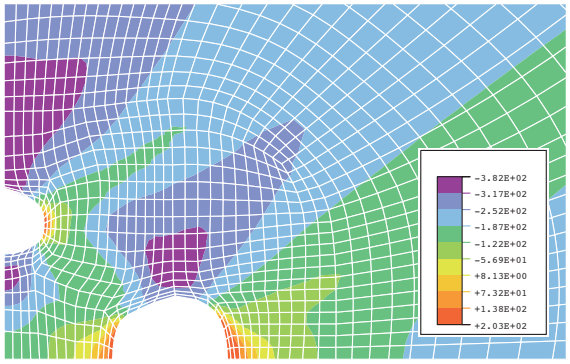

Figure 4.14. Contour plot of pressure to illustrate the effect of hydrostatic stress on void growth and coalescence.

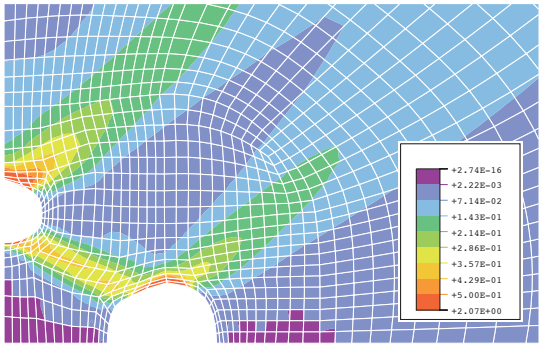

Figure 4.15. Contour plot of equivalent plastic strain to illustrate the effect of strain on void growth and coalescence.

4.2.2.1. FINITE ELEMENT PRELIMINARIES

The ABAQUS-Standard finite element program (Hibbitt *et al.*, 1998) was used to simulate the large strain, void growth problems in this study. By using finite element analysis, we determined the void configuration and temperature effects upon void growth and coalescence. Quarter space analyses were used with one void and half space analyses were used with two voids. Nodal constraints were placed on the free boundaries to ensure that planar boundary conditions remained planar during the simulations. The various void configurations are shown in Figure 4.16. Most of the two void calculations included an ILD of one void diameter to ensure coalescence. However, we also performed calculations varying the ILD to determine a critical ILD that defines the point of coalescence.

The term configuration used in the context of this study was the orientation of two voids with the loading direction. Two types of configurations were run for the axisymmetric calculations. One might suggest that fully three dimensional simulations are warranted to accurately model void growth; however, Thomson *et al.* (1998) showed that one void axisymmetric simulations gave practically identical results as three dimensional simulations.

The microstructure-property model constants (C_1-C_{18}) were determined from quasistatic compression tests of A356-T6 aluminum at different temperatures. Applied strain rates were imposed under quasistatic conditions at 0.001/sec.

4.2.2.2 PORE-PORE TEMPERATURE COALESCENCE RESULTS

One major finding of this study is that when multiple voids are present within a dense ductile material, the void growth rate is greater than for a one void material with the same initial void volume. Figure 4.17 illustrates that for the material with two voids that had an ILD of one diameter always incurred a higher void growth rate than the material with only one void under biaxial stretching at 297 K. This void growth enhancement in the multiple void material occurs because the free surface of the neighboring void introduces a local stress concentration and plastic strain enhancement in the ligament between the voids. The ligament stress concentration and plastic strain enhancement encourages the voids to grow larger and toward each other at a rate that is higher than if they were alone.

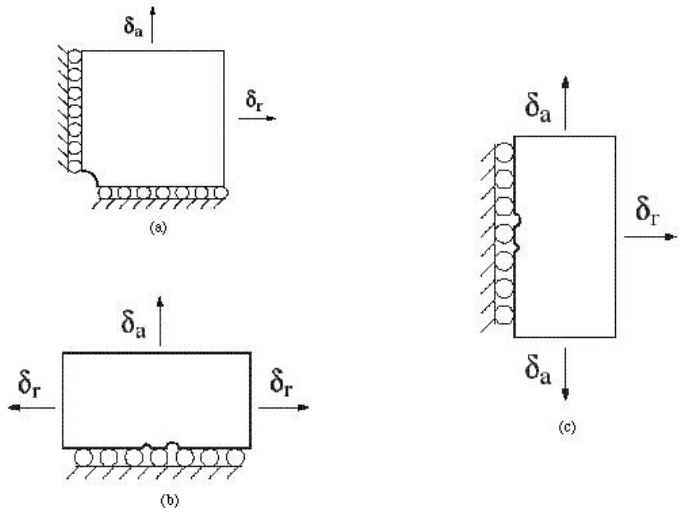

Figure 4.16. One void and two void configurations.

Another major finding of this study is that as the temperature increases, the void growth rate is more enhanced for a material with two voids. For example, Figure 4.18 and 4.19 show the normalized void volume fraction as a function of strain for two voids and one void, respectively. Figure 4.19 shows that the one void material experienced void growth in an almost linear fashion, whereas the two void material experienced exponential growth. Other calculations showed that material with two voids always grew faster.

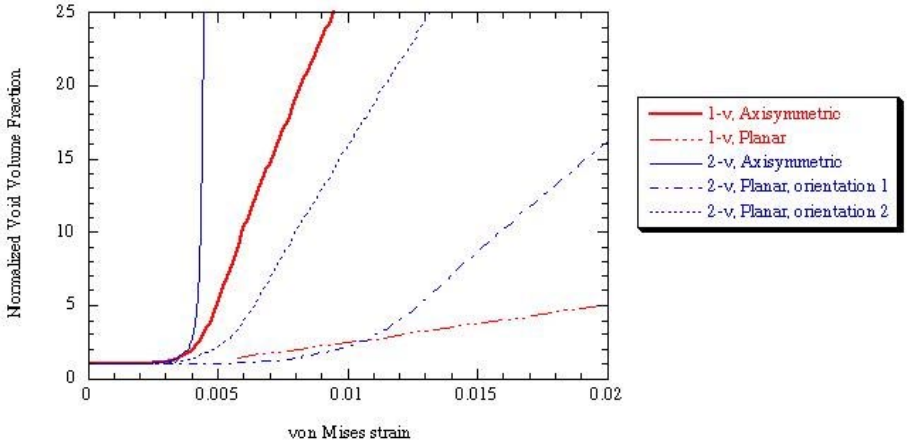

Figure 4.17. Void volume fraction normalized by the initial void volume fraction versus von Mises strain illustrating the two void aluminum material will experience greater void growth than the one void case given the same initial void volume fractions. The boundary condition in this case is biaxial (stretch forming) displacement boundary conditions at room temperature. ($\delta r/\delta a=0.5$)

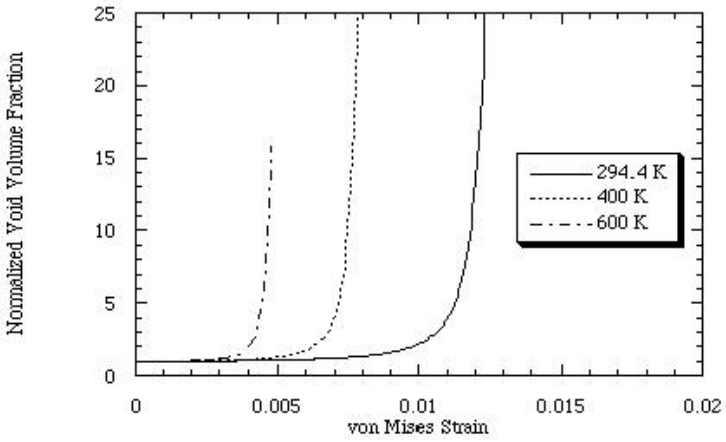

Figure 4.18. Void volume fraction normalized by the initial void volume fraction versus von Mises strain illustrating that greater void growth occurs as the temperature increases. The boundary condition is plane strain in the axisymmetric geometry with two void aluminum material. (δr/δa=0.0)

The difference in void growth for one and two void material evokes the question, "Why is there such a difference?" Voids grow in ductile metals based on the level of stress triaxiality, defined here as the hydrostatic stress divided by the equivalent deviatoric stress, and plastic deformation (cf. Cocks-Ashby, 1980; 1982). In the one void material, the stress triaxiality remains essentially constant for the different temperatures although the total stress decreases as temperature increases. However, the plastic deformation increases as temperature increases, yet the one void material experiences about the same void growth up to approximately 15% strain independent of temperature. This result implies that the plastic deformation is less influential on void growth than the stress triaxiality for the one void material. Although not shown in Figure 4.19, when the von Mises strain level reached 30% for the one void material, the void grew at a different rate at different temperatures. At these larger strains, the plastic deformation played an increased role in promoting void growth. Figure 4.20 shows contour plots of effective plastic strain at the same applied strain for two different temperatures of the two void material. Figure 4.20 shows that the effective plastic strain for the 600 K two void material is an order of magnitude higher than for the 297 K material. As such, the large difference of void growth rates from one void material versus two void material is a function of the competing roles of the plastic deformation and stress triaxiality.

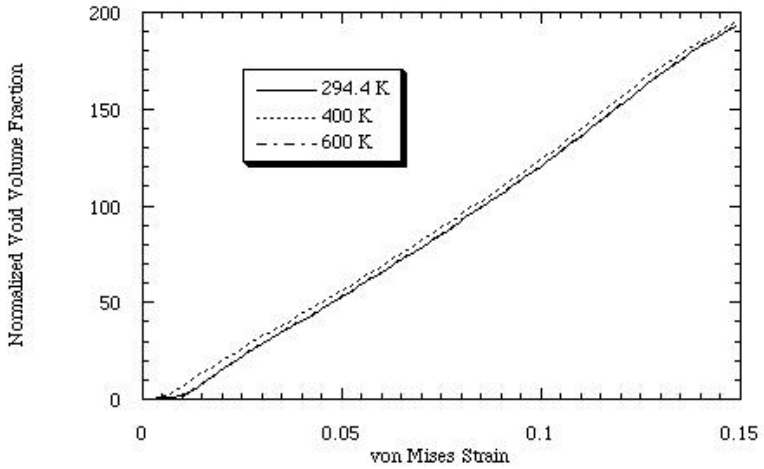

Figure 4.19. Void volume fraction normalized by the initial void volume fraction versus von Mises strain illustrating that greater void growth occurs as the temperature increases. The boundary condition is plane strain in the axisymmetric geometry with one void aluminum material. ($\delta r/\delta a=0.0$)

At higher temperatures, the plastic deformation seems to be more important than the stress triaxiality. At lower temperatures, the stress triaxiality is more important than the plastic deformation. A critical temperature exists at which both the stress triaxiality and effective plastic strain have an equal amount of influence.

Up to this point, the ILD was initially one void diameter. Brown and Embury (1973) noted that voids coalesce by impingement when they grow to a dimension in which the diameter is equal to the spacing. This assertion was based upon the observation that the void shapes did not change until they were one void diameter apart. Since Brown and Embury (1973) did not perform a detailed finite element study of various intervoid distances, they could not determine if the void growth rate was higher for ILDs greater than one diameter. Granted, a void may "spherically" grow until a void one diameter away is sensed, but the void growth rate could be higher before the strain level is achieved that changes the void shape. To study this, we performed different calculations by varying the ILD, as shown in Figure 4.21, to determine a critical ILD. We define void coalescence as a point of deviation from single void growth. As such, we do not designate the onset of void coalescence when the shape changes, but when the growth rate changes from the one void case.

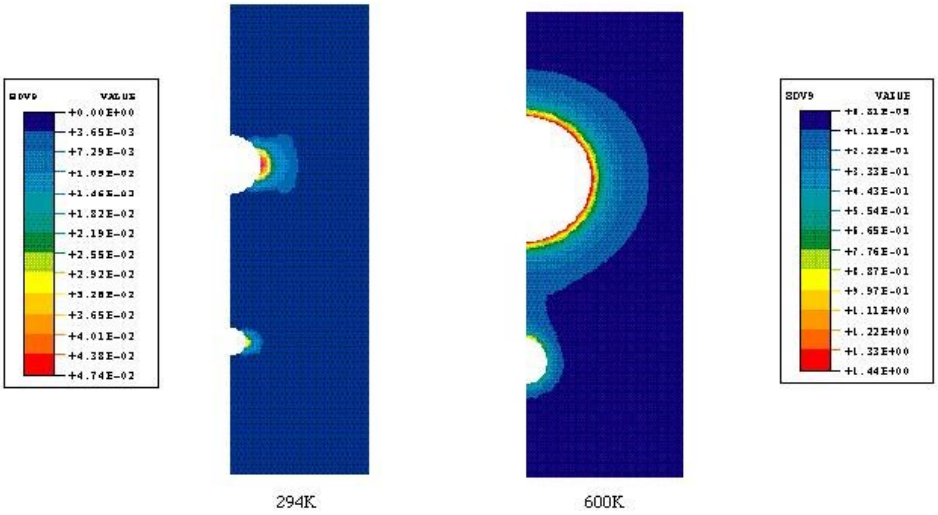

Figure 4.20. Effective plastic strain contours at the same snapshot in time illustrate the increase in plastic deformation as the temperature increases. This increase in plastic deformation enhances void growth. The boundary condition is plane strain, axisymmetric geometry with the two void aluminum material. ($\delta r/\delta a=0.0$)

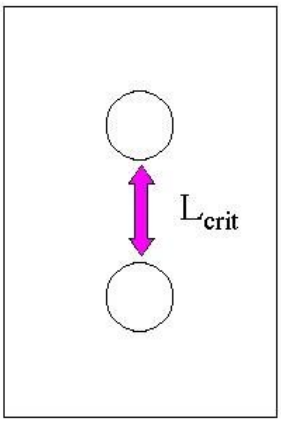

Figure 4.21. The critical intervoidligament distance is examined by determination of enhanced void growth. The critical L determines if the distribution of voids can be considered dilute or concentrated.

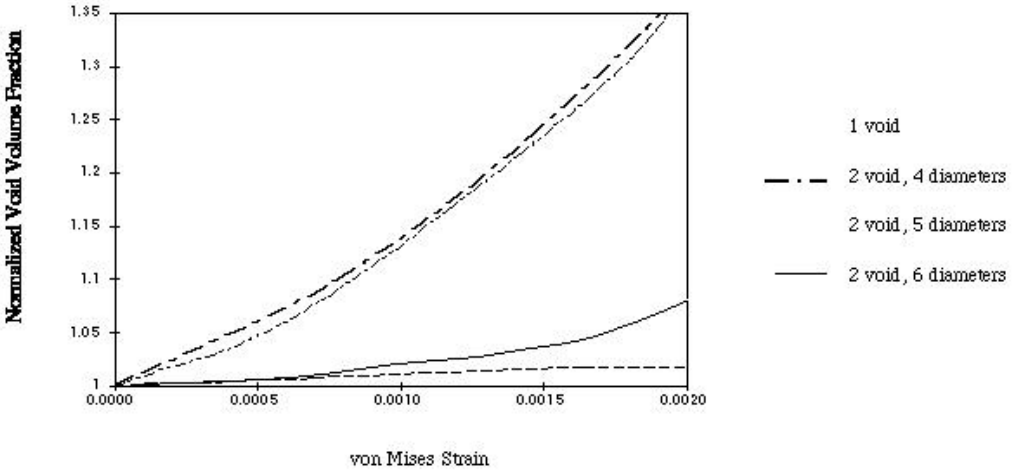

Figure 4.22. The critical intervoid distances were determined by comparing responses of multiple voids growing to the single void case. The six void diameter case was identical to the single void case below a strain of 0.0005. This calculation was a biaxial, axisymmetric calculation at room temperature.

A typical example is shown in Figure 4.22 of the void growth in terms of void size normalized by the initial void size plotted versus the applied strain for a biaxial calculation at 297 K. Figure 4.22 illustrates that at strains below 0.0005, the one void result and the result for two voids with an ILD of six diameters are similar. From this result, we assert that if the ILD is less than six diameters at the beginning of loading or during loading at some strain level, we claim that coalescence has occurred.

Figure 4.23 summarizes the results showing that a critical ILD for coalescence is dependent on temperature and boundary condition. The results indicate that for macroscale modeling of void coalescence microstructural quantification of the initial void distribution is needed. For engineering materials, coalescence is a continual process starts at the beginning of deformation as different size voids grow together before final failure occurs. The void growth functions often used in finite element simulations (cf. McClintock, 1968; Rice and Tracey, 1969; and Cocks and Ashby, 1980, 1982) are based on a single void growing and need modification to account for coalescence to accurately model engineering materials.

Since the previous calculations were displacement controlled, the evolving stress triaxiality can make it difficult for macroscale modeling of coalescence. Therefore, we examined the multiple void effects and temperature effects in the context of constant applied stress triaxiality. Force controlled boundary conditions are actually used to determine the stress state. Constant

triaxialities ranging from 0.3 (representing uniaxial tension) to 10 were applied. Stress triaxialities up to 10 can potentially be reached in shock environments.

The void growth enhancement trends observed for the constant stress triaxiality calculations are similar to those of the displacement controlled boundary value problems. Figure 4.24 shows the void volume fraction normalized by its initial void volume fraction as a function of von Mises strain for finite element simulations in which the triaxialities were varied with one and two voids at 297 K. From the displacement controlled two void simulations, we observed that the void growth was always enhanced in the presence of two voids. The stress triaxialities can be fairly small (~2) and still a large difference in void growth occurs. We can observe that the greater difference in void volume increase as the stress triaxiality increases. For a one void material, at strains below 5%, the growth is almost linear and the nonlinearity does not occur until larger strains. For the two void material, the nonlinearity starts almost immediately at strains below 1% for stress triaxialities above 0.3. Above a stress triaxiality of five, the void growth rate does not change much for the two void material.

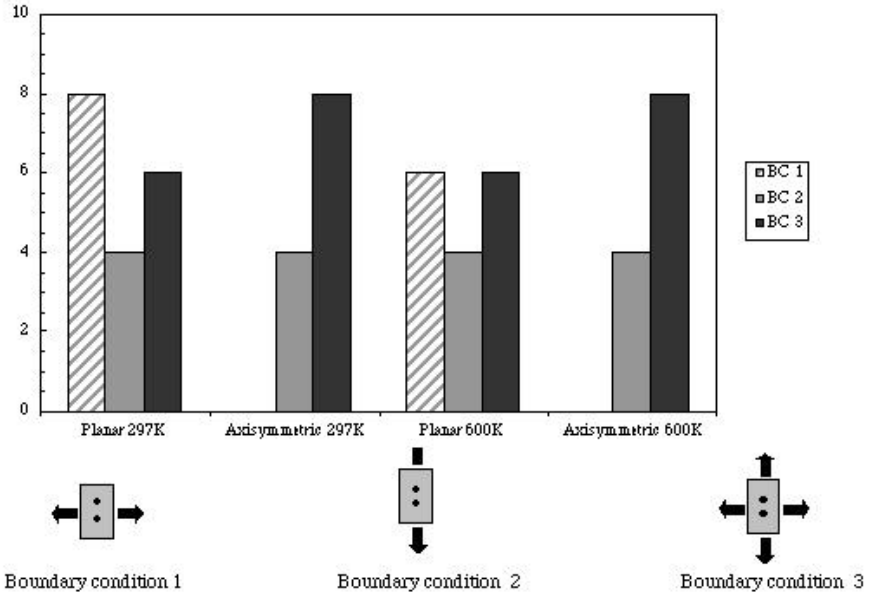

Figure 4.23. The critical intervoid distances determined to enhance void growth. The critical length , L, is determined for different loading conditions, temperatures, and void configurations.

Not covered in the analyses thus far have been strain rate effects. Budiansky *et al.*, (1982) first showed that a decrease in the strain rate sensitivity parameter enhanced void growth from a single void in a dense solid. Briottet *et al.* (1996) showed a similar trend albeit less pronounced for a single void in a compressible solid. Benson (1993; 1995) from numerical simulations noted different locations of failure from clustering effects in high strain rate micromechanical simulations of different void configurations. One can reason based upon dislocation motion and

interaction that void coalescence would occur in the opposite trend as that of the temperature trend. Further studies of strain rate effects are planned to quantify this effect, but let us consider a power law plasticity equation with strain rate and temperature effects,

$$\sigma = A\varepsilon^n \dot{\varepsilon}^m \exp\left(-\Delta G/kT\right) \qquad \text{Equation 4.1}$$

where the state of stress is a function of the Gibbs free activation energy G, temperature T, the Boltzmann constant k, the strain rate $\dot{\varepsilon}$, hardening exponent n, hardening coefficient A, and strain rate exponent m. Equation 4.1 represents thermally activated dislocation glide past obstacles. Equation 4.1 also reveals that as the temperature increases, the stress decreases, but as the strain rate increases, the stress increases. Hence, one can observe the inverse relation that temperature and strain rate have on the stress state. Because the stress state and strain state determine the void growth and coalescence rates, void growth and coalescence trends for increasing strain rates are anticipated to display the opposite trend of increasing temperatures. Since void coalescence is enhanced at higher temperatures, we anticipate that void coalescence would be enhanced at lower strain rates. Conversely, since void coalescence is inhibited at lower temperatures, we anticipate that void coalescence would be inhibited at higher strain rates. This inhibited void coalescence is observed in spall tests, which occur at high strain rates and can induce stress triaxialities on the order of ten (cf. Eftis *et al.*, 1991; Zurek *et al.*, 1997). Nemes and Eftis (1993) showed numerically for notch tensile bars that the place of final fracture occurs at different locations depending on the applied strain rate. One could expect this with temperature effects too (cf. Lu *et al.*, 1998).

In terms of continuum damage modeling, one must consider distribution effects of voids or at least a spatial dimension that relates neighboring voids as demonstrated by this numerical study. Experimental studies have shown this in a qualitative manner in the past (cf. Garrison and Moody, 1987). In particular, if the critical ILD is broached, then the continuum damage model should include this coalescence effect. One can cast this into an internal state variable framework, because the creation of new surface area is enhanced by coalescence. By assuming generalized normality, the Kelvin inequality of the Second Law of Thermodynamics is unconditionally satisfied (nonnegative intrinsic dissipation) and is expressed in the following equation

$$\underline{\sigma} : \underline{D}^{in} - \underline{b} : \overset{\circ}{\underline{\alpha}} - \kappa \bullet \dot{R} - \phi_n \bullet \dot{D}_n - \phi_g \bullet \dot{D}_g - \phi_c \bullet \dot{D}_c \geq 0 . \qquad \text{Equation 4.2}$$

in which, ϕ_c, is the generalized coalescence thermodynamic force conjugate (energy release rate) of the macroscale internal variable damage coalescence parameter, D_c; ϕ_g is the generalized growth thermodynamic force conjugate (energy release rate) of the macroscale internal variable damage growth parameter, D_g; and ϕ_n is the generalized nucleation thermodynamic force conjugate (energy release rate) of the macroscale internal variable damage nucleation parameter, D_n. In essence, an increment of damage will have associated energy released per unit damage extension as new damaged area (or volume) is developed. The dissipation relation between the

thermodynamic conjugates including a coalescence term (and nucleation term for completeness) with a standard single void growth term.

One can certainly argue that separating void growth and coalescence may not be appropriate because of their intimate connection. But typical equations for single void growth have been formulated and have been used successfully in engineering practice thus encouraging their use. Hence, another term for coalescence would be needed in that context. Needleman and Tvergaard (1984) and Koplik and Needleman (1988) have proposed modifications to the Gurson model (1977) to account for coalescence. However, it was not until recently that Tvergaard and Needleman (1995; 1997) proposed a spatial gradient that represents effects of coalescence with a spatial characteristic size. If coalescence is modeled with spatial gradients such as the one proposed by Tvergaard and Needleman (1997), then one would need to include temperature effects based on the current study.

4.2.3. PORE-PORE SUMMARY

Displacement and force boundary conditions with one and two voids at three different temperatures to show the effect of different states of plastic deformation and stress triaxialities acting upon the material were used in the context of finite element simulations. In general, the results confirm the need for including stress triaxiality and plastic deformation in a phenomenological void growth model (cf. Cocks and Ashby, 1980). However, these one void growth models typically do not capture multiple void effects. In this context, we propose a quantifiable definition of coalescence that is amenable to macroscale damage modeling. The major conclusions can be summarized as follows:

1. When multiple voids are present and within a critical intervoid ligament distance (ILD), the void growth rate is greater than a one void material with the same initial void volume.
2. Finite element calculations show that as temperature increases in the presence of multiple voids, the void growth rate increases. This occurs because plastic deformation greatly increases at higher temperatures although the stress triaxialities are almost equivalent.
3. Above a critical temperature, the effective plastic strain influences void growth more than stress triaxiality, but below a critical temperature, the stress triaxiality influences void growth more than the effective plastic strain.
4. The critical ILD for coalescence to enhance void growth depends on temperature and boundary conditions.
5. Temperature and pore size distributions are needed for the macroscale model.

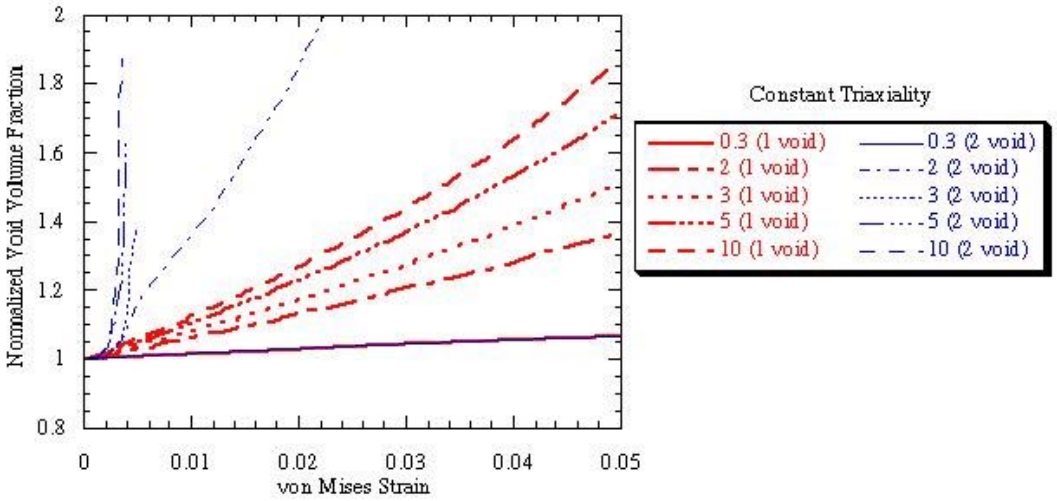

Figure 4.24. Void volume fraction normalized by the initial void volume fraction versus von Mises strain illustrating the increase in void growth as the stress triaxiality increasess with two voids over one void. These calculations were performed under constant triaxiality conditions, at room temperature, and for the axisymmetric geometry.

5. MODEL IMPLEMENTATION INTO FINITE ELEMENT CODE

Now that the macroscale microstructure-property model has been derived as discussed in the previous chapters, a few comments are warranted regarding the implementation of the microstructure-property model. When damage ϕ approaches unity, failure is assumed to occur. The goal is to implement the damage framework into a finite element code for solving complex boundary value problems, so failure occurs as $\phi \rightarrow 1.0$ within an element. Damage accumulation less than unity would be designated as failed material by many engineers. In fact, Budiansky (1970) stated that a damage level of 50% is the limitation on the degraded elastic moduli. Practically, the total damage for final failure should perhaps be even less than 50%, but in applications (cf. Bammann et al. 1993) using the Cocks and Ashby void growth rule (1980, 1982), the damage goes rapidly to unity just after a few percent void volume fraction. More complicated functions for the damaged elastic moduli can be used such as Zhao et al. (1989), but these are computationally expensive. The final percentage of damage to determine failure can be determined by the finite element analyst or micromechanical calculations. For the sake of this writing, damage is allowed to approach unity.

To implement the model in a finite element code, we replace the deviatoric plastic rate of deformation with the total rate of deformation in the recovery terms of the hardening rate equations (Equations 2.31 and 2.32). This substitution makes the hardening rate equations directly solvable. Equations 2.31 and 2.32 become:

$$\dot{\underline{\alpha}} = h(T)\underline{D}_d^p - \left[\sqrt{2/3}\, r_d(T)\|\underline{D}\| + r_s(T)\right]\sqrt{2/3}\|\underline{\alpha}\|\underline{\alpha} \qquad \text{Equation 5.1}$$

$$\dot{R} = \sqrt{2/3}\, H(T)\|\underline{D}_d^p\| - \left[\sqrt{2/3}\, R_d(T)\|\underline{D}\| + R_s(T)\right]|R|R \qquad \text{Equation 5.2}$$

At the beginning of each time step, we determine the values for J_2 and J_3 from the previous step to modify r_d, R_d, h, and H. We then employ a radial return method to determine the plastic part of the strain by assuming the strain to be all elastic (i.e. $\underline{D}_d^p = 0$). Figure 5.1 schematically illustrates the method. This gives the following trial values for the deviatoric stress and internal hardening variables,

$$\underline{\sigma}^*_{n+1} = \underline{\sigma}'_n + \int_{t_n}^{t_{n+1}} 2\mu(1-\phi)\underline{D}' dt - \int_{t_n}^{t_{n+1}} \frac{\dot{\phi}\underline{\sigma}'}{1+\phi} dt \approx \underline{\sigma}'_n\left(1 - \frac{\dot{\phi}\Delta t}{1+\phi}\right) + 2\mu(1-\phi)\underline{D}'\Delta t \qquad \text{Equation 5.3}$$

$$\underline{\alpha}^*_{n+1} = \underline{\alpha}_n - \int_{t_n}^{t_{n+1}} \left(r_d\sqrt{2/3}\|\underline{D}\| + r_s\right)\sqrt{2/3}\|\underline{\alpha}\|\underline{\alpha} dt \approx \left\{1 - \left(r_d\sqrt{2/3}\|\underline{D}\| + r_s\right)\sqrt{2/3}\|\underline{\alpha}\|\Delta t\right\}\underline{\alpha}_n \qquad \text{Equation 5.4}$$

$$R^*_{n+1} = R_n - \int_{t_n}^{t_{n+1}} \left(R_d\sqrt{2/3}\|\underline{D}\| + R_s\right)|R|R \approx \left\{1 - \left(R_d\sqrt{2/3}\|\underline{D}\| + R_s\right)|R|\Delta t\right\}R_n \qquad \text{Equation 5.5}$$

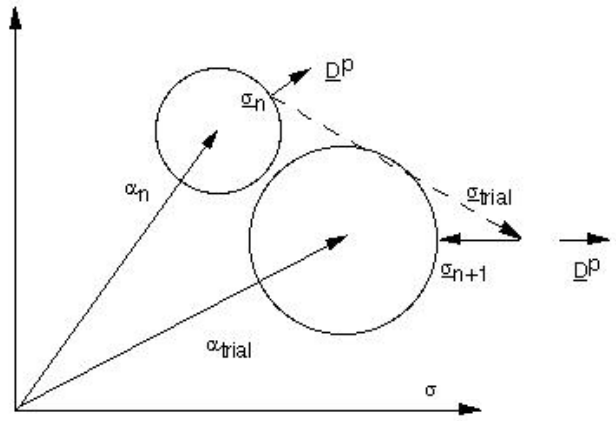

Figure 5.1. Radial return algorithm used to update new state as predicted by model.

Note that a differential equation of the form $\dot{R} = -kR$ has a solution that tends to zero, but if we take too large a time step, our approximate integration could oscillate about zero. To avoid this behavior, we limit the terms multiplying a_n and R_n in Equations 5.4 and 5.5 to be greater than or equal to zero.

If we define the tensor $\underline{\xi} = \underline{\sigma}^* - \frac{2}{3}\underline{\alpha}$, the flow rule can be written as

$$\underline{D}_d^p = \sqrt{\frac{3}{2}} f(T) \sinh\left(\frac{\sqrt{\frac{3}{2}}\|\underline{\xi}\| - (R + Y(T))(1-\phi)}{V(T)(1-\phi)} \right) \frac{\underline{\xi}}{\|\underline{\xi}\|}. \qquad \text{Equation 5.6}$$

By taking take the norm of both sides, we can then invert Equation 5.6 to get

$$\Phi = \sqrt{\frac{3}{2}}\|\underline{\xi}\| - (1-\phi)[R + Y + V\sinh^{-1}(\frac{\sqrt{\frac{2}{3}}\|\underline{D}\|}{f})] = 0 \qquad \text{Equation 5.7}$$

If on evaluation of Φ we find $\Phi \le 0$, then the elastic assumption is valid, and we can use the trial values of $\underline{\alpha}$, $\underline{\sigma}$, and R as the actual values. Otherwise, we look for a deviatoric plastic strain component $\underline{D}$ such that

$$\int_{t_n}^{t_{n+1}} D^p dt = \frac{\gamma}{\|\xi\|}\xi$$
$$\int_{t_n}^{t_{n+1}} \|D^p\| \, dt = \gamma$$

Equation 5.8a,b

This leads to corrections to the trial values of

$$\sigma'_{n+1} = \sigma^*_{n+1} - \int_{t_n}^{t_{n+1}} 2\mu(1-\varphi)D^p dt = \sigma^*_{n+1} - \frac{2\mu(1-\varphi)\gamma}{\|\xi\|}\xi \qquad \text{Equation 5.9}$$

$$\alpha_{n+1} = \alpha^*_{n+1} + \int_{t_n}^{t_{n+1}} h(T)D^p dt = \alpha^*_{n+1} + \frac{h\gamma}{\|\xi\|}\xi \qquad \text{Equation 5.10}$$

$$R_{n+1} = R^*_{n+1} + \sqrt{2/3}\int H(T)\|D^p\|dt = R^*_{n+1} + \sqrt{2/3}H\gamma \qquad \text{Equation 5.11}$$

Substituting these corrected values back into the inverted flow rule, it is easy to show that $\Phi = 0$ is satisfied by choosing γ as:

$$\gamma = \frac{\|\xi\| - \sqrt{2/3}(1-\varphi)(Y + R + V\sinh^{-1}(\frac{\|D\|}{f}))}{2\mu(1-\varphi) + 2/3(h + H(1-\varphi))} \qquad \text{Equation 5.12}$$

Equation 5.12 is then used to correct the trial values. At this point we can calculate J_2 and J_3 from the corrected σ'_{n+1} and calculate a new damage term φ from updated nucleation, void growth, and coalescence from Equations 2.33-2.38. Finally, we add the pressure term to update the total stress as

$$\sigma_{n+1} = \sigma'_{n+1} + p_{n+1}, \qquad \text{Equation 5.13}$$

where

$$p_{n+1} = \tfrac{1}{3}tr(\sigma_n)(1-\varphi) + (1-\varphi)\Delta t K tr(D). \qquad \text{Equation 5.14}$$

This is all that is needed for the implementation of the model. However, some work needs to be done ahead of time to determine the appropriate values for the void nucleation constants. We determine the void nucleation rate under tension, compression, and torsion in the following manner. First, the material constant C_{coeff} was determined by using a trial-and-error method to match the data from both tension and compression. For tension, the total void nucleation density, which included fracture of silicon particles and debonding of the silicon/aluminum interface, was used to determine the material constants. For compression, only fracture of silicon was observed.

Equation 2.35 was solved for independently for tension and compression by using a program that correlates the experimental data with an exponential function,

$$\eta_{tension}(t) = 90\exp\left(25.608\varepsilon(t)\right) \qquad \text{Equation 5.15}$$

$$\eta_{compression}(t) = 90\exp\left(10.102\varepsilon(t)\right) \qquad \text{Equation 5.16}$$

The tension exponential term can be equated to the exponential term as

$$25.608 = \frac{d^{1/2}}{K_{1C}f^{1/3}}\left[b\frac{2}{3\sqrt{3}} + c\right]. \qquad \text{Equation 5.17}$$

The compression exponential term can be equated to the exponential term as

$$10.102 = \frac{d^{1/2}}{K_{1C}f^{1/3}}\left[-b\frac{2}{3\sqrt{3}} + c\right]. \qquad \text{Equation 5.18}$$

Here, the two equations can be used to solve for the two constants b and c, since K_{1C}=17.3 MPa-m^0.5, (d=6 μm), and (f_i=0.07). From this procedure, the material constants b=58,630 MPa, c= 30,011 MPa, and C_{coeff} =90 result.

The constant a in torsion can be determined independently of constants b and c because of the stress invariant forms. As such, the following equation

$$31.32 = \frac{d^{1/2}}{K_{1C}f^{1/3}}\left[a\frac{4}{27}\right] \qquad \text{Equation 5.19}$$

gives a=615,369 MPa.

6. MACROSCALE MODEL-EXPERIMENT COMPARISONS

In this chapter, we present three different macroscale validation tests and use the model to optimize a control arm. First, we show how the microstructure-mechanical property model captures the void nucleation rate and stress-strain responses under compression, tension, and torsion. Second, we show that the microstructure-mechanical property model captures path history effects that arise from Bauschinger effect tests. Third, we compare finite element results of the microstructure-mechanical property model to notch tensile test experimental data, optical methods, and x-ray tomography analysis. These validation experiments reveal the model's capability and bring confidence regarding larger scale structural analyses which oftentimes are not testable. Finally, we use the model to optimize a control arm based on mass and strength.

6.1. VOID NUCLEATION COMPRESSION, TENSION, AND TORSION ANALYSIS

A series of tension, compression, and torsion experiments were performed to different strain levels to quantify void nucleation evolution of this cast A356-T6 aluminum alloy. The tests were stopped at various effective strain levels, and the specimens were cut, polished, and examined for void nucleation. The accumulation of new voids occurred by fracture of the second phase silicon and by debonding of the silicon with the aluminum. The void nucleation sites were counted over a statistically significant region of the material at the different strain levels, and then the void nucleation model constants were determined. Figures 6.1, 6.2, and 6.3 show representative optical micrographs of specimens strained under tensile, compressive, and torsional loading conditions. In Figure 6.3, the arrow represents the torsional rotation axis. In each micrograph, the loading direction is parallel to the height of the micrograph (see arrow). Observe that fractured Si particles are observed under all three loading conditions. Note that the cracks-voids in the tensile test specimen (6.1) are perpendicular to the loading direction, whereas the majority of the cracks-voids in the compression test specimen (Figure 6.2) are parallel to the loading direction. In the torsion specimen (Figure 6.3), the cracks-voids are observed in all directions. The fraction of damaged particles is defined as the void nucleation density divided by the total number of silicon particles. Under tension, both silicon fracture and interfacial debonding occurred, but under compression and torsion only silicon fracture occurred. In each specimen, the broken/debonded Si particles were counted, and their sizes and orientations were measured by using interactive digital image analysis. These measurements were performed on more than one hundred continuous fields of view at 500X in each specimen to obtain statistically reliable data for the fraction of damaged Si particles, their average size, and corresponding orientation distribution.

Figure 6.4 shows a comparison of the void nucleation model to void nucleation-strain data from compression, tension, and torsion tests at ambient temperature and quasi-static loading conditions (10^{-4}/sec). These curves reflect the inclusion of the void nucleation, growth, and coalescence terms. The hardening rate differences arising from these different global stress states is driven more by void nucleation than the growth and coalescence as illustrated by the model comparison to the void nucleation data in Figure 6.4. One can see from Figure 6.4 that the void nucleation rate increases from compression to tension to torsion. The void nucleation relaxes the local dislocation density, which was building up around the particles as to relieve the stress. As such, the global hardening rate is increasing as you go from torsion to tension to compression, the reverse order of the void nucleation rate. Figure 6.5 shows that the effective stress-strain

responses are in reverse order of the void nucleation data indicating the direct link between the microstructure and mechanical work hardening rate. Figure 6.5 also shows the microstructure-property model captures the work hardening differences arising in tension, compression, and torsion, but this will be discussed more later.

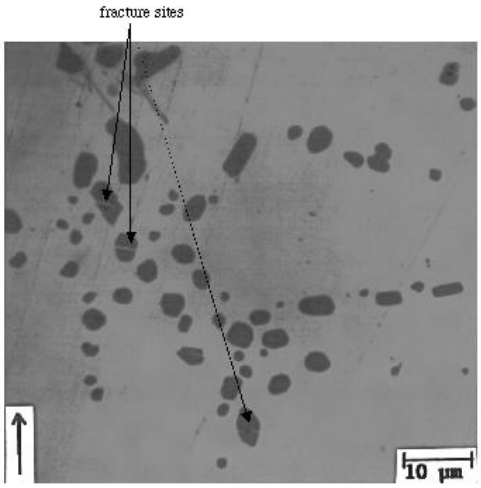

Figure 6.1. Micrograph of fracture sites of silicon in tension.

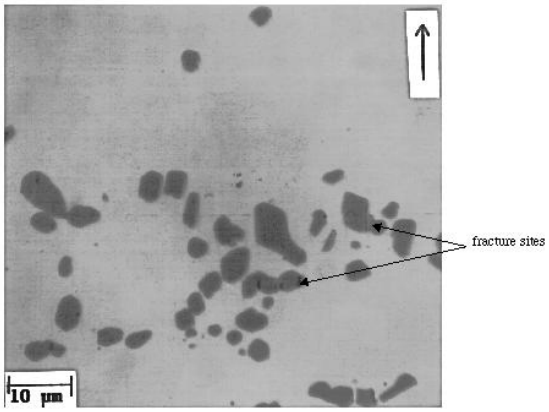

Figure 6.2. Micrograph of fracture sites of silicon in compression.

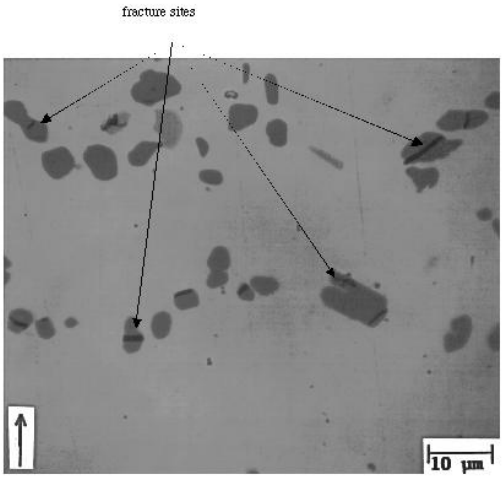

Figure 6.3. Micrograph of fracture sites of silicon in torsion

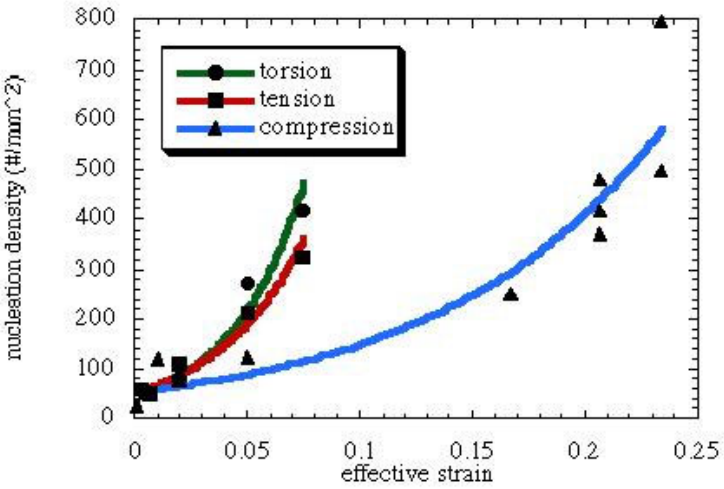

Figure 6.4. Number density of void nucleated as a function of strain comparing the microstructure-property model results and test data for compression, tension, and torsion for cast A356 aluminum alloy at ambient temperature and a strain rate of 1e-4/sec.

A comment should be made regarding the plotting of the nucleation density of voids in a finite element code. First, measurements of the nucleation density are represented by the number count per unit area, so in 2D finite element calculations, the void growth area must be used. Also, if a

total number of voids nucleated is desired as opposed to a number density, then the area of the element must be included with the corresponding units conversion. The current measure is a number count per millimeter squared.

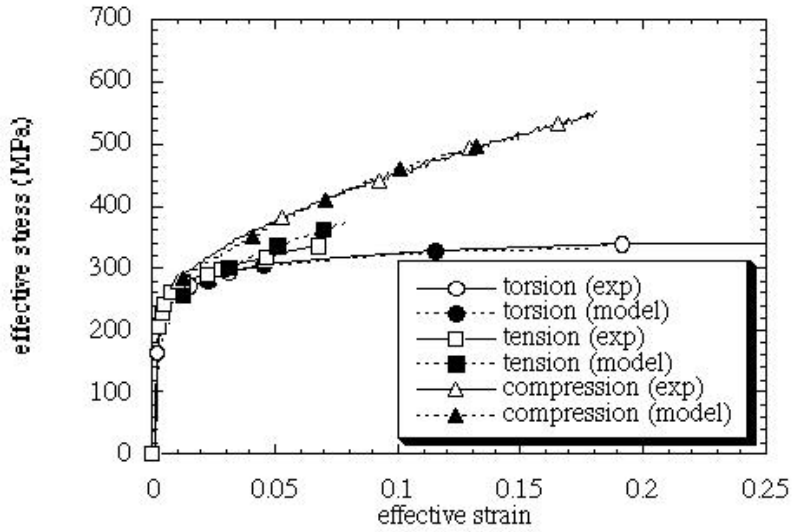

Figure 6.5. Stress-strain comparison of microstructure-property model results and test data for compression, tension, and torsion for cast A356 aluminum alloy at ambient temperature and a strain rate of 1e-4/sec.

6.2. VOID GROWTH AND COALESCENCE ANALYSIS

Experiments were performed to understand the void growth and coalescence mechanisms within the A356-T6 material. The micromechanical finite element analyses showed a definite trend: that multiple voids interacting increased the total damage level at a greater rate than just a single void with the same initial void volume fraction. To help separate these effects experimentally, we conducted interrupted tensile tests in which the specimen surfaces were polished so that individual pores could be monitored and measured for their size increase throughout deformation. In particular, their centroids and sizes were measured before and after each loading. On the order of 50 to 100 pores were measured for each specimen. The change in area was used to give an area fraction. Because of nearest neighbor distances and surface effects, the scatter in the data was large; however, it is worth noting the results because a qualitative trend was observed. The specimens were machined from the horizontally cast plates that had an initial void volume fraction of approximately 0.0015. We conducted these experiments at three temperatures: 222 K, 298 K, and 394 K. Table 6.1 summarizes the results.

Table 6.1. Void area fraction as a function of strain level and temperature.

Strain level	*222 K*	*298 K*	*394 K*
0.01	0.29	0.15	0.87
0.015	0.008	0.35	1.60
0.02	0.012	0.36	0.83
0.035	0.01	0.40	1.97
0.05	-	0.51	-

One can see from the data the void growth is not very dramatic and though there exists much scatter in the data as a function of strain certain qualitative trends are apparent related to temperature. Remember that these results couple the void growth and void coalescence together. Void growth and coalescence reach higher values as the temperature increases. This trend was identically observed in the micromechanical simulations due to the higher plastic strains achieved. This trend is included in the macroscale modeling of the void growth and void coalescence as described in this report.

Coalescence is mathematically described in Equation 2.37. Before determining the coefficient for the coalescence term, we varied the coefficient as shown in Figure 6.6 to illustrate the influence of coalescence on the total damage state. Recall that coalescence is not just the final joining of voids at the end of deformation but is defined as the enhancement of void growth as two or more voids interact. Certainly other mathematical forms can be developed for coalescence. Future studies should emphasize this; however, we developed a simple form that relates the interaction of the void nucleation and void growth laws as prescribed by Equation 2.35 and Equation 2.36. In the context of this A356-T6 Al alloy, coalescence is complicated as interactions from voids started at fractured or debonded silicon sites can interact with casting pores and casting pores can interact with other casting pores.

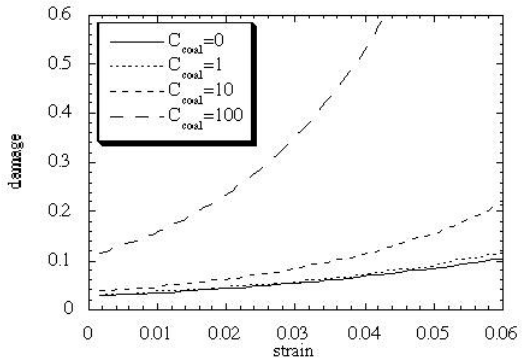

Figure 6.6. Damage evolution as a function of strain. The coefficient in the coalescence term is varied to illustrate its influence on total damage.

6.3 PLASTICITY ANALYSIS

A nonlinear regression algorithm was developed to fit the plasticity model constants once the damage parameter constants were determined. One set of constants found in Appendix A were able to capture a wide range of the mechanical responses that arose from the experiments. Figure 6.5 shows how the model captured the differences between the work hardening rate in tension, compression, and torsion. Figure 6.7 shows the stress-strain curves comparing the microstructure-property model to experiments at different strain rates and temperatures for a material with a dendrite cell size of 20 μm. The amount of residual error in matching the constants was just less than 4% from all the plots. Figure 6.8 is a plot of yield stress as a function of temperature for various strain rates for the A356-T6 aluminum alloy. These data come from the microstructure-property model, and the "x" data points represent experimental data. This type of plot can be useful if an elastic design is used. Figure 6.9 illustrates that the DCS differences in the work hardening rate were captured very well by the model.

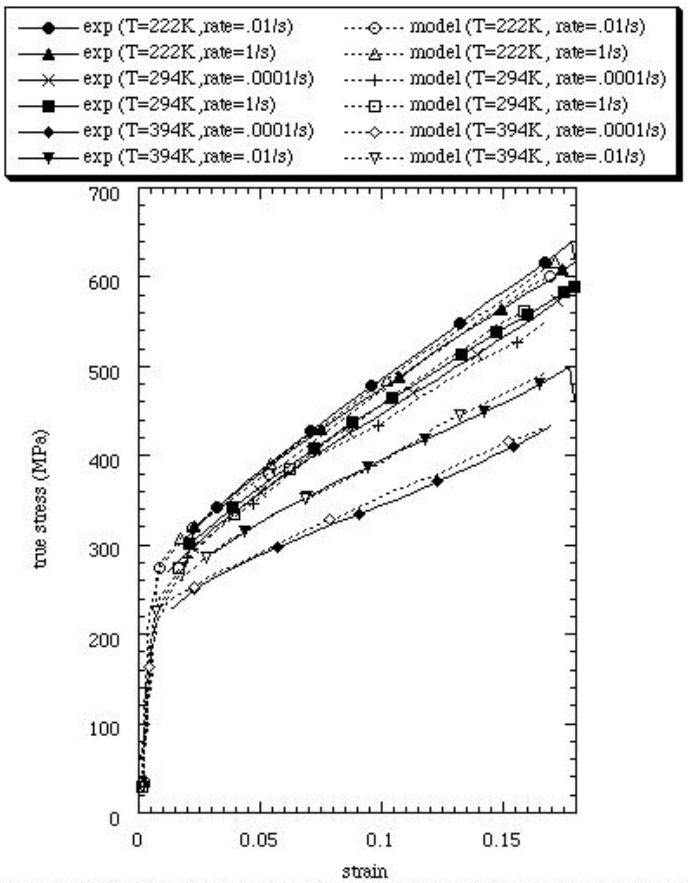

Figure 6.7. Stress-strain curves comparing the model to experiments at different strain rates and temperatures for a material with a dendrite cell size of 20 μm.

6.4. BAUSCHINGER EFFECT ANALYSIS

The Bauschinger effect is interpreted as anisotropic “yielding” that arises upon reverse loading from internal backstresses that are attributed to dislocations accumulating at obstacles. Studies to describe the Bauschinger effect have either focused on continuum mechanics modeling or on

analyzing dislocation build-up at a microscopic scale. In continuum mechanics, the focus often is on the relationship of the ratio of kinematic (anisotropic) hardening to isotropic hardening. In materials science, the focus is often on determining mechanisms related to dislocation arrangement. Few have studied both aspects together and fewer yet have considered cast Al-Si-Mg aluminum alloys (Caceres *et al.*, 1996). In (Caceres *et al.*, 1996), only tension-followed-by-compression was studied without consideration of damage accumulation. To the author's knowledge, no studies have examined the effect of void damage with regard to second phase particles on the Bauschinger effect for a cast A356-T6 aluminum alloy that was mechanically tested in tension-followed-by-compression and compression-followed-by-tension up to different moderate prestrain levels.

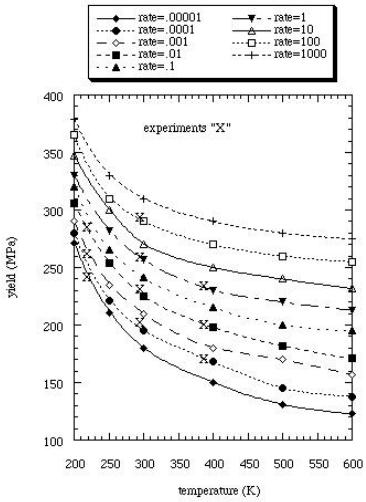

Figure 6.8. Yield stress responses at different strain rates and temperatures.

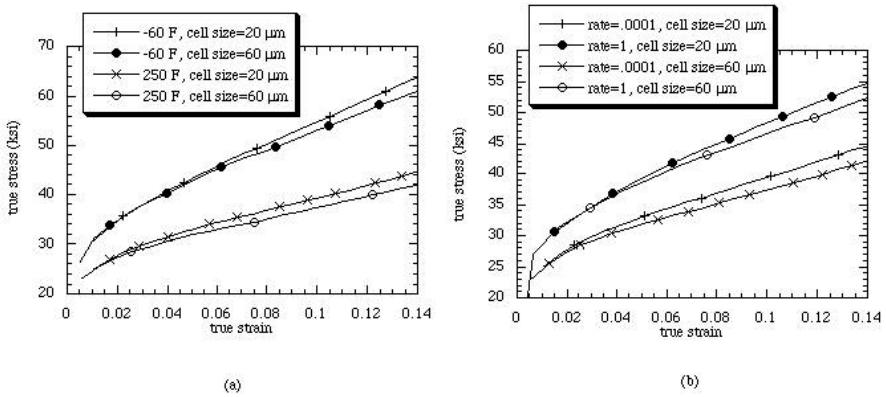

Figure 6.9. Stress-strain comparison of microstructure-property model results and test data for compression of two different dendrite cell sizes 20 μm and 60 μm at (a) two different temperatures and (b) strain rates for cast A356 aluminum alloy. The lines represent the model and the markings represent the experiments.

Test specimens were machined from the chill end of the casting, where the amount of microporosity was measured to be low (< 0.1% volume fraction), to determine the number of voids nucleated under tension, compression, and uniaxial cyclic boundary conditions. Test specimens were stopped at different strain levels, and then the specimens were sectioned in two pieces so that image analysis could be performed to quantify the void nucleation density.

The specimens used for the testing were ASTM-E606 low cycle fatigue specimens with an outside diameter of 9.525 mm. The strain rate was 0.0001/sec and the test temperature was in ambient conditions. A servohydraulic Instron test frame was used to test the specimens under displacement control.

Figure 6.4 shows that the number of damaged sites is higher in tension than in compression. In tension, voids can nucleate by silicon particle fracture or by silicon particles debonding from the aluminum matrix, but in compression, voids nucleate by silicon particle fracture. Because the fracture stress of the silicon particles is much higher than the ductile aluminum matrix because the stiffness of the Si particle is greater than the ductile Al matrix, the particles incur a greater stress upon loading as the aluminum incurs plastic deformation. This greater stress serves as a driving force for voids to form by particle fracture or by debonding of the silicon particle-aluminum interface. Eventually, void growth and coalescence in a tensile state lead to final failure. The local voids weaken the material and reduce the work hardening rate, which in turn directly influences the global stress state. Figure 6.5 shows the compression stress-strain curve is higher than the tension stress-strain curve after yield. The trend of higher work hardening rate for compression over tension was replicated for many specimens.

The Bauschinger effect is a phenomenon that is exhibited under a cyclic load when reverse yield is lower than forward yield. The Bauschinger effect can be expressed by either the Bauschinger stress parameter (BSP) or the Bauschinger effect parameter (BEP). The BSP is defined in terms of the total forward and reverse flow stresses given by

$$BSP = \frac{\left|\sigma^f\right| - \left|\sigma^r\right|}{\left|\sigma^f\right|} \qquad \text{Equation 6.1}$$

in which the forward stress, σ^f, is determined by the largest forward stress just before reversal and the reverse stress, σ^r, is determined typically by a reloading in the reverse direction. Caceres *et al.* (1996) used the BSP to illustrate the Bauschinger effect of an Al-Si-Mg casting alloy. The BEP is given by

$$BEP = \frac{1}{2}\left\{\frac{\left|\sigma^f\right| - \left|\sigma^r\right|}{\left|\sigma^f\right| - \left|\sigma^y\right|}\right\} \qquad \text{Equation 6.2}$$

where σ^y is the initial forward yield stress, determined typically by an 0.002 offset strain upon the forward loading. Embury (1987) employed the BEP to describe the Bauschinger effect. From a continuum mechanics perspective, the BEP is indirectly related to the amount of the kinematic (anisotropic) hardening and isotropic hardening that occurs. As such, it reflects how much plastic

anisotropy is induced during the deformation. The BSP is used to illustrate comparisons with Caceres *et al.* (1996), and the BEP is used to explain the influence of damage on the stress-strain response.

The forward applied prestrain levels reached for the tests were 2%, 3%, and 5% after which the straining was reversed to the same level as the forward prestrain. Tests were performed in two sequences: tension-followed-by-compression and compression-followed-by-tension. When a specimen was strained to 5% in tension first followed by a compression unloading, a different BEP (or BSP) arose than if the specimen were strained 5% in compression first followed by tension. The same can be said for the 2% and 3% prestrains as well. Table 6.2 illustrates results for the BEP and BSP for the stress-strain curves shown in Figure 6.10.

Table 6.2. Comparison of BSP and BEP for various one cycle tests at different strains.

experiment	$\lvert\sigma^y\rvert$ (MPa)	$\lvert\sigma^f\rvert$ (MPa)	$\lvert\sigma^r\rvert$ (MPa)	BSP	BEP
2% tens-comp	241	276	186	0.326	1.286
3% tens-comp	241	296	193	0.348	0.936
5% tens-comp	241	310	207	0.332	0.746
2% comp-tens	241	303	190	0.373	0.911
3% comp-tens	241	331	197	0.405	0.744
5% comp-tens	241	365	214	0.414	0.609

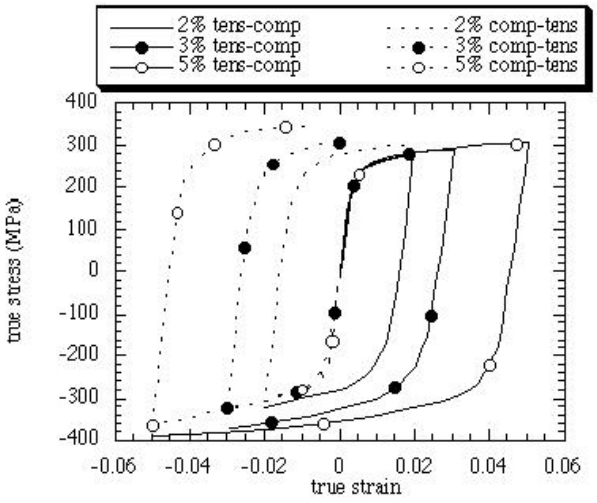

Figure 6.10. Reverse true stress-true strain data for a cast A356 aluminum alloy comparing tension-followed-by-compression and compression-followed-by-tension boundary conditions for different prestrains (2%, 3%, and 5%).

Several observations can be drawn from these results. In Table 6.2, one can see that the BSP and BEP for the tension-followed-by-compression case was lower than for the compression-followed-by-tension case. The reason this phenomena occurs is because voids nucleate at a higher rate under tension than for compression. As a consequence, the σ^f is lower for the forward prestrain in tension than in compression because the void nucleation rate is higher in tension. The lower σ^f reflects that the internal stresses have relaxed because of the fracturing process, which in turn reduce the BSP and BEP. Furthermore, this lowering of the BEP reveals the kinematic hardening to isotropic hardening ratio is reduced, indicating that the plastic anisotropy is reduced. This phenomenon should be captured in the microstructure-property model. Figure 6.11 shows a comparison of the microstructure-property model to the tension-followed-by-compression experimental data. This comparison illustrates that the microstructure-property model can indeed capture the history effects that intimately couple the damage progression and work hardening rate.

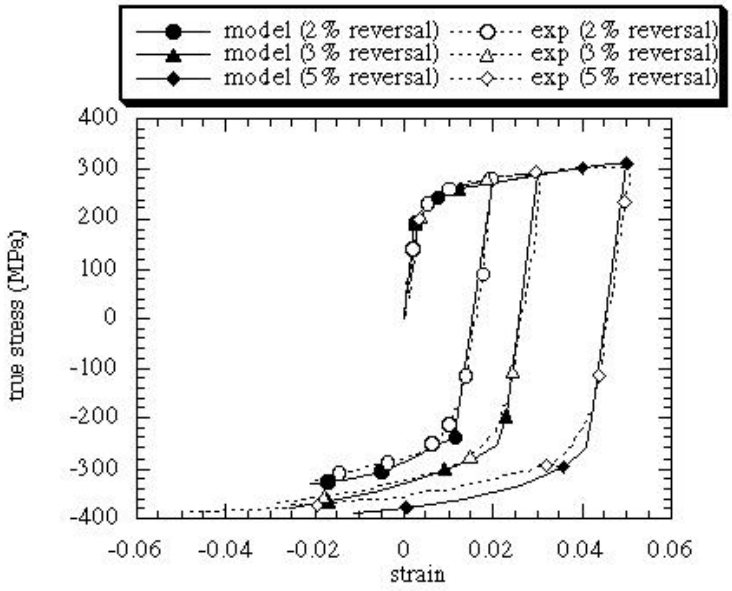

Figure 6.11. Reverse true stress-true strain data for a cast A356 aluminum alloy comparing experiments and microstructure-property model for tension-followed-by-compression boundary conditions with different prestrains (2%, 3%, and 5%).

Figure 6.12 illustrates data from Caceres *et al.* (1996) and from this current study. The BSP for tension-followed-by-compression falls in the range of the Caceres *et al.* (1996) study, but the BSP for compression-followed-by-tension is higher. Furthermore, Caceres *et al.* (1996) do not mention that the tests were tension-followed-by-compression, but the data from this study indicates that they probably were tension-followed-by-compression tests.

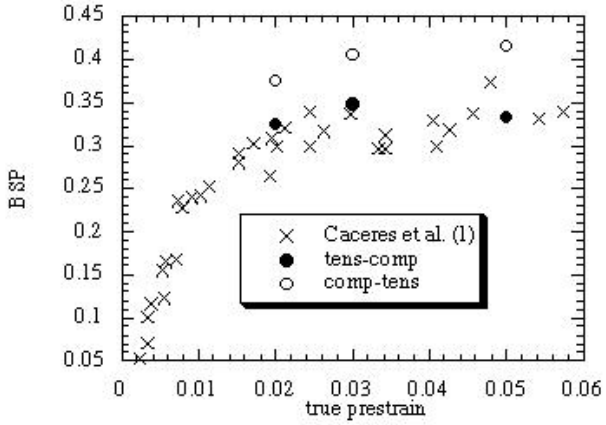

Figure 6.12. The Bauschinger Stress Parameter (BSP) as a function of applied prestrain comparing data from Caceres et al. (1996) and the current study for a cast A356 aluminum alloy. Caceres et al. (1996) used specimens with an average dendrite cell size (DCS) ranging from 25 μm to 120 μm. The current study included an average DCS of 20 μm.

The second conclusion of the study is that as the forward prestrain increased, the plastic anisotropy (backstress), which is reflected by the BEP, decreased. An attribute of the aluminum matrix is a high stacking fault energy that allows for increased cross slip, which accommodates screw dislocations. In the eutectic region, the screw dislocations can be impeded by the formation of jogs. This would allow the buildup of dislocations around silicon particles. As the dislocation population induces a certain local internal stress, fracture of the particle or debonding at the aluminum-silicon interface occurs. When this happens, the internal stresses are relaxed and the backstress is reduced. As the applied prestrain increased, damage accumulation increased relieving the internal backstress in this cast A356-T6 aluminum alloy. This indicates that plastic anisotropy (as reflected by the backstress) decreased as the number of fractured or debonding particles increased.

It is noted that backstress can develop for "pure" aluminum, which means that the dendrite cell could have some backstress. The amount of backstress in the dendrite cell would be expected to be lower than within the eutectic region, where the hard silicon particles act as barriers for dislocation build-up. The high stacking fault energy of aluminum accommodates screw dislocations. Screw dislocations can move around barriers fairly easily, but in the eutectic region screw dislocations would be impeded by jogs. This allows the build-up of dislocations at the silicon particle-aluminum interface. As the dislocation population induces a local stress, fracture of the particle or debonding of the particle-aluminum interface occurs. When this happens, internal backstresses are relaxed and thus reduced.

6.5. NOTCH TENSILE FINITE ELEMENT ANALYSIS

Damage progression from void nucleation, growth, and coalescence in cast A356-T6 aluminum notch specimens was determined from a combination of experiments, finite element analysis, nondestructive analysis, and image analysis. Experiments were performed on notch Bridgman specimens to failure and then other specimens were tested to 98%, 95%, and 90% of the failure load. The specimens were then evaluated with nondestructive x-ray tomographic methods. Regions of the specimens were then sampled for optical image analysis. Finite element simulations of the notch tests were performed with the microstructure-property model that incorporated the pertinent microstructures related to the cast A356-T6 aluminum alloy such as the silicon particle volume fraction and size distribution and porosity volume fraction and size distribution. The various methods all corroborated the damage progression in terms of void volume fraction evolution.

This work includes an unprecedented, comparative study of experimental data, numerical finite element simulations, optical microscopy and stereology, and x-ray computed tomography of notch tensile tests in a cast A356-T6 aluminum alloy. Notch Bridgman tensile specimens were monotonically loaded to different levels up to and including failure. The notch geometry is used to create stress triaxiality gradients in the specimen to validate the experimental and numerical methods. After mechanical testing, the damage in the specimens was first determined using a computed tomography (CT) method.

6.5.1. NUMERICAL MODELING

Figure 6.13 shows the load-displacement curves for the finite element simulations in which random and homogeneous initial porosity distributions were assumed with porosity levels of 0.001 and 0.0001. One observes from these simulations that the initially randomized porosity gives lower failure displacements than the homogeneous case. This difference lessens as the initial porosity level increases. One can see from these initial assumptions that the failure displacements ranged from approximately 0.05 mm to 0.11 mm. Later, we will show that the experimental failure displacement was approximately 0.11 mm indicating that our initial porosity assumptions were comparable to the experimental specimens.

Figure 6.14 illustrates that the point of failure can occur at different locations and applied “strain” levels with different initial porosity levels and distributions. The notch geometry generates stress and strain gradients from the notch center to the edge. The highest stress triaxiality is at the specimen center, but the highest strain level occurs at the notch edge. This affects the void growth much differently depending upon the initial void distribution and porosity level. Figure 6.15 shows the progression of total damage for the case with a random initial porosity level of 0.001.

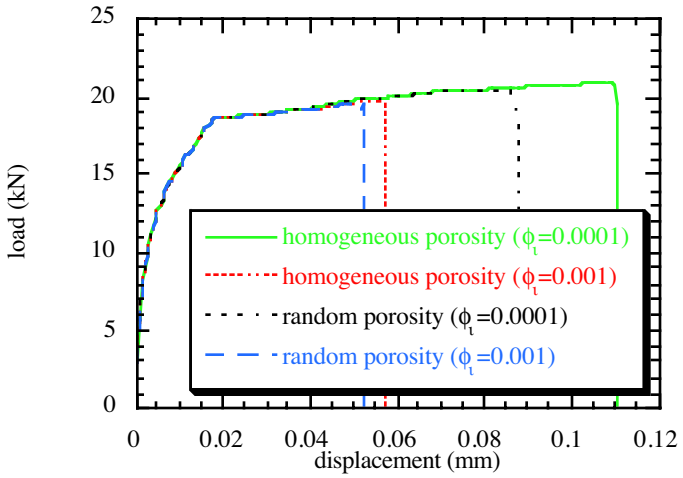

Figure 6.13. Finite element simulations of load-displacement curves with four different initial assumptions for the microstructure: (a) initially homogeneous casting porosity with a level of 0.0001, (b) initially homogeneous casting porosity with a level of 0.001, (c) initially random casting porosity with a level of 0.0001, and (d) initially random casting porosity with a level of 0.001.

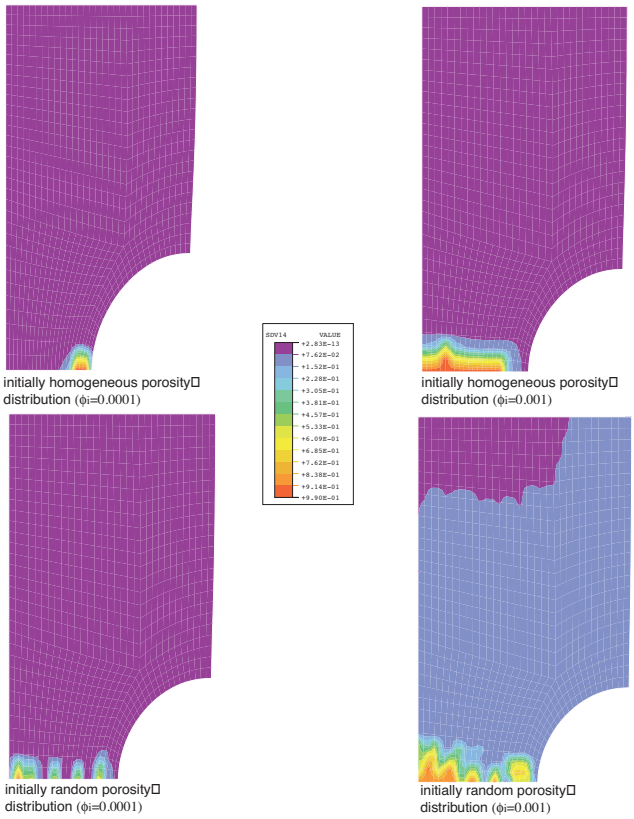

Figure 6.14. Contour plots of total void volume fraction comparing the finite element simulations at first element failure assuming initial random and homogeneous distributions.

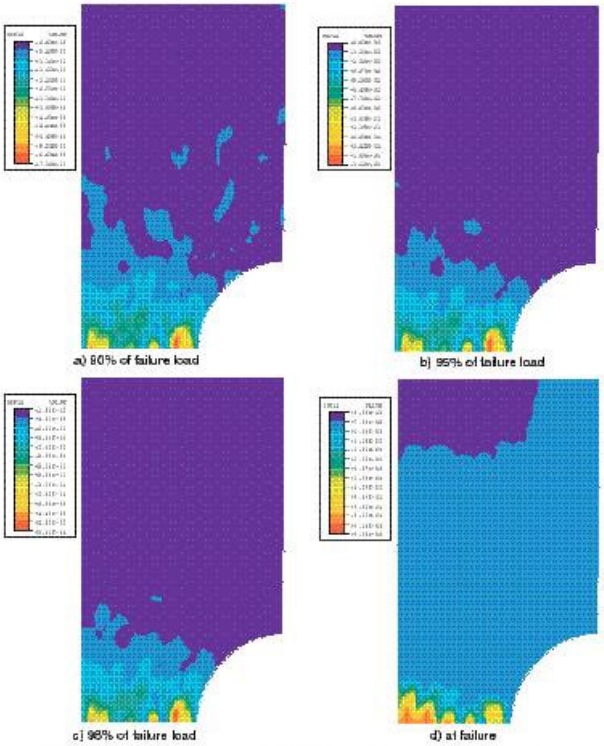

Figure 6.15 Progression of damage in FEM simulation with initial random porosity level of 0.001.

In the case of initial homogeneous porosity distribution two cases arise. When the initial void volume fraction is 0.0001, the first element failure location occurs near the notch edge. This happens because when the initial porosity level is small, total damage is not driven by casting pores but by voids nucleating from second phase particles. Although voids nucleate as a function of stress triaxiality their dependence on the stress triaxiality is much less than for void growth. As such, the effective plastic strain, which is highest near the notch edge, drives the void nucleation and in this case the total damage. As the initial porosity level increases, damage from the second phase particles becomes less important compared to the void volume fraction of the casting pores. When the casting pore volume fraction is high, the initial voids grow as a function of mostly the stress triaxiality, which is highest at the notch center. Figure 6.15 illustrates that for this case the voids with an initial porosity level of 0.001 (and above), failure occurs at the notch center as opposed to the notch edge. Horstemeyer and Revelli (1997) showed a similar trend for a wider range of initial porosity levels for wrought 6061–T6 aluminum, but no random initialization of porosity was performed.

When comparing a random versus a homogeneous distribution of voids, one can see from Figure 6.14 that very different failure locations can arise. When initializing the random distributions, the overall porosity level of the total notch specimen was the same as in the homogeneous case. Just like different initial porosity level simulations were run with the homogeneous distribution, simulations with the same initial porosity levels were run with random distributions. The motive for analyzing the random case arises because the casting process can yield various sizes of porosity throughout the specimen. Interestingly though based upon these few simulations, the triaxiality seems to play more of a role than the effective plastic strain as both the low and

high initial porosity levels tend to show failure towards the notch center regardless if a random or homogeneous distribution exists.

6.5.2. NOTCH EXPERIMENTS

Subsequent mechanical test specimens were cut from two separate cast plates (s1 and s4 from plate 1, s2 and s3 from horizontally cast plate). The samples were taken from different regions of the plate assuring that different initial porosity levels would result. A variation in the initial conditions of the test samples provided an additional dimension to evaluate the performance of the damage characterization and prediction techniques. In addition, the different levels of initial porosity in the specimens were helpful in determining if the driving force for ductile damage is more dependent on the initial material characteristics, such as, pore size, volume fraction, and distribution or the applied boundary conditions. The specimen notch radius was 2.97 mm, with a notch root diameter of 9.23 mm and a shoulder diameter of 12.7 mm. Cross sectional views of the samples are provided on several of the visual damage images. All specimens were loaded at an approximate strain rate of 10^{-4}/sec at room temperature.

The load-displacement responses of the four different cast A356-T6 Al specimens are shown in Figure 6.16. The specimens had a notch size of 2.97 mm and a gage radius of 4.7625 mm. Hence, the ratio of gage radius to notch size, which reflects the stress triaxiality, is 1.6, a moderate triaxiality. The displacements were measured using an extensometer with a 25.4 mm gage length placed across the notch. The Bridgman specimen numbers s1, s2, and s3 were unloaded prior to failure at 90%, 95%, and 98% of the failure load on the curves in Figure 6.16. Specimen s4 was loaded until failure as indicated in Figure 6.16. By monitoring the loads instead of displacements to determine the pre-failure point, we retrieved a more reliable result. When trying to control with displacements, premature failure of the specimen would result because of the variability in the initial porosity level and distribution. Because increased porosity can degrade the effective elastic modulus, s2 and s3 (both from plate 2) have larger initial porosity levels as evident from the immediately smaller effective elastic stiffness observed in these curves.

The maximum effective elastic stiffness among the four specimens, S_{max}, can be used in part to estimate the relative difference in total damage between the Bridgman specimens. The value of S_{max} represents the "elastic" response of the Bridgman specimen with the lowest initial porosity level. As shown in Figure 6.16 by the dashed lines, the unloading of all specimens is assumed to occur along S_{max}. With this construction, the area between the actual load-displacement response and the idealized unloading curve is a relative measure of the initial porosity superposed with the subsequent damage (plasticity) in the specimens. For example, in Figure 6.16 specimen s1 is brought to a higher load level than specimen s2. However, the total damage in specimen s2 is larger (greater area between the S_{max} line and the load-displacement curve) due to its increased initial porosity. Using the area criterion, the curves in Figure 6.16 are arranged in order of ascending total damage. The developed trend in total specimen damage is consistent with nondestructive and metallographic damage measurements that will be discussed later.

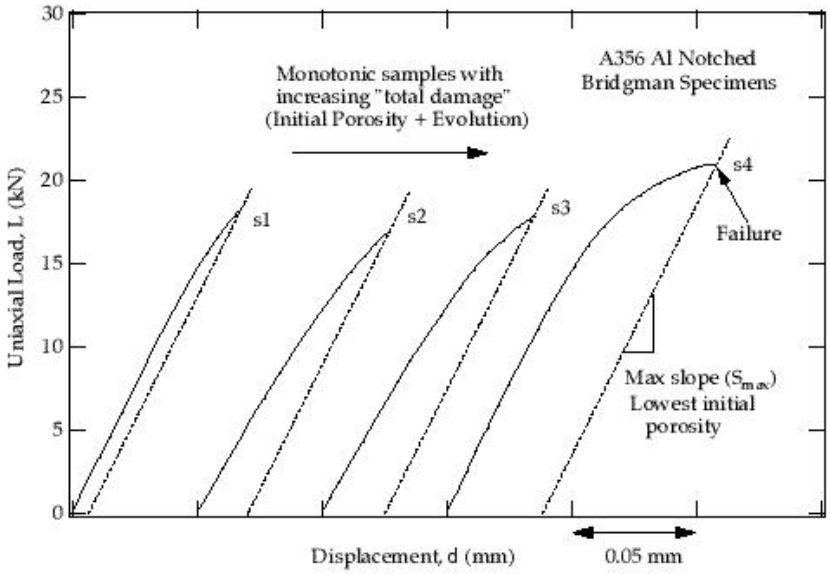

Figure 6.16. Load displacement curves for notched cast A356 Al specimens. The displacement was measured across the notch using an extensometer with a 25.4 mm gage length. The area between the maximum observed effective elastic stiffness, S_{max} and the curve is a relative measurement of total specimen damage.

6.5.3. COMPUTED TOMOGRAPHY

Computed tomography is a non-destructive testing technique that uses x-rays to accurately determine the local density changes. For the optical image analysis, the specimens were split and metallographically prepared. Optical microscopy coupled with digital image analysis techniques were used to obtain high precision pictures of the pertinent surface. The metallographic study was used to provide a benchmark comparison tool for the CT technique. The CT method determines three dimensional porosity distributions, while the sectioning method only provides information for a representative two dimensional cross section. However, the two dimensional cross section technique represents the most widespread method for determining the evolution of many microstructural parameters such as casting porosity (Tewari *et al.,* 1998).

Computed tomography produces two and three dimensional spatial data convolved with a fourth dimension which is the x-ray linear attenuation coefficient. The linear attenuation coefficient (LAT) is a function of material density, elemental composition, and x-ray energy. For specimens that have homogeneous elemental composition, changes in the LAT represent changes in material density. For inhomogeneous samples, changes in the LAT represent either density changes or segregation of elemental constituents, or both. Voids in the material result in LAT values of zero or near zero depending on spatial resolution.

Volumetric data is produced by first obtaining two dimensional x-ray transmission images (projections) for a systematic set of specimen rotations. Computed tomography reconstruction software converts the two dimensional projections into a complete volumetric representation of the object. This volumetric data can be sectioned in any two dimensional plane to provide arbitrary cross-sectional planes (tomograms) of the specimen. The tomograms, coupled with volumetric image rendering techniques, accurately depict internal structures, geometries, and density/elemental variations within the specimen. Discontinuities such as gas holes and porosity are well defined in the computed tomography image, depending on the system resolution and discontinuity size. When individual pores in a local region are smaller than the system resolution, that region will appear to have a lower density than the surrounding nonporous material.

Two system parameters of importance for image interpretation are contrast sensitivity and spatial resolution. Contrast sensitivity is the ability of the CT system to detect variations in thickness and/or density. Spatial resolution is the ability of the system to resolve small features or details. The CT system can detect density variations as small as 0.1 per cent, and provide this information as a function of spatial location in the object. Spatial resolution depends on system design, sampling plan, and image reconstruction method. The detector element size and projection magnification together with sampling plan (i.e., number of projection angles) determine both pixel size for two dimensional slice images and voxel (volume element) size for three dimensional images. For the experimental setup employed here, the pixel (voxel) dimension was 28 μm. Structural features smaller than approximately two pixel (voxel) dimensions are not resolved, rather they lead to a lower average density measurement. Deconvolution of image blur using a measured point spread function is accomplished before CT reconstruction to produce sharper (higher contrast and resolution) reconstructed images.

The computed tomography data acquisition system used in the present study is an area-array (two dimensional) third-generation (rotation only) system (Figure 6.17). It consists of a 450 kV constant potential x-ray machine source with a 1.0 mm focal spot, and a detector system that uses a thermoelectrically cooled CCD camera (14-bit, 1024 x 1024 pixels) optically coupled to a high-density glass scintillator plate (100 x 100 x 6 mm) by a photographic lens. The mechanical staging for the system consists of three degrees of freedom: rotational, and x- and y-translation. These are driven by a computer-controlled system that provides movement in all three axes. Data preprocessing, image reconstruction, and analysis are typically done on a high level workstation. The system was configured with a projection magnification of nearly 1.0, and source-to-detector distance of 3000 mm. All data were acquired at 80-kV peak energy over a range of 180˚ with 1° scanning increments. Prior to reconstruction the images were preprocessed to subtract the camera dark current, correct for the source and detector variations correct for point-spread function and convert the raw data to CT number (i.e. linear attenuation coefficient). Ring removal and beam hardening were also performed in preprocessing.

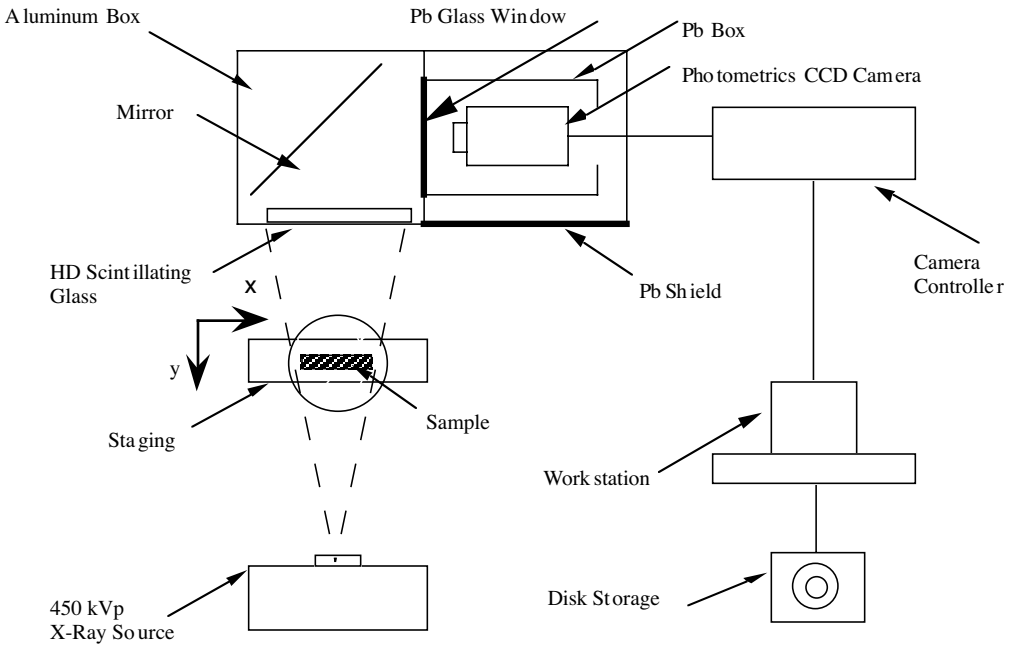

Figure 6.17 Schematic of the computed tomography (CT) system and data acquisition setup.

6.5.4. OPTICAL METHOD EVALUATION

As metals are opaque to visible light, optical microscopy of metals involves observations on two dimensional planes (metallographic planes) through three dimensional microstructural space. It is possible to estimate mean values (or statistical expected values) of some geometric attributes of three dimensional microstructure by using unbiased stereological estimators that can be measured from observations on lower dimensional manifolds such as two dimensional planes or one dimensional lines through the three dimensional microstructure, or projected images of three dimensional microstructure. For example, volume fraction of constituents (Underwood, 1968), total surface area of internal surfaces (Smith and Guttman, 1953, Baddeley, Gundersen, and Cruz Orive, 1986, Gokhale and Drury, 1994), some attributes of curvatures of microstructural surfaces (DeHoff, 1968, Gokhale, 1998), length density of lines (Gokhale, 1990), etc. can be estimated by using unbiased equations of stereology. The stereological relationships have in their roots stochastic geometry and global analysis (Santalo, 1976). In practice, stereological equations provide a simple and efficient way for quantitative characterization of homogenous microstructures, because any one plane at a location in the three dimensional structure is statistically representative of all planes of that angular orientation. Therefore, measurements on few such planes can yield unbiased and precise estimates of the attributes of three dimensional structure.

Design based efficient stereological sampling techniques are available to obtain reliable averages of measured quantities over angular orientations of test planes or test lines, which provide practical means for handling anisotropic microstructures (see Baddeley, Gundersen, and Cruz Orive, 1986, Gokhale and Drury, 1994, Gokhale, 1990, 1998). Microstructural features having sizes one micron or larger can be easily detected and measured by using optical microscopy, and thus mean

values corresponding to their populations can be precisely estimated by using the stereological equations, in an unbiased manner. However, in the inhomogeneous microstructures (such as those in the present study), a variation in the microstructure from one location to another exists, and therefore, no one plane is representative of all the planes of that orientation. Consequently, stereological measurements are needed on two dimensional planes at different locations to estimate the microstructural mean values with good precision, which may be too tedious, and may lead to large statistical variances and low precision. For the inhomogeneous three dimensional microstructures, the direct three dimensional x-ray computed tomography appears to be an attractive technique for characterizing microstructural geometry. However, in commercially available x-ray tomographic equipment, the voxel size is usually larger than twenty-five microns, and therefore, sizes of features (say a void) smaller than fifty microns or so (i.e., those occupying about two or less voxels) cannot be measured with good precision. Consequently, a precise estimate of three dimensional microstructural attributes of features may not be possible, if a significant fraction of feature (say voids) population is smaller than about fifty microns. For inhomogeneous microstructures encountered in the present investigation where sizes of features of interest (voids) span over a wide range of length scales (five microns to five hundred microns), we verify the microstructural damage data by using optical metallography and stereology (two dimensional analysis) and x-ray computed tomography (three dimensional analysis). If both the techniques generate comparable microstructural damage data, then such data can be used to draw objective conclusions regarding damage evolution. Furthermore, these two approaches can be used for comparative purposes of numerical predictions.

For optical microscopy, the specimens were sectioned along a central vertical plane in the loading direction and were metallographically prepared using standard techniques (Tewari *et al.*, 1998). To quantify variations in the volume fraction of voids (void volume fraction is equal to the statistical expected value of area fraction in a metallographic plane) as a function of radial and axial distance in the notch specimen, many measurements are made. Typically, only a few random individual frames are examined to obtain mean values, because homogeneous microstructures are assumed to be present. However, to capture a large region such as desired for these notch specimens, measurements must to be performed on high-resolution images captured at sufficiently high magnification. The area of the observed microstructural field of view is inversely proportional to the square of the magnification, and therefore, at a high magnification only a very small region of the metallographic plane is observed in one field of view. To observe a large area of the metallographic plane at high resolution (high magnification) a digital image processing based technique (Louis and Gokhale, 1995, 1996, Yang, Tewari, and Gokhale, 1997) was used to create a large area image "montage" from contiguous microstructural fields digitally grabbed at high magnification. The procedure is equivalent to "cutting, matching, and pasting" of large number of high magnification contiguous microstructural frames; the borders of individual microstructural fields are matched within one pixel precision. Figure 6.18 illustrates the technique. In the present work, image analysis was conducted on a Zeiss optical microscope using KS-400 image analysis software from Kontron, Inc. To create a montage, the microstructure was observed at 100X and the first field of view was selected at one end of the specimen. The image of this first field of view was then stored in the memory of image analysis computer. The right border (of about 60 pixel width) of this first image was then placed on the left edge of a live second image. This resulted in a superimposed image on the left border of the screen (of the previous right border and live image) with rest of the screen having the live image as

shown in Figure 6.18. The computer controlled microscope stage was then automatically moved so that the right border of the live image moved to the left border and gave a reasonable match with the superimposed image. The physical movement of the automatic stage cannot achieve a perfect match with the previous image, but small movements (to a least count of one pixel) of the live image were made manually using image analyzer to achieve a perfect match. This resulted in a match of the first and the second image with an accuracy of one pixel. This second image was then stored in the computer memory. All successive images were grabbed by using the same procedure, and finally a contiguous montage of fields was made.

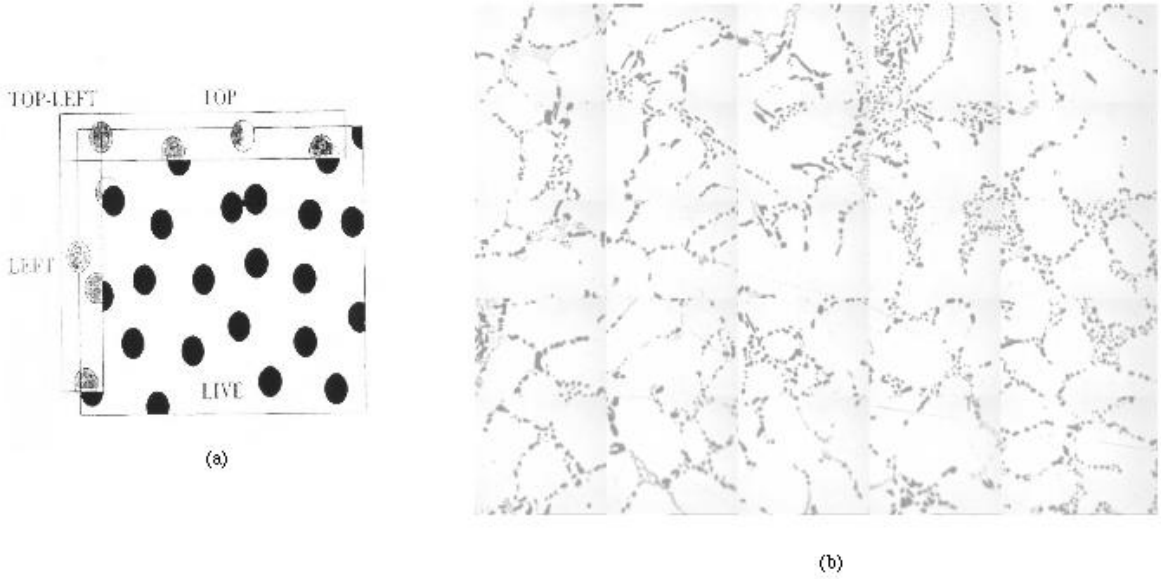

Figure 6.18. Optical method micrograph picture illustrating (a) the overlap of the stored image and adjacent live image and (b) a collection 25 images.

Figures 6.19-6.21 are high resolution large area montage of microstructure created in this manner and show the porosity distribution in the entire notch region of the specimens. Note that in Figures 6.19-6.21, the large area montages have been digitally compressed for presentation. These figures the porosity distribution and were used to estimate the size distribution of pores and their area fraction as a function of radial distance and distance along the length of the specimen.

6.5.5. NDE/OPTICAL METHOD/FEM COMPARISONS

The typical progression of damage evolution for wrought materials in notch tensile tests arises from voids growing at the center of the specimen because of the high stress triaxialities. Actually, the peak stress triaxiality starts at the notch edge at the start of the deformation because of the stress concentration but moves fairly rapidly to the center as deformation proceeds. The stress

triaxiality is nonuniform throughout the cross section of the specimen and reaches a level sufficient to start void growth when its peak reaches the center of the notch specimen. Figure 6.22 shows contour plots of the stress triaxiality (hydrostatic stress/deviatoric stress) of a notch tensile test illustrating spatial movement of the peak stress triaxiality. Again, this is typical for wrought, ductile materials.

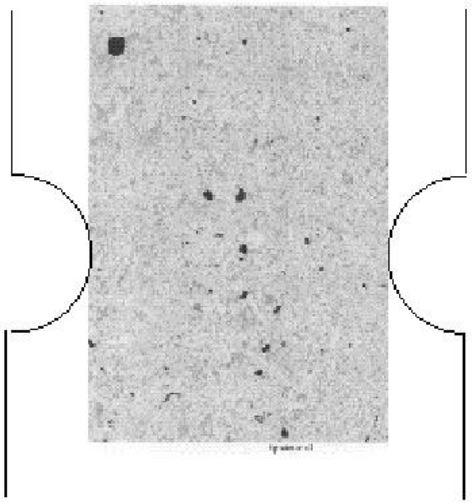

Figure 6.19. Montage of many contiguous optical micrographs of notch specimen 1.

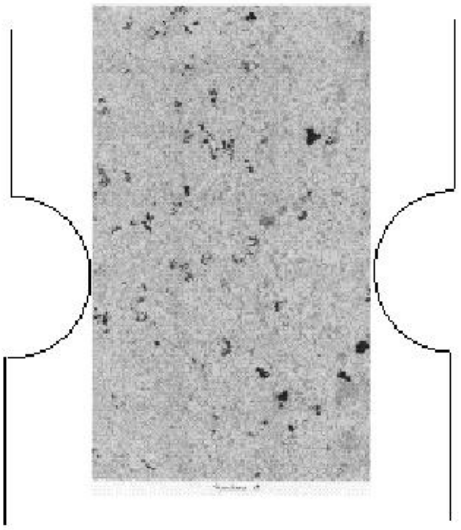

Figure 6.20. Montage of many contiguous optical micrographs of notch specimen 2.

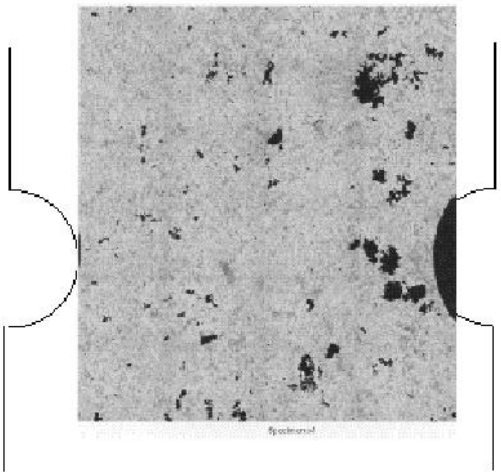

Figure 6.21. Montage of many contiguous optical micrographs of notch specimen 3.

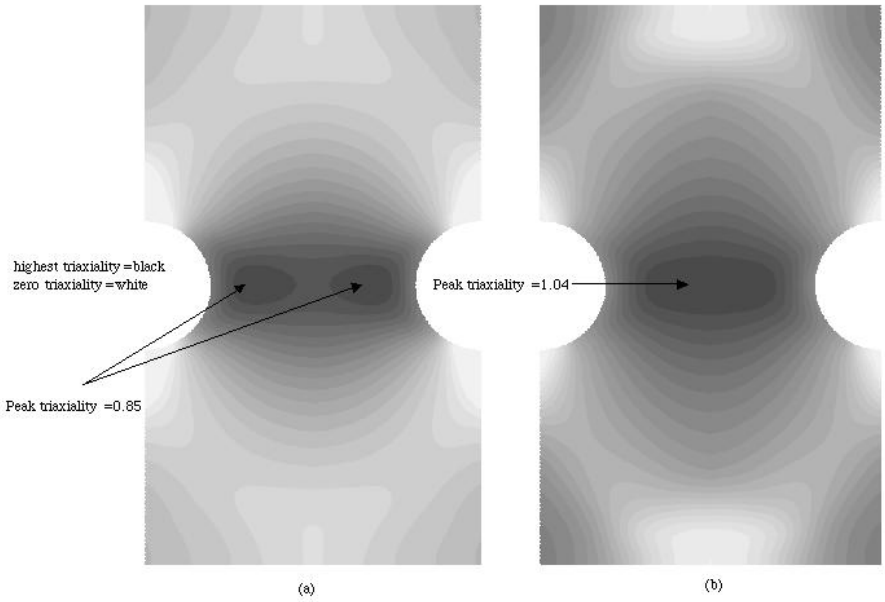

Figure 6.22. Progression of stress triaxialities (hydrostatic stress/deviatoric stress) over the spatial domain of a notch specimen under tensile deformation.

For ductile materials with brittle phases, such as the cast A356-T6 aluminum alloy examined in this study, the final failure location may not occur at the specimen center depending on the fracture mechanisms of pore growth from casting porosity versus from silicon particle breakage. As the peak stress triaxiality increases in magnitude and moves toward the center of the specimen, voids have been nucleated by the fracture of the particles and/or by debonding of the particle-aluminum interface. As such, the damage increases by not only voids growing but by new voids initiating and then growing. Damage reaches a certain level (interpreted as defining a hole in the material the size of the finite element) before it reaches the center of the specimen like

a wrought alloy. In a wrought alloy at first element failure, the highest level of plastic strain occurs at the notch edge, but the highest stress triaxiality occurs at the center of the specimen. As such, we conclude that the stress triaxiality drives the void growth as opposed to the plastic deformation, because damage evolves mainly at the specimen center. For this cast aluminum, the highest plastic strain occurs at the notch edge and the stress triaxiality occurs away from the edge similar to wrought materials, but Figure 6.23 illustrates that the highest damage (which comprises void nucleation, growth, and coalescence) occurs at two different locations when the initially homogenous distribution of 0.0001 was used. The two different locations are aligned with the peak plastic strain and peak stress triaxiality as shown in Figures 6.24 and 6.25, respectively. In Figure 6.24, the dark contour shows that the plastic strain reached a level of 42% at the notch edge and around only 1% near notch center. In Figure 6.25, the lightest contour shows that the highest negative tensile pressure (stress triaxiality equals the negative pressure over the deviatoric stress) occurs between the notch edge and specimen center. Figure 6.26 shows contour levels of void nucleation in which the dark contour shows the peak levels occurring near the notch edge and near the peak stress triaxiality. Figure 6.27 shows contours of void volume throughout the specimen. Note in Figure 6.27 that the peak void growth occurs at the peak stress triaxiality.

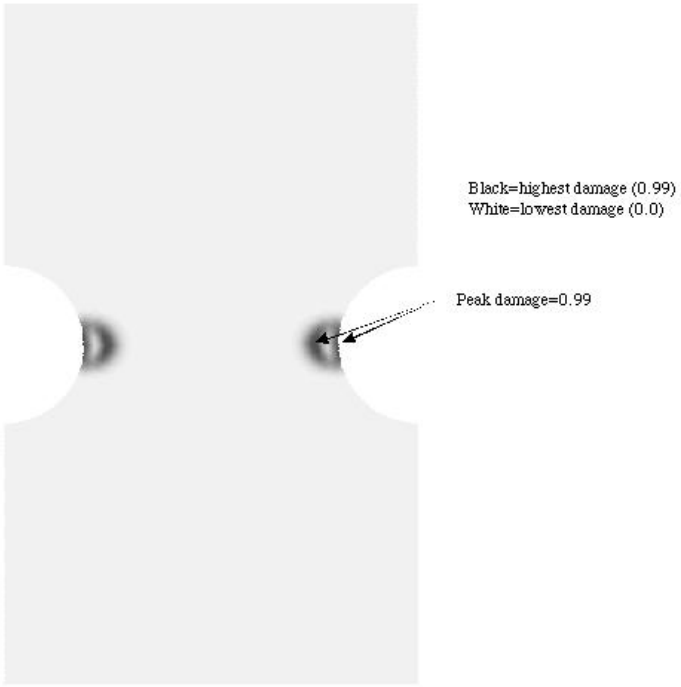

Figure 6.23. Total damage contours just before final failure of a notch tensile specimen with a notch acuity to radius ratio of 0.117 for a cast A356 aluminum alloy. Note that the dark region indicates the peak damage level in two locations along the radial plane of symmetry.

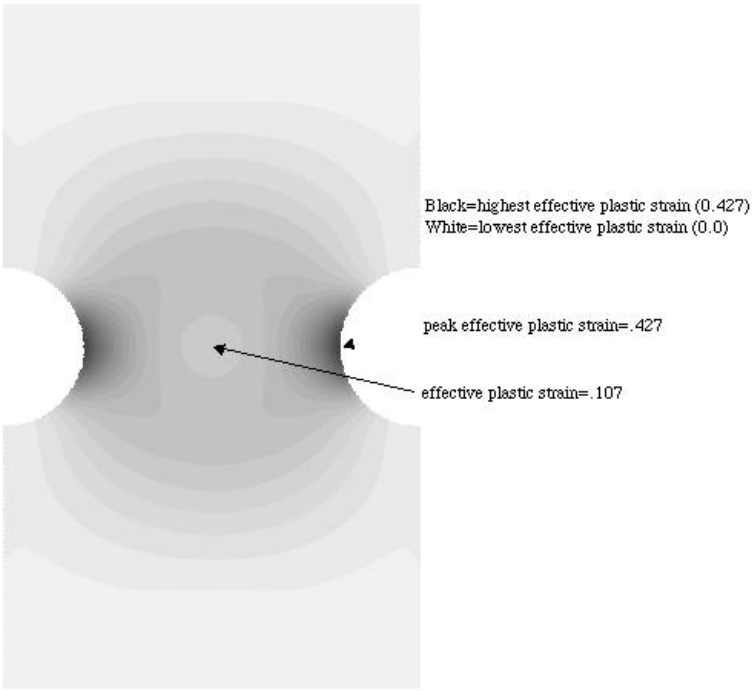

Figure 6.24. Plastic strain contours just before final failure of a notch tensile specimen with a notch acuity to radius ratio of 0.117 for a cast A356 aluminum alloy. Note that the dark region indicates the peak plastic strain level near the notch edge.

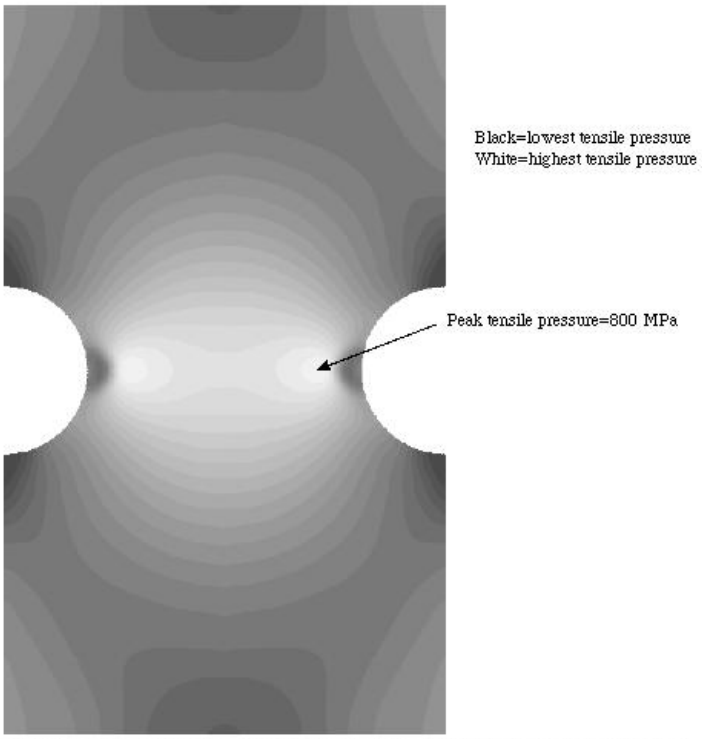

Figure 6.25. Pressure contours just before final failure of a notch tensile specimen with a notch acuity to radius ratio of 0.117 for a cast A356 aluminum alloy. Note that the light region indicates the peak tensile hydrostatic stress between the notch center and notch edge.

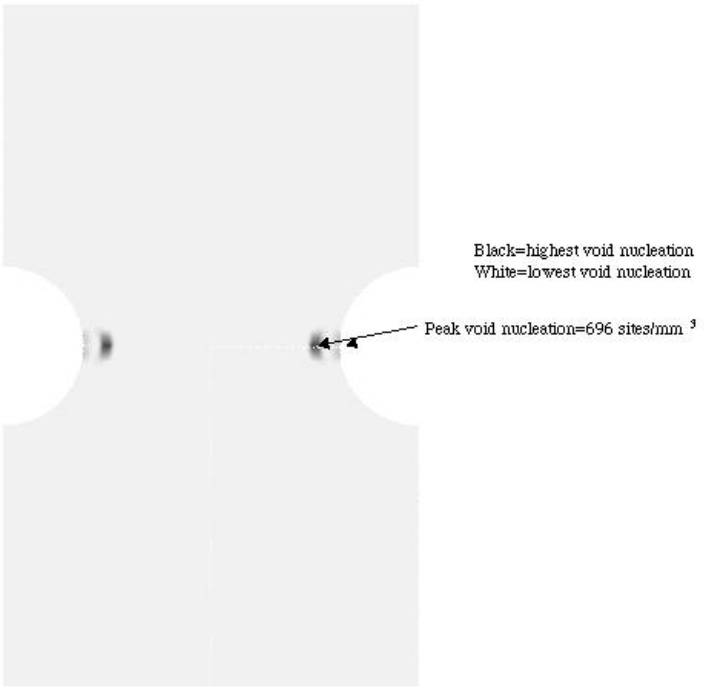

Figure 6.26. Void nucleation contours just before final failure of a notch tensile specimen with a notch acuity to radius ratio of 0.117 for a cast A356 aluminum alloy. Note that the dark region indicates the peak nucleation level at two locations.

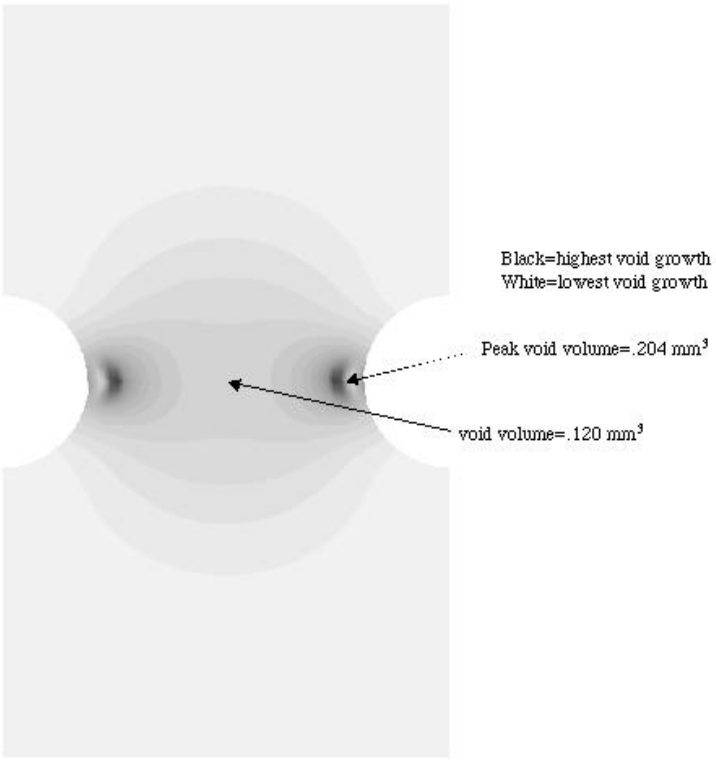

Figure 6.27. Void growth contours just before final failure of a notch tensile specimen with a notch acuity to radius ratio of 0.117 for a cast A356 aluminum alloy. Note that the dark region indicates the peak void growth level between the notch center and notch edge.

The coalescence constant, C_{coal}, in Equation 2.37 was assumed to be unity for the above finite element analysis. Other analyses were performed in which the coalescence term was increased. The results showed that as the coalescence term increased, the total damage level reached 15% (limit observed in the x-ray tomography measurements) closer to the notch edge. One can interpret this as the following: as coalescence increases, the void microlinking increases. This in turn makes the response look more brittle on a macroscale, since the more ductile the material, the closer to the center of the specimen would final failure occur.

This progression of damage in notch tensile specimens for this cast A356-T6 aluminum alloy gives understanding of the role of the nonhomogeneous distribution of initial porosity and second phase silicon on the final failure state. With this understanding, we now focus on comparisons of the finite element simulations and experimental results, which include image analysis and x-ray tomography of the physical specimens.

Numerical-experimental comparisons of the peak void volume indicate that initial void volume fraction was about 0.001. Table 6.3 summarizes results from the damage progression from the x-ray tomography and finite element analyses. The finite element results show that similar porosity levels compared to the experimental results can be achieved by the right combination of initial porosity level and the distribution. When the finite element results were averaged over a larger region, the results were much closer to the optical image results. Figures 6.28-6.34 clearly illustrate this point.

Table 6.3. Peak void volume fractions within notch specimen at different strain levels.

Failure load %	x-ray tom.	FEM ($\phi_i = 0.0001$ homog.)	FEM ($\phi_i = 0.0001$ random)	FEM ($\phi_i = 0.001$ homog.)	FEM ($\phi_i = 0.001$ random)
90	0.09	0.004	0.076	0.095	0.097
95	0.13	0.013	0.096	0.12	0.13
98	0.15	0.033	0.12	0.13	0.14

Figure 6.28 shows a comparison of the image analysis montage, x-ray tomography picture, and a contour plot of total void volume fraction from the finite element simulation in which an initially random porosity with a level of 0.001 was assumed for the 90% of fracture load case. The differences in the montage and x-ray tomography picture arise because the image analysis only shows one plane cutting axially through the specimen. The x-ray tomography results average 360 planes rotated at one degree throughout the specimen. As one would expect, the x-ray tomography would be slightly different than the image analysis but would be expected to be close the finite element analysis, since they are averaged in the annular regions radially throughout the specimen. The comparisons are encouraging.

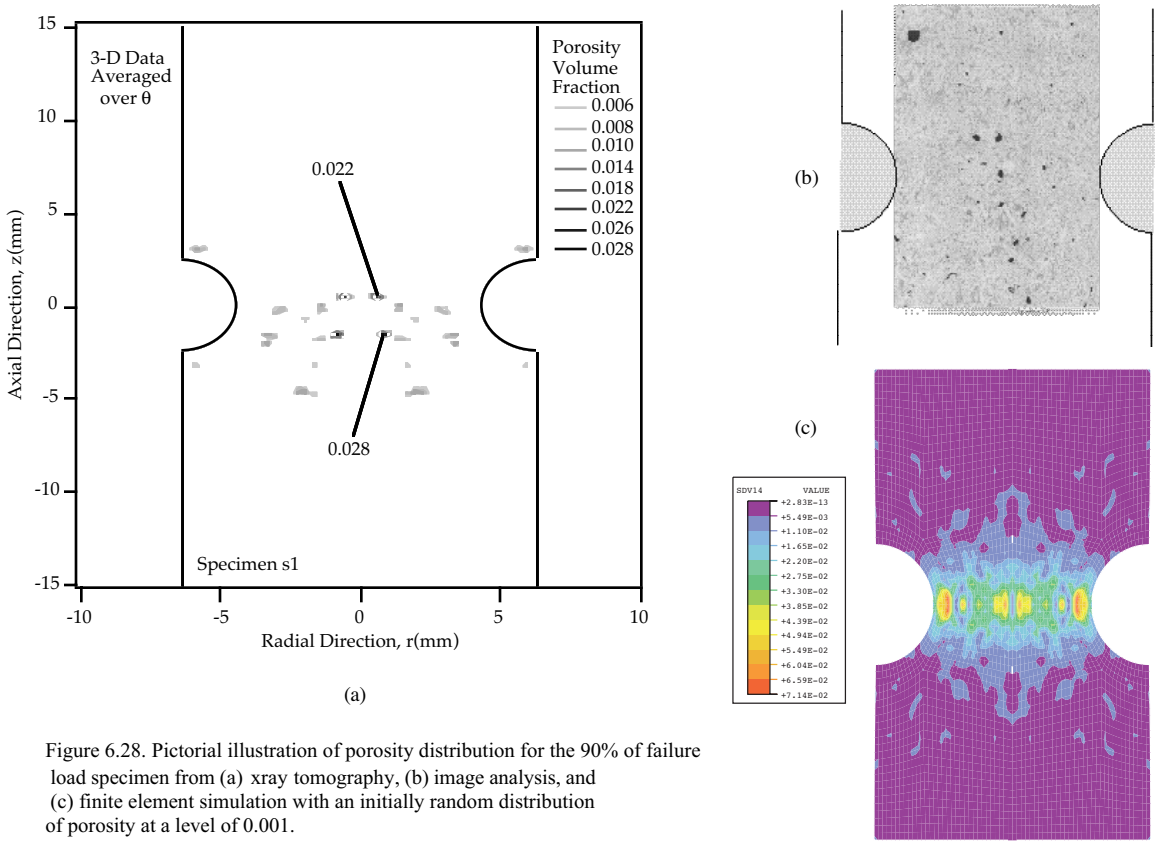

Figure 6.28. Pictorial illustration of porosity distribution for the 90% of failure load specimen from (a) xray tomography, (b) image analysis, and (c) finite element simulation with an initially random distribution of porosity at a level of 0.001.

Figure 6.29 is the quantitative data retrieved from Figure 6.28. From the finite element simulations, two averages were conducted. One in which the area fraction was the same as the image analysis, and another in which the area was the same as the x-ray tomography. For the optical image analysis (large area average) three sections were averaged as a function of the radius of the specimen in the notched region. The larger area average give slightly different results compared to the image analysis because the image analysis results were determined from one plane, and the finite element analysis results were taken circumferentially around the axisymmetric geometry. The x-ray tomography and finite element analysis gave much closer results.

Comparisons along the radial and axial dimensions were made within the specimen. Since the notch induces a stress triaxiality that drives void growth from the center, one can observe a higher void volume fraction at the center than at the edge. Figures 6.28-6.34 confirm this notion.

Figures 6.30 and 6.31 showed similar qualitative trends as Figures 6.28 and 6.29 but for the 95% of failure load case. Here, the porosity levels are higher than the 90% case (Figures 6.28 and 6.29) as damage has progressed, and all three methods (x-ray tomography, optical metallography, and finite element analysis) quantitatively capture the trend fairly well.

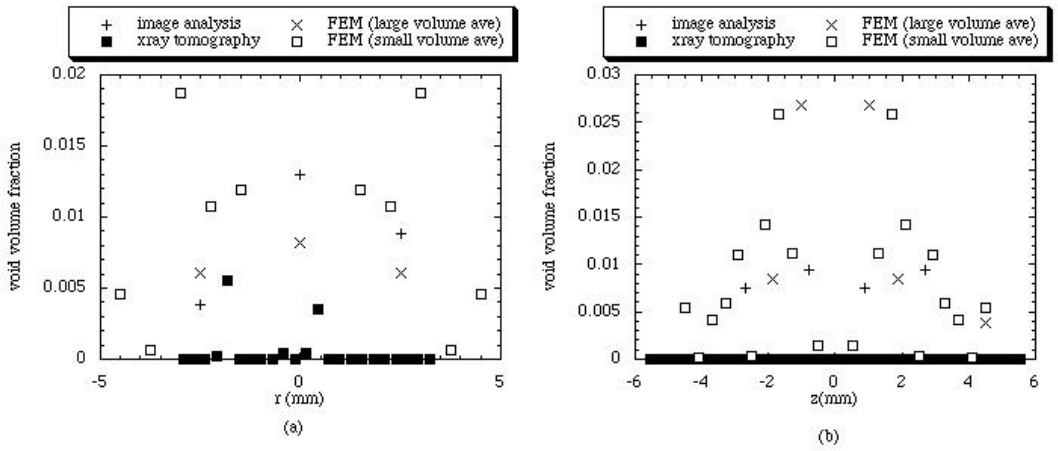

Figure 6.29. Total void volume fraction along (a) radial distance and (b) axial distance determined from 90% of failure load specimen from xray tomography , image analysis, and finite element analysis with averaged regions similar to those taken for the tomography and image analysis measurements.

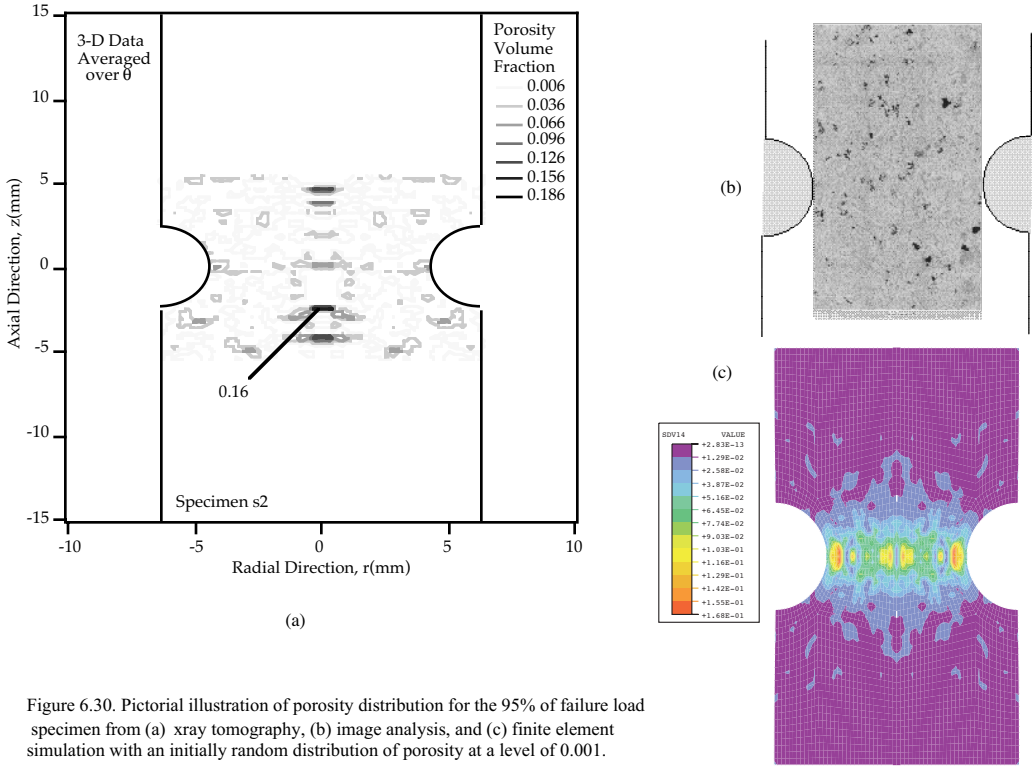

Figure 6.30. Pictorial illustration of porosity distribution for the 95% of failure load specimen from (a) xray tomography, (b) image analysis, and (c) finite element simulation with an initially random distribution of porosity at a level of 0.001.

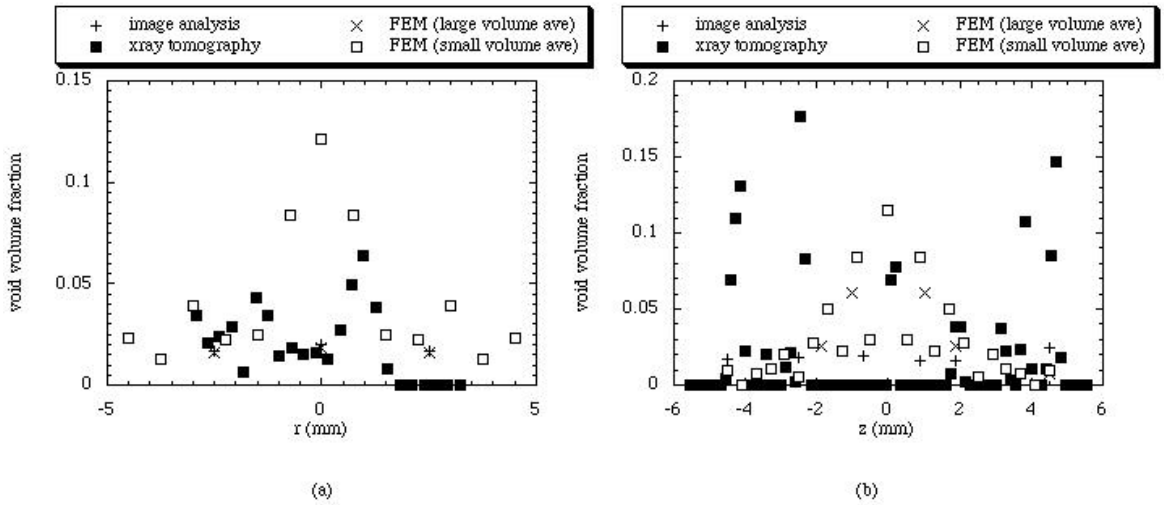

Figure 6.31. Total void volume fraction along (a) radial distance and (b) axial distance determined from 95% of failure load specimen from xray tomography, image analysis, and finite element analysis with averaged regions similar to those taken for the tomography and image analysis measurements.

Figures 6.32 and 6.33 show the comparisons for the 98% of fracture load case. Again, all three methods appear to reflect the expected damage progression. Based on these six figures, one's confidence in all three methods is enhanced since they seem to independently corroborate each other's results. Differences in the x-ray tomography and optical metallography results arise because each of the measurements were from different specimens which had different initial porosity levels, while the finite element simulations were from a single calculation using an initial starting porosity level of 0.001 that provided qualitative damage progression agreement with both the x-ray tomography and optical metallography. One must not forget that the optical metallography results were obtained in a two dimensional plane, but the x-ray tomography and finite element analyses results were obtained in three dimensions.

One last point of extreme importance can be extracted from this data. The final porosity level at which final fracture occurs is material dependent and has not been clearly defined for many materials. Based upon the x-ray tomography data shown in Figure 6.34, we can conclude that the peak void volume fraction at which specimen fracture occurs is about 15%. This percentage of porosity can be viewed as a percolation limit in the sense that 100% of an aggregate need not fail before the aggregate loses its strength holding capacity. Voids grow from the initial porosity and from particles that fracture or debond. The voids can then coalesce from the original pore-pore interactions or from the pore-silicon void interactions. Upon reaching a certain total damage level upon coalescence, a certain level of void volume fraction is present to finally fracture the specimen, in this case approximately 15%. This final porosity level may be stress state

dependent and hence further studies should be done at different triaxialities to determine if this is true.

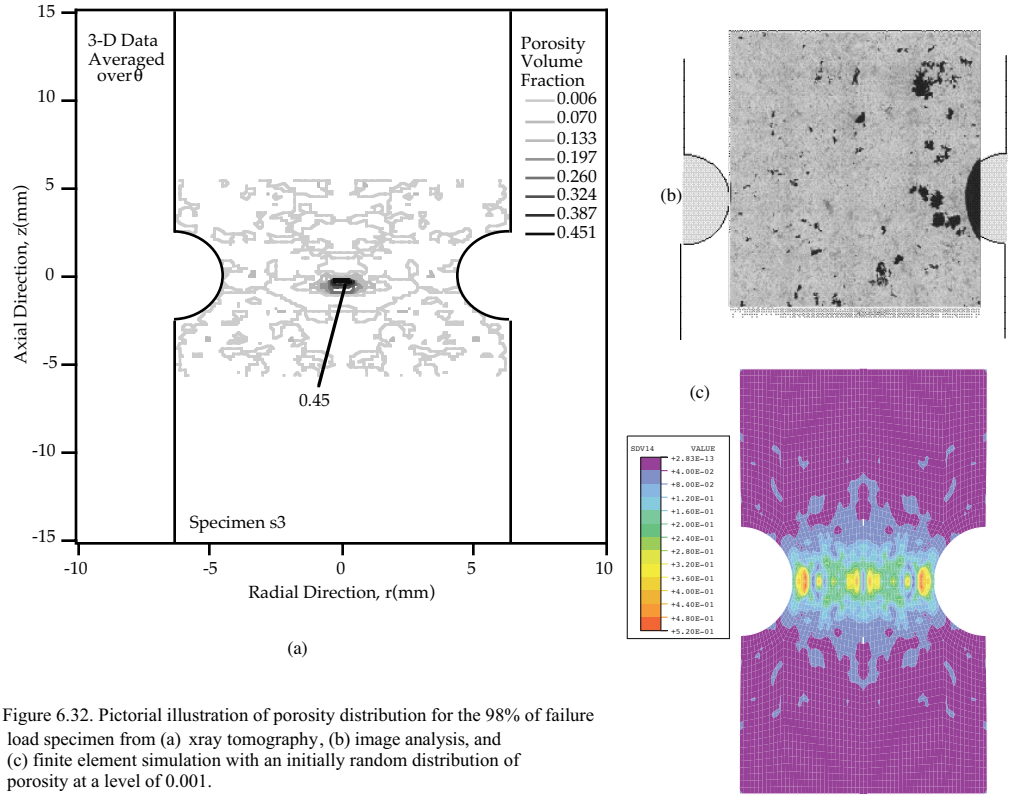

Figure 6.32. Pictorial illustration of porosity distribution for the 98% of failure load specimen from (a) xray tomography, (b) image analysis, and (c) finite element simulation with an initially random distribution of porosity at a level of 0.001.

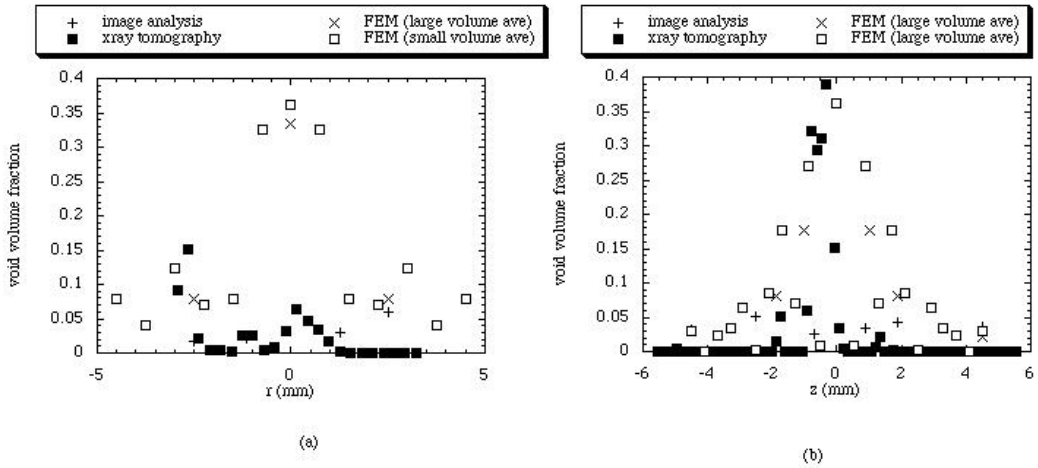

Figure 6.33. Total void volume fraction along (a) radial distance and (b) axial distance determined from 98% of failure load specimen from xray tomography, image analysis, and finite element analysis with averaged regions similar to those taken for the tomography and image analysis measurements.

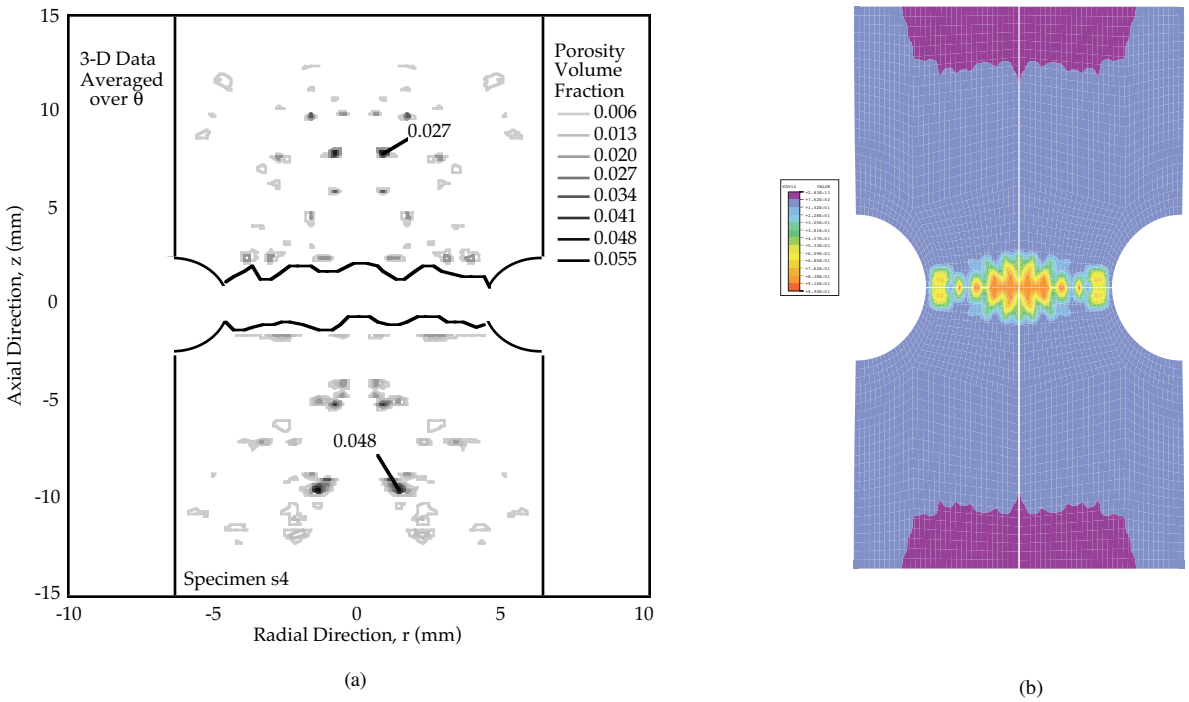

Figure 6.34. (a) Xray tomography data and (b) finite element simulation at final failure.

In summary, damage progression has been quantified and confirmed by independent methods of evalution for a cast A356-T6 aluminum alloy notch tensile testing. The methods include experiments, finite element simulations that include a history dependent elastic-plastic internal state variable plasticity model involving evolution equations for void nucleation, growth, and coalescence; x-ray computed tomography; and optical microscopy/stereology metallography analysis. This study provides a new methodology of evaluating metal damage progression and provides the quantitative data needed to establish increased confidence in using a simulation-based finite element analysis to achieve optimal geometries and reduced masses for structural components.

6.6. WEAPONS CARRIER ANALYSIS

In this numerical/experimental study we simulate the response of a transportation carrier, used to transport U.S. Department of Energy weapons, to levels exceeding the design load. This loading environment is similar to certain impacts on automotive parts in a crash. Good agreement between the numerical analyses which used the microstructure-property model and tests on the transportation carrier illustrates the usefulness of these simulations.

Cast A356 aluminum has been used in a U.S. Department of Energy (DOE) weapon transportation carrier as a load bearing structure subjected to shipping environments. Cracks were observed in some carrier brackets when two weapons were stacked.

Optical microscopy of the cast material in several regions of the transportation carrier was performed. The porosity was fairly uniformly distributed amongst the eutectic region in the interdendritic boundaries. The dendrites consisted of silicon lean cores with eutectic silicon distributed as particles along interdendritic boundaries and may play a role in the damage evolution. The dendrite cell spacing (DCS) was approximately 50 mm. The initial porosity ranged from 1.0% to 1.5% volume, with pores as large as 0.5 mm. As such the dominant mechanism for failure was porosity growth and coalescence with only minor influences from silicon fracture and debonding.

Experiments in which the weapon and tranportation carrier were tested under vertical compressive, monotonically increasing quasistatic loads were performed until fracture of the weakest structural component was observed. The failure occurred suddenly at a vertical load of approximately 121.5 kN; the crack initiation load could not be determined. Post-test evaluation revealed three radially aligned cracks around the periphery of the quick release pin housing made of cast A356 aluminum. The location of the cracks were consistent in the four brackets tested. The location of the first crack can be deduced from examining the cracks observed in the quasi-static tests mentioned here and in transportation carriers pulled from actual field use. In some of the failed transportation carrier brackets from the field, one crack was consistently observed. This radial crack emanated from the edge of the bracket toward the center of the quick release pin housing, terminating at the housing where the quick release pin made contact with the bracket.

With model parameters determined from the experimental data, the internal state variable plasticity/damage model was used to analyze the boundary value problem related to the transportation carrier bracket failure. The finite element analysis included the A356 cast aluminum bracket with a 303 stainless steel sleeve. Approximately 4500 elements were employed in this 3D analysis which included one plane of symmetry. A “welded” interface was assumed between the sleeve and the bracket. The load was applied at an angle of 27˚ from the horizontal on the sleeve as indicated in Figure 6.35 to simulate the experimental loading. The load amplitude was increased in increments of 26.7 kN to 133.5 kN, the final load corresponding to a 5 g acceleration of the weapon and carrier. The finite element calculations took approximately nine hours of CPU time on a Cray J90.

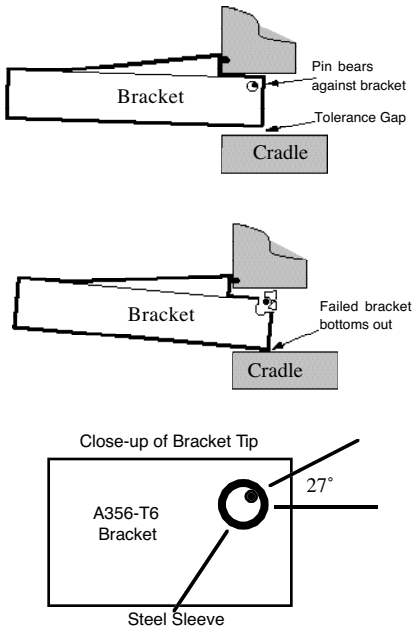

Figure 6.35. Boundary conditions for weapons carrier analysis.

The calculations indicated that damage accumulation starts at the three critical areas, where the high tensile hydrostatic stresses arise. Figure 6.36 shows the highest tensile pressure areas showing three failed location points in the bracket material around the pin housing. This corresponds to the three failed areas in the experiment. Figure 6.36 reveals that damage first occurred at the bracket edge towards the direction of the load. This damage accumulation, which is represented by porosity level, initiated failure in the bracket. This corroborates the location of the bracket failures observed in the field. Note that the regions of high stress (negative) pressure and high damage accumulation in the finite element calculations compare closely to the locations of the cracks resulting from the experiment. The results in Figure 6.36 occurred at 109.5 kN, about a 10% lower load level than the experimental results. The calculations "died" at 109.5 kN, so the propagation of failure in the three locations was not reached, although the highest tensile pressures indicated where the three failed regions were located. Hence, the locations and load levels of the damaged areas experienced from the tests were verified fairly well with the finite element analyses. This also verifies that the model parameters from the other tests described in this report were accurately determined.

This structural analysis and a corroborative metallographic analysis of the failed A356 cast aluminum carrier bracket revealed that poor design and poor cast properties led to crack formation in the bracket. A sizable tolerance between the bracket and cradle caused the quick release pin to bear against the steel sleeve which in turn loaded the A356 bracket.

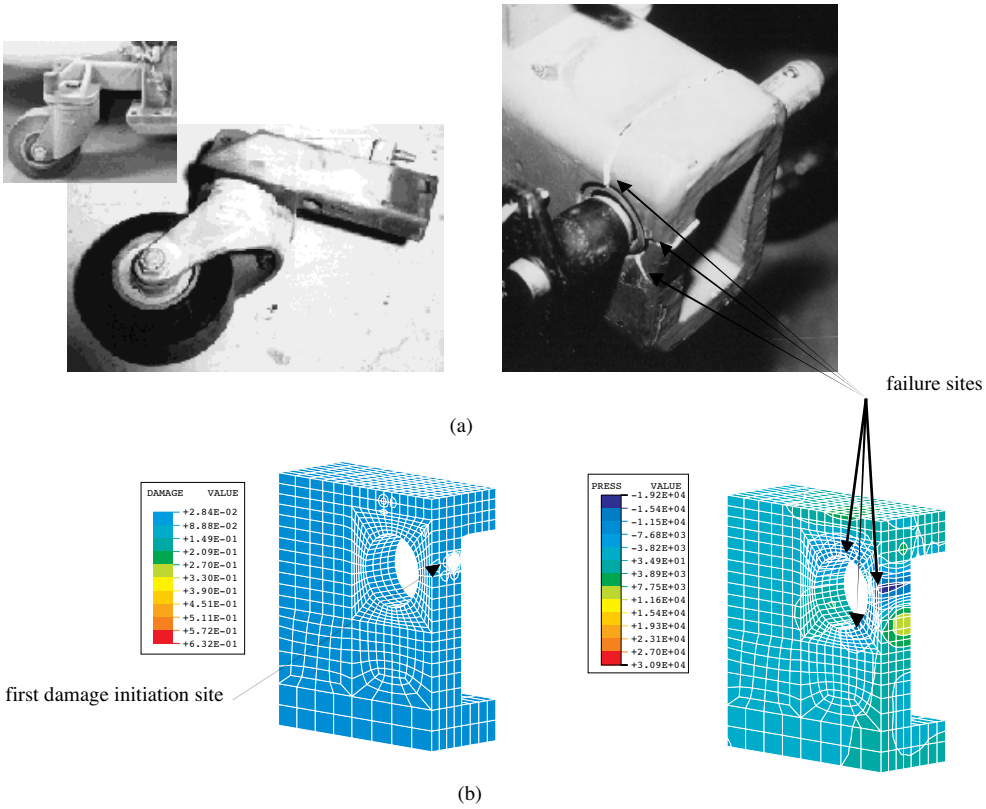

Figure 6.36. Comparison of (a) experiment and (b) microstructure-property model failure prediction (damage=SDV14) for weapons carrier analysis.

6.7. AUTOMOTIVE CONTROL ARM ANALYSIS

In this numerical/experimental study we use the microstructure-mechanical property model to simulate the response of a control arm given certain boundary conditions. Three types of simulations were conducted at the structural scale. The first type were related to validating the microstructure-property model. Previous to this work, the simulations using the microstructure-property model have been correlative in nature. The simulations presented in this section were completely predictive. In fact, all of the simulations were performed ahead of the experiments. In the end, the finite element simulations matched rather well with the experimental results. The second two types of simulations were related to the design of the control arm. Over twenty boundary conditions and loading conditions were used to evaluate the design of the control arm several years before this study started. We ran simulations on the two worst cast boundary and loading conditions to show the usefulness of the microstructure-property model.

One item to keep in mind. Often, the Mises stress is used by analysts to determine the location of failure. Discussed earlier was the how ductile damage progresses via the hydrostatic stress

divided by the Mises stress. This would argue that as the Mises stress has an inverse affect on the damage. However, in some cases (maybe many) the Mises stress will be the highest in locations that have the highest tensile hydrostatic stress. In these cases, the Mises stress will work; unfortunately, one does not know ahead of time if the Mises stress will be the primary location of failure; it depends on boundary conditions, part geometry, and microstructure/inclusion content. The microstructure-property model provides a safer design.

6.7.1. Validation Experiments/Analysis

In order to evaluate the predictive capability of the microstructure-property model within the context of finite element modeling, control arm experiments were designed to validate the model. Figure 6.37 shows the boundary conditions for the validation experiments of the control arm. Two different control arms, labeled later as Control Arm 1 and Control Arm 2, were cast that would ensure different levels of initial porosity. The microstructure/inclusion content was quantified by NDE using radiography and by optical imaging and analysis. The pertinent features of interest were the spatial location of the following entities:

1. porosity volume fraction,
2. pore size distribution,
3. pore nearest neighbor distances,
4. silicon particle volume fraction,
5. silicon particle size distribution,
6. silicon particle nearest neighbor distances, and
7. dendrite cell size.

Before analyzing the actual microstructure/inclusion content, future finite element analyses using the microstructure-property model may not have the benefit of having radiography and optical imaging. What should an analyst do in this case? To answer this question, several finite element analyses were performed with different initial microstructure/inclusion levels so that an analyst can see the relative differences in responses. Consequently, we ran several simulations in which we varied the silicon particle size distribution and the porosity volume fraction with homogeneous and random distributions throughout the control arm at levels of 0.001 and 0.0001.

Figures 6.38-6.41 illustrate the results of the damage distribution at first element failure. For ease of discussion Figure 6.42 shows five regions of importance on the control arm. Several conclusions can be drawn from the simulations. First, no difference in location or displacement at failure was observed between the cases homogeneous versus random distributions except for the case with an initially random porosity distribution with a level 0.001. All of the simulations showed first element failure near Region 3 in Figure 6.42. In the case with an initially random porosity at a level 0.001, Region 1 also experienced failure at the same elongation as Region 3. The trend is evident. As the porosity level increases, the location of failure can change to that region, especially if porosity gradients are observed. The comparable results of the homogeneous to random distributions can be attributed somewhat to the component geometry inducing stress concentrations and the boundary conditions applied. In the notch tensile tests described earlier in this chapter, the trend was similar. One might expect differences in damage locations with the random initializations if the stress concentrations from the component geometry were lessened.

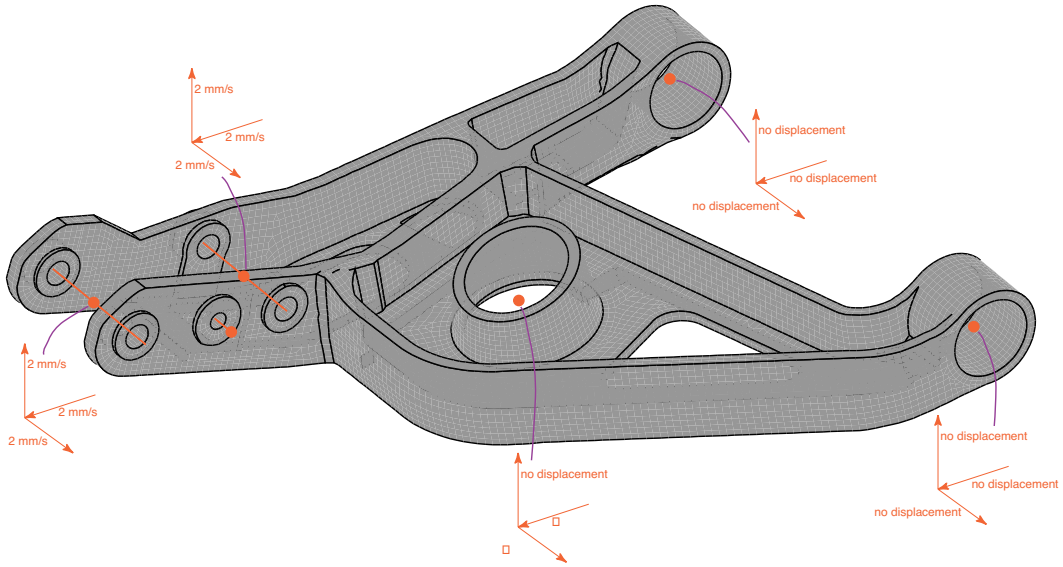

Figure 6.37. Boundary conditions for model validation tests.

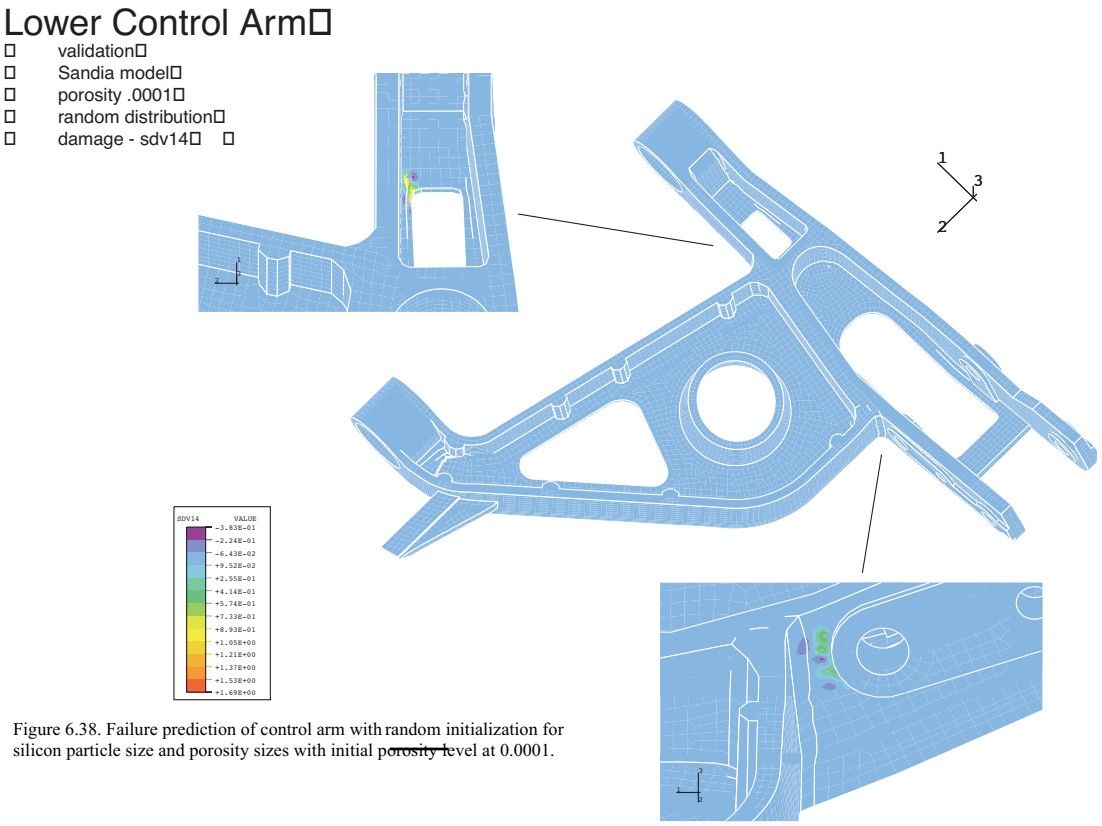

Figure 6.38. Failure prediction of control arm with random initialization for silicon particle size and porosity sizes with initial porosity level at 0.0001.

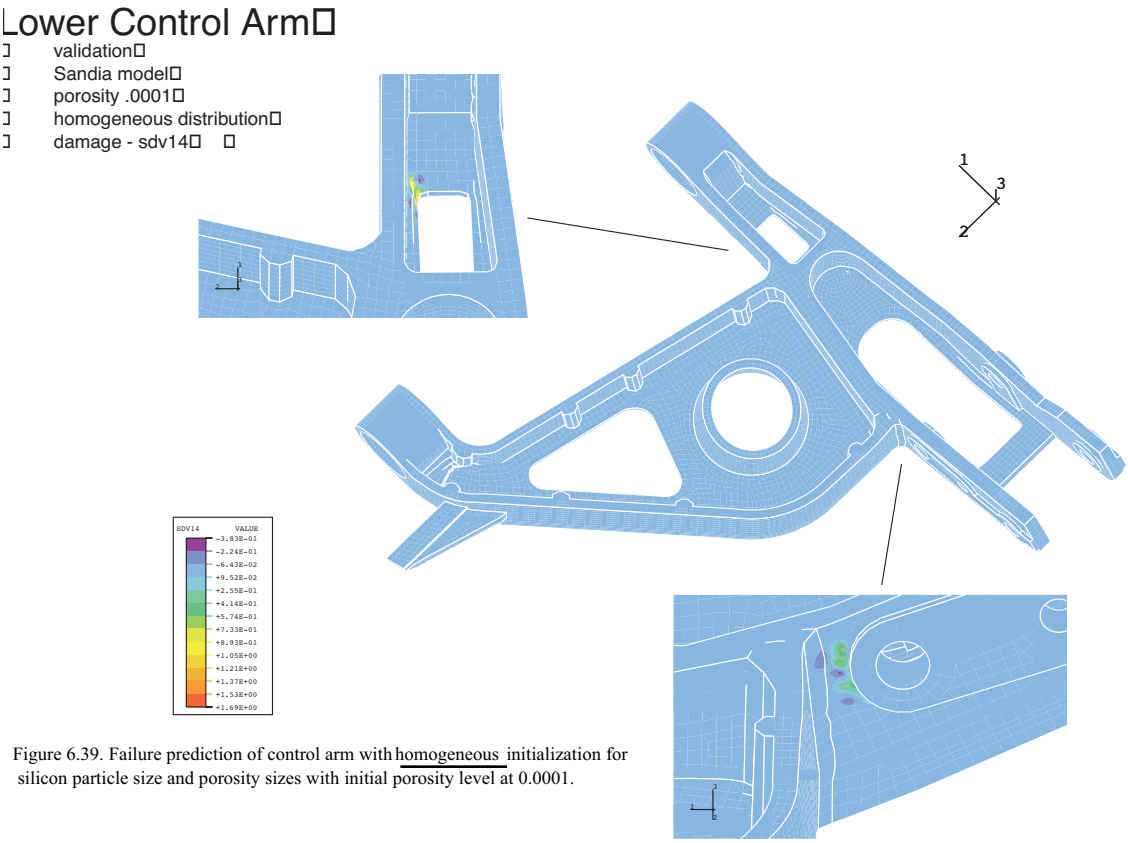

Figure 6.39. Failure prediction of control arm with homogeneous initialization for silicon particle size and porosity sizes with initial porosity level at 0.0001.

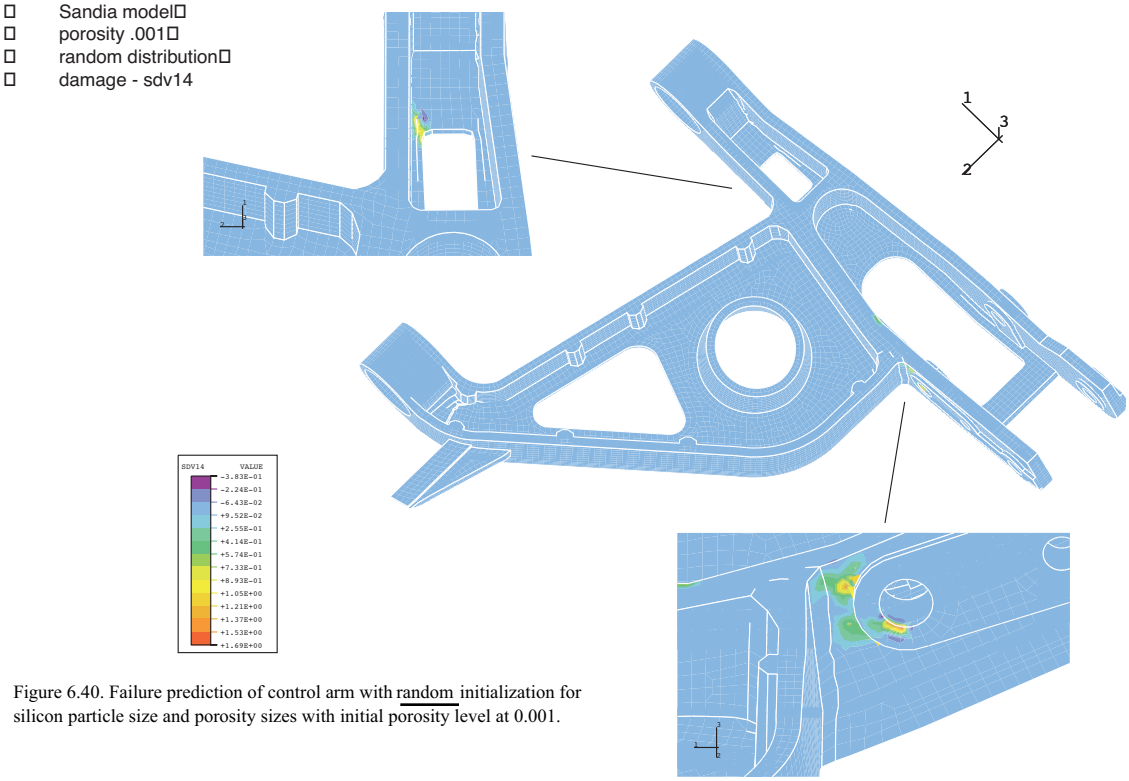

Figure 6.40. Failure prediction of control arm with random initialization for silicon particle size and porosity sizes with initial porosity level at 0.001.

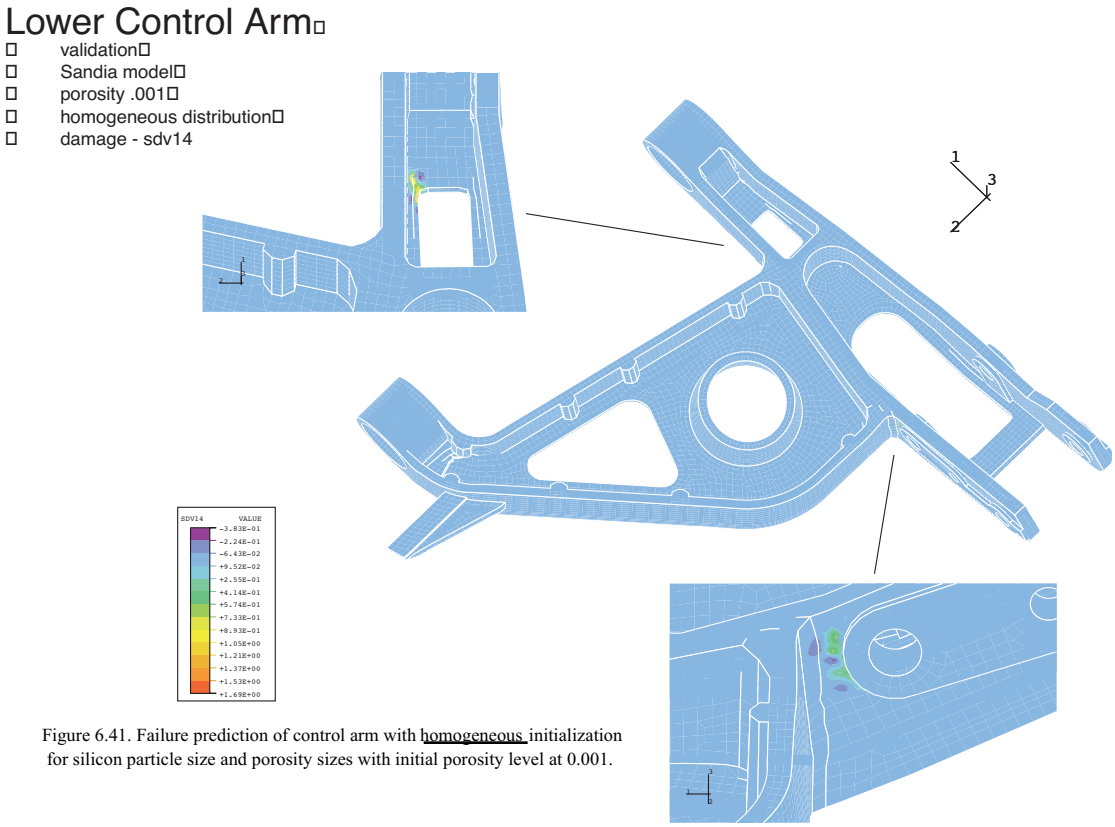

Figure 6.41. Failure prediction of control arm with homogeneous initialization for silicon particle size and porosity sizes with initial porosity level at 0.001.

Figure 6.42. Lower control arm casting showing five locations from which samples are extracted for metallography and computed tomography analyses.

The second conclusion one can draw from these simulations is related to the elongation at failure. Because we prescribed the velocity at the load points, we can compare the displacements at failure for the different simulations. In all four of the simulations, the final displacement for each component of the velocity vector was 0.24 mm. Hence, first element failure occurred at the same displacement regardless of the microstructure-inclusion initialization. From these simulations, it is apparent that the distribution of the porosity and silicon sizes and volume fractions have a second order influence on the results when compared to the boundary conditions and component geometry, at least with those examined here. This conclusion cannot be made for every part but is problem dependent as illustrated by the notch tensile tests/analyses. Furthermore, because the calculation with the initially random porosity at a level of 0.001 incurred two failed regions, one might strongly suspect that if the porosity level were higher that we would see Region 1 be the location of failure at the expense of Region 3.

In the next set of calculations we initialized the microstructure/inclusion content with data from radiography and optical imaging. Table 6.4 summarizes the microstructure/inclusion content for the five regions on the control arm as discussed above.

Table 6.4. Summary of results for control arm microstructure/inclusion content from optical images and radiography.

region	$\%V_v$	pore size (μm)	Nearest neighbor dist (μm)	3D pore size (μm)	Si particle Size (μm)	Si density (#/mm^2)	DCS (μm)
Control Arm 1 (optical imaging results)							
1	2.35	67.3	315	129	5.8	7088	50
2	0.30	38.9	669	54	4.8	7557	-
3	0.19	38.8	652	56	4.9	7738	-
4	0.19	45.0	402	66	4.6	6950	39
5	0.31	44.8	395	55	4.6	7659	42
Control Arm 1 (Radiography results)							
1	0.72	-	-	-	-	-	-
2	0.33	-	-	-	-	-	-
3	0.33	-	-	-	-	-	-
4	0.33	-	-	-	-	-	-
5	0.41	-	-	-	-	-	-
Control Arm 2 (optical imaging results)							
1	0.43	68.7	-	-	4.7	4251	-
2	-	-	-	-	5.2	5389	-
3	0.34	62.7	-	-	4.8	6318	-
4	-	-	-	-	-	-	-
5	0.32	57.8	-	-	4.7	6803	-
Control Arm 2 (Radiography results)							
1	0.48	-	-	-	-	-	-
2	0.33	-	-	-	-	-	-
3	0.33	-	-	-	-	-	-
4	0.33	-	-	-	-	-	-
5	0.33	-	-	-	-	-	-

The results in Table 6.4 are averages of the at least three measurements for two different control arms using optical imaging (Gokhale, 2000) and radiography (Dolan, 2000). Table 6.4 shows that the radiography and optical imaging results are very close for each of the control arms. One can see that the initial porosity volume fraction for Control Arm 1 is larger in certain regions than for Control Arm 2. Moreover, these initial values are larger than those used for the results shown in Figures 6.38-6.41.

Finite element simulations for Control Arms 1 and 2 were performed with the bounding limits of the microstructures that were averaged in Table 6.4. Table 6.5 shows the lower and upper limits of the quantitites measured by optical imaging in Regions 1 and 3. The other regions gave very similar results and hence were included as limiting bounds for the rest of the control arm. The simulation predictions for the failure locations were all near Region 1 but the previous calculations in which homogeneous or random distributions were used with a much lower initial void volume fraction incurred failure in Region 3. This was mainly due to the initial void volume fraction and not the assumption of the homogeneous or random distribution. The experiments for both control arms showed that they failed in Region 1. Figures 3.43-6.44 show the results for Control Arm 1 with the best and worst initial microstructure/inclusion content. Figures 3.45-6.46 show the results for Control Arm 2 with the best and worst initial microstructure/inclusion content. The exact location of failure initiation in the control arm was document by video during the testing. Figure 6.47 shows that Region 1 did indeed fail first followed by the fracture of that strut. The parallel strut then fractured as shown in Figure 6.47. This verified the predictability of the microstructure-property model.

Table 6.5. Summary of mininum/maximum optical image results for control arms microstructure/inclusion content.

	Region 1		Region 3		Other regions	
Control Arm 1						
attribute	min	max	min	max	min	max
%Vv	0.003	0.1118	0.0001	0.0032	0	0.00061
Pores size	34	118	25	63	0	67
Particle size	4.5	7.1	4.5	5.5	4.1	5.2
DCS	49	54	40	54	40	40
Control Arm 2						
%Vv	0.00085	0.005	0.00095	0.0056	0.00015	0.0069
Pores size	29	100	43	82	31	82
Particle size	4.6	4.9	4.4	5.2	4.5	5.2
DCS	49	54	40	54	40	40

For the calculations using the minimum values for the microstructure/inclusion content, the region of failure in both control arms was Region 1. However, in Control Arm 1, Region 3 failed shortly

after Region 1. For the maximum values, two different results arose for the different control arms. The calculation for Control Arm 1 showed failure in Region 3, but the calculation for Control Arm 2 showed failure in Region 1 for the maximum values. These trends are similar to the results discussed earlier in which the initial void volume fraction appears to drive final failure up to a point. When the void volume fraction is low enough, final fracture is dependent upon silicon.

We also took specimens from these different regions and tested them under monotonic uniaxial tension (Table 6.6). Note that the stress state experienced by the control arm under the boundary conditions considered was not uniaxial but was a multiaxial stress state. What is clear in these data is the ambiguity in the results. First, the stress state in the uniaxial test specimens is not the same as in the control arm. Second, these data give a wide range of scatter that makes it difficult to assess the final elongations at failure microstructure-property relations. Third, it is not really clear which control arm is "better" in terms of structural performance based on these data. If Region 1 were the first location of failure, one would not expect that from this data. Since Regions 3 and 4 have the lowest elongations at failure, a designer/analyst would be tempted to pick those locations to redesign. The moral of this story is that taking uniaxial tensile data from specimens from a structural component could give erroneous and, at best, tenuous information about designing a control arm.

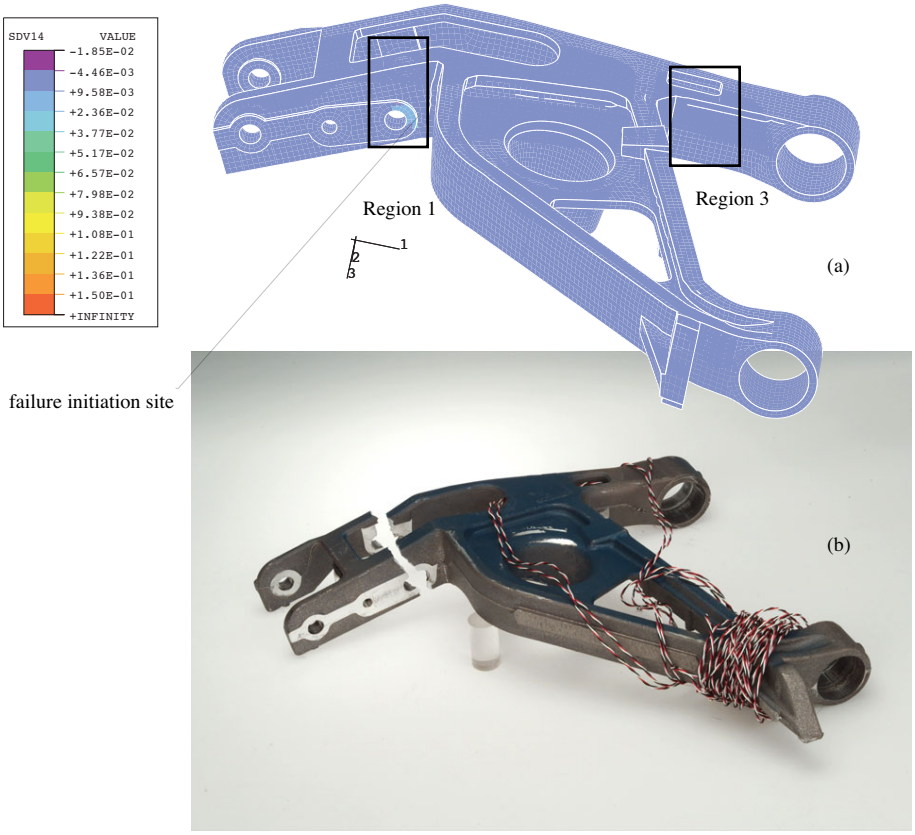

Figure 6.43 Comparison of microstructure-property model failure prediction (damage=DSV14) with experiment for Control Arm 1. The best case microstructure/inclusion content was assumed in the calculation.

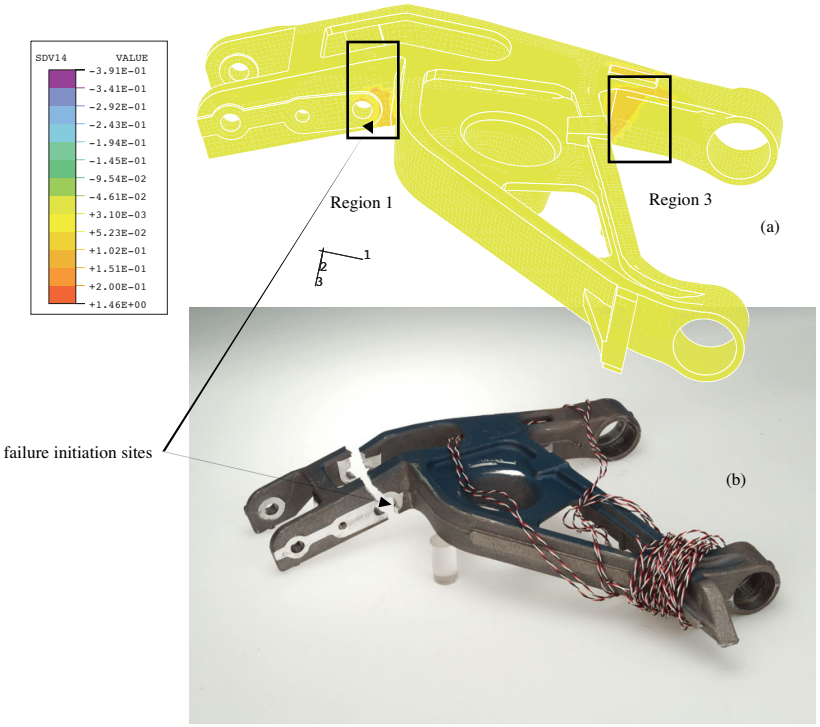

Figure 6.44 Comparison of microstructure-property model failure prediction (damage=SDV14) with experiment for Control Arm 1. The worst case microstructure/inclusion content was assumed in the calculation.

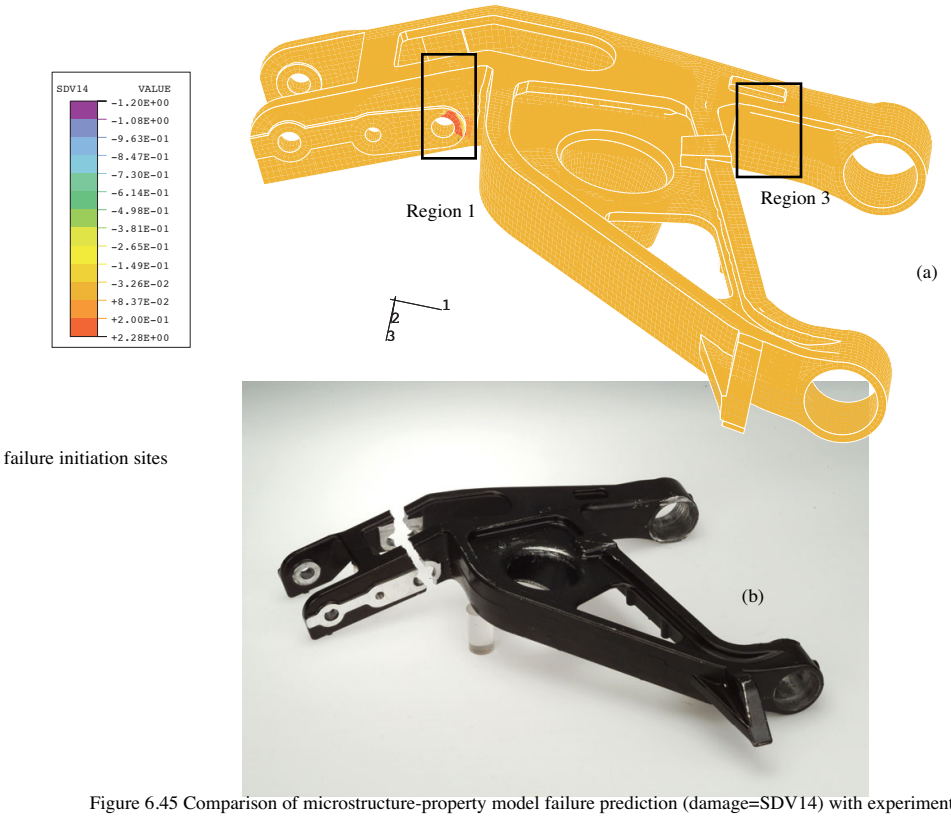

Figure 6.45 Comparison of microstructure-property model failure prediction (damage=SDV14) with experiment for Control Arm 2. The best case microstructure/inclusion content was assumed in the calculation.

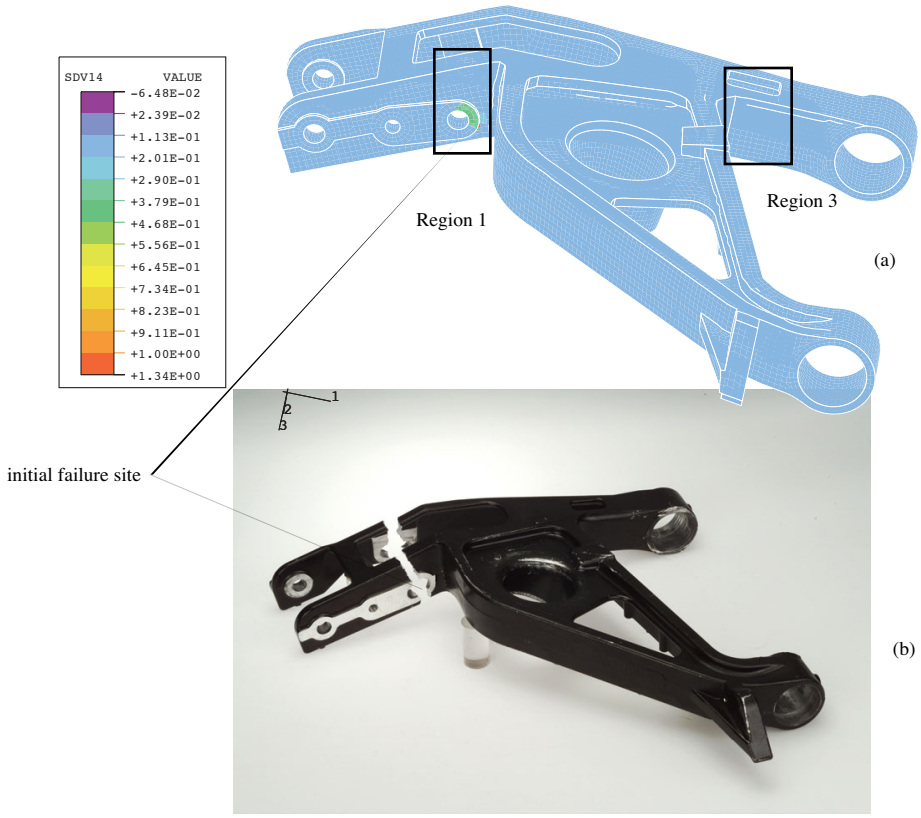

Figure 6.46 Comparison of microstructure-property model failure prediction (damage=SDV14) with experiment for Control Arm 2. The worst case microstructure/inclusion content was assumed in the calculation.

Table 6.6. Summary of % strains at failure taken from uniaxial tension experiments in which specimens within the five regions of the control arm were extracted.

Region	*Control Arm 1 (min-max)*	*Control Arm 2 (min-max)*
1	6.3-8.6	6.1-9.7
2	1.6-10.1	6.9-9.3
3	4.7-7.1	10.8-23.4
4	4.0-8.6	4.2-8.5
5	6.3-16.1	9.8-16.2

6.7.2. 0.8 g Panic Brake Analysis

One of the worst case design scenarios comes from the 0.8 g panic brake condition. Boundary and loading conditions were applied to the control arm, as shown in Figure 6.48, in a finite element simulation that used the microstructure-property model. Figure 6.49 shows the Mises stress contours at failure, and Figure 6.50 shows the damage level contours at failure. Designers sometimes use the Mises stress to determine the failure locations. This can be dangerous since the final location of failure can be different than the highest Mises stress. Voids grow and

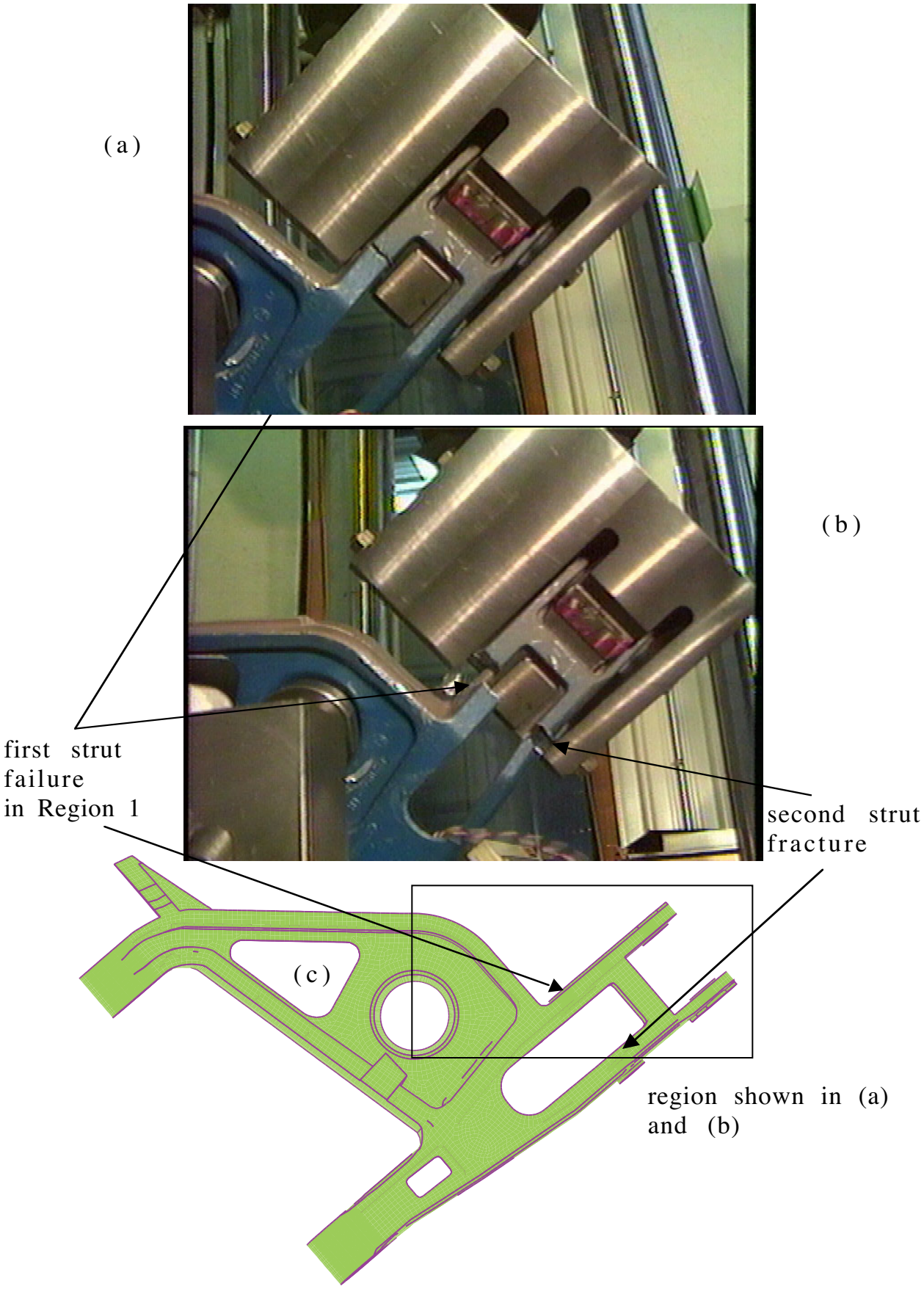

Figure 6.47. Experiment control arm test showing that (a) the strut with Region 1 failed before the(b) other strut as illustrated in (c) the diagram.

coalesce where the highest stress triaxiality occurs, which is defined as the hydrostatic stress over the Mises stress. Hence, hydrostatic stress is more of an indicator of failure than the Mises stress. In notch tensile specimens, the location of final failure starts at the center of the notch where the triaxiality is the highest. The same is true in these control arm simulations. Figure 6.49 shows several locations where the Mises stress is the highest, but Figure 6.50 shows one particular region where first failure will occur. The design can be optimized better if damage is used instead of the Mises stress. Although the Mises stress is high near the first failure region, many times it may not be, so Mises stress can be a false indicator of failure locations.

6.7.3. Pothole Strike Analysis

The pothole strike is another worst case loading/boundary condition used for design of the control arm. Boundary and loading conditions for the pothole strike were applied to the control arm, as shown in Figure 6.51, in a finite element simulation that used the microstructure-property model. Figure 6.52 shows the Mises stress contours at failure, and Figure 6.53 shows the damage level contours at failure. Although the boundary/loading conditions were different than the 0.8 g panic brake analysis, the results were very similar. In fact, the first failure location was observed in the same location as that from the 0.8 g panic brake analysis. Here again, the Mises stress shows peak values in several regions, but the actual failure occurs in one local region.

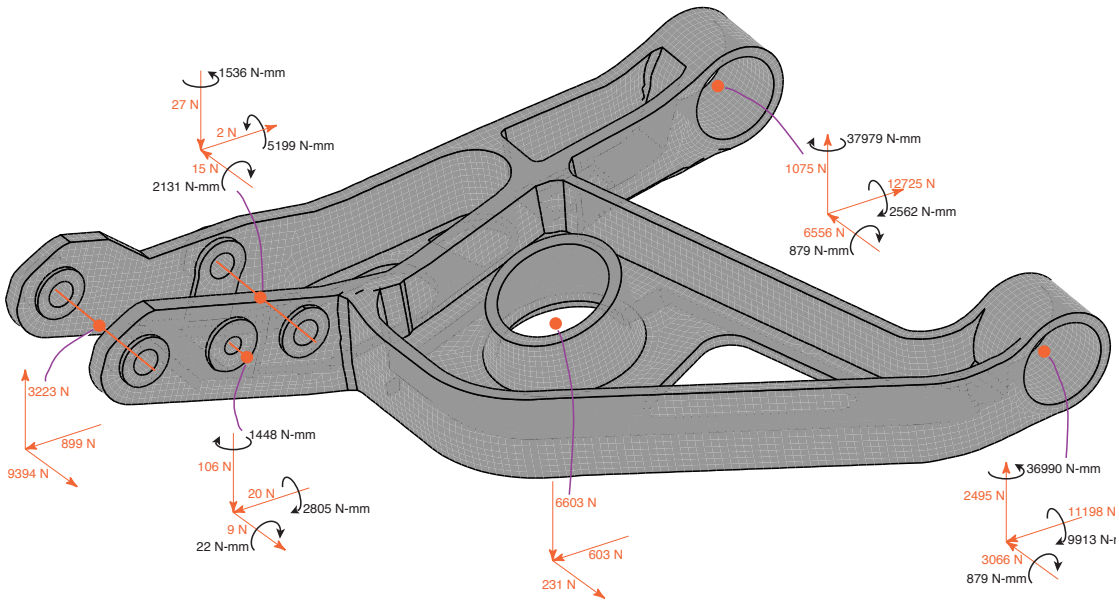

Figure 6.48. Boundary conditions for 0.8g panic brake analysis.

6.7.4. Optimization of Control Arm

Based on the simulations using the microstructure-property model we optimized the control arm using the pothole strike/0.8 g panic brake analyses boundary/loading conditions. Here, we define "optimized" to mean that we reduced the total weight of the control arm by reducing mass from regions that were overdesigned. Alternatively, we add mass to regions where the damage was the highest. Overall a weight reduction of approximately 26% was achieved. Interestingly, in the original design much of the control arm was still in the elastic region when failure was first observed in the regions shown in Figures 6.50 and 6.53. Hence, mass in these regions was reduced just to allow the component to uniformly reach yield under the boundary/loading conditions used here. Figure 6.54 shows the regions in which mass was reduced according to Table 6.7, and Figure 6.55 shows the lightweight design. Hence, the weight was reduced from 2.92 kg to 2.18 kg.

Table 6.7 Summary of regions with their corresponding mass on control arm.

Region	*Initial mass (kg)*	*Final mass (kg)*
1	0.31951	0.22952
2	0.070447	0.055449
3	0.10408	0.078174
4	0.10408	0.073174
5	0.41132	0.25452
6	0.13635	0.10226
7	0.49859	0.36178
8	0.31860	0.23907
9	0.26452	0.19771
10	0.022270	0.022270
11	0.050904	0.065903
12	0.0090900	0.0086355
13	0.20271	0.19134
14	0.12726	0.095445
15	0.12726	0.095445
16	0.020453	0.015453
17	0.039996	0.029997
18	0.0095445	0.0000
19	0.099990	0.055994
20	0.030906	0.0000
Total	2.922	2.177

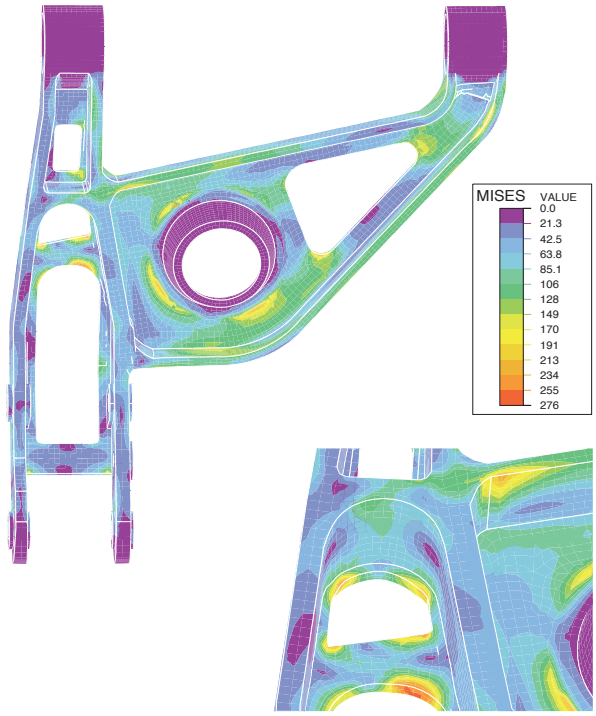

Figure 6.49. Mises stress contours for 0.8 g panic brake using microstructure-property model.

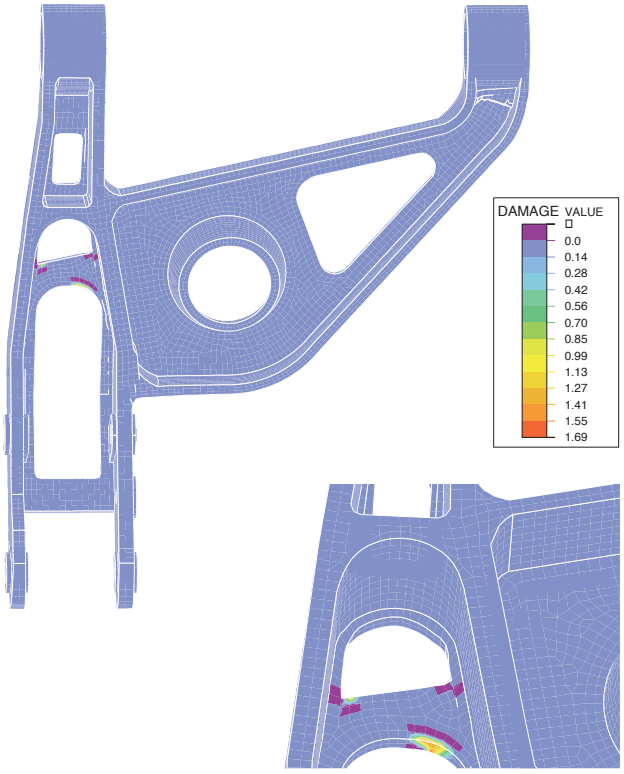

Figure 6.50. Damage contours for 0.8 g panic brake using microstructure-property model.

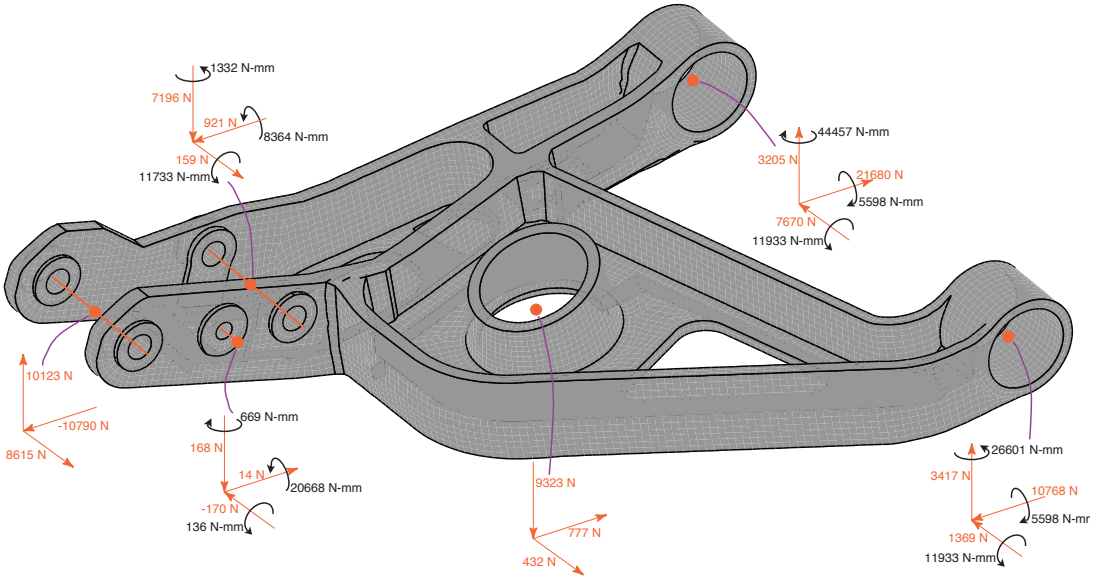

Figure 6.51. Boundary conditions for pothole strike.

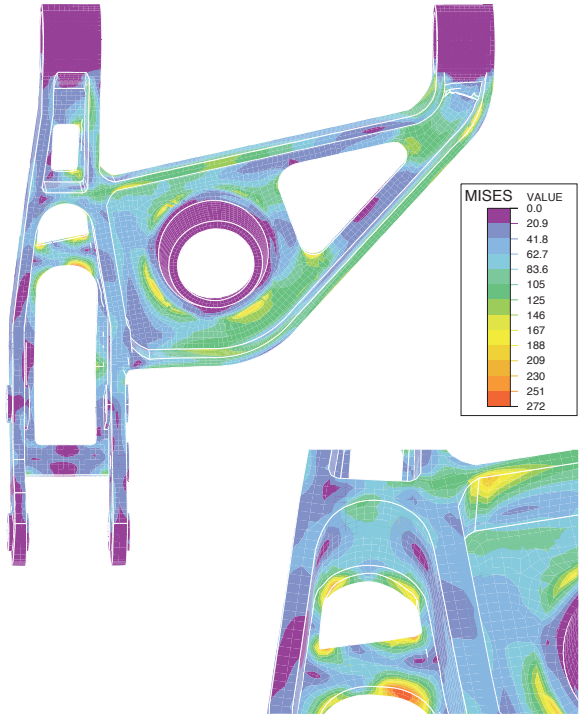

Figure 6.52. Mises stress contours for pothole strike using microstructure-property model.

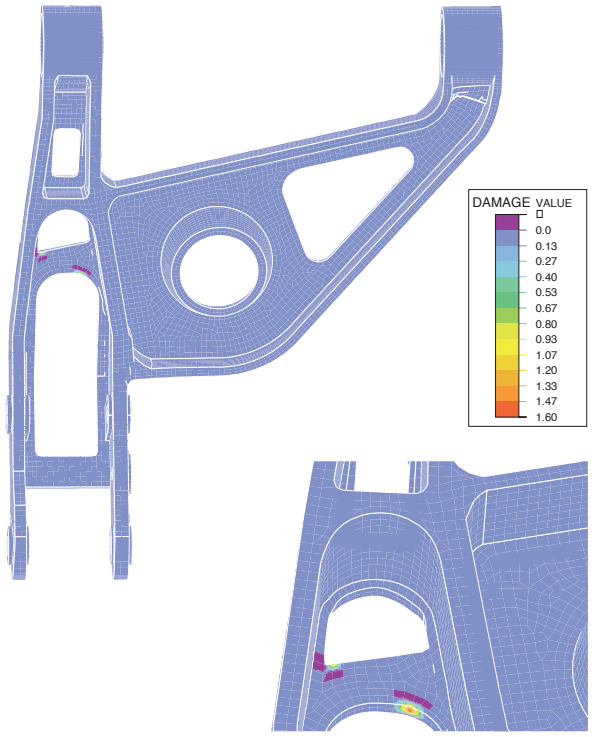

Figure 6.53. Damage contours for pothole strike using microstructure-property model.

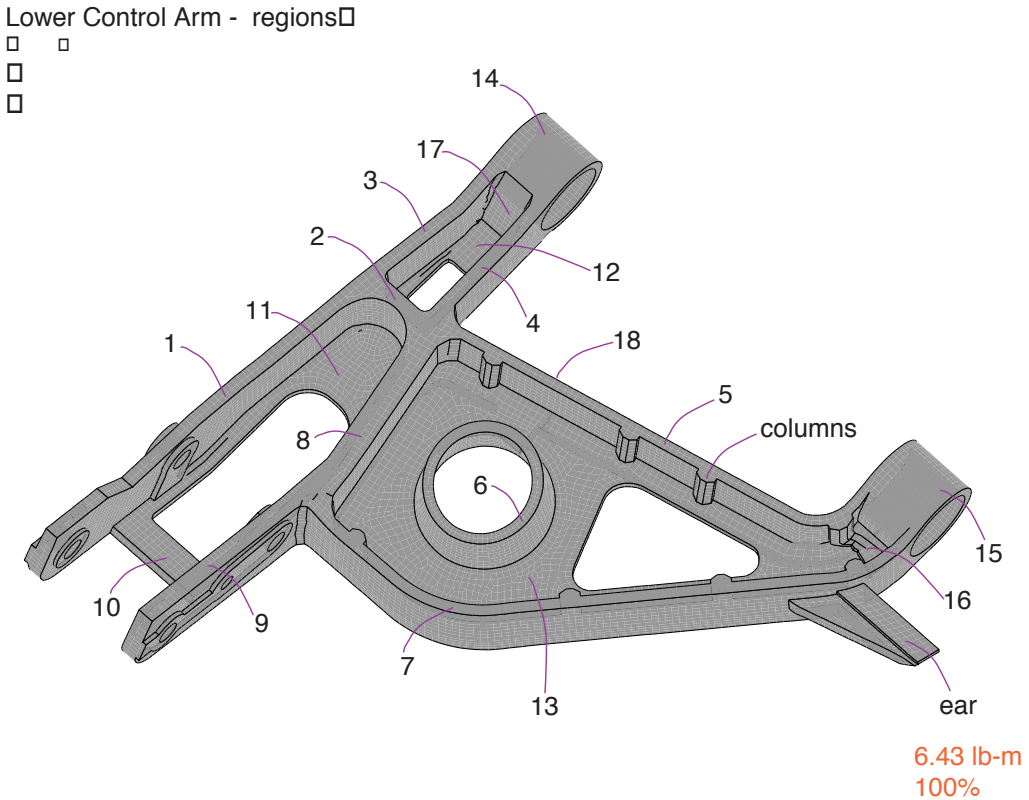

Figure 6.54. Control arm regions designated for reduced weight opportunities.

Figure 6.55. Picture of optimized, lightweight design.

Figure 6.56 shows a load-displacement comparison of control arm 1, control arm 2, and the new lightweight design. In Figure 6.56, one can examine that two major peaks arise for each specimen. These two peaks correlate with the fracture of the two struts on the control arms as observed in Figure 6.47. The first fracture site corresponds to Region 1, and the second site corresponds to the strut opposite of Region 1. Hence, for a designer the first peak is most important since an elastic design is assumed here. We should note that all of the control arms failed in the same Region 1. Several replicates were performed on each test showing less than 10% difference on the peak loads at first damage initiation. On average, Control Arm 1 exhibited a design load of 48 kN (10850 lbs); Control Arm 2 exhibited a design load of 45 kN (10200 lbs); and the lightweight design exhibited a design load of 70 kN (15700 lbs), approximately a 40% increase in load-bearing capacity!

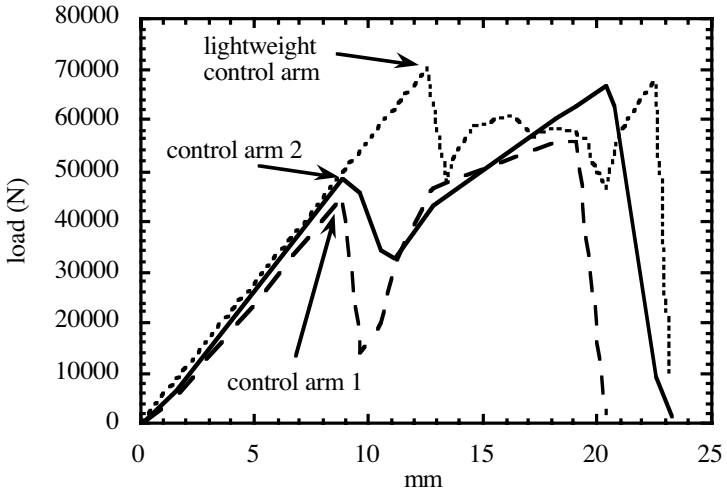

Figure 6.56. Load-displacement comparison of different control arms.

This page intentionally blank

7. SUMMARY

Previous material models used in finite element analyses for elastic and plastic responses cannot capture changing history effects from temperature, strain rate, damage states, and deformation paths. For example, power law forms for plasticity are limited in this scope. Presented in this work is a microstructure-property material model that has been implemented and used in finite element codes that reflects microstructural behavior so that material history effects and damage progression are captured, thus enabling an accurate, predictive tool. A multi-length scale approach, from atoms to large structural scale analyses, to relate the key microstructural features to the mechanical properties.

The specific inputs to microstructure-property model include the following:
(1) silicon volume fraction
(2) silicon particle size distribution
(3) pore volume fraction
(4) pore size distribution
(5) pore nearest neighbor distance
(6) dendrite cell size distribution

The material constants were determined from:
(1) varying strain rate and temperature compression tests
(2) tension tests
(3) torsion tests

The validation tests include the following:
(1) notch tensile tests
(2) Bauschinger effect tests
(3) control arm component tests

The microstructure-property model is capable of capturing the same trends for other castings, such as magnesium or iron, for forgings, and for any wrought material because the mechanisms are similar to this A356 aluminum alloy. Experiments would be needed to determine the material constants. If some experiments are not available, the microstructure-property model can still be used without that particular feature. In fact, the microstructure-property model can be reduced all the way back to just an elastic model if so desired without loss of generality. The model was validated by component scale experiments and was used to optimize a part. Moreover, the microstructure-property model can be used for more just design purposes. It can be used for crashworthiness and impact analyses.

List of Papers as a Result of This Monotonic Loading Study:

18. Gall, K., Horstemeyer, M.F., Van Schilfgaarde, M., and Baskes, M.I., "Atomistic Simulations on the Tensile Debonding of an Aluminum-Silicon Interface," accepted Journal of Mech. Phys. Solids

17. Horstemeyer, M. F. and Gokhale, A.M., "A Void Nucleation Model for Ductile Materials," International Journal of Solids and Structures, Vol. 36, pp. 5029-5055, 1999.

16. Dighe, M.D., Gokhale, A.M., and Horstemeyer, M. F., "Effect of Temperature on Silicon Particle Damage in Cast Microstructure of A356 Alloy," Metallurgical and Materials Transactions, 1997, Vol 29a, pp. 905-908, 1998.

15. Horstemeyer, M.F., "Damage Influence on the Bauschinger Effect of a Cast A356 Aluminum Alloy," Scripta Materialia, Vol. 39, No. 11, pp. 1491-1495, 1998.

14. Horstemeyer, M.F. and Ramaswamy, S., "On Factors Affecting Localization and Void Growth in Ductile Metals: A Parametric Study," Int. J. Damage Mech., Vol. 9, pp. 6-28, 2000.

13. Dighe, M.D., Gokhale, A.M., and Horstemeyer, M.F., "Second Phase Cracking and Debonding Observations in the Fatigue Damage Evolution of a Cast Al-Si-Mg Alloy," accepted in Acta Met.

12. Dighe, M.D., Gokhale, A.M., Horstemeyer, M.F., and Mosher, D.A., "Observations of Strain Rate Effects on Damage Evolution in a Cast Al-Si-Mg Base Alloy," accepted in Acta Met.

11. Horstemeyer, M.F., Matalanis, M.M., Sieber, A.M., and Botos, M.L., "Micromechanical Finite Element Calculations of Temperature and Void Configuration Effects on Void Growth and Coalescence," accepted in IJP.

10. Horstemeyer, M.F., Gall, K., Dolan, K., Haskins, J., Gokhale, A.M., and Dighe, M.D., "Numerical, Experimental, and Image Analyses of Damage Progression in Cast A356 Aluminum Notch Tensile Bars," submitted to Royal London Soc.

9. Gall, K. and Horstemeyer, M.F., Integration of Basic Materials research into the Design of Cast Components by a Multi-Scale Methodology," accepted JEMT

8. Horstemeyer, M.F., Negrete, M., and Ramaswamy, S., "On Factors Affecting Void-Crack Nucleation in Ductile Metals: A Parametric Study," in progress (Scripta Met)

7. Horstemeyer, M.F. and Degner, B.W., "Finite Element Damage Analysis Using a Microstructure-Property Material Model for Automotive Components," in progress (Int. Journal of Crashworthiness)

6. Waters, A., Martz, H., Dolan, K., Horstemeyer, M.F., Rikard, D., and Green, R., "Characterization of Damage Evolution in an AM60 Magnesium Alloy by Computed Tomography," Ninth International Symposium on Nondestructive Characterization of Materials, Darling Harbours, Sydney, Australia, June 28 - July 2, 1999.

5. Horstemeyer, M.F. and Mosher, D.A., "Damage Progression in Ductile Metals," International Conf. On Plasticity, ed. A. Khan, Cancun, Mexico 1999.

4. Horstemeyer, M.F., "Multi-Scale Analysis of Monotonically Loaded A356 Cast Aluminum Alloy," AFS, St. Louis, 1999.

3. Horstemeyer, M.F. and Mosher, D.A., "High Strain Rate Effects on a Cast A356 Aluminum Alloy," TMS, Rosemont, IL, 1998.

2. Horstemeyer, M. F., "Mechanical Property Characterization of A356 Cast Aluminum Alloy Under Monotonic Loads," American Foundry Society, 5/1998.

1. Horstemeyer, M. F., Jin, P.S., "Damage Modeling of A356 Cast Aluminum," Proc. of ISATA Conference, ed. J. T. Solimon, 97PNM009 Florence, Italy, 1997.

This page intentionally blank

8. REFERENCES

Al-Ostaz, A. and Jasiuk, I., "Crack Initiation and Propagation in Materials with Randomly Distributed Holes," *Engin. Fract. Mech*., Vol . 58, No.5-6, p. 395, (1997).

Argon, A.S., Im, J., and Safoglu, R., "Cavity Formation from Inclusions in Ductile Fracture," *Metall. Trans.,* Vol. 6A, pp. 825-837, (1975).

Asaro, R.J., "Geometrical Effects in the Inhomogeneous Deformation of Ductile Single Crystals," *Acta Metall*., Vol. 27, p. 445, (1979).

Ashby, M.F., "Work Hardening of Dispersion-Hardened Crystals," *Phil. Mag*., Vol 14, pp. 1157-1178, (1966).

Avrami, M., "Kinetics of Phase Change," *J. Chem. Phys*., Vol. 7, pp. 1103-1112, (1939)

Baddley, A.J., Gundersen, H.J.G., and Cruz Orive, L.M., "Estimation of Surface Area From Vertical Sections," *Journal of Microscopy*, Vol. 142, pp. 259-276, (1986).

Bammann, D.J., "Modeling the Large Strain-High Temperature Response of Metals in Modeling and Control of Casting and Welding Processes IV," eds. Giamei, A.F. and Abbaschian, G.J. *TMS Publications*, Warrendale, PA, (1988).

Bammann, D.J. and Aifantis, E.C., "A Damage Model for Ductile Metals," *Nuclear Engineering and Design*, Vol. 116, pp. 355-362, (1989).

Bammann, D.J., Chiesa, M.L. and Johnson, G.C., "Modeling Large Deformation and Failure in Manufacturing Processes," *The. App. Mech.*, eds. Tatsumi, Wannabe, and Kambe, Elsevier Science, pp. 259-276 (1996).

Bammann, D. J., Chiesa, M. L., Horstemeyer, M. F. and Weingarten, L. I., "Failure in Ductile Materials Using Finite Element Methods," *Structural Crashworthiness and Failure*, eds. N. Jones and T. Weirzbicki, Elsevier Applied Science, pp. 1-52, (1993).

Bammann, D.J., "Modeling Temperature and Strain Rate Dependent Large Deformations of Metals," *Appl. Mech. Rev*., Vol. 1, pp. 312-318, (1990).

Bammann, D.J., Chiesa, M.L., and Johnson, G.C., "A State Variable Damage Model for Temperature and Strain Rate Dependent Metals" *Contitutive laws: theory, experiments, and numerical implementation*, eds. A.M. Rajendran and R.C. Batra, CIMNE, Barcelona, pp. 84-97, (1995).

Bammann, D.J., Chiesa, M.L., Johnson, G.C., "Modeling Large Deformation and Failure in Manufacturing Processes," *Theoretical and Applied Mechanics*, eds. T. Tatsumi, E. Wannabe, and T. Kambe, Elsevier Science, pp. 359-376, (1996).

Bandstra, J.P., Goto, D.M., and Koss, D.A., "Ductile Failure as a Result of a Void Sheet Instability: Experiment and Computational Modeling*," Matls. Sci. Engin. A, Structural Matls. Props. Micro. Proc.*, Vol. 249, No.1, p. 46, (1998).

Barbee, T.W., Seaman, L., Crewdson, R., and Curran, D., "Dynamic Fracture Criteria for Ductile and Brittle Metals," *J. Materials, JMLSA*, Vol. 7, No. 3, pp. 393-401, (1972).

Barenblatt, G. I., "Mathematical Theory of Equilibrium Cracks," *Adv. Appl. Mech.* Vol. 7, pp. 56-129, (1962).

Bartlett, A., and Evans, A.G., "The Effect of Reaction Products on the Fracture Resistance of a Metal/Ceramic Interface," *Acta. Metall. Mater,* Vol. 41, pp. 497-504, (1993).

Baskes, M.I. "Modified Embedded-Atom Potentials for Cubic Materials and Impurities," *Phys. Rev. B* Vol. 46, pp. 2727-2742, (1992).

Baskes, M.I., Angelo, J.E., and Bison, C.L., "Atomistic Calculations of Composite Interfaces," *Model. Simul. Mater. Sci. Eng*. Vol. 2, pp. 505-518, (1994).

Becker, R.C., and Needleman, A., "Effect of Yield Surface Curvature on Necking and Failure in Porous Plastic Solids," *ASME J. Applied Mech*., Vol. 53, pp. 491-499, (1986).

Becker, R.C., "The effect of porosity distribution on failure," *J. Mech. Phys. Solids*, Vol. 35, pp. 577-599 (1987).

Benson, D.J., "An Analysis of Void Distribution Effects on the Dynamic Growth and Coalescence of Voids in Ductile Metals," *J. Mech. Phys. Solids*, Vol. 41, No. 8, p. 1285, (1993).

Benson, D.J., "The Effect of Void Cluster Size on Ductile Fracture," *Int. J. Plasicity*, Vol. 11, No. 5, pp. 571-582, (1995).

Bigoni, D., Ortiz, M., and Needleman, A., "Effect of Interfacial Compliance on Bifurcation of a Layer Bonded to a Substrate," *Int. J. Solids Struc.* Vol. 34, pp. 4305-4326, (1997).

Boone, T.J., Wawrzynek, P.A., and Ingraffea, A.R., "Imulation of the Fracture Process in Rock with Application to Hydrofracturing," *Int. J. Rock Mech. Min. Sci. & Geomech. Abstr.,* Vol. 23, pp. 255-265, (1986).

Bourcier, R. and Koss, D., "Ductile fracture under multiaxial stress states between pairs of holes," Advances in Fracture Research, Vol. 1, pp. 187-194 (1981).

Box, G.E., Hunter, W.G., Hunter, J.S., *Statistics for Experimenters*, John Wiley and Sons, Inc., (1978).

Bray, J.W., "Aluminum Mill and Engineered Wrought Products," *ASM Handbook*, ASM International, Vol. 2, pp. 29-62, (1990).

Brenner, D.W., "Chemical Dynamics and Bond-Order Potentials," *MRS Bulletin, Feb.,* pp. 36-41, (1996).

Brickstad, B., "A Viscoplastic Analysis of Rapid Crack Propagation Experiments in Steel," *J. Mech. Phys. of Solids*, Vol. 31, pp. 307-327, (1983).

Bridgman, P.W., "Compressibility of Thirty Metals as a Function of Pressure and Temperature," *Proc. of the American Academy of Arts and Sciences*, Vol. 58, No. 5, pp. 164-242, (1923).

Briottet, L., Klocker, H., and Montheillet, F., "Damage in a Viscoplastic Material Part 1: Cavity Growth," *Int. J. Plasticity*, Vol. 12, No. 4, pp. 481-505, (1996).

Broek, D., "The role of Inclusions in Ductile Fracture and Fracture Toughness," *Eng. Frac. Mech.* Vol. 5, pp. 55-66, (1973).

Budiansky, B.J., "Composite Materials," Vol. 4, p. 4028, (1970).

Budiansky, B.J., Hutchinson, J.W., and Slutsky, S., "Void Growth and Collapse in Viscous Solids," *Mechanics of Solids: The Rodney Hill 60th Anniversary Volume*,, eds. H.G. Hopkins and M.J. Sewell, Pergamon Press, Oxford, pp. 13-45, (1982).

Caceres, C.H., Davidson, C.J., and Griffiths, J.R., "The Deformation and Fracture Behavior of an Al-Si-Mg Casting Alloy," *Mat. Sci. Eng.*, Vol. A197, pp. 171-179, (1995).

Caceres, C.H., Griffiths, J.R., and Reiner, P., "The Influence of Microstructure on the Bauschinger Effect in an Al-Si-Mg Casting Alloy," *Acta Mater*., Vol. 44, No. 1, pp.15-23, (1996).

Camacho, G.T., and Ortiz, M., "Computational Modeling of Impact Damage in Brittle Materials," *Int. J. Solid. Struct.* Vol. 33, pp. 2899-2938, (1996).

Castaneda, P.P., and Zaidman, M., "Constitutive Models for Porous Materials with Evolving Microstructure," *J. Mech. Phys. Solids*, Vol. 42, pp. 1459-1497, (1994).

Chan, K.S., "The Constitutive Representation of High Temperature Creep Damage," *Int. J. Plast*, Vol. 4, pp. 355-370, (1988).

Chen, E.P., Kipp, M.E., and Grady, D.E., "A Strain-Rate Sensitive Rock Fragmentation Model," *Mechanics of Oil Shale*, eds. K.P. Chong, J. Ward Smith, Elsevier Applied Science Publishers, NY., pp. 423-456, (1984).

Closset, B., and Gruzleski, J.E., "Mechanical Properties of A356.0 Alloys Modified with Pure Strontium," *AFS Trans.,* Vol. 90, pp. 453-464, (1982).

Cocks, A.C.F., "Inelastic Deformation of Porous Materials," *J. Mech. Phys*. *Solids*, Vol. 37, No. 6, pp. 693-715, (1989).

Cocks, A.C.F., and Ashby, M.F., "Intergranular Fracture During Power Law Creep Under Multixial Stresses," *J. Metal Science*, pp. 395-402, (1980).

Cocks, A.C.F., and Ashby, M.F., "On Creep Fracture by Void Growth," *Prog. Mater. Sci.* Vol. 27, pp. 189-244, (1982).

Coleman, B.D., and Gurtin, M.E., "Thermodynamics with Internal State Variables," *J. Chem. Phys*., Vol. 47, p. 597, (1967).

Comninou, M., "An Overview of Interface Crack," *Eng. Frac. Mech*. Vol. 37, pp. 197-208, (1990).

Cottrell, A.H., *Fracture*, eds. B.L. Averbach, D.R., Felbeck, G.T. Hahn, and D.A. Thomas, Technology Press of MIT and John Wiley, New York, (1959).

Cox, T.B., and Low, J.R., "An Investigation of the Plastic Fracture of AISI 4340 and 18 Nickel-200 Grade Maraging Steels," *Metall. Trans.* Vol. 5A, pp. 1457-1470, (1974).

Cox, T.B., and Low, J.R. Jr., *Metall. Trans*., Vol. 5, pp. 1457-1470, (1974).

Cuitino, A., and Ortiz, M., "A Material Independent Method for Extending Stress Update Algorithms from Small Strain Plasticity to Finite Strain Plasticity with Multiplicative Kinematics," *Engineering Computations*, Vol. 9, p. 437, (1992).

Daniel, I. M., and Ishai, O., *Engineering Mechanics of Composite Materials,* Oxford University Press, New York, (1994).

Davison, L., Stevens, A.L., and Kipp, M.E., "Theory of Spall Damage Accumulation in Ductile Metals," *J. Mech. Phys. Solids*, Vol. 25, pp. 11-28, (1977).

Daw, M.S., and Baskes, M.I., "Embedded-Atom Method: Derivation and Application to Impurities and Other Defects in Metals, *Phys. Rev. B* Vol. 29, pp. 6443-6453, (1984).

Daw, M. S., Foiles, S. M., and Baskes, M.I., "The Embedded-Atom Method: A Review of Theory and Applications," *Materials Science Reports, A Review Journal* 9, pp. 251-287, (1993).

De Boer, R., and Dresenkamp, H.T., "Constitutive Equations for Concrete in Failure State," *J. Eng. Mech*., Vol. 115, No. 8, pp. 1591-1608, (1989).

DeHoff, R.T., "The Quantitative Estimation of Mean Surface Curvature, Trans" *Met. Soc. AIME*, Vol. 239, pp. 617-623, (1967).

Desai, C.S., and Siriwardane, H.J., *Constitutive Laws for Engineering Materials with Emphasis on Geologic Materials*, Prentice-Hall, Inc., Englewood Cliffs, NJ, (1984).

Desai, C. S., Somasundaram, S., and Frantziskonis, G., "A Heirarchical Approach for Constitutive Modeling of Geologic Materials," *Int. J. Num. Methods Eng*., Vol. 10, pp. 225-257, (1986).

Dighe, M.D., and Gokhale, A.M., "Relationship between Microstructural Extremum and Fracture Path in a Cast Al-Si-Mg alloy," *Scr. Mater.* Vol. 37, pp. 1435-1440, (1997).

Dighe, M.D., Gokhale, A.M., Horstemeyer, M.F., "Quantitative Characterization of Stress State and Microstructure on the Fracture Path of an Al-Si-Mg Alloy," to be published.

Dorris, J. F., and Nemat-Nasser, S., "A Plasticity Model for Flow of Granular Materials Under Triaxial Stress States," *Int. J. Solids Structures*, Vol. 18, No. 6, pp. 497-531, (1980).

Drucker, D.C., "Stress-Strain Relations for Strain Hardening Materials: Discussion and Proposed Experiments," *Proc. Symposia Appl. Math*., Vol. 1, p. 181, (1949).

Dugdale, D.S., "Yielding of Steel Sheets Containing Slits," *J. Mech. Phys. Solids* Vol. 8, pp. 100-104, (1960).

Edelman, F., *On the Coincidence of Plasticity Solutions Obtained with Incremental and Deformation Theories*, Ph.D. thesis, Brown University, (1950).

Eftis, J., and Nemes, J.A., "Evolution Equation for the Void Volume Growth Rate in a Viscoplastic-Damage Constitutive Model," *Int. J. Plasticity*, Vol. 7, pp. 275-293, (1991).

Eftis, J., Nemes, J.A., and Randles, P.W., "Viscoplastic Analysis of Plate-Impact Spallation," *Int. J. Plast.,* Vol. 7, pp. 15-39, (1991).

Embury, J.D., "Structural Aspects of the Bauschinger Effect," *Materials Forum*, Vol.10, pp. 27-32, (1987).

Embury, J.D., *Mater. Forum*., Vol. 10, pp. 27-32 (1987)

Erdogan, F., "Stress Distribution in Non-Homogeneous Elastic Plane with Cracks," *J. Appl. Mech.* Vol. 32, pp. 403-410, (1963).

Eshelby, J.D., "The Elastic Field Outside an Elliptical Inclusion," *Prc. Roy. Soc. Lond.* Vol. A252, p. 561, (1957).

Espey, G.B., Jones, M.H., and Brown, W.F. Jr., "The Sharp Edge Notch Tensile Strength of Several High-Strength Steel Sheet Alloys," *Am. Soc. Test. Mater. Proc.,* Vol. 59, p. 837, (1959).

Evans, A.G., Dalgleish, B.J., He, M., and Hutchinson, J.W., "On Crack Path Selection and the Interface Fracture Energy in Bimaterial Systems," *Acta. Metall. Mater*., Vol. 37, pp. 3249-3254, (1989).

Everett, R.K., and Arsenault, R.J., *Metal Matrix Composites: Processing and Interfaces.* Academic Press, (1991).

Faleskog, J., and Shih C.F., "Micromechanics of Coalescence-I. Synegistic Effects of Elasticity, Plastic Yielding, and Multi-Size Scale Voids," *J. Mech. Phys. Solids*, Vol. 45, No.1, p. 21, (1997).

Ferrante, J., and Smith, J.R., "Theory of Bimetallic Interfaces," *Phys. Rev.* Vol. 31B, pp. 3427-3434, (1985).

Fisher, J.R., and Gurland, J., "Void Nucleation in Spheroidized Carbon Steels Part 1: Experimental," *Metal Science*, pp. 185-192, (1981).

Fisher, R.A., *Statistical Methods for Research Workers*, Oliver and Boyd, (1935).

Fisher, R.A., *The Design of Experiments*, Oliver and Boyd, (1935).

Fleck, N.A., Muller, G.M., Ashby, M.F., and Hutchinson, J.W., "Strain Gradiant Plasticity: Theory and Experiments," *Acta. Metall. Mater.* Vol. 42, pp. 475-487, (1994).

Frederick, S.F., and Bailey, W.A., "The Relation of Ductility to Dendrite Cell Size in a Cast Al-Si-Mg Alloy," *Trans. Metall. Soc. AIME*, Vol. 242, pp. 2063-2067, (1968).

Freidel, J., *Phil. Mag.* Vol. 43, p. 153, (1952).

French, I.E., and Weinrich, D.F., "The Influence of Hydrostatic Pressure on the Tensile Deformation of a Spheroidized 0.5%C Steel," *Scripta Metall*., Vol. 8, p. 87, (1974).

Gall, K., Horstemeyer M.F., McDowell D.L., and Fan J.H., "Finite Element Analysis of the Debonding and Fracture of Si Particle Clusters in Cast Al-Si Alloys Subjected to Cyclic Loading Conditions," *In Press Mech. Mater.,* (1999-B).

Gall, K., Yang, N., Horstemeyer, M.F., McDowell, D.L., and Fan, J.H., "The Debonding and Fracture of Si Particles During the Fatigue of a Cast Al-Si Alloy," *In Press Metall. Trans.,* (1999).

Gangalee, A., and Gurland, J., "On the Fracture of Silicon Particles in Aluminum-Silicon Alloys," *Trans. Metall. Soc. of AIME*, Vol. 239, pp. 269-272, (1967).

Garber, R., Bernstein, I.M., and Thompson, A.W., *Scripta Metall*., Vol. 10, p. 341, (1976).

Garrison, W.M. Jr., "The Effect of Silicon and Nickel Additions on the Sulfide Spacing and Fracture Toughness of a 0.4 Carbon Low Alloy Steel," *Metall. Trans. A*, Vol. 17A, pp. 669-678, (1986).

Garrison, W.M. Jr., *Metall. Trans. A*, Vol. 17A, pp. 669-678, (1986).

Garrison, W.M. Jr., and Moody, N.R., "Ductile Fracture," *J. Phys. Chem. Soldis*, Vol. 48, pp. 1035-1074, (1987).

Geltmacher, A., Koss, D.A., Matic, P., and Stout, M.G., "A Modeling Study of the Effect of Stress State on Void Linking During Ductile Fracture," *Acta Mater.,* Vol. 44, No. 6, p. 2201, (1996).

Geltmacher, A., Koss, D.A., Stout, M.G., and Matic, P., "Flow Localizaion in Sheet Specimens with Pairs of Holes," *Met. Trans. A, Phys. Metall. Matls Sci.,* Vol. 29, No. 3, p. 775, (1998).

Gokhale, A.M., and Drury, W.J., "Efficient Measurement of Microstructural Surface Area Using Trisector," *Metallurgical Transactions-A*, Vol. 25A, pp. 919-928, (1994).

Gokhale, A.M., "Unbiased Estimation of Curve Length in 3D Using Vertical Slices," *Journal of Microscopy*, Vol. 159, Pt. 2, pp. 133-141, (1990).

Gokhale, A.M., "Estimation of Integral Mixed Curvature From Vertical Sections," *Acta Materialia,* Vol. 46, pp. 1741-1748, (1998).

Goldman, A.Y., Freidin, A.B., and Lebedev, A.A., "Dependence of the Yield Point of Polymer Materials on Hydrostatic Pressure and Certain Plasticity Criteria," *Journal of Problemy Prochnosti*, Vol.15, No.3 pp.62-66, (1983).

Gologanu, M., Leblond, J.P. and Devaux, J., "Approximate models for ductile metals containing nonspherical voids - case of axisymmetric prolate ellipsoidal cavities," *J. Mech. Phys. Solids*, Vol. 41, pp. 1723-1754 (1993).

Gologanu, M., Leblond, J.P. and Devaux, J., "Approximate models for ductile metals containing nonspherical voids - case of axisymmetric oblate ellipsoidal cavities," *Int. J. Eng. Matl. Tech*, Vol. 116, pp. 290-297 (1994).

Goods, S.H., and Brown, L.M., "The Nucleation of Cavities by Plastic Deformation," *Acta. Metall.,* Vol. 27, pp. 1-15, (1979).

Green, G., and Knott, J.F., "The Initiation and Propagation of Ductile Fracture in Low Strength Steels," *J. Eng. Mater. Tech*., ASME, Fairfield, NJ, Vol. 98, pp. 37-46, (1976).

Grosskreutz, J.C., and Shaw, G.G., "Critical Mechanisms in the Development of Fatigue Cracks in 2024-T4 Aluminum," *Fracture 1969*, *Proc. 2nd Int. Conf. Frac.*, Brighton, pp. 620-629, (1969).

Gupta, N.K., "A Description of Experimental Yield Surfaces," *Proc. Plasticity 1989, Second Int. Symp. Plasticity*, Pergamom Press, Oxford-NY, pp. 91-94, (1989).

Gupta, V., Yuan, J., and Martinez, D., "Calculation, Measurement, and Control of Interface Strength in Composites," *J. Am. Ceram. Soc.* Vol. 76, pp. 305-315, (1993).

Gurland, J., "Observations on the Fracture of Cementite Particles in a Spheroidized 1.05%C Steel Deformed at Room Temperature," *Acta Metall*., Vol. 20, pp. 735-741, (1972).

Gurland, J., and Plateau, J., "The Mechanism of Ductile Rupture of Metals Containing Inclusions," *Trans. ASM*, Vol. 56, p. 442, (1963).

Gurson, A.L., "Continuum Theory of Ductile Rupture by Void Nucleation and Growth-1. Yield Criteria a and Flow Rules for Porous Ductile Media," *J. Engng. Mat. Tech.*, Vol. 99, pp. 2-15, (1977).

Gurson, A.L., "Continuum Theory of Ductile Rupture by Void Nucleation and Growth-1. Yield Criteria and Flow Rules for Porous Ductile Media," *J. Engng. Materials Techn.,* Vol. 99, pp. 2-15, (1977a).

Gurson, A.L., "Porous Rigid-Plastic Materials Containing Rigid Inclusions-Yield Function, Plastic Potential, and Void Nucleation," *Proc. Int. Conf. Fracture* (edited by D.M.R. Taplin), Vol. 2A, pp. 357-364, (1977b).

Gysler, A., Lutjering, G., and Gerold, V., "Deformation Behavior of Age-Hardened Ti-Mo Alloys," *Acta Metall*., Vol. 22, p. 901, (1974).

Hahn, G.T., and Rosenfield, A.R., "Metallurgical Factors Affecting Fracture Toughness of Aluminum Alloys," *Metall. Trans.* Vol. 6A, pp. 653-668, (1975).

Hahn, G.T., Kanninen, M.F., and Rosenfield, A.R., "Fracture Toughness of Materials," *A. Rev. Mater. Sci*, Vol. 2, p. 381, (1968).

Harkegard, G., "A Finite Element Analysis of Elastic-Plastic Plates Containing Cavities and Inclusions with Reference to Fatigue Crack Initiation," *Int. J. Frac.* Vol. 9, pp. 437-447, (1973).

Harris, R.C., Lipson, S., Rosenthal, H., "Tensile Properties of Aluminum-Silicon Magnesium Alloys and the Effect of Sodium Modification," *AFS Trans.*, Vol. 64, pp. 470-481, (1956).

He, M.Y., Evans, A.G., and Hutchinson, J.W., "Crack Deflection at an Interface Between Dissimilar Elastic Materials: Role of Residual Stresses," *Int. J. Solids Struc.* Vol. 31, pp. 3443-3455, (1994).

He, M.Y., Evans, A.G., and Hutchinson, J.W., "Interface Cracking Phenomena in Constrained Metal Layers," *Acta. Metall. Mater.* Vol. 44, pp. 2963-2971, (1996).

Hess, P.D., and Blackman, E.V., "Strontium as a Modifying Agent for Hypoeutectic Aluminum Silicon Alloys," *AFS Trans.*, Vol. 83, pp. 87-90, (1975).

Hibbit, H.D., "ABAQUS/EPGEN—A General Purpose Finite Element Code with Emphasis on Nonlinear Applications," *Nucl. Engng. Des*., Vol. 77, pp. 271-297, (1984).

Hibbitt, H.D., Karlsson, B.I., and Sorensen, E.P. "ABAQUS-Standard, User Manual," Providence, RI, (1998).

Hirth, J.P., and Nix, W.D., "Analysis of Cavity Nucleation in Solids Subjected to External and Internal Stresses," *Acta. Metall. Mater.*, Vol. 33, p. 359, (1985).

Hom, C.L., and McMeeking, R.M., "Void Growth in Elastic-Plastic Materials," *J. App. Mech.*, Vol. 56, pp. 309-317, (1989).

Horstemeyer, M.F., and Baskes, M.I., "Atomistic Finite Deformation Simulations: A Discussion in Relation to Mechanical Stresses," *J. Eng. Mat. Tech.* Vol. 121, pp. 114-119, (1999).

Horstemeyer, M.F., and Gokhale, A.M., "A Void-Crack Nucleation Model for Ductile Metals," *Int. J. Solids and Structures,* Vol. 36, pp. 5029-5055, (1999).

Horstemeyer, M.F., and Revelli, V., "Stress History Dependent Localization and Failure Using Continuum Damage Mechanics Concepts," *ASTM Symposium the Applications of Continuum Damage Mechanics to Fatigue and Fracture*, STP1315, ed. D. McDowell, (1996).

Horstemeyer, M.F., "Structural Analysis of a Submarine Using Statistical Design of Experiments,"*, Advances in Numerical Simulation Techniques for Penetration and Perforation of Solids*, eds. E. P. Chen and V. K. Luk, ASME-AMD-Vol. 171, pp. 189-200, (1993).

Horstemeyer, M.F., Lathrop, J., Gokhale, A.M., and Dighe, M., "Modeling Stress State Dependent Damage Evolution in a Cast Al-Si-Mg Aluminum Alloy," A*ccepted Theoretical and Applied Mechanics*, (1999).

Horstemeyer, M.F., McDowell, D.L., and Bammann, D.J., "Torsional Softening and the Forming Limit Diagram," SAE Tech. Ser. 960599, ed. K. Chen, *Analysis of Autobody Stamping Technology,* (1995).

Horstemeyer, M.F. and McDowell, D.L., "Using Statistical Design of Experiments for Parameter Study of Crystal Plasticity Modeling Features under Different Strain Paths," Sandia National Laboratory Report, SAND96-8683, (1997).

Horstemeyer, M.F. and Ramaswamy, S., "On Factors Affecting Localization and Void Growth in Ductile Metals: A Parametric Study," accepted *Int. J. Damage Mech* , (1999).

Horstemeyer, M.F., and Gokhale, A.M., "A Void Nucleation Model for Ductile Materials," accepted by *Internal J. Solids and Structures,* (1998).

Irwin, G.R., "Fracture I," *Handbuch der Physik VI*, ed. Flugge, pp. 558-590, Springer.

Izawa, N., Lu, Y. and Nishida, Y., "Shear Strength at the Interface Between Aluminum and Ceramics in Model Composites Fabricated by Squeeze Casting," *Mater. Trans., JIM* 37, pp. 259-264, (1996).

Johnson, W.A. and Mehl, R.F., Trans. AIME, Vol. 135, p. 416, (1949).

Josell, D. and Spaepen, F., "Determination of the Interfacial Tension by Zero Creep Experiments—I. Theory, *Acta. Metall. Mater*., Vol. 41, pp. 3007-3015, (1993-a).

Josell, D. and Spaepen, F., "Determination of the Interfacial Tension by Zero Creep Experiments—I. Experiment, *Acta. Metall. Mater*., Vol. 41, pp. 3017-3027, (1993-b).

Jun, S., “Effect of Stress Triaxiality on Micro-Mechanisms of Void Coalescence and Micro-Fracture Ductility of Materials,” *Engineering Fracture Mechanics*, Vol. 39, No.5, p. 799, (1991).

Kachanov, M.L., "Time of the Fractured Process Under Creep Conditions," *Izv. Akad. Nauk. SSSR OTN Tekh. Nauk*., Vol. 8, p. 26, (1958).

Kanninen, M.F. and Popelar, C.H., *Advanced Fracture Mechanics*, Oxford Univ. Press, (1985).

Kearsley, E.A., "Strain Invariants Expressed as Average Stretches," *Journal of Rheology*, Vol.33, no.5, pp. 757-60, (1989).

Kim, K.T. and Carroll M.M., "Compaction Equations for Strain-Hardening Porous Materials," *Int. J. Plasticity*, Vol. 3, pp. 63-73, (1987).

Koh, S.K. and Stephens, R.I., “Fracture Toughness of A356-T6 Cast Aluminum,” SAE-SP760, *Fatigue and Fracture Toughness of A356-T6 Cast Aluminum Alloy*, 881705, pp. 61-69, (1988).

Kolmogorov, A.N. *Bull. Acad. Sci. USSR*, No. 3, (1937).

Koplik, J. and Needleman, A., “Void Growth and Coalescence in Porous Plastic Solids,” *Int. J. Solids Structures*, Vol. 24, No.8, pp. 835, (1988).

Kurtz, R.J.M. and Hoagland, R.G., "Effect of Grain-Boundary Dislocations on the Sliding Resistance of Sigma-11 Grain Boundaries in Aluminum, *Scr. Mater.,* Vol. 39, pp. 653-659, (1998).

Lamon, J., Rebillat, F., and Evans, A.G., "Microcomposite Test Procedure for Evaluating the Interface properties of Ceramic Matrix Composites, *J. Am. Cer. Soc.* Vol. 78, pp. 401-405, (1995).

Lankford, J. and Kusenberger, F.N., "Initiation of Fatigue Cracks in 4340 Steel," *Mett. Trans.* Vol. 4, pp. 553-559, (1973).

Leblond, J.B., Perrin, G., and Devaux, J., “An Improved Gurson-type Model for Hardenable Ductile Metals,” *European J. of Mechanics* A, Solids, Vol.14, No. 4, pp. 499-527, (1995).

Lee, S., Majno, L., and Asaro, R.J., “Correlation of Microstructure and Fracture Toughness in Two 4340 Steels,” *Metall. Trans. A*, Vol. 16A, pp. 1633-1648, (1985).

Lee, Y.K., "A Finite Elastoplastic Flow Theory for Porous Media," *Int. J. Plasticity*, Vol. 4, pp. 301-316, (1988).

Lee, Y.S., "*Modeling Ductile Damage Evolution in Metal Forming Processes*, Ph.D. Thesis, Mechanical Engineering, Cornell University, Ithica, NY, (1991).

Lee, Y.S. and Dawson, P.R., “Modeling Ductile Void Growth in Viscoplastic Materials: Void Growth Model,” *Mech. Of Matls*., Vol. 15, No.1, p. 21, (1993).

Leung, D.K., Zhamg, N.T., McMeeking, R.M., and Evans, A.G., "Crack Progression and Interface Debonding in Brittle/Ductile Nanoscale Multilayers," *J. Mater. Res.*, Vol. 10, pp. 1958-1968, (1995).

Loboda, V.V., "Analytical Derivation and Investigation of the Interface Crack Models," *Int. J. Solids Struc*. Vol. 335, pp. 4477-4489, (1998).

Louis, P. and Gokhale, A.M., "Computer Simulation of Spatial Arrangement and Connectivity of Particles in Three Dimensional Microstructure: Application to Model Electrical Conductivity of Polymer Matrix Composite," *Acta Metallurgica et Materiallia*, Vol. 44, pp. 1519-1528, (1996).

Louis, P. and Gokhale, A.M., "Application of Image Analysis for Characterization of Spatial Arrangement of Features in Microstructures," *Metallurgical and Materials Transactions*, Vol. 26A, pp. 1449-1456, (1995).

Lu, W.Y., Horstemeyer, M.F., Korellis, J.S., Grishibar, R.B., and Mosher, D., "High Temperature Sensitivity of Notched AISI 304L Stainless Steel Tests," *Theoretical and Applied Fracture Mechanics*, Vol. 30, p. 139 (1998).

MacKenzie, A.C., Hancock, J.W., Brown, D.K., "On the Influence of State of Stress on Ductile Failure Initiation in High Strength Steels," *Engrng. Fract. Mech.,* Vol. 9, pp. 167-188, (1977).

Mackin, T.J., Warren, P.D., and Evans, A.G., "Effects of Fiber Roughness on Interface Sliding in Composites," *Acta. Metall. Mater*., Vol. 40, pp. 1251-1257, (1992).

Magnusen, P.E., Dubensky, E.M., and Koss, D.A., "The Effect of Void Arrays on Void Linking During Ductile Fracture," *Acta Metall*., Vol. 36, No. 6, pp. 1503-1509, (1988).

Major, J.F., Makinde, A., Lee, P.D., Chamberlain, B., Scappaticci, T., and Richman, D., "The Lincoln Mark VIII Cast Aluminum Suspension Control Arm (Parallel Development)," SAE 1994 Transacations, J. Mater. & Manufacturing, Section 5, Vol. 103, SAE940874, pp. 635-646.

Maloney, J.L. and Garrison, Jr., W.M., "Comparison of Void Nucleation and Growth at MnS and TI_2CS Inclusions in HY180 Steel," *Scripta Metall*., Vol. 23, pp. 2097-2100, (1989).

Marin, E., "A Critical Study of Finite Strain Porous Inelasticity", PhD Thesis, Georgia Institute of Technology, (1993).

McClintock, F.A., "A Criterion for Ductile Fracture by the Growth of Holes," *ASME J. Appl. Mech*., Vol. 35, pp. 363, (1968).

McDowell, D.L., Marin, E., Lee, Y.K., Miller, M.P., and Bertoncelli, C., "Considerations for a 'Complete' Continuum Theory of Multiaxial Inelasticity for Ductile Metals," MECAMAT'92 International Seminar on Multiaxial Plasticity, Sept. 1-4, Cachan, France, (1992).

Mear, M.E., "On the Plastic Yielding of Porous Metals," *Mech. Matls*., Vol. 9, pp. 33-48, (1990).

Melander, A. and Stahlberg, U., "The effect of void size and distribution on ductile fracture," *Int. J. Fracture*, Vol. 16, pp. 431-440 (1980).

Methfessel, M., *Phys. Rev*. B38, 1537, (1988).

Meyers, M. A. and Chawla, K.K., *Mechanical Metallurgy*. Prentice-Hall Inc., Englewood Cliffs, New Jersey, (1984).

Miller, M.P. and McDowell, D.L. "Stress State Dependence of Finite Strain Inelasticity," ASME Summer Applied Mechanics Meeting, Tucson, AZ, ASME AMD-Vol. 32, *Microstructural Characterization in Constitutive Modeling of Metals and Granular Media*, pp. 27-44, (1992).

Miller, M.P. and McDowell, D.L., "The Effect of Stress State on the Large Strain Inelastic Deformation Behavior of 304L Stainless Steel," *J. Enging. Matls. Techn., Trans. of ASME*, Vol. 118, No. 1, pp. 28-36, (1996).

Miller, M.P., Dawson, P.R., and Bammann, D.J., "Reflecting Microstructrual Evolution in Hardening Models for Polycrystalline Metals," *Simulation of Materials*

Processing: Theory, Methods, and Applications, eds. Shen and Dawson, Balkema, Rotterdam, (1995).

Moody, N.R., Garrison, Jr., W.M., Smugeresky, J.E., and Costa, J.E., "The Role of Inclusion and Pore Content on the Fracture Toughness of Powder-Processed Blended Elemental Titatium Alloys," *Metall. Trans. A*, Vol. 24A, pp. 161-174, (1993).

Moran, B., Ortiz, M., and Shih, C.F., "Formulation of Implicit Finite Element Methods for Multiplicative Finite Deformation Plasticity," *Int. J. Numerical Methods in Engineering*, Vol. 29, p. 483 (1990).

Nagaki, S., Goya, M. and Sowerby, R., "The Influence of Void Distribution on the Yielding of an Elastic-Plastic Porous Solid," Vol. 9, pp. 199-211, (1993).

Nair, V.N., *Technometrics*, Vol. 34, No. 2, pp. 127-161, (1992).

Nair, V.N., Shoemaker, A.C., "The Role of Experimentation in Quality Engineering: A Review of Taguchi's Contributions, Statistical Design and Analysis of Industrial Experiments," ed. S. Ghosh, Marcel Dekker, Inc., pp. 247-277, (1990).

Needleman, A., "Void Growth in an Elastic-Plastic Medium," Journal of Applied Mechanics, Vol. 39, pp. 964-970 (1972).

Needleman, A., "A Continuum Model for Void Nucleation by Inclusion Debonding," *J. App. Mech*., Vol. 54, pp. 525-531, (1987).

Needleman, A., "An Analysis of Tensile Decohesion Along an Interface," *J. Mech. Phys. Solids,* Vol. 38, pp. 289-324, (1990-a).

Needleman, A., "An Analysis of Decohesion Along an Imperfect Interface," *Int. J. Frac.* Vol. 42, pp. 21-40, (1990-b).

Needleman, A., "Micromechanical Modeling of Interfacial Decohesion," *Ultramicroscopy,* Vol. 40, pp. 203-214, (1992).

Needleman, A., Tvergaard, V., and Van der Giessen, E., "Evolution of void shape and size in creeping solids," *Int. J. Damage Mechanics*, Vol. 4, pp. 134-152 (1995).

Needleman, A., "Numerical Modeling of Crack Growth Under Dynamic Loading Conditions," *Comp. Mech.,* Vol. 19, pp. 463-469, (1997).

Needleman, A., "A Continuum Model for Void Nucleation by Inclusion Debonding," *J. App. Mech.*, Vol. 54, pp. 525-531, (1987).

Needleman, A. and Rice, J.R., "Limits to Ductility Set by Plastic Flow Localization," *Mech. Sheet Metal Form.*, eds. Koistinen and Wang, Plenum Publishing Co., pp. 237-265, (1978).

Nieh, T.G. and Nix, W.D., *Scripta Metall*., Vol. 14, p. 365, (1980).

Needleman, A. and Tvergaard, V., "An Analysis of Ductile Rupture in Notched Bars," *J. Mech. Phys. Solids*, Vol. 32, p. 461, (1984).

Nelder, J. A., and Lee, Y., "Applied Stochastic Models and Data Analysis," Vol. 7, pp. 107-120, (1991).

Nemat-Nasser, S. and Shokooh, A., "On Finite Plastic Flows of compressible Materials with Internal Friction," *Int. J. Solids Structures*, Vol. 16, pp. 495-514, (1980).

Nemes, J.A. and Eftis, J., "Constitutive Modeling of the Dynamic Fracture of Smooth Tensile Bars," *Int. J. Plast*., Vol. 9, pp. 243-270, (1993).

Nieh and Nix W., "A Comparison of the Dimple Spacing on Intergranular Creep Fracture Surfaces with the Slip Band Spacing for Copper," *Scripta Metall*., Vol. 14, p. 365, (1980).

Nielan, P.E., Perano, K.J. and Mason, W.E., "ANTIPASTO: An Interactive Mesh Generator and Preprocessor for Two-dimensional Analysis Programs', Sandia National Laboratories Report SAND90-8203, (1990).

Ohtaki, S., "An Anlysis of the Two-dimensional Elasti-Plastic Stress Problem Using Quadratic Programming: The Case of Adopting the Seventh-degree Yield Function Containing the Third Invariant of the Deviatoric Stress Tensor," *Nippon Kikai Cakkai Ronbunshui*, Vol. 54, No. 502, (1988).

Olson, G. B., "Computational Design of Hierarchically Structured Materials," *Science,* Vol. 277, pp. 1237-1242, (1997).

Palmer, I. G. and Smith, G. C., "Fracture of Internally Oxidized Copper Alloys," *Proc. AIME Conf. Oxide Dispersion Strengthening*, Bolton Landing, NY, Gordon and Breach, NY, (1967).

Palmer, I.G. and Smith, G.C., "Fracture of Internally Oxidized Copper Alloys," *Proc. AIME Conf. Oxide Dispersion Strengthening*, Bolton Landing, NY, June 1966, Gordon & Beach, NY, (1967).

Pan, E.N., Chiou, H.S. and Liao, G.J., "Effects of Modification and Solidification Conditions on the Feeding Behavior of A356 Al Alloy," *AFS Trans.,* Vol. 99, pp. 605-621, (1991).

Pan, E.N., Lin, C.S. and Lopez, C.R., "Effects of Solidification Parameters on the Feeding Efficiency of A356 Aluminum Alloy. *AFS Trans.,* Vol. 98, pp. 735-746, (1990)

Papadopoilos, G.A., "Dynamic Crack-Bifurcation by the Det-Criterion," *Engineering Fracture Mechanics*, Vol. 31, No. 5, pp. 887-893, (1988).

Papadopoilos, G.A. and Ponridis, P.I. "Crack Initiation Under Biaxial Loading with Higher-Order Approximation," *Engineering Fracture Mechanics*, Vol. 32, No. 3, pp. 351-360, (1989).

Pardoen, T., Doghri, I. and Delannay, F., "Experimental and Numerical Comparison of Void Growth Models and Void Coalescence Criteria for the Prediction of Ductile Fracture in Copper Bars," *Acta Mater*., Vol. 46, No.2, p. 541, (1998).

Perzyna, P., "Constitutive Modeling of Dissipative Solids for Postcritical Behavior and Fracture," *ASME J. Engr. Mater. Tech*., Vol. 106, pp. 410-419, (1985).

Plumtree, A. and Schafer, S., "Initiation and Short Crack Behavior in Aluminum Alloy Casting," *The Mechanical Behavior of Short Fatigue Cracks*, Eds. K.J. Miller and E.R. de los Rios, EGF Publication 1, Suffolk, UK, pp. 215-227, (1986).

Poorooshasb, H. B., "Description of Flow of Sand Using State Parameters," *Computers and Geotechnics*, Vol. 8, pp. 195-218, (1989).

Puttick, K.E., "Ductile Fracture in Metals," *Phil. Mag.* Vol. 4, pp. 964-969, (1959).

Rabotnov, Y.N., "*Creep Problems in Structural Members*," North-Holland, Amsterdam (1969).

Raj, R. and Ashby, M.F., "Intergranular Fracture at Elevated Temperature," *Acta. Metall. Mater.*, Vol. 23, p. 653, (1975).

Ramaswamy, S. and Aravas, N., "Finite Element Implementation of Gradient Plasticity Models – Part 1: Gradient Dependent Evolution Equations," *Computer Methods Applied Mech. Engin.*, Vol. 163, No.1, p. 33, (1998).

Rashid, M.M., “A Multiaxial Constitutive Model for Creep Cavitation Damage in Metals,” ASME AMD-Vol. 132, *Recent Advances in Damage Mechanics and Plasticity*, ed. J.W. Ju, Book No. H00734, pp. 219-234, (1992).

Reimanis, I.E., Dalgleish, B.J., and Evans, A.G., "The Fracture Resistance of a Model Metal/ceramic Interface," *Acta. Metall. Mater*., Vol. 39, pp. 3133-3141, (1991).

Reimanis, I.E., Dalgleish, B.J., Brahy, M., Ruhle, M., and Evans, A.G., "Effects of Plasticity on the Crack Propagation Resistance of a Metal/ceramic Interface," *Acta. Metall. Mater*., Vol. 38, pp. 2645-2652, (1990).

Rice J.R. and Tracey, D.M., "On the Ductile Enlargement of Voids in Triaxial Stress Fields," *J. Mech. Phys. Solids.*, Vol. 17, p. 201, (1969).

Rice, J.R. and Sih, G.C., "Plane Problem of Cracks in Dissimilar Media," *J. App. Mech.,* Vol. 55, pp. 299-316, (1965).

Rice, J.R. and Wang, J.S., "Embrittlement of Interfaces by Solute Segregation," *Mat. Sci. Eng. A*, Vol. 107, pp. 23-40, (1989).

Rice, J. R., *J. Mech. Phys. Solids*, Vol. 9, pp. 433-455, (1971).

Rice, J.R., "Inelastic Constitutive Relations for Solids: an Internal Variable Theory and Its Application to Metal Plasticity," *J. Mech. Phys. Solids*, Vol. 9, pp. 433-455, (1971).

Rice, J.R. and Johnson, M.A., “The Role of Large Crack Tip Geometry Changes in Plane Strain Fracture,” *Inelastic Behavior of Solids*, eds. M.F. Kanninen, W.G. Adler, A.R. Rosenfield, and R.J. Jaffee,, McGraw-Hill, New York, NY, pp. 641-672, (1970).

Rogers, H.C., *Trans. AIME*, Vol. 218, p. 498, (1960).

Rose, J.H., Smith, J.R., and Ferrante, J., "Universal Binding Energy Curves for Metals and Bimetallic Interfaces," *Phys. Rev. Lett.*, Vol. 47, pp. 675-678, (1983).

Rose, J. H., Smith, J.R., and Ferrante, J., "Universal Features of Bonding in Metals," *Phys. Rev. B*, Vol. 28, pp. 1835-1845, (1983).

Rose, J.H., Smith, J.R., Guinea, F. and Ferrante, J., *Phys. Rev. B*, Vol. 29, p. 2963, (1984).

Rosenfield, A.R., "Criteria for Ductile Fracture of Two-Phase Alloys," *Metall. Rev.*, Vol. 13, pp. 29-40, (1969).

Rousselier, G., "Finite Deformation Constitutive Relation Including Ductile Fracture Damage," *Three Dimensional Constitutive Relations and Ductile Fracture*, eds. S. Nemat-Nasser, North Holland Publ., pp. 331-355, (1981).

Rudnicki, J.W. and Rice, J.R., "Conditions for Localization of Deformation in Pressure-sensitive Dilatant Materials," *J. Mech. Phys. Solids*, Vol. 23, pp. 371-394, (1975).

Sage, M., Pan, J., and Needleman, A., "Void Nucleation Effects on Shear Localization in Porous Plastic Solids," *Int. J. Frac.*, Vol. 19, pp. 163-182, (1982).

Samuel, A. M. and Samuel, F. H., "A Metallographic Study of Porosity and Fracture Behavior in Relation to the Tensile Properties in 319.2 End Chill Castings," *Metall. Mater. Trans.,* Vol. 26A, pp. 2359-2372, (1994).

Santalo, L.A., "Integral Geometry and Geometric Probability, Encyclopedia of Mathematics and its Applications," Gian-Carlo Rota, ed., Addison-Wesley, (1976).

Schreyer, H.L.,"A Third-Invariant Plasticity Theory for Frictional Materials," *Journal of Structural Mechanics*, Vol.11, No.2 pp. 177-196, (1983b).

Schreyer, H. L., "*Development of a Third-Invariant Plasticity Theory for Concrete and Soils*," Final Report, AFWL-TR-83-119, February (1984).

Schreyer, H.L. and Bean, J.E., "A Simplified Viscoplastic Theory for Frictional Materials," *Symp. Proc. U. S. Air Force Academy*, Colorado, AD-A132 115, pp. 77-80, (1983a).

Seweryn, A., and Mroz, Z., "On the Criterion of Damage Evolution for Variable Multiaxial Stress States," *Int. J. Solids Struc.*, Vol. 35, pp. 1589-1616, (1998).

Siegmund, T., Fleck, N.A., and Needleman, A., "Dynamic Crack Growth Across an Interface," *Int. J. Frac*. Vol. 85, pp. 381-402, (1997).

Simo, J.C., and Meschke, G., "A New Class of Algorithms for Classical Plasticity Extended to Finite Strains: Applications to Geomaterials," *Computational Mechanics*, Springer Verlag, Vol. 11, pp. 253-278, (1993).

Smith, C.S., and Guttman, L., *Trans. AIME*, Vol. 197, pp. 81-92, (1953).

Spear, R.E., "Dendrite Cell Size," *AFS Trans.,* Vol. 71, pp. 209-215, (1963).

Stoneham, M., Harding, J., and Harker, T., "The Shell Model and Interatomic Potentials for Ceramics," *MRS Bulletin*, Feb., p. 29-35, (1996).

Stott M.J., and Zaremba, E., *Phys. Rev.,* Vol. B22, p. 1564, (1980).

Stutsman, R., Chamberlain, B., and Evans, M., "The Design of an Experiment to Choose an Aluminum Die Casting Alloy for Energy Absorbing Automotive Components," SAE-SP-1164, No. 960159, pp. 1-7, (1996).

Suo, Z., Ortiz, M., and Needleman, A., "Stability of Solids with Interfaces," *J. Mech. Phys. Solids* Vol. 40, pp. 613-640, (1992).

Suwito, W., Dunn, M.L., and Cunningham, S.J., "Fracture Initiation at Sharp Notches in Single Crystal Silicon," *J. App. Phys*. Vol. 83, pp. 3574-3582, (1998).

Taguchi, G., "Table of Orthogonal Arrays and Linear Graphs," *Reports of Statistical Application Research*, JUSE, Vol. 6, pp. 1-52, (1960).

Taguchi, G., *System of Experimental Design*, UNIPUB, New York, Vol. I and II, (1987).

Takeda, T., Kikuchi, S., and Nasu, Y., "Experimental Evaluation of Yield Condition Containing Third Invariant of Deviatoric Stresses," *Proceedings of the Thirtieth Japan Congress on Materials Research*, pp. 13-18, (1987).

Tewari, A., Dighe, M., and Gokhale, A.M., "Quantitative Characterization of Spatial Arrangement of Micropores in Cast Microstructures," *Mat. Chara.*, Vol. 40, pp. 119-132, (1998).

Thomson, C.I.A., Worswick,M.J., Pilkey, A.K., Lloyd, D.J., and Burger, G., "Modeling Void Nucleation and Growth Within Periodic Clusters of Particles," *Mech. Phys. Solids*, Vol. 47, p. 1, (1998).

Tonks, D.L., Thissell, W.R., Zurek, A.K., and Hixson, R., "Quantitative Analysis of Damage Clustering in Void Linking for Spallation Modeling in Tantalum," *J. de Physique IV France*, Vol. 7, No. C3, p. 841, (1997).

Trinh, K.T., and Gruda, J., "Failure Resistance of Thin Shells Against Projectile Penetration," *Sandia Report SAND91-8486*, Sandia National Laboratories, Livermore, Ca., (1991).

Turner, M.R., and Evans, A.G., "An Experimental Study of the Mechanisms of Crack Extension Along an Oxide/Metal Interface," *Acta. Metall. Mater*., Vol. 44, pp. 863-871, (1996).

Tvergaard, V., "Influence of Voids on Shear Band Instability Under Plane Strain Conditions," *Int. J. Frac*., Vol. 17, No. 4, pp. 389-407, (1981).

Tvergaard, V., "On Localization in Ductile Materials Constaining Spherical Voids," *Int. J. Frac*., Vol. 18, pp. 237-252, (1982b).
Tvergaard, V., "Material Failure by Void Growth to Coalescence," *Advances in Applied Mechanics*, eds. J.W. Hutchinson and T. Y. Wu, Vol. 27, pp. 83-151, (1990).
Tvergaard, V., "Ductile Fracture by Cavity Nucleation Between Larger Voids," *J. Mech. Phys. Solids.*, Vol. 30, pp. 265-286, (1982a).
Tvergaard, V., "On Localization in Ductile Materials Containing Spherical Voids," *Int. J. Frac.*, Vol. 18, pp. 237-252, (1982b).
Tvergaard, V., "Material Failure by Void Coalescence *Adv. App. Mech.*, Vol. 27, pp. 83-151, (1990).
Tvergaard, V., and Hutchinson, J.W., "The Relation Between Crack Growth Resistance and Fracture Process Parameters in Elastic-Plastic Solids," *J. Mech. Phys. Solids* Vol. 40, pp. 1377-1397, (1992).
Tvergaard, V., and Hutchinson, J.W., "Toughness of an Interface Along a Thin Ductile Layer Joining Elastic Solids," *Phil. Mag.* Vol. 70A, pp. 641-656, (1994).
Tvergaard, V., and Hutchinson, J.W., "On the Toughness of Ductile Adhesive Joints," *J. Mech. Phys. Solids* Vol. 44, pp. 789-800, (1996).
Tvergaard, V., and Needleman, A., "Effects of Nonlocal Damage in Porous Plastic Solids," *Int. J. Solids Structures*, Vol. 32, No.8-9, p. 1063, (1995).
Tvergaard, V., and Needleman, A., "Nonlocal Effects on Localization in a Void Sheet," *Int. J. Solids Structures*, Vol. 34, No.18, p. 2221, (1997).
Tvergard, V., "Ductile Fracture by Cavity Nucleation Between Larger Voids," *J. Mech. Phys. Solids*, Vol. 30, pp. 265-286, (1982a).
Underwood, E.E., "Quantitative Stereology," *Addison- Wesley, Reading*, Mass, (1970).
Van Stone, R.H., and Cox, T.B., "Use of Fractography and Sectioning Techniques to Study Fracture Mechanisms," *Fractography-Microscopic Cracking Processes*, ASTM STP 600, 5, ASTM, Philadelphia, (1976).
Vorren, O., Evensen, J.E., and Pedersen, T.B., "Microstructure and Mechanical Properties of AlSi(Mg) Casting Alloys," *AFS Trans.,* Vol. 92, pp. 459-466, (1984).
Warren, P.D., Mackin, T.J., and Evans, A.G., "Design, Analysis and Application of an Improved Push-Through Test for the Measurement of Interface Properties in Composites," *Acta. Metall. Mater*, Vol. 40, pp. 1243-1249, (1992).
Weng, G.J., "Anisotropic Hardening in Single Crystals and the Plasticity of Polycrystals," *Int. J. Plast*., Vol. 3, pp. 315-339, (1987).
Wilsdorf, H.G.F., "The Ductile Fracture of Metals: A Microstructural Viewpoint," *Mater. Sci. Engng*,. Vol. 59, p. 1, (1983).
Wojcieszynski, A., *Particle Spacing and Grain Size Effects on Fracture Toughness*, PhD Thesis, Carnegie Mellon University, Pittsburgh, Pa., (1993).
Worswick, M.J., and Pick, R.J., "Void Growth and Coalescence During High Velocity Impact," *Mech. Of Matls.,* Vol. 19, No.4, p. 239, (1995).
Worswick, M.J., Nahme, H., and Fowler, J., "Spall Through Void Nucleation, Growth, and Coalescence," *J. de Physique IV France*, Vol. 4, No. C8, p. 707, (1994).
Xu, X.P., and Needleman, A., "Void Nucleation by Inclusion Debonding in a Crystal Matrix," *Model. Simul. Mater. Sci. Eng*. Vol. 1, pp. 111-132, (1993).

Xu, X.P., and Needleman, A., "Numerical Simulations of Dynamic Interfacial Crack Growth Allowing for Crack Growth Away From the Bond Line," *Int. J. Frac.* Vol. 74, pp. 253-275, (1995).

Xu, X.P., and Needleman, A., "Numerical Simulations of Dynamic Crack Growth Along an Interface," *Int. J. Frac*. Vol. 74, pp. 289-324, (1996).

Xu, X.P., Needleman, A., and Abraham, F.F., "Effect of Inhomogeneities on Dynamic Crack Growth in an Elastic Solid," *Model. Simul. Mater. Sci. Eng*. Vol. 5, pp. 489-516, (1997).

Yang, S., Tewari, A., and Gokhale, A.M., "Modeling of Non-Uniform Spatial Arrangement of Fibers in a Ceramic Matrix Composite," *Acta Materiallia*, Vol. 45, pp. 3059-3069, (1997).

Yeh, J.W., and Liu, W.P., *Metall. Mater. Trans. A*, Vol. 27a, pp. 3558-3568, (1996).

Yeh, J.W., and Liu, W.P., "The Cracking Mechanism of Silicon Particles in an A357 Aluminum Alloy," *Metall. Mater. Trans.*, Vol. 27A, pp. 3558-3568, (1996).

Yoshino, Y., and Shibata, T., "Structure and Bond Strength of a Copper-Alumina Interface," *J. Am. Ceram. Soc*. Vol. 75, pp. 2756-2760, (1992).

Young, S.H., "An Optimization Technique Using the Finite Element Method and Orthogonal Arrays," Ph.D. thesis, Naval Postgraduate School, Monterey, California, (1996).

Zhao, Y.H., Tandon, G.P., and Weng, G.J., "Elastic Moduli for a Class of Porous Materials," *Acta Mechanica*, Vol. 76, pp. 105-130, (1989).

Zurek, A.K., Thissell, W.R., Tonks, D.L., Hixson, R., and Addessio, F., "Quantification of Damage Evolution for a Micromechanical Model of Ductile Fracture in Spallation of Tantalum," *J. de Physique IV. France*, Vol. 7, No. C3, p. 903, (1997).

This page intentionally blank

APPENDIX A. MICROSTRUCTURE-PROPERTY MODEL CONSTANTS

Microstructure-property model constants for Al-Si-Mg castings with varying amounts of silicon are shown in Table A.1. The 1% silicon represents the dendritic aluminum material. The 7% silicon represents the cast A356 aluminum alloy. The 12% silicon represents the eutectic material.

Table A.1. Microstructure-property (elastic-plastic) model constants for Al-Si-Mg castings with varying amounts of silicon.

Constant	1% silicon	7% silicon	12% silicon
shear modulus (MPa)	25920	25920	25920
bulk modulus (MPa)	67630	67630	67630
density (kg/m^3)	2700	2700	2700
C1 (MPa)	0	53.09	53.09
C2 (K)	0	945.3	945.3
C3 (MPa)	142.5	155.9	155.9
C4 (K)	51.8	110.5	110.5
C5 (1/sec)	1e-5	1e-5	1e-5
C6 (K)	0	0	0
C7 (1/MPa)	0.00392	0.001128	0.0008704
C8 (K)	-1731	-1796.2	-1877
C9 (MPa)	42630	4820	4820
C10 (K)	129.6	10.94	8
C11 (sec/MPa)	0	0.002385	0.01369
C12 (K)	0	1441	2000
C13 (1/MPa)	0.224	0.001674	0.00001644
C14 (K)	898.5	0	1000
C15 (MPa)	2305	2818	2818
C16 (K)	1.48	4.622	4.622
C17 (sec/MPa)	0	0	0
C18 (K)	0	0	0
C19	0	-5	-7
C20 (K)	0	-0.3895	-0.3776

Note: base units in MPa, m, s, K.

Table A.2. Microstructure-property (damage) model constants for A356 aluminum alloy.

Constant	A356
C21	4.28
C22	37.97
C23	0.0035
C24	0.009
n	.3
initial small void radius (m)	2e-6
a (MPa)	61546
b (MPa)	58640
c (MPa)	30011
C_{coeff}	86.6
fracture toughness (MPa-mm^0.5)	17.3
silicon particle size (m)	4e-6
silicon volume fraction	0.07
DCS0 (μm)	20
z	0.0509

Note: base units in MPa, m, s, K.

APPENDIX B. FAILURE STRAIN MAPS BASED ON THE INITIAL MICROSTRUCTURE

The following set of design failure maps based on the strain to failure were generated from the microstructure-property that was validated by several experiments from idealized cast plates and from real automotive components. Each failure strain level was determined with different initial silicon particle sizes and with different initial void volume fraction of porosity. They are to be used as a guide. The parameters that were varied include:
(1) temperature (222 K, 297 K, and 394 K)
(2) applied strain rate (2e-4/sec and 1000/sec)
(3) dendrite cell size (20 μm, 50 μm, and 100 μm)
(4) deformation path (uniaxial tension, biaxail tension, and plane strain)

Table B.1. List of failure strain maps.

map	temp. (K)	DCS (mm)	strain rate (1/s)	loading
1	297	20	0.0002	uniaxial
2	297	20	0.0002	biaxial
3	297	20	0.0002	plane strain
4	297	20	1000	uniaxial
5	297	20	1000	biaxial
6	297	20	1000	plane strain
7	297	50	0.0002	uniaxial
8	297	50	0.0002	biaxial
9	297	50	0.0002	plane strain
10	297	50	1000	uniaxial
11	297	50	1000	biaxial
12	297	50	1000	plane strain
13	297	100	0.0002	uniaxial
14	297	100	0.0002	biaxial
15	297	100	0.0002	plane strain
16	297	100	1000	uniaxial
17	297	100	1000	biaxial
18	297	100	1000	plane strain
19	222	20	0.0002	uniaxial
20	222	20	0.0002	biaxial
21	222	20	0.0002	plane strain
22	222	20	1000	uniaxial
23	222	20	1000	biaxial
24	222	20	1000	plane strain
25	222	50	0.0002	uniaxial
26	222	50	0.0002	biaxial
27	222	50	0.0002	plane strain
28	222	50	1000	uniaxial
29	222	50	1000	biaxial
30	222	50	1000	plane strain
31	222	100	0.0002	uniaxial
32	222	100	0.0002	biaxial
33	222	100	0.0002	plane strain
34	222	100	1000	uniaxial
35	222	100	1000	biaxial
36	222	100	1000	plane strain
37	394	20	0.0002	uniaxial
38	394	20	0.0002	biaxial
39	394	20	0.0002	plane strain
40	394	20	1000	uniaxial
41	394	20	1000	biaxial
42	394	20	1000	plane strain
43	394	50	0.0002	uniaxial
44	394	50	0.0002	biaxial
45	394	50	0.0002	plane strain
46	394	50	1000	uniaxial
47	394	50	1000	biaxial
48	394	50	1000	plane strain
49	394	100	0.0002	uniaxial
50	394	100	0.0002	biaxial
51	394	100	0.0002	plane strain
52	394	100	1000	uniaxial
53	394	100	1000	biaxial
54	394	100	1000	plane strain

Failure Strain - Map01

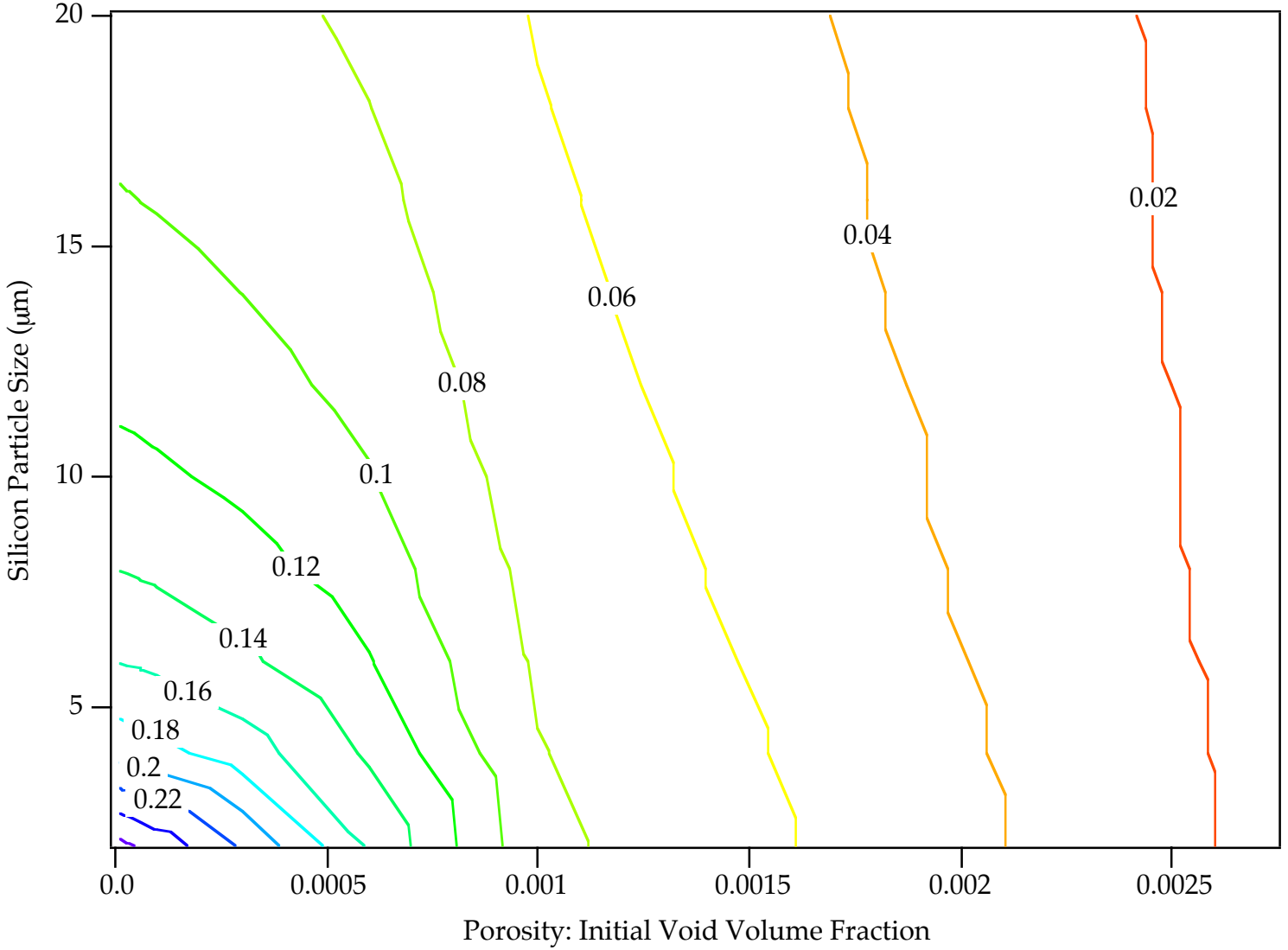

T = 297K
$\dot{\varepsilon}$ = .0002 / sec
DCS = 20 μm

f(Si) = 7%
K_{IC} = 17.3 MPa-$mm^{1/2}$
Uniaxial Tension

Failure Strain - Map02

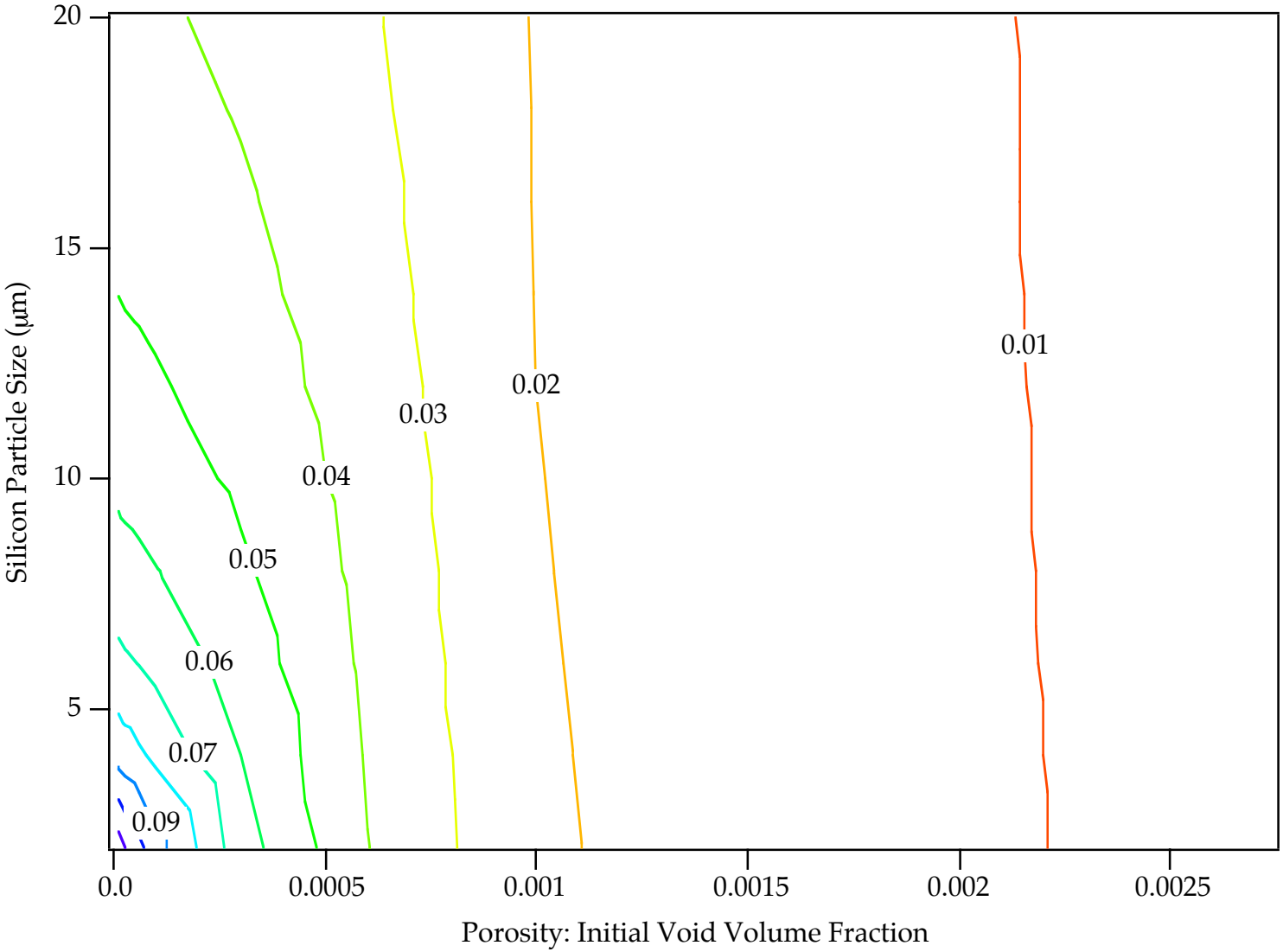

T = 297K
$\dot{\varepsilon}$ = .0002 / sec
DCS = 20 μm

f(Si) = 7%
K_{IC} = 17.3 MPa-$mm^{1/2}$
Biaxial Tension

Failure Strain - Map03

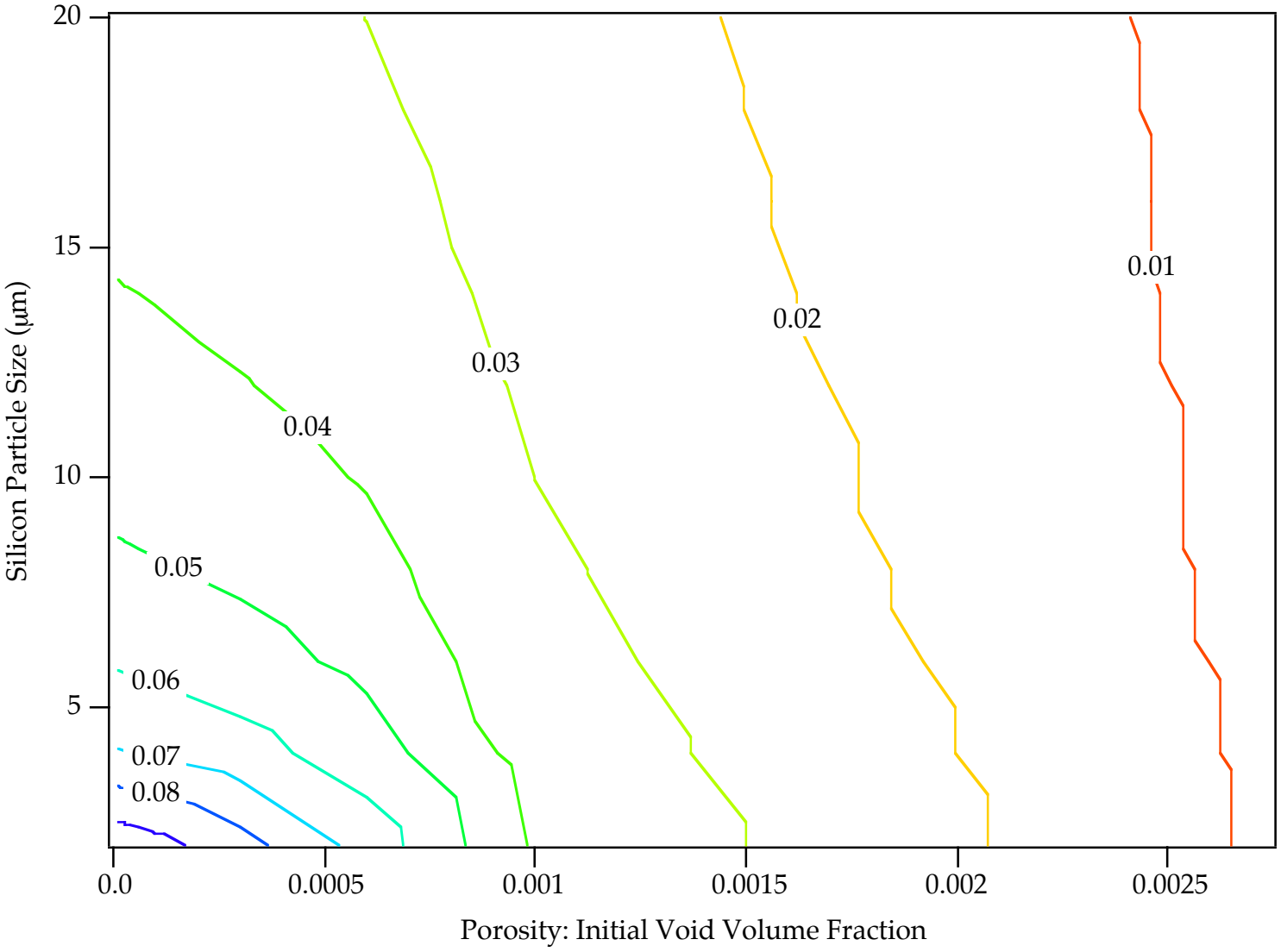

T = 297K
$\dot{\varepsilon}$ = .0002 / sec
DCS = 20 μm

f(Si) = 7%
K_{IC} = 17.3 MPa-$mm^{1/2}$
Plane Strain

Failure Strain - Map04

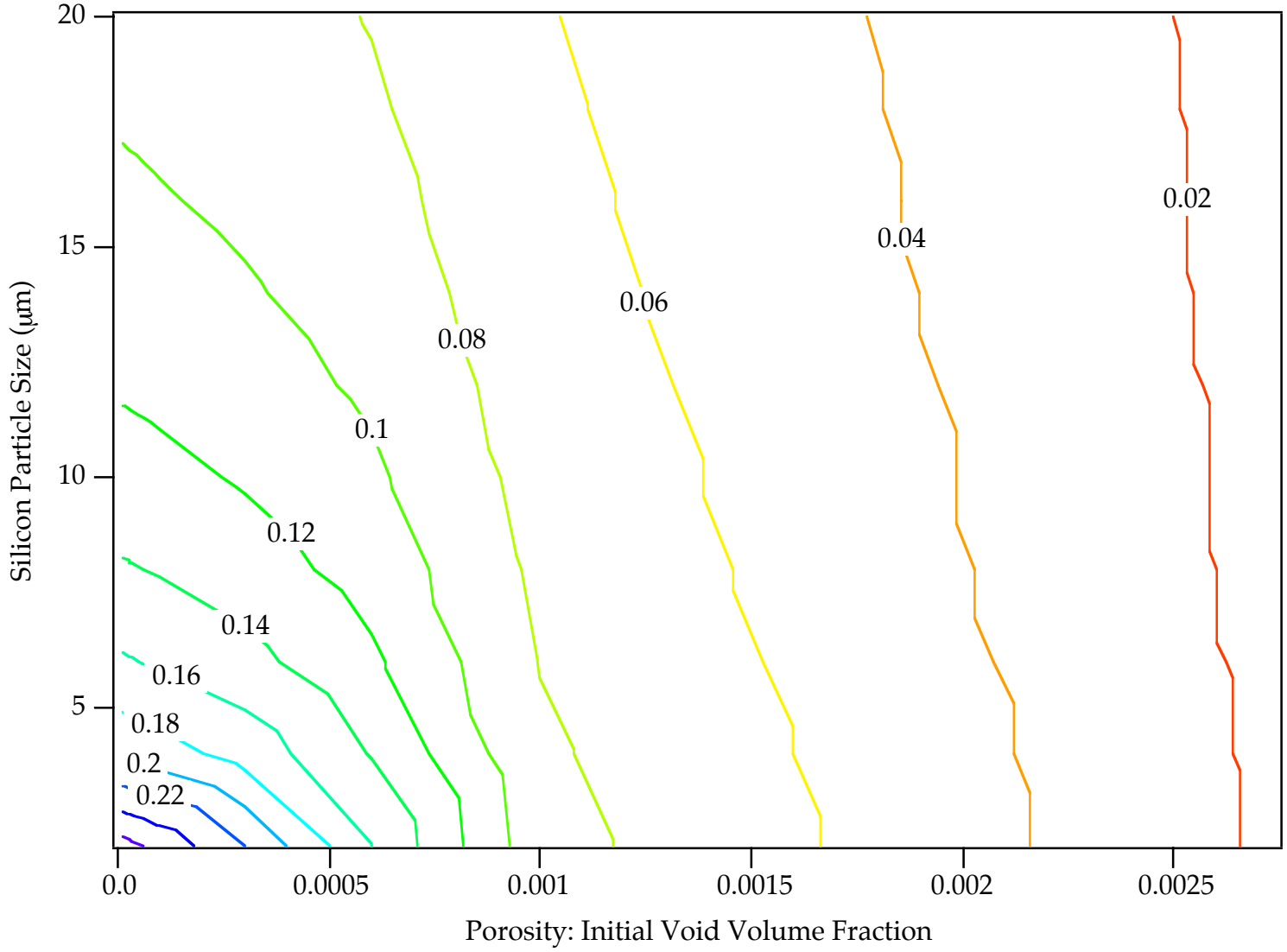

T = 297K
$\dot{\varepsilon}$ = 1000 / sec
DCS = 20 μm

f(Si) = 7%
K_{IC} = 17.3 MPa-mm$^{1/2}$
Uniaxial Tension

Failure Strain - Map05

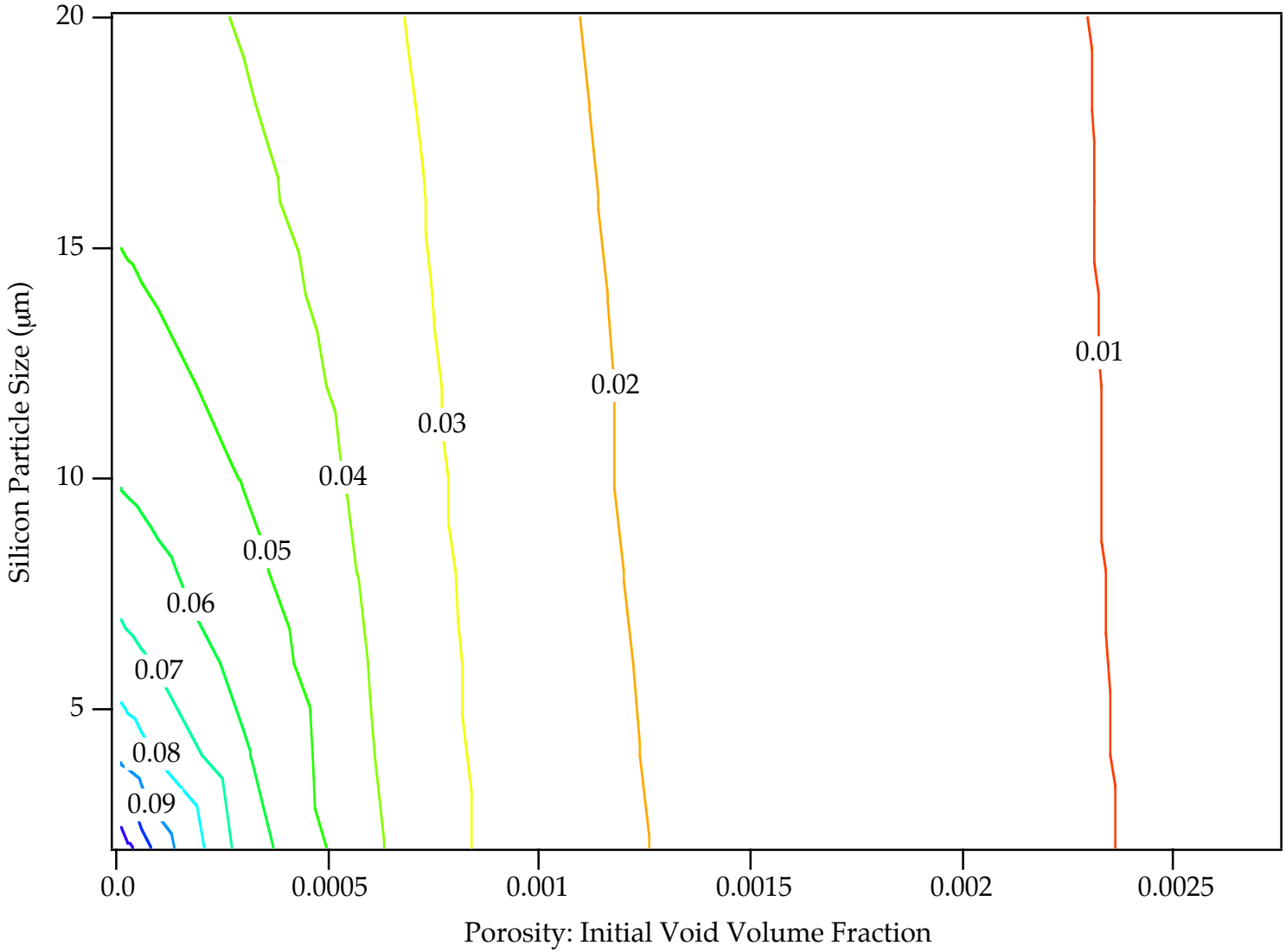

T = 297K
$\dot{\varepsilon}$ = 1000 / sec
DCS = 20 μm

f(Si) = 7%
K_{IC} = 17.3 MPa-mm$^{1/2}$
Biaxial Tension

Failure Strain - Map06

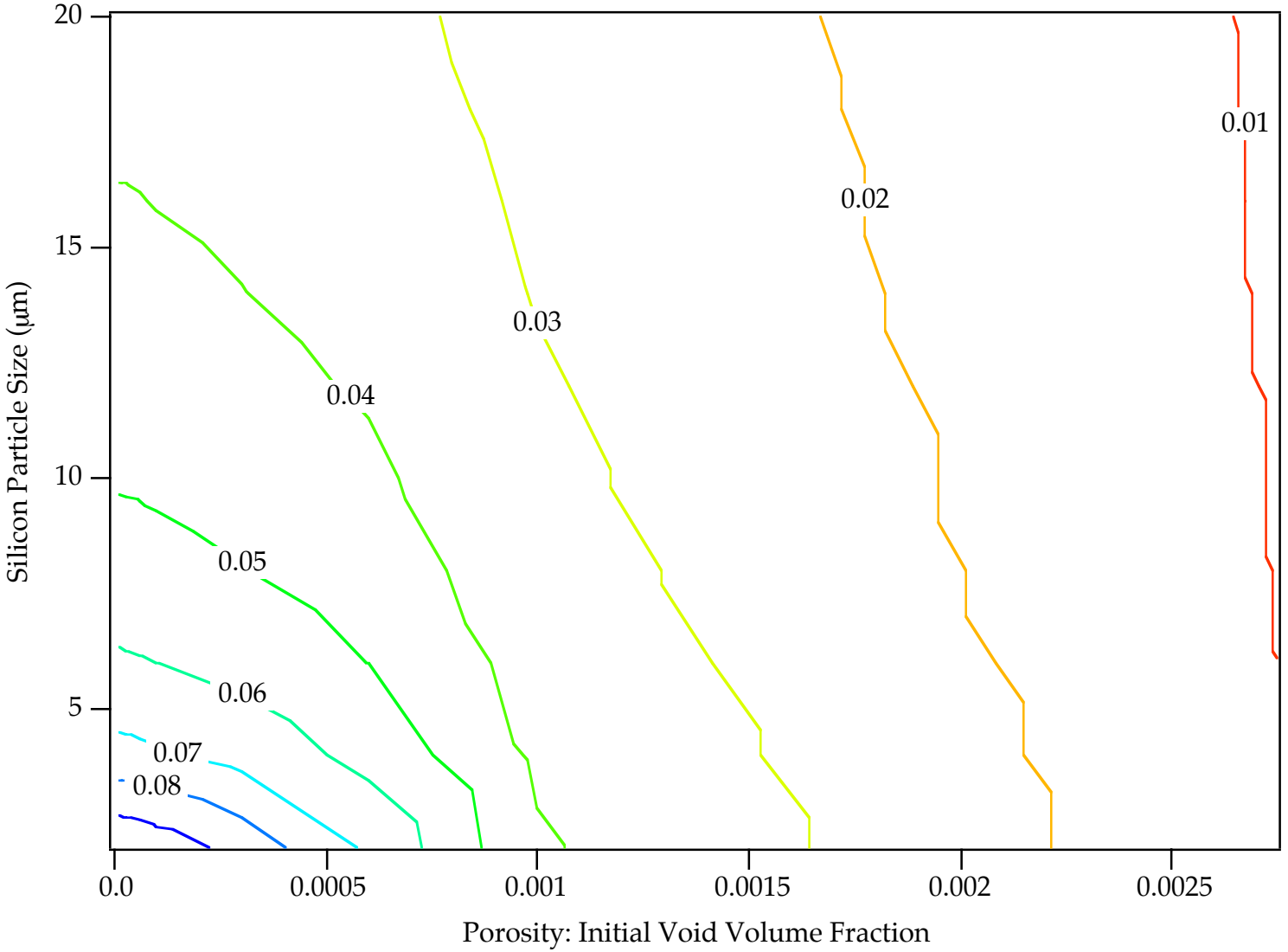

T = 297K
$\dot{\varepsilon}$ = 1000 /sec
DCS = 20 μm

f(Si) = 7%
K_{IC} = 17.3 MPa-$mm^{1/2}$
Plane Strain

Failure Strain - Map07

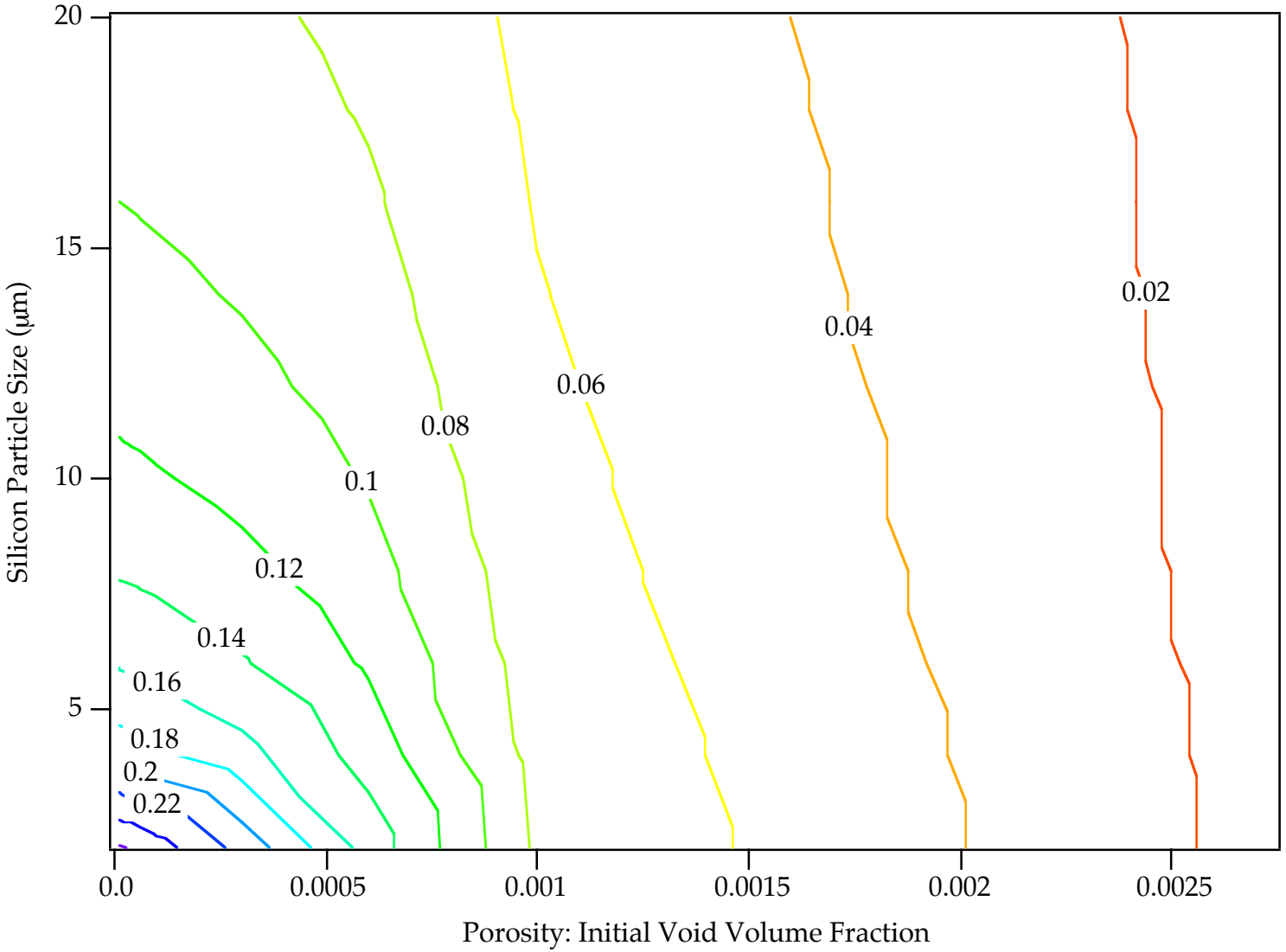

T = 297K
$\dot{\varepsilon}$ = .0002 / sec
DCS = 50 μm

f(Si) = 7%
K_{IC} = 17.3 MPa-mm$^{1/2}$
Uniaxial Tension

Failure Strain - Map08

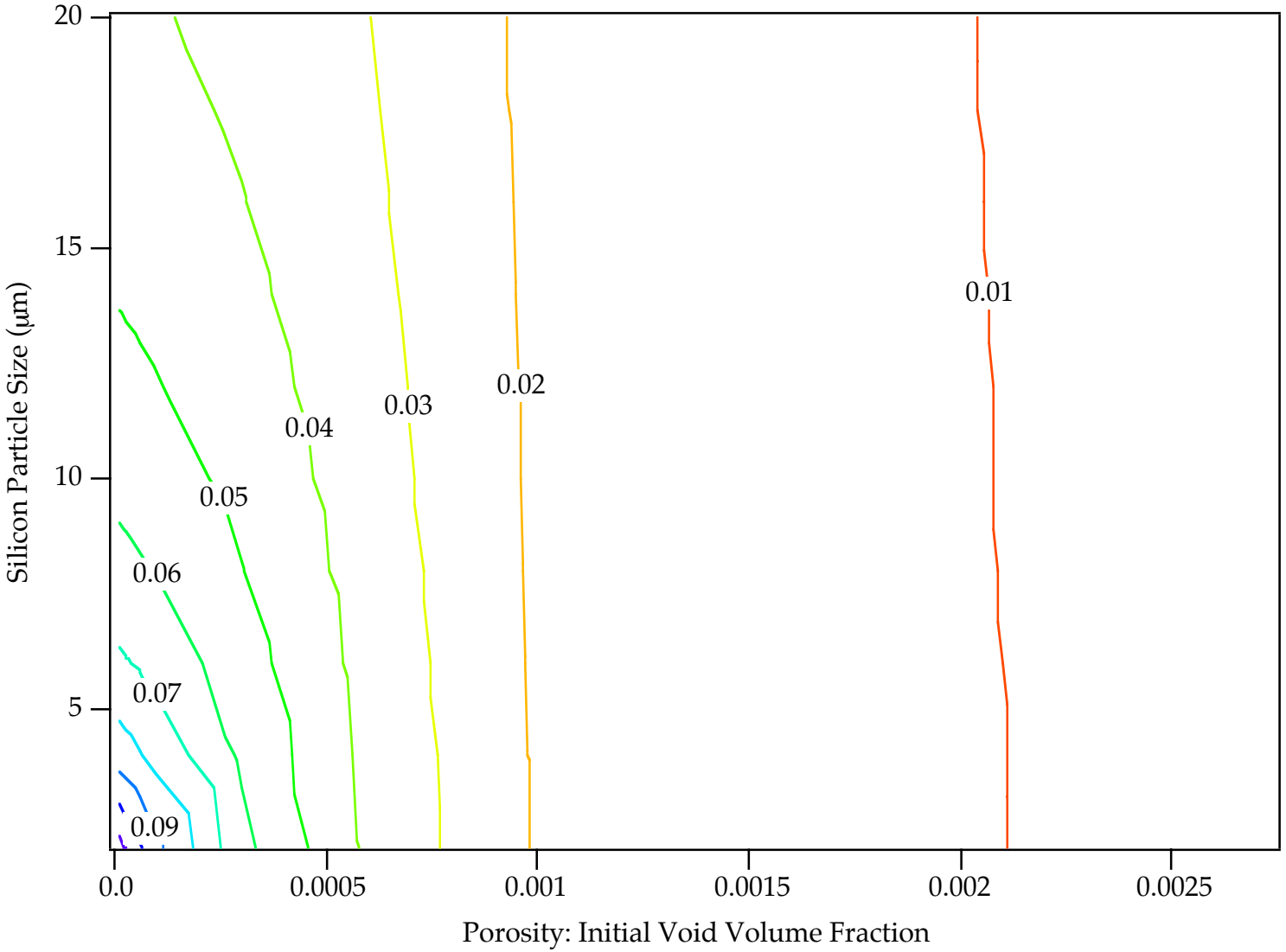

T = 297K
$\dot{\varepsilon}$ = .0002 / sec
DCS = 50 μm

f(Si) = 7%
K_{IC} = 17.3 MPa-mm$^{1/2}$
Biaxial Tension

Failure Strain - Map09

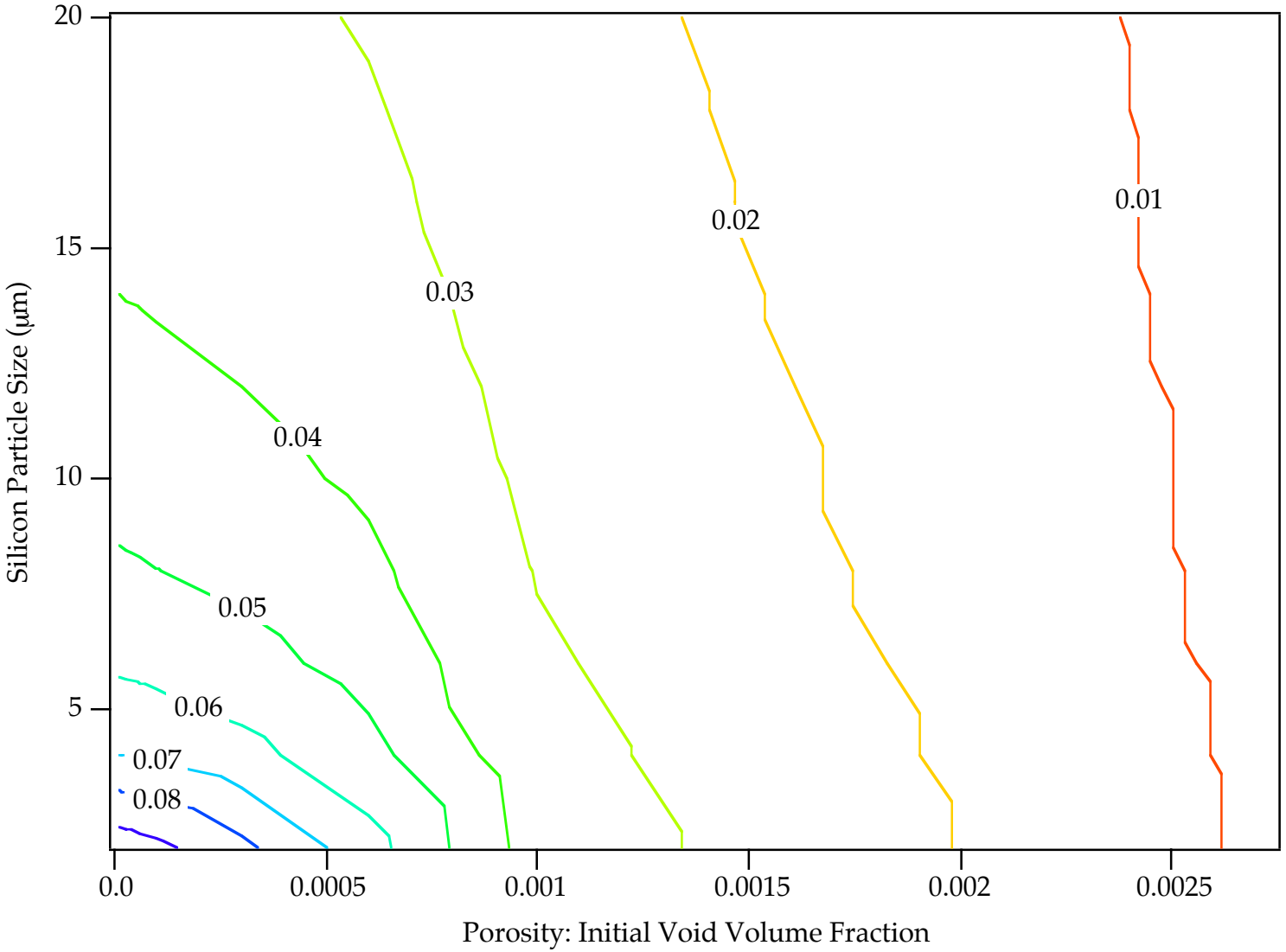

T = 297K
$\dot{\varepsilon}$ = .0002 / sec
DCS = 50 μm

f(Si) = 7%
K_{IC} = 17.3 MPa-mm$^{1/2}$
Plane Strain

Failure Strain - Map10

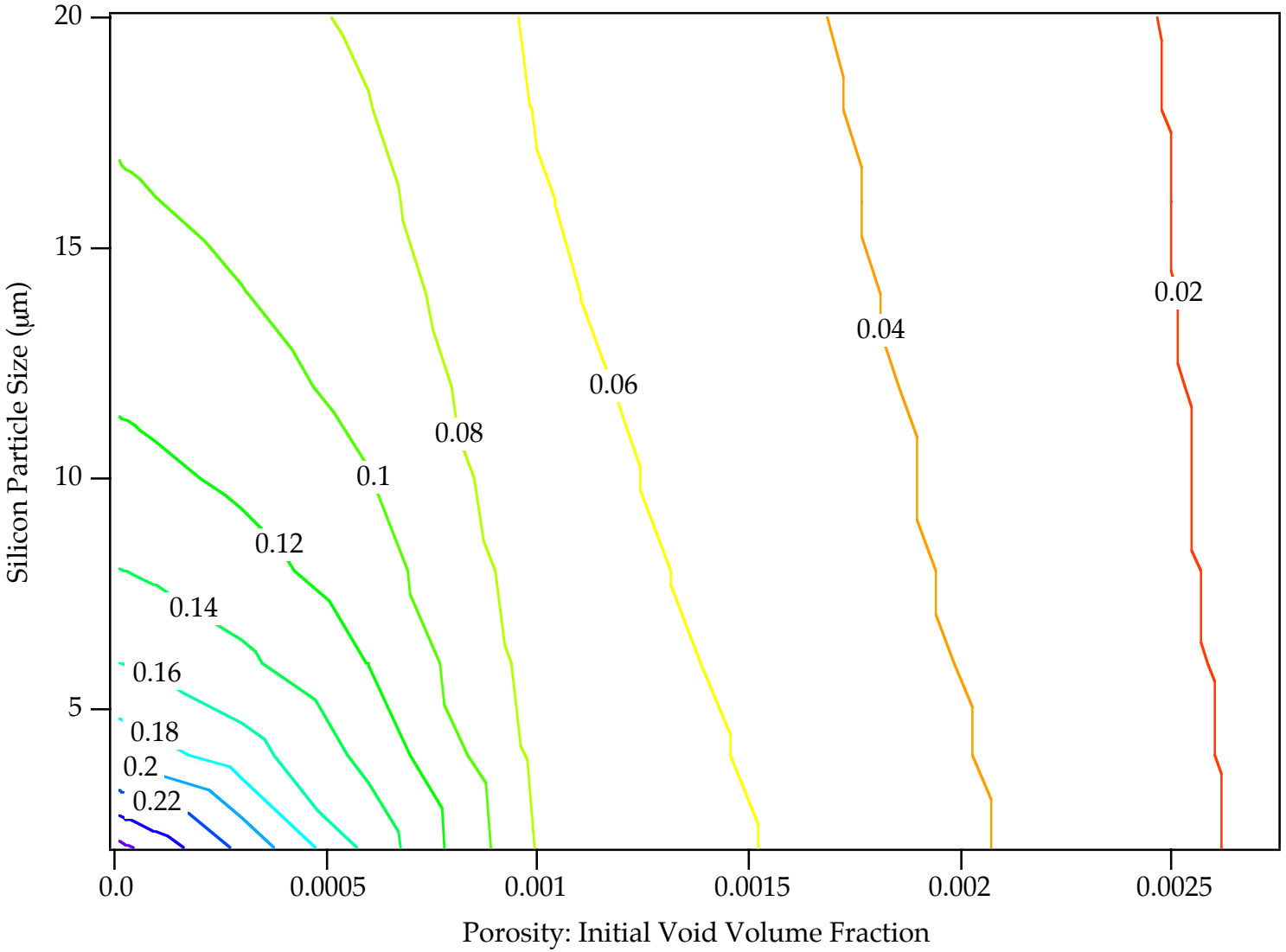

T = 297K
$\dot{\varepsilon}$ = 1000 /sec
DCS = 50 μm

f(Si) = 7%
K_{IC} = 17.3 MPa-mm$^{1/2}$
Uniaxial Tension

Failure Strain - Map11

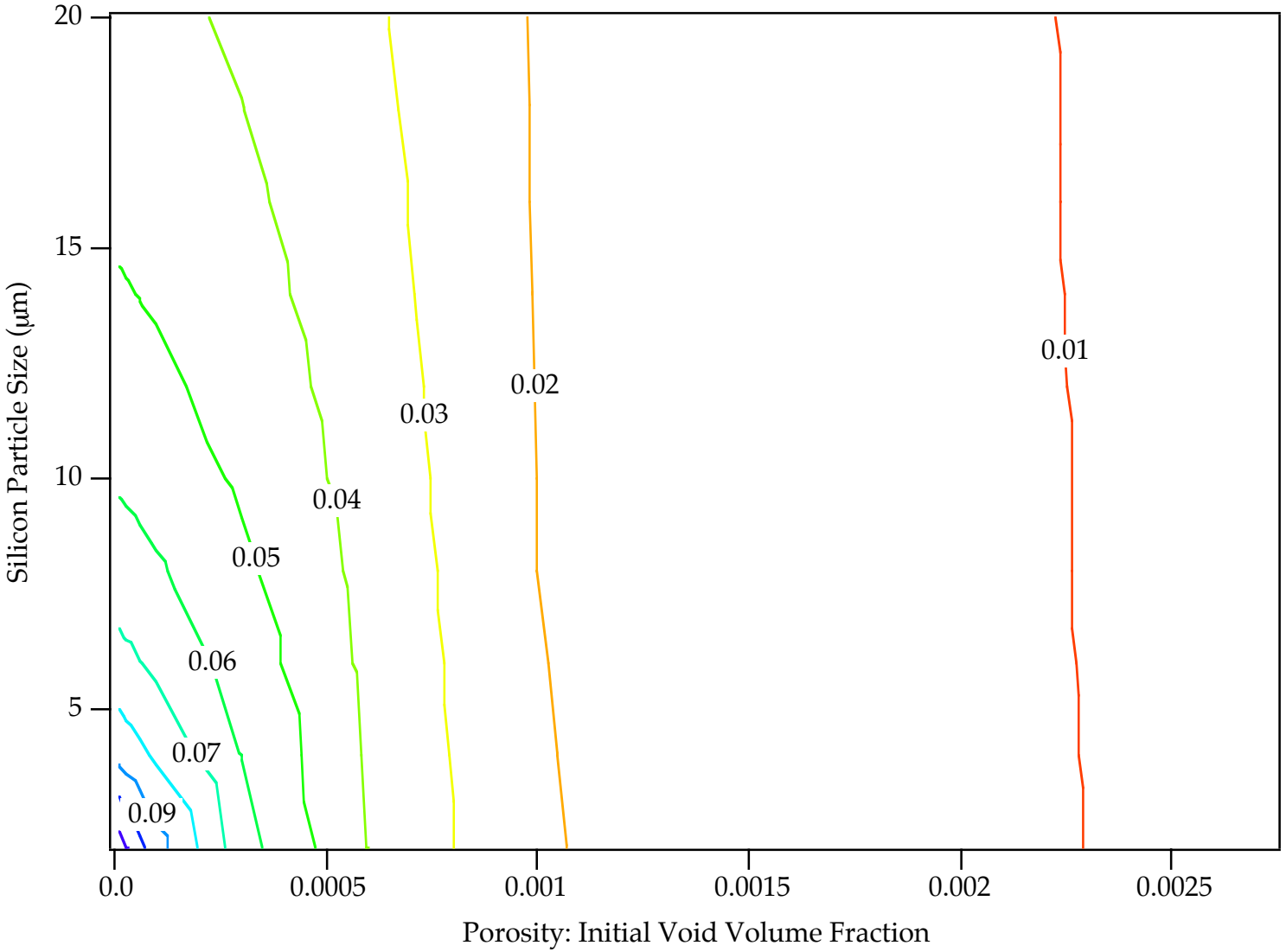

T = 297K
$\dot{\varepsilon}$ = 1000 /sec
DCS = 50 µm

f(Si) = 7%
K_{IC} = 17.3 MPa-mm$^{1/2}$
Biaxial Tension

Failure Strain - Map12

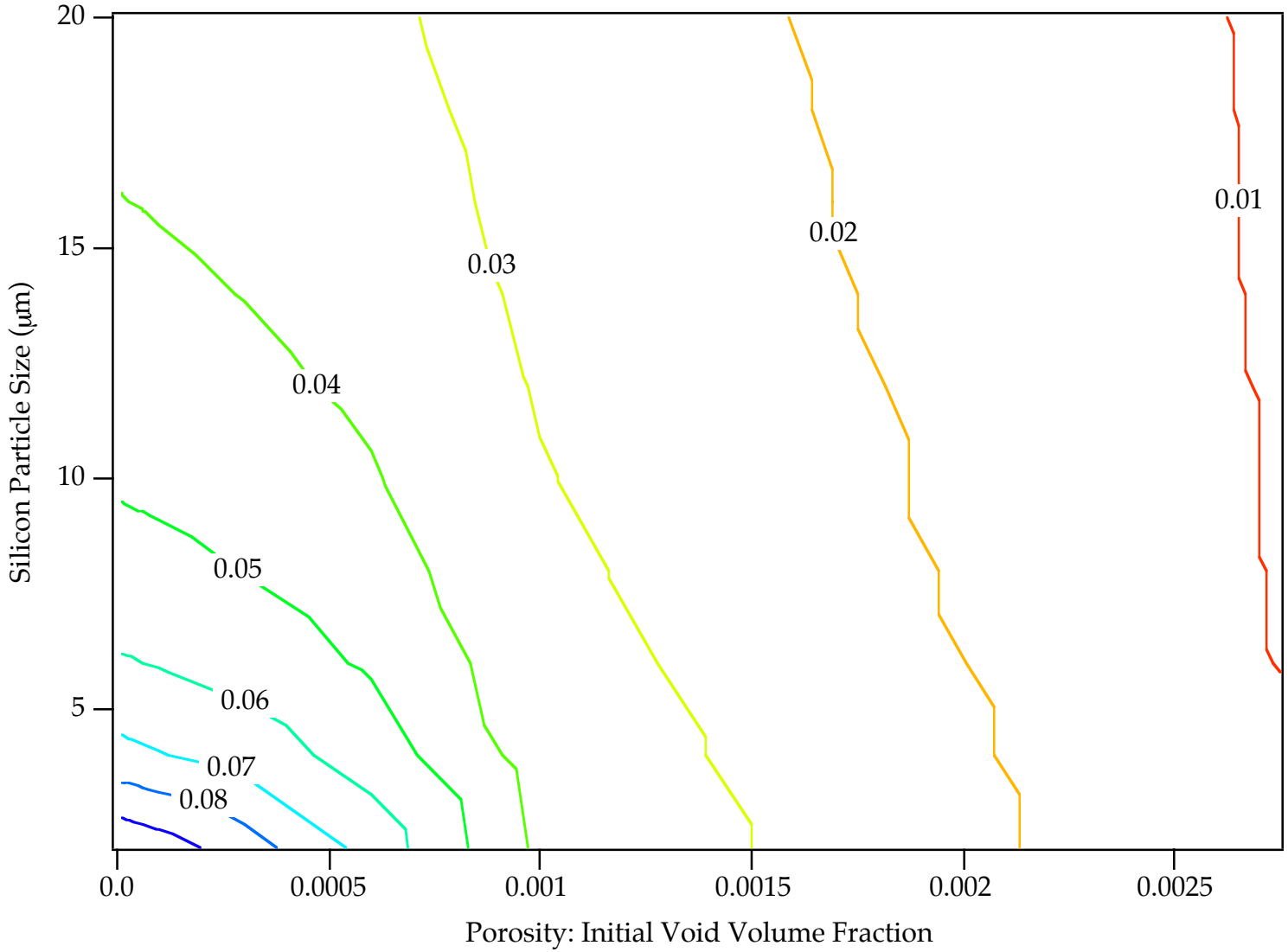

T = 297K
$\dot{\varepsilon}$ = 1000 /sec
DCS = 50 μm

f(Si) = 7%
K_{IC} = 17.3 MPa-mm$^{1/2}$
Plane Strain

Failure Strain - Map13

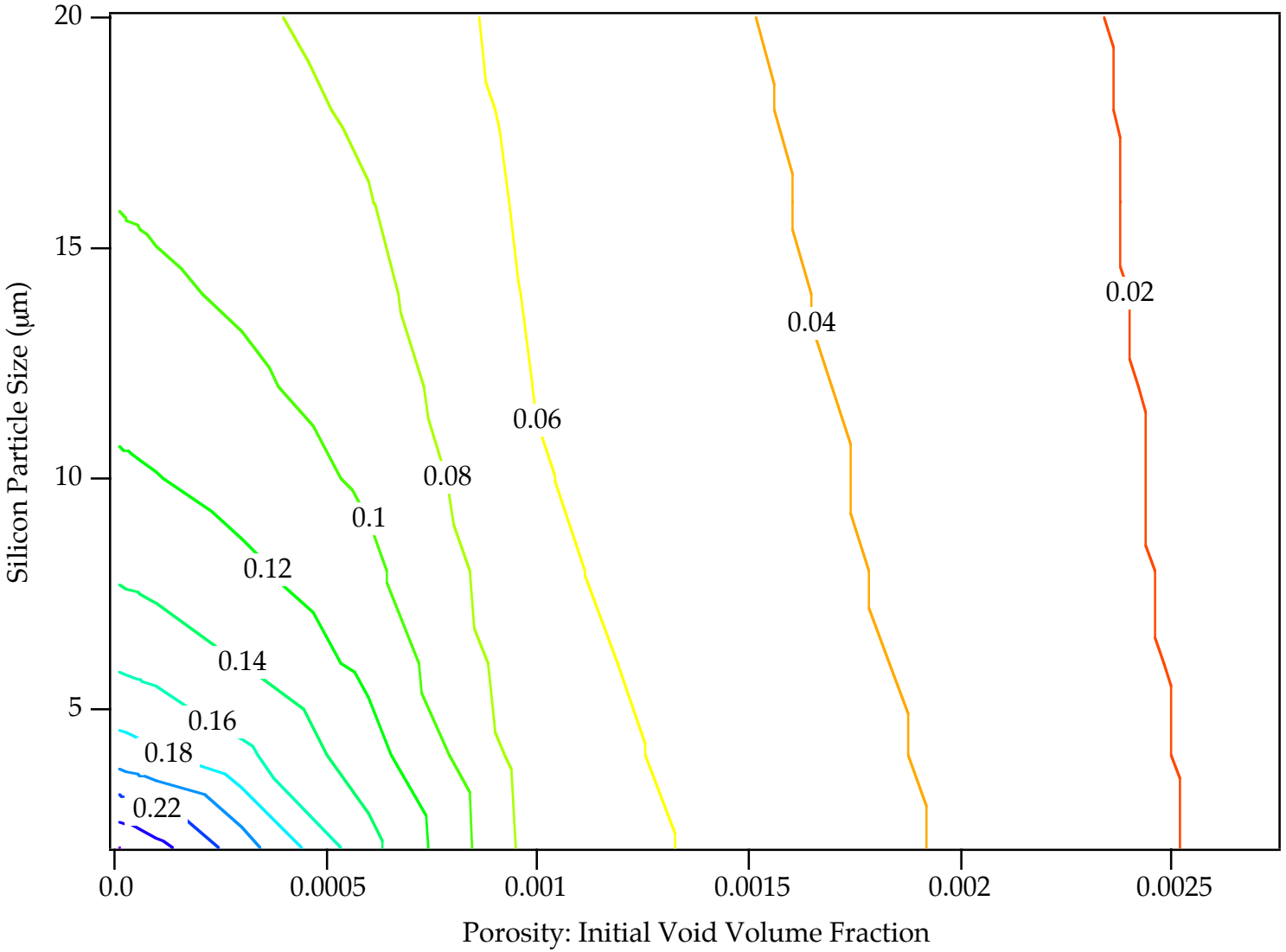

T = 297K
$\dot{\varepsilon}$ = .0002 / sec
DCS = 100 μm

f(Si) = 7%
K_{IC} = 17.3 MPa-mm$^{1/2}$
Uniaxial Tension

Failure Strain - Map14

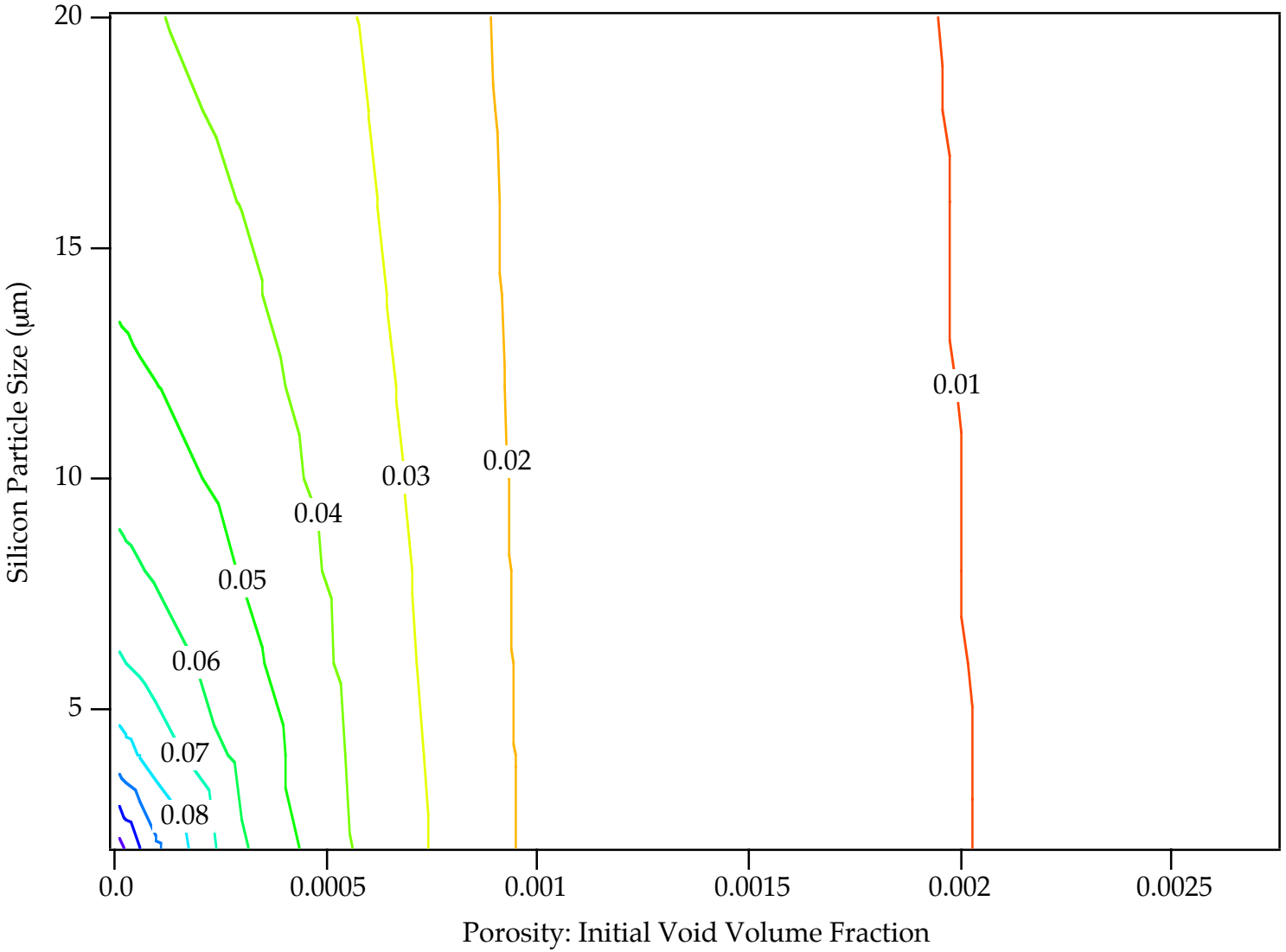

T = 297K
$\dot{\varepsilon}$ = .0002 / sec
DCS = 100 μm

f(Si) = 7%
K_{IC} = 17.3 MPa-mm$^{1/2}$
Biaxial Tension

Failure Strain - Map15

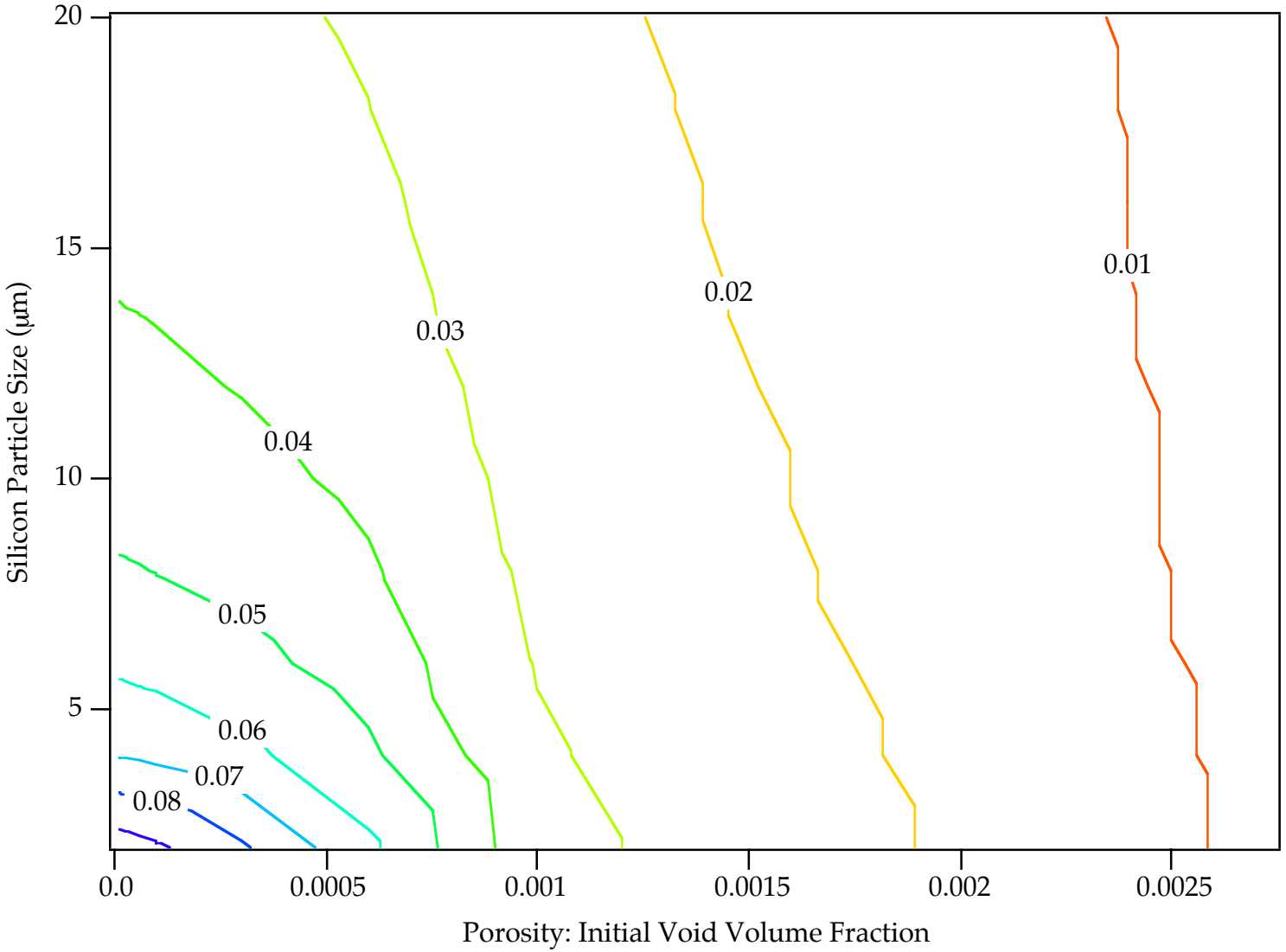

T = 297K
$\dot{\varepsilon}$ = .0002 / sec
DCS = 100 μm

f(Si) = 7%
K_{IC} = 17.3 MPa-mm$^{1/2}$
Plane Strain

Failure Strain - Map16

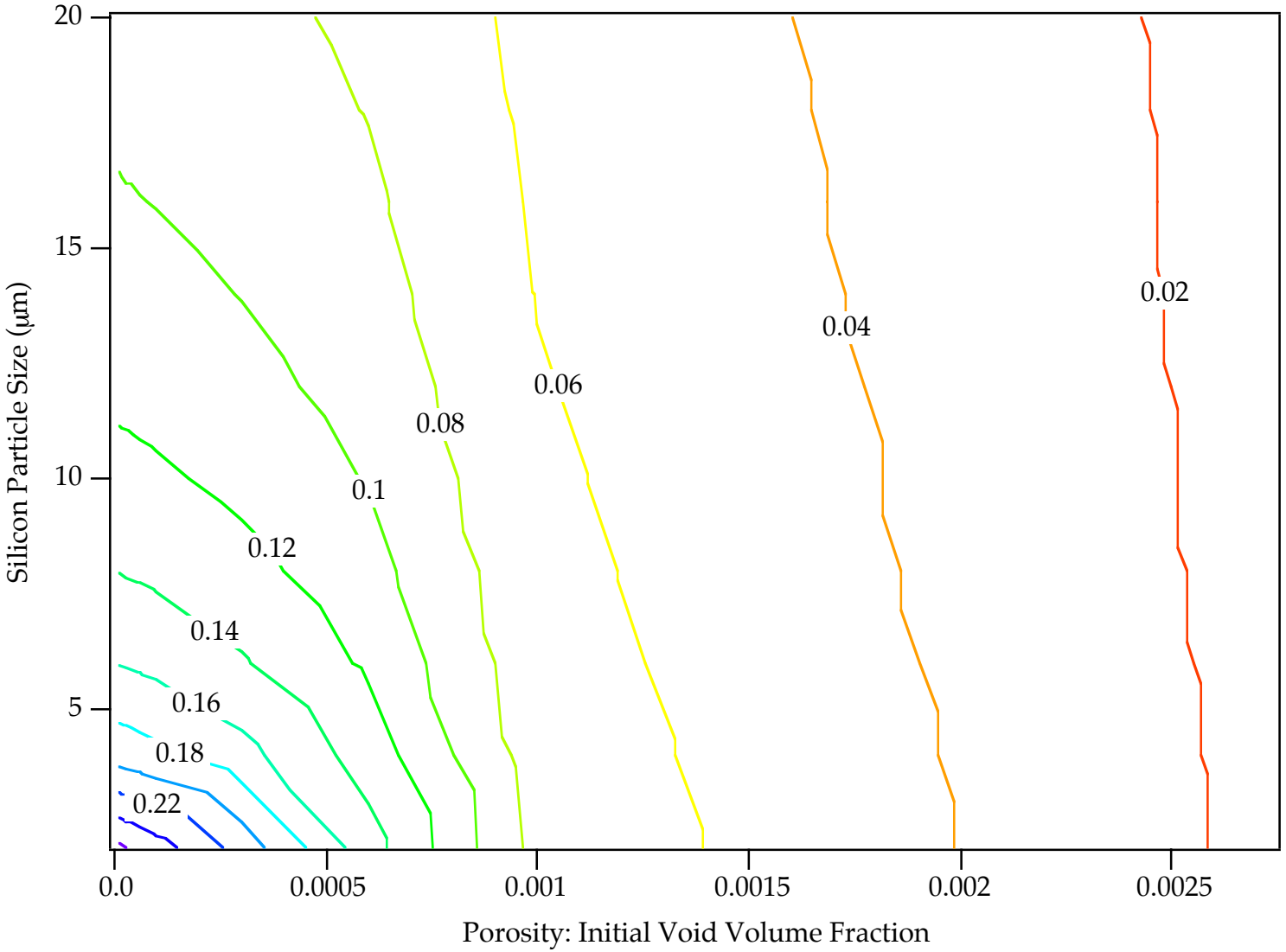

T = 297K
$\dot{\varepsilon}$ = 1000 /sec
DCS = 100 μm

f(Si) = 7%
K_{IC} = 17.3 MPa-mm$^{1/2}$
Uniaxial Tension

Failure Strain - Map17

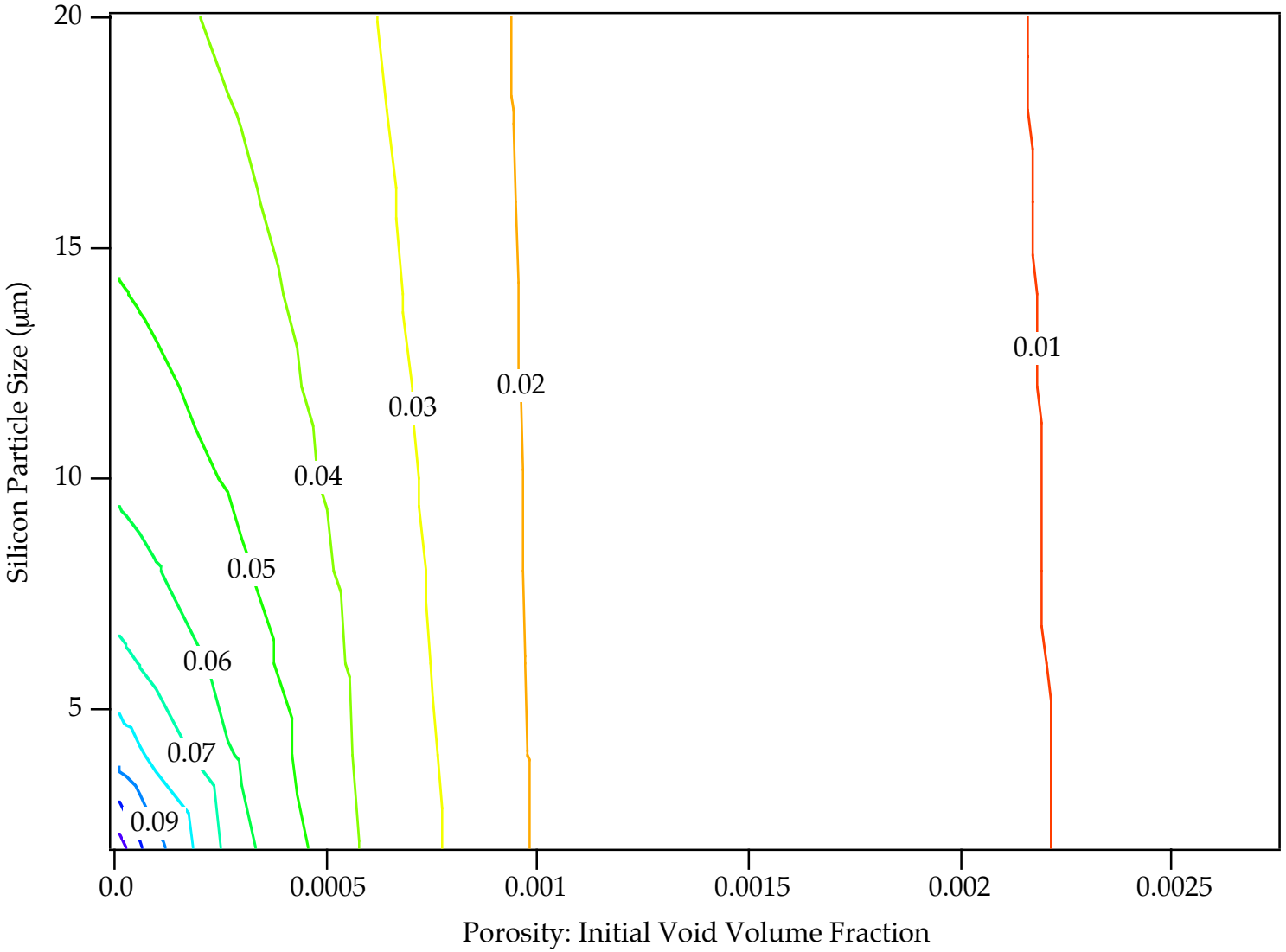

T = 297K
$\dot{\varepsilon}$ = 1000 /sec
DCS = 100 μm

f(Si) = 7%
K_{IC} = 17.3 MPa-mm$^{1/2}$
Biaxial Tension

Failure Strain - Map18

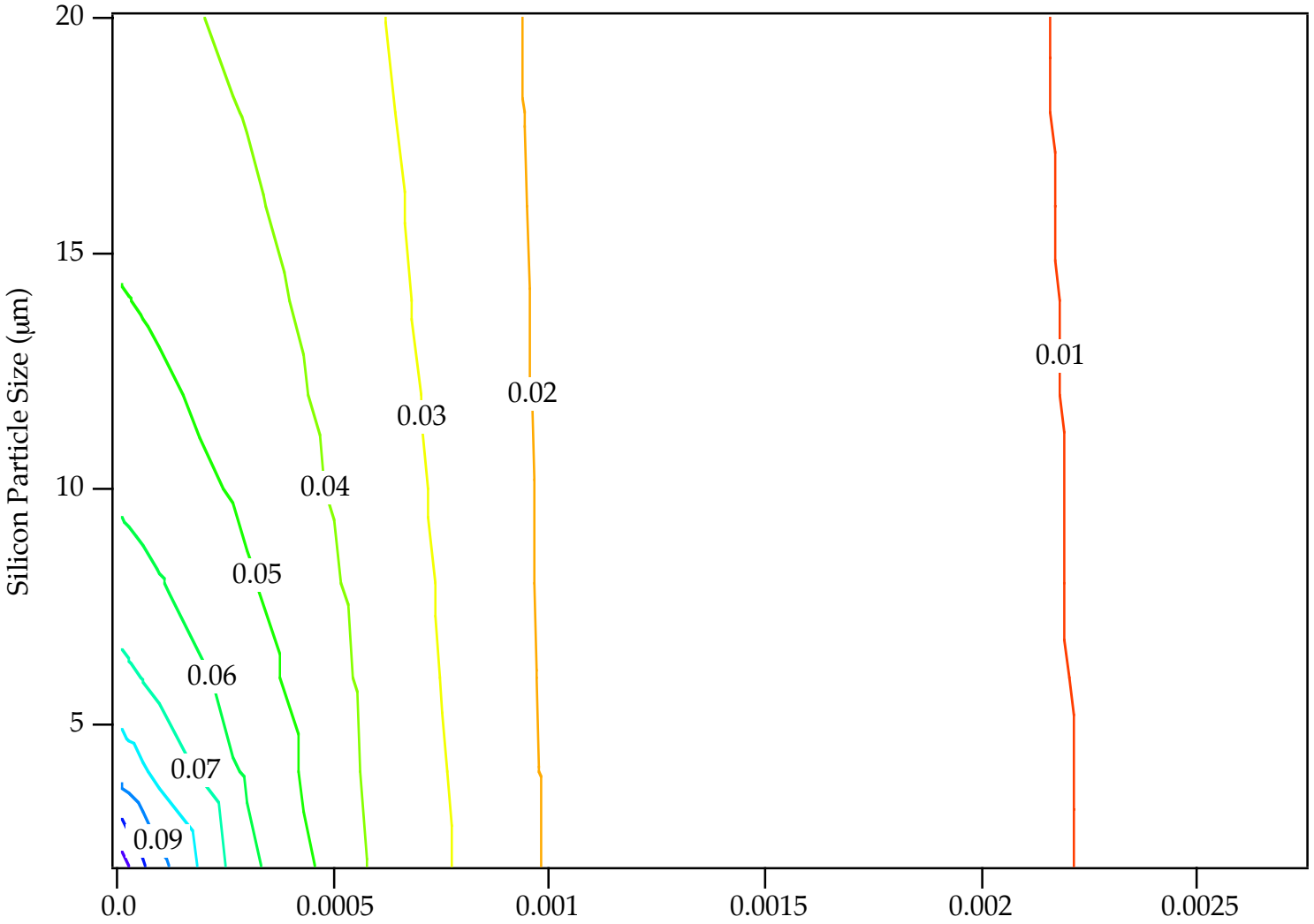

T = 297K
$\dot{\varepsilon}$ = 1000 /sec
DCS = 100 µm

f(Si) = 7%
K_{IC} = 17.3 MPa-mm$^{1/2}$
Plane Strain

Failure Strain - Map19

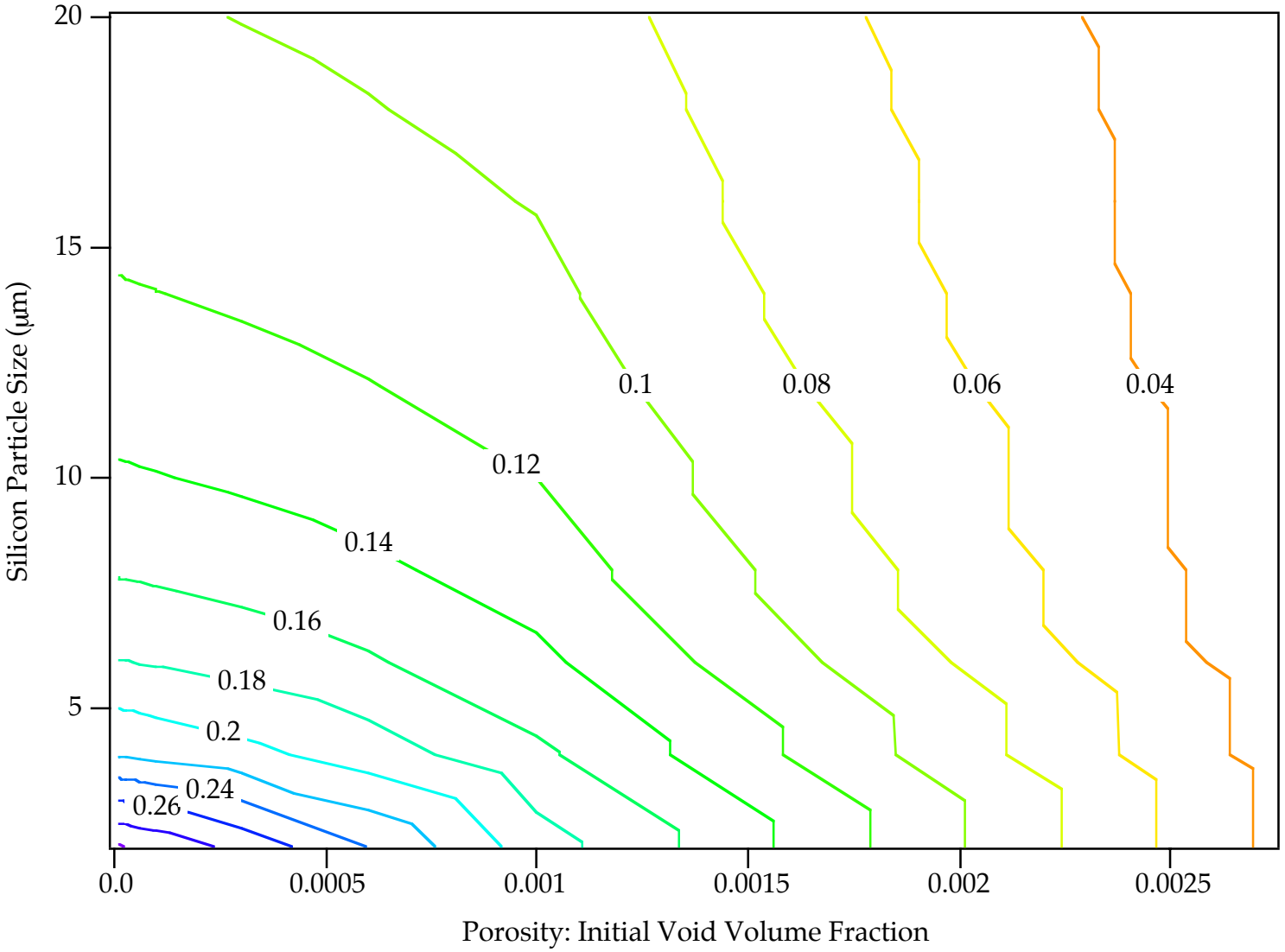

T = 222K
$\dot{\varepsilon}$ = .0002 /sec
DCS = 20 μm

f(Si) = 7%
K_{IC} = 17.3 MPa-$mm^{1/2}$
Uniaxial Tension

Failure Strain - Map20

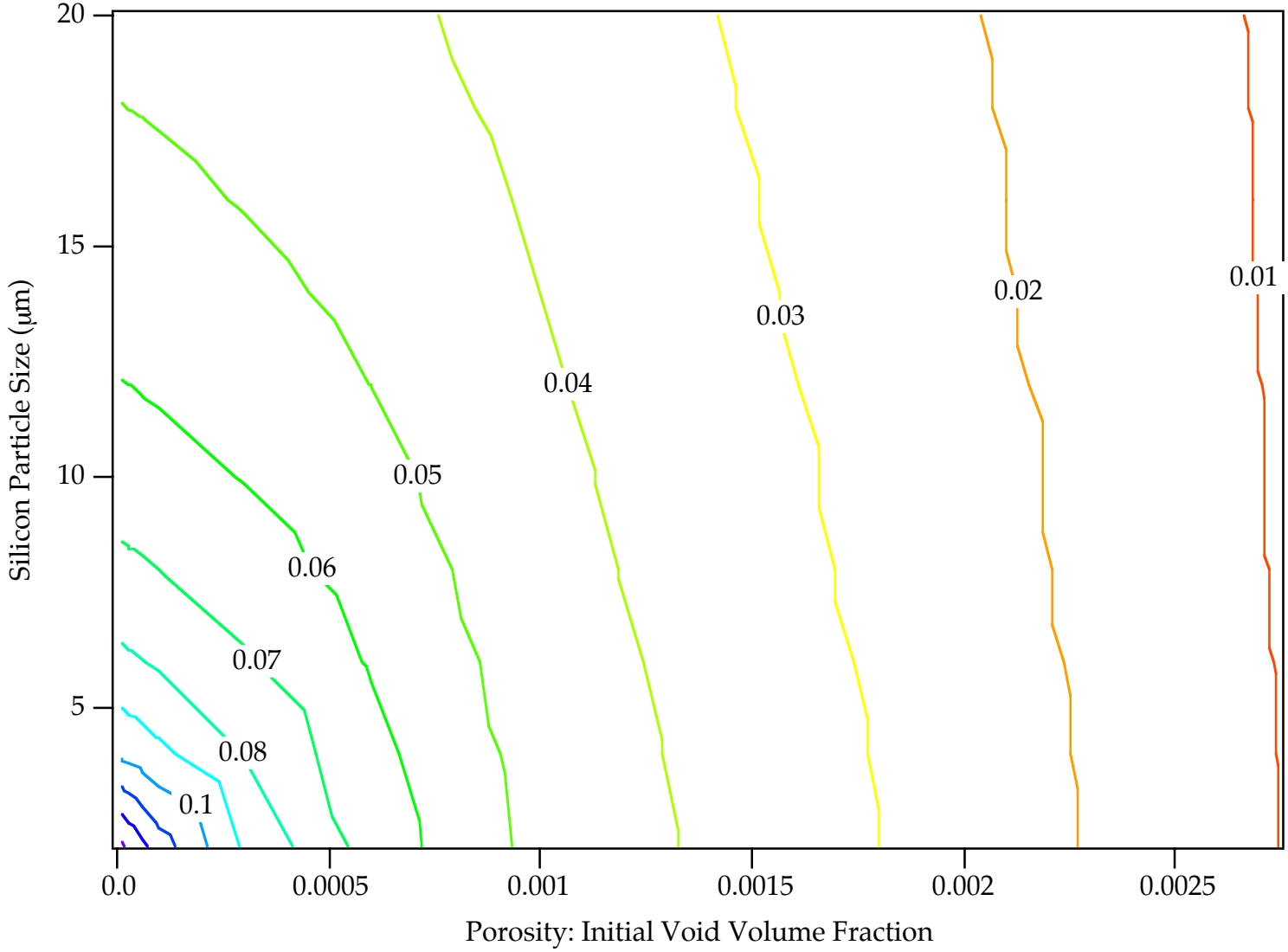

T = 222K
$\dot{\varepsilon}$ = .0002 /sec
DCS = 20 μm

f(Si) = 7%
K_{IC} = 17.3 MPa-$mm^{1/2}$
Biaxial Tension

Failure Strain - Map21

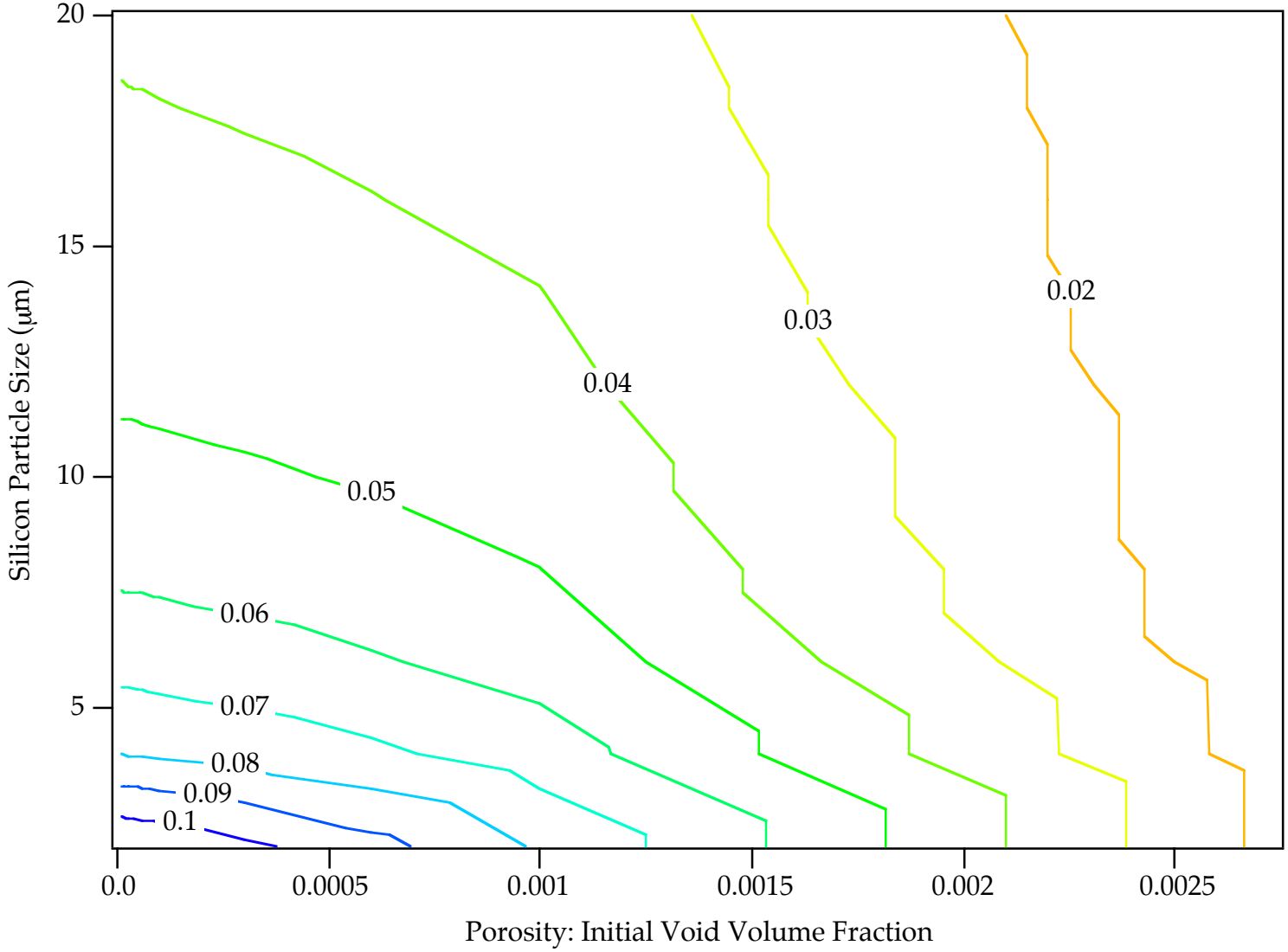

T = 222K
$\dot{\varepsilon}$ = .0002 /sec
DCS = 20 μm

f(Si) = 7%
K_{IC} = 17.3 MPa-$mm^{1/2}$
Plane Strain

Failure Strain - Map22

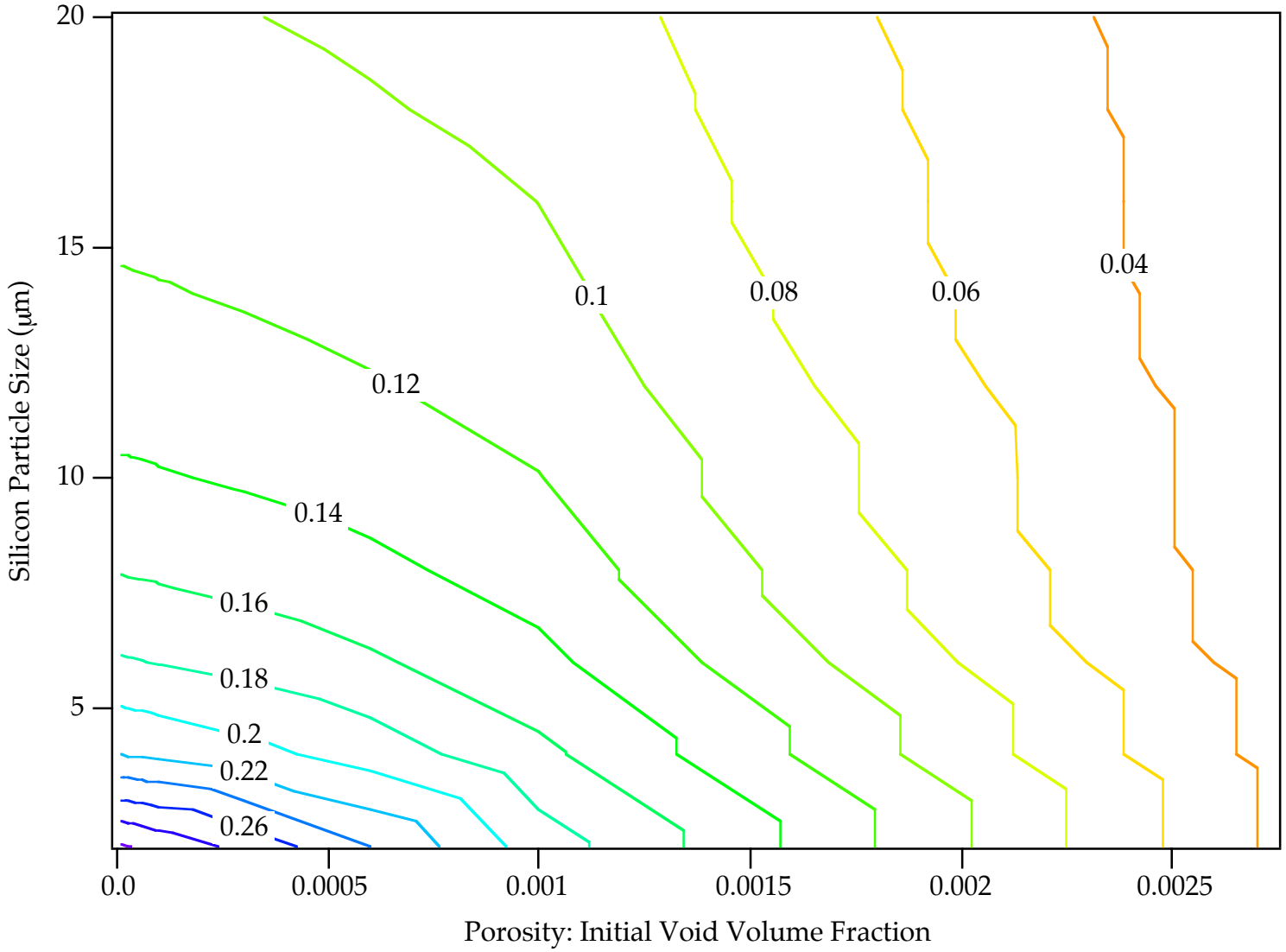

T = 222K
$\dot{\varepsilon}$ = 1000 /sec
DCS = 20 μm

f(Si) = 7%
K_{IC} = 17.3 MPa-$mm^{1/2}$
Uniaxial Tension

Failure Strain - Map23

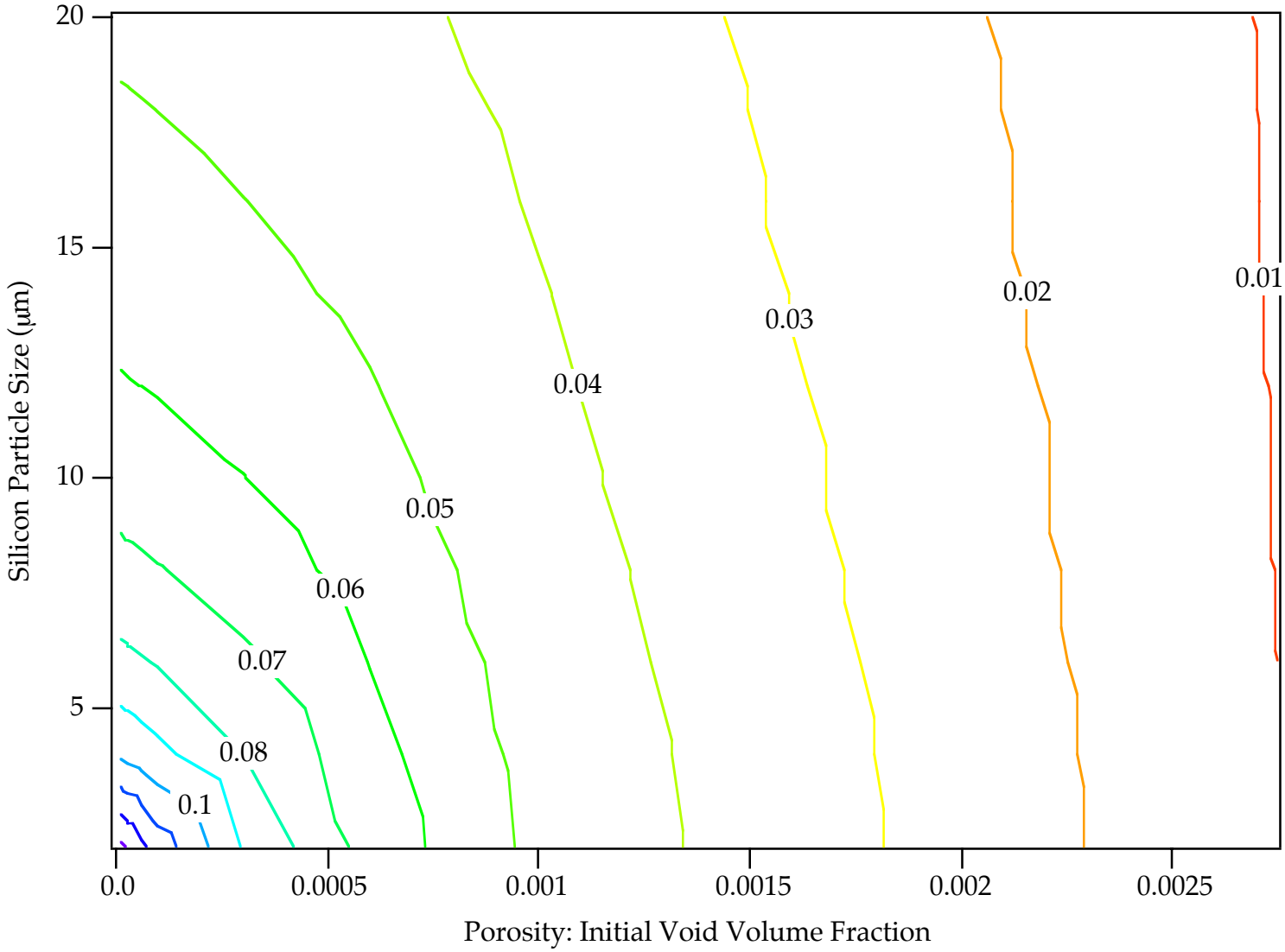

T = 222K
$\dot{\varepsilon}$ = 1000 /sec
DCS = 20 μm

f(Si) = 7%
K_{IC} = 17.3 MPa-mm$^{1/2}$
Biaxial Tension

Failure Strain - Map24

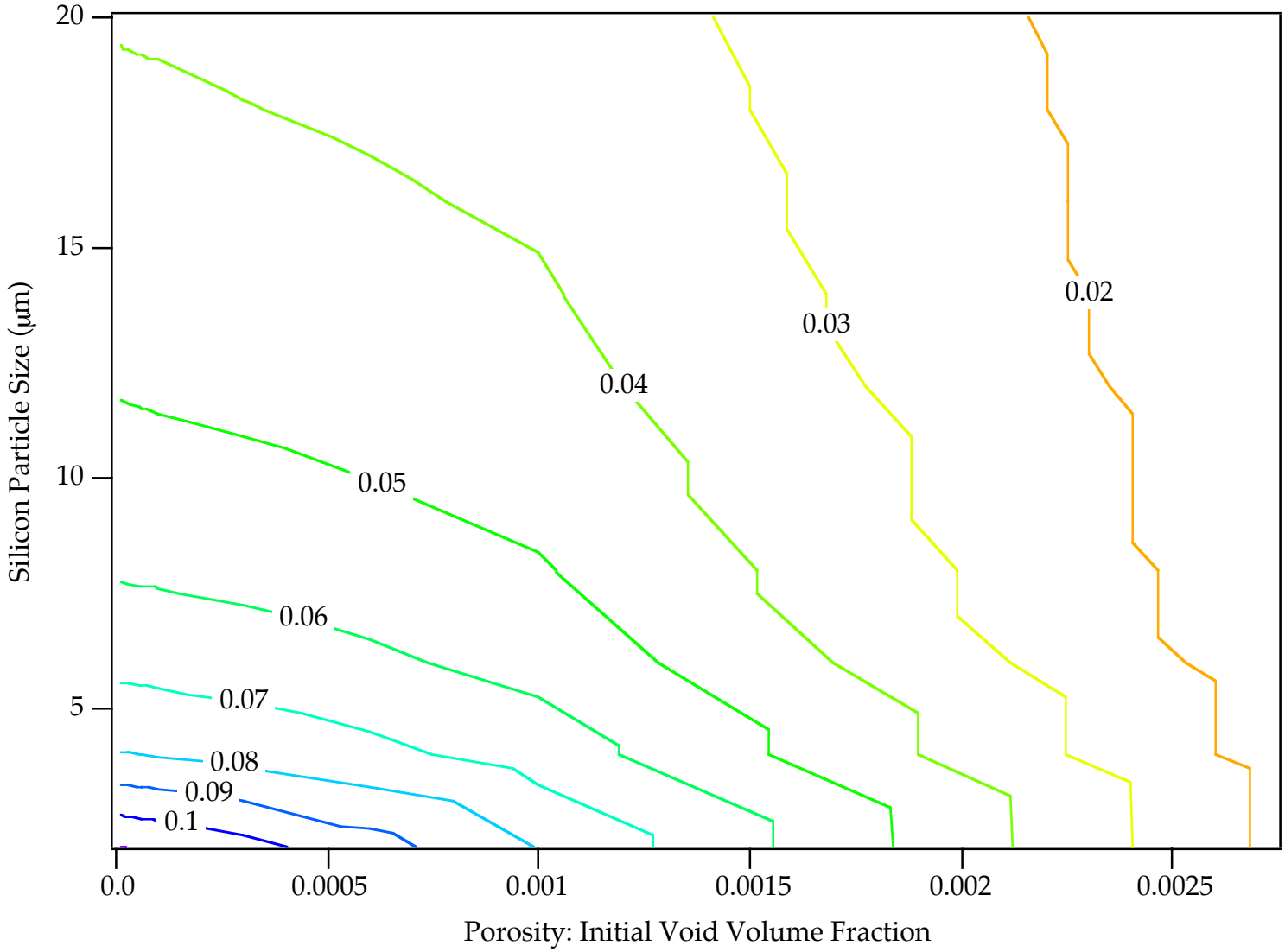

T = 222K
$\dot{\varepsilon}$ = 1000 / sec
DCS = 20 μm

f(Si) = 7%
K_{IC} = 17.3 MPa-mm$^{1/2}$
Plane Strain

Failure Strain - Map25

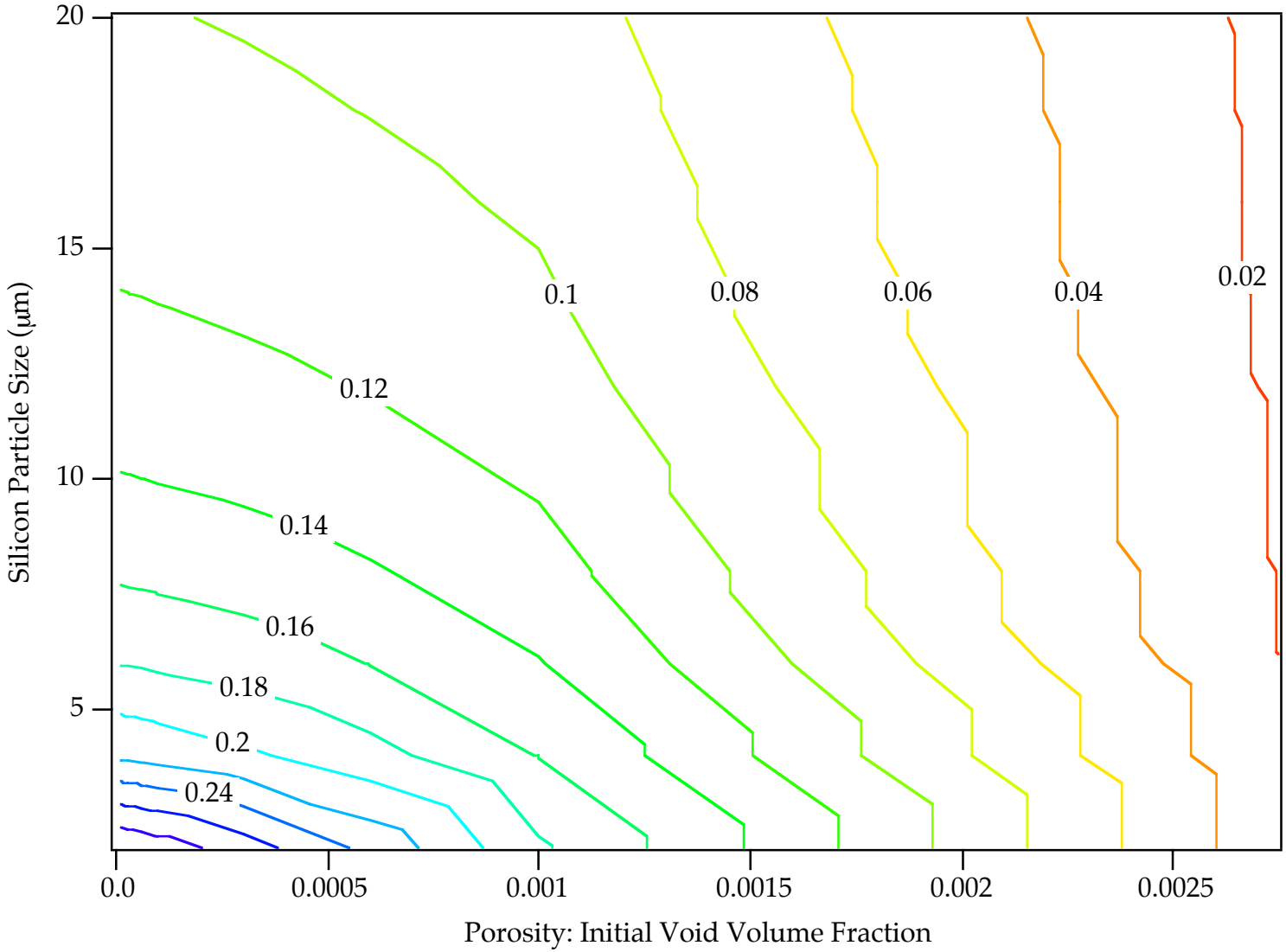

T = 222K
$\dot{\varepsilon}$ = .0002 /sec
DCS = 50 μm

f(Si) = 7%
K_{IC} = 17.3 MPa-mm$^{1/2}$
Uniaxial Tension

Failure Strain - Map26

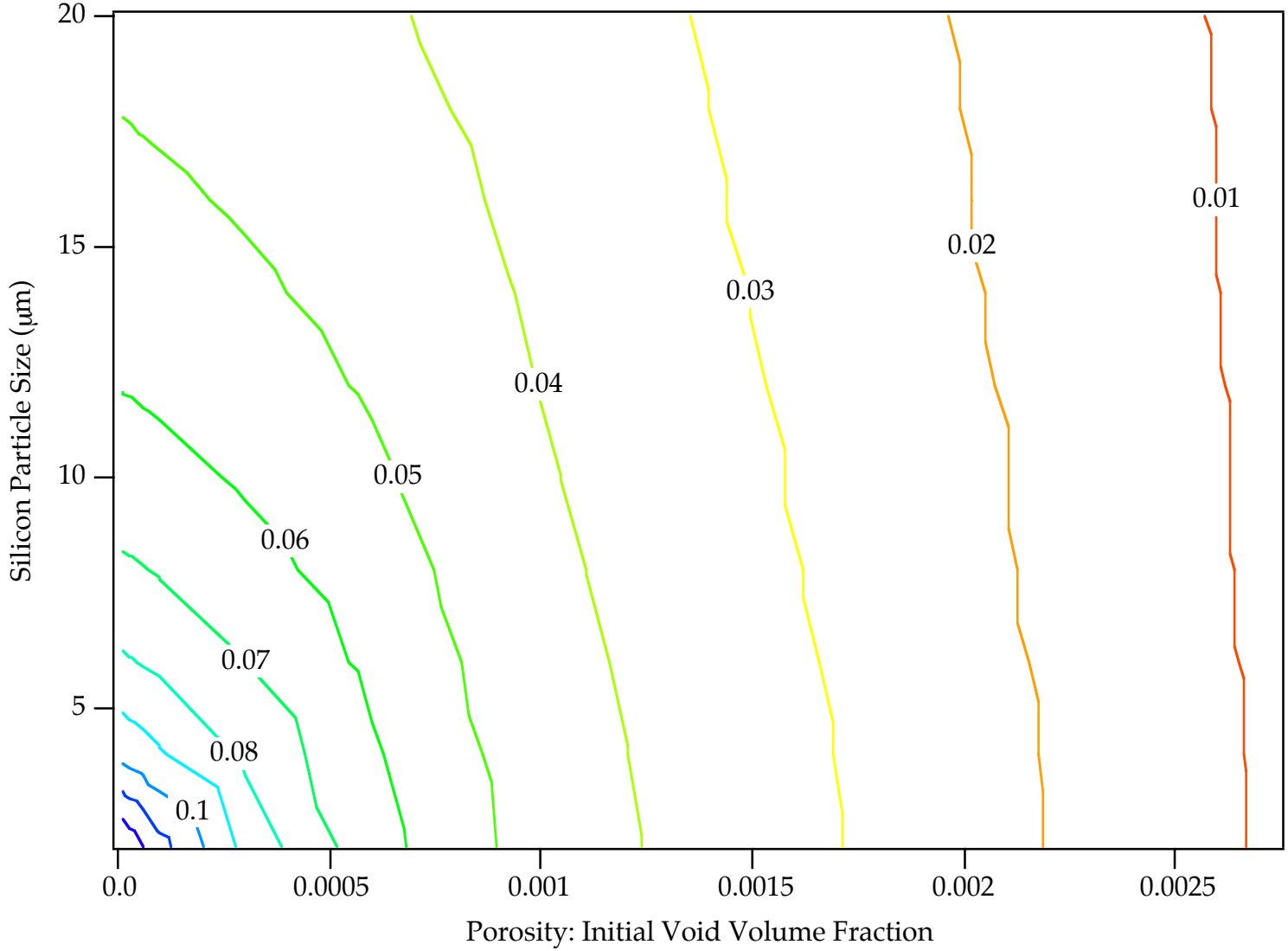

T = 222K
$\dot{\varepsilon}$ = .0002 /sec
DCS = 50 μm

f(Si) = 7%
K_{IC} = 17.3 MPa-mm$^{1/2}$
Biaxial Tension

Failure Strain - Map27

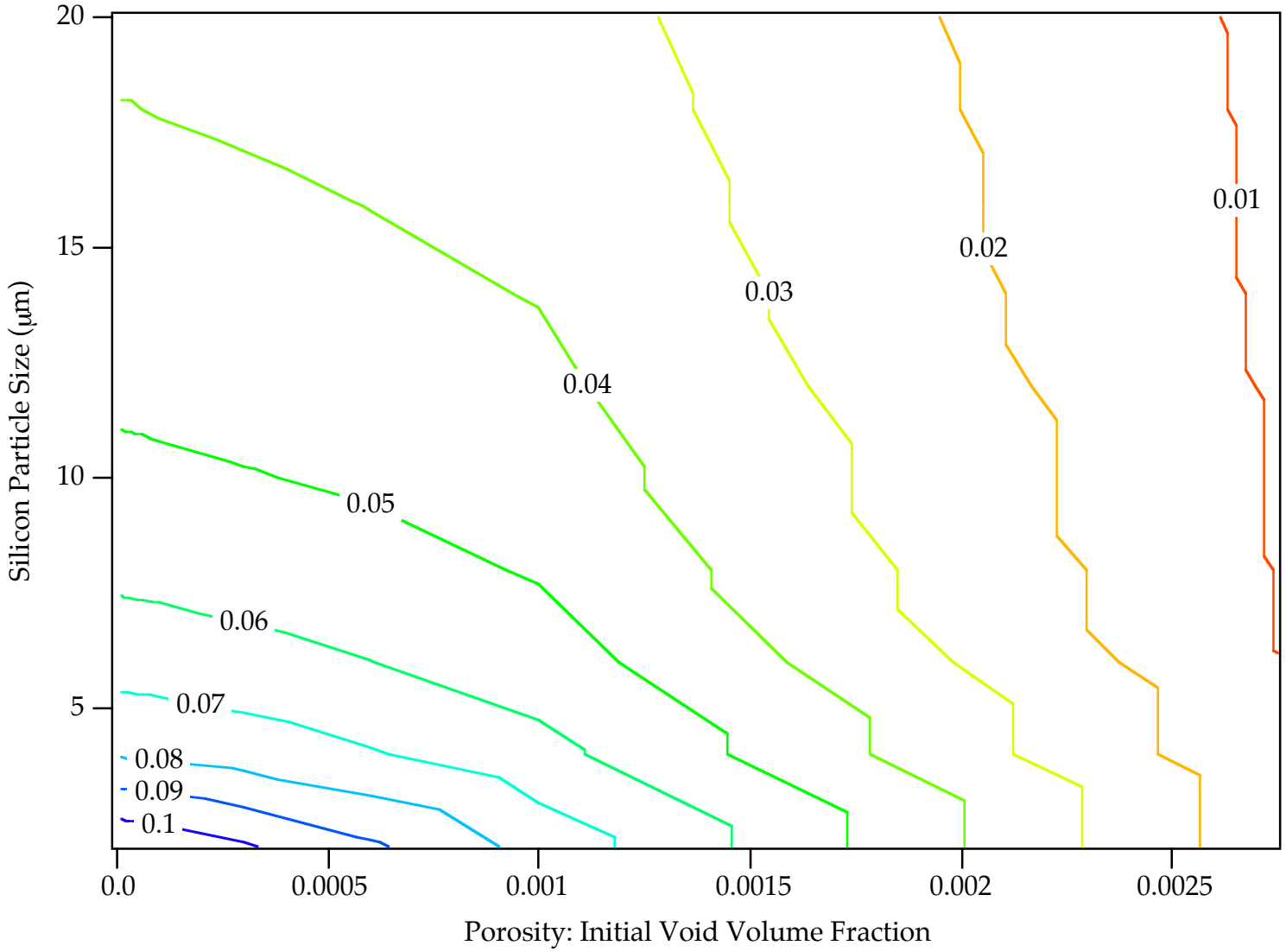

T = 222K
$\dot{\varepsilon}$ = .0002 /sec
DCS = 50 μm

f(Si) = 7%
K_{IC} = 17.3 MPa-$mm^{1/2}$
Plane Strain

Failure Strain - Map28

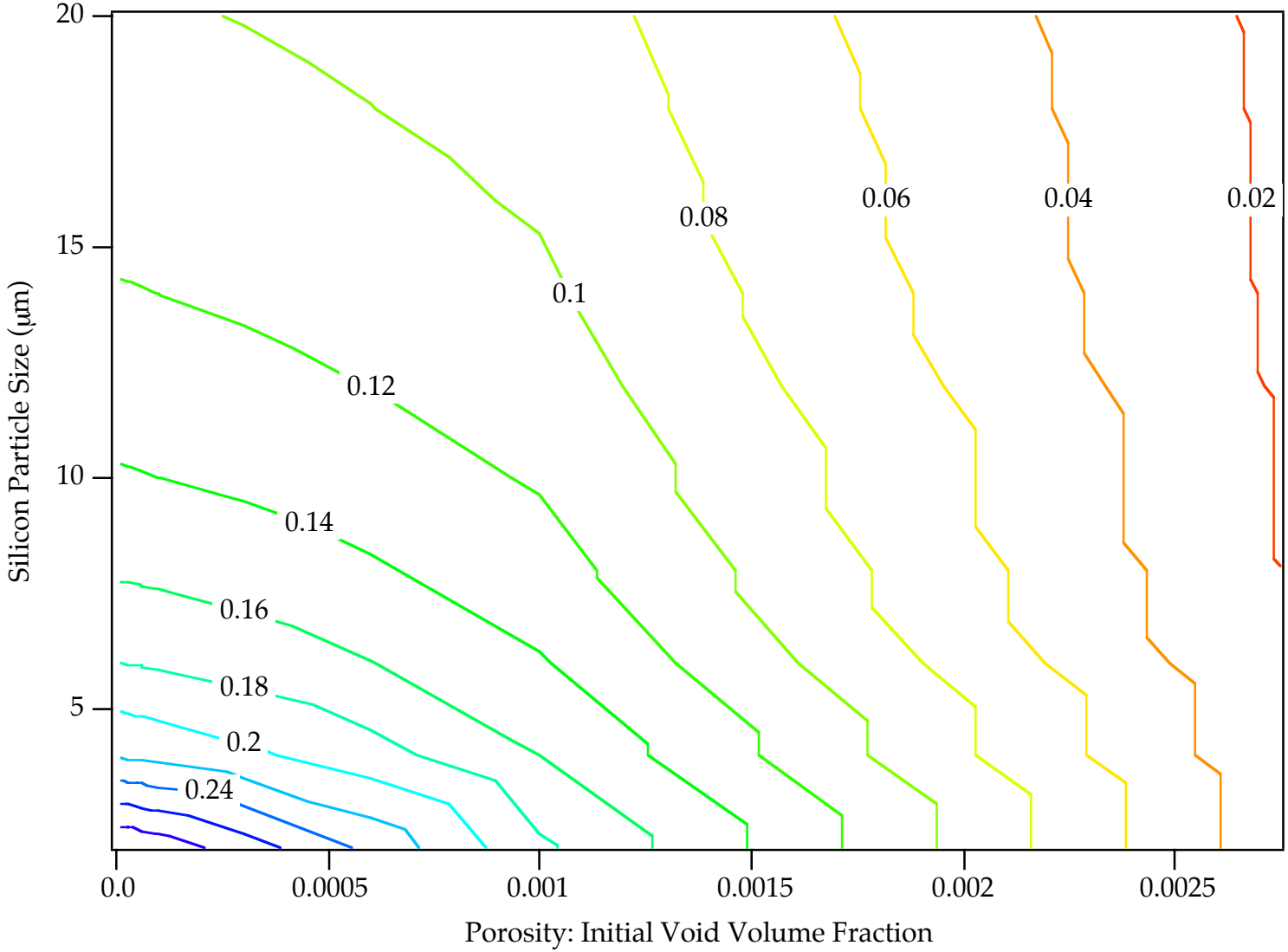

T = 222K
$\dot{\varepsilon}$ = 1000 /sec
DCS = 50 μm

f(Si) = 7%
K_{IC} = 17.3 MPa-mm$^{1/2}$
Uniaxial Tension

Failure Strain - Map29

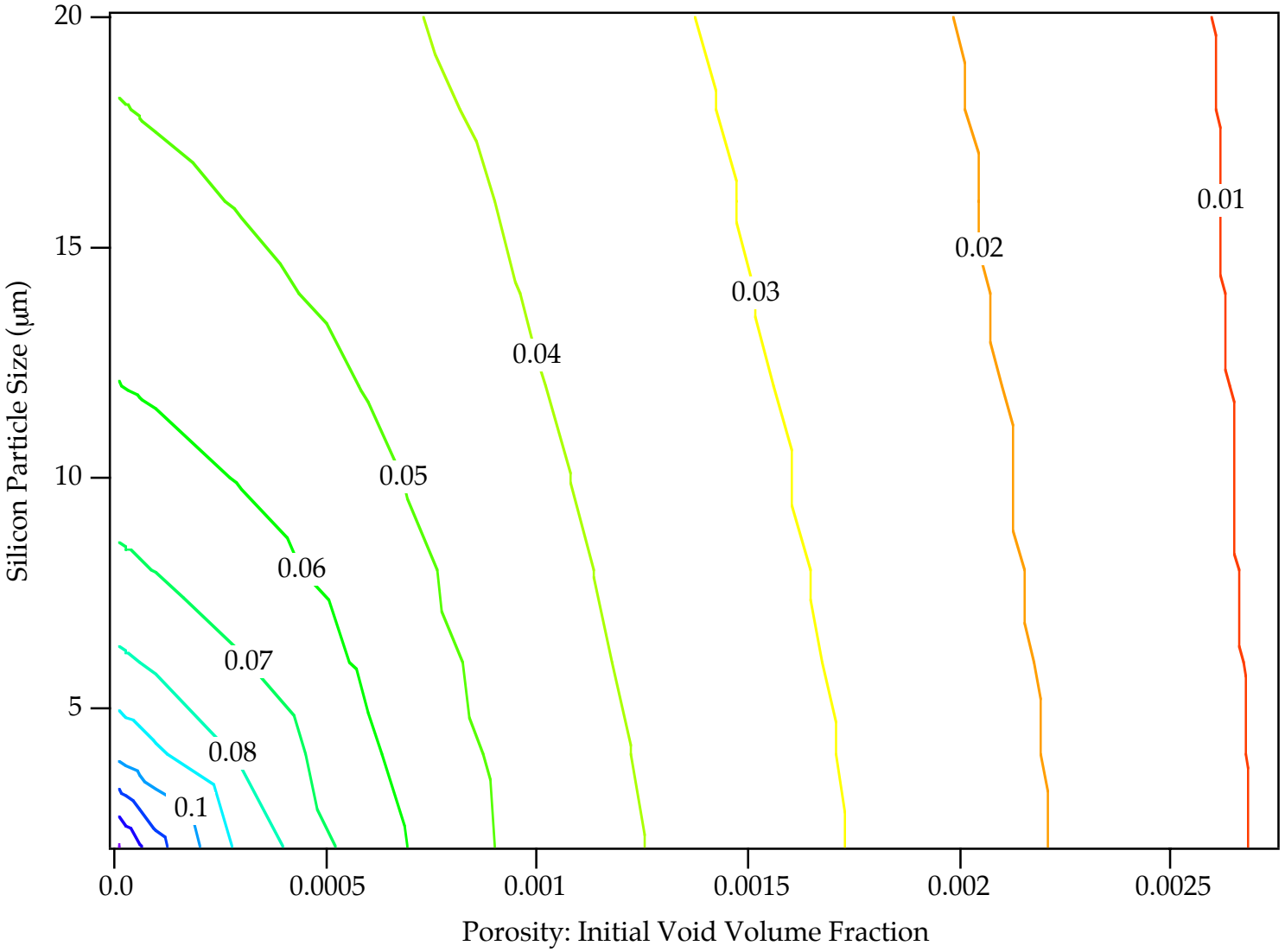

T = 222K
$\dot{\varepsilon}$ = 1000 /sec
DCS = 50 μm

f(Si) = 7%
K_{IC} = 17.3 MPa-$mm^{1/2}$
Biaxial Tension

Failure Strain - Map30

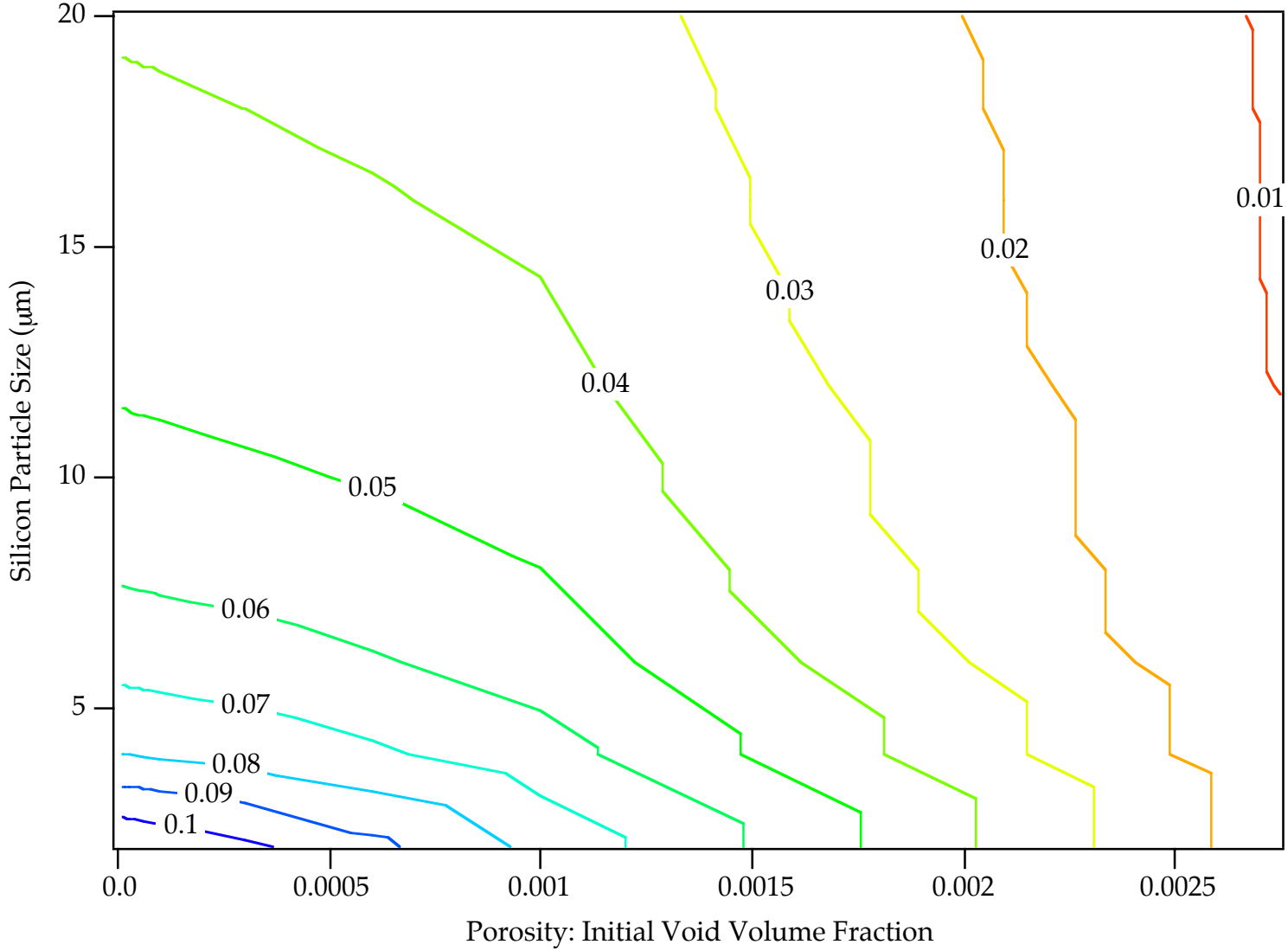

T = 222K
$\dot{\varepsilon}$ = 1000 /sec
DCS = 50 μm

f(Si) = 7%
K_{IC} = 17.3 MPa-mm$^{1/2}$
Plane Strain

Failure Strain - Map31

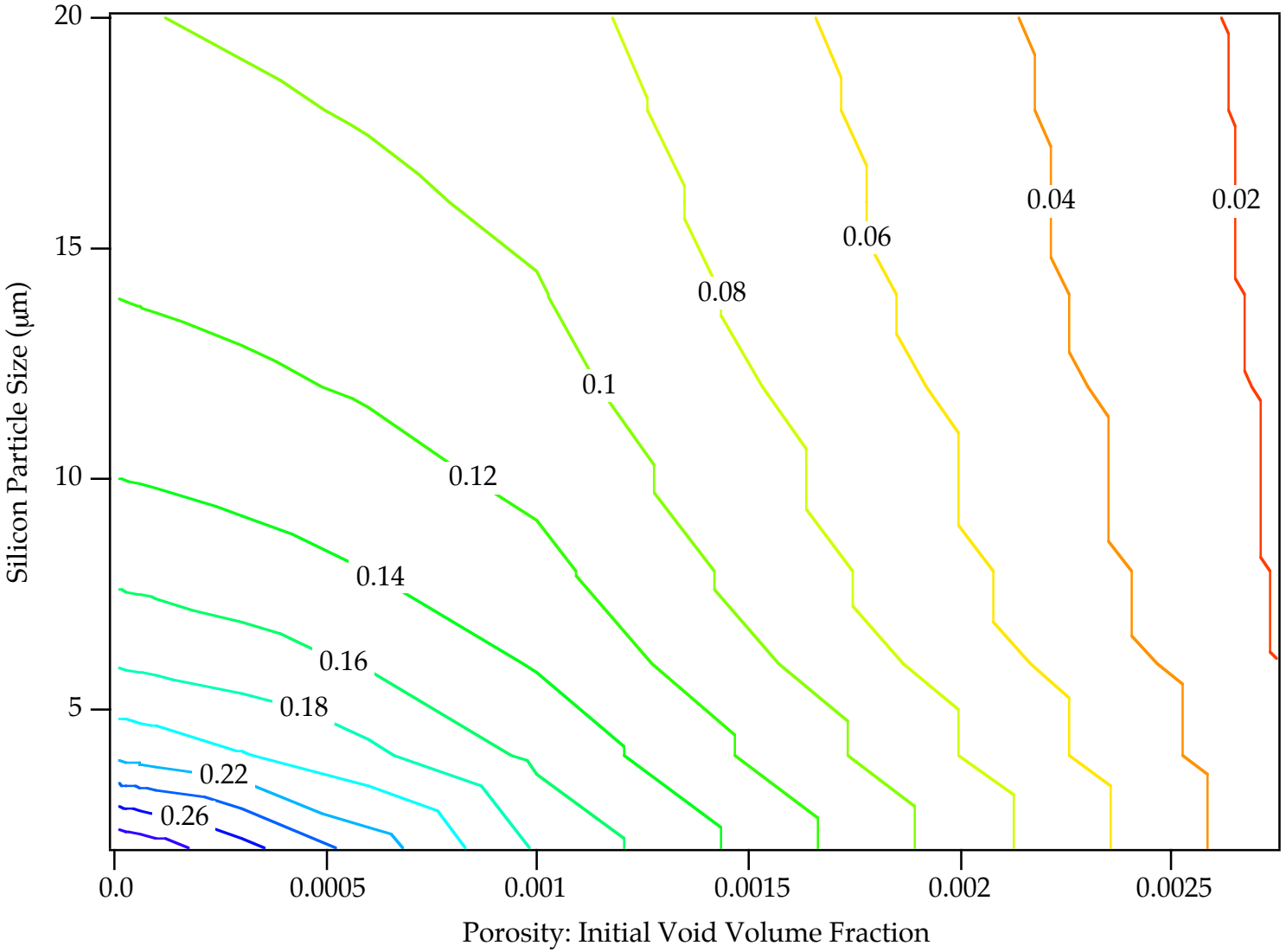

T = 222K
$\dot{\varepsilon}$ = .0002 /sec
DCS = 100 μm

f(Si) = 7%
K_{IC} = 17.3 MPa-mm$^{1/2}$
Uniaxial Tension

Failure Strain - Map32

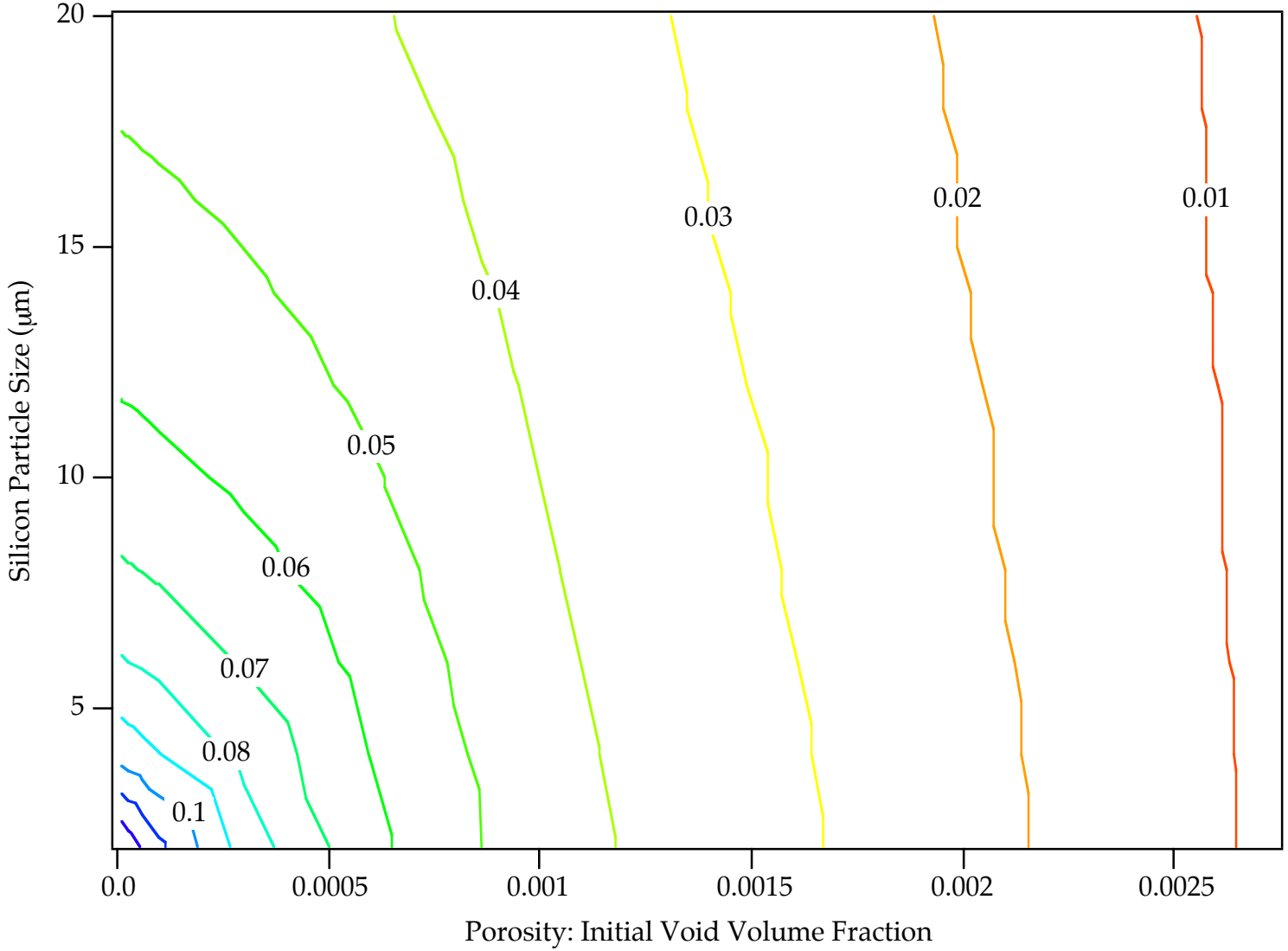

T = 222K
$\dot{\varepsilon}$ = .0002 /sec
DCS = 100 μm

f(Si) = 7%
K_{IC} = 17.3 MPa-$mm^{1/2}$
Biaxial Tension

Failure Strain - Map33

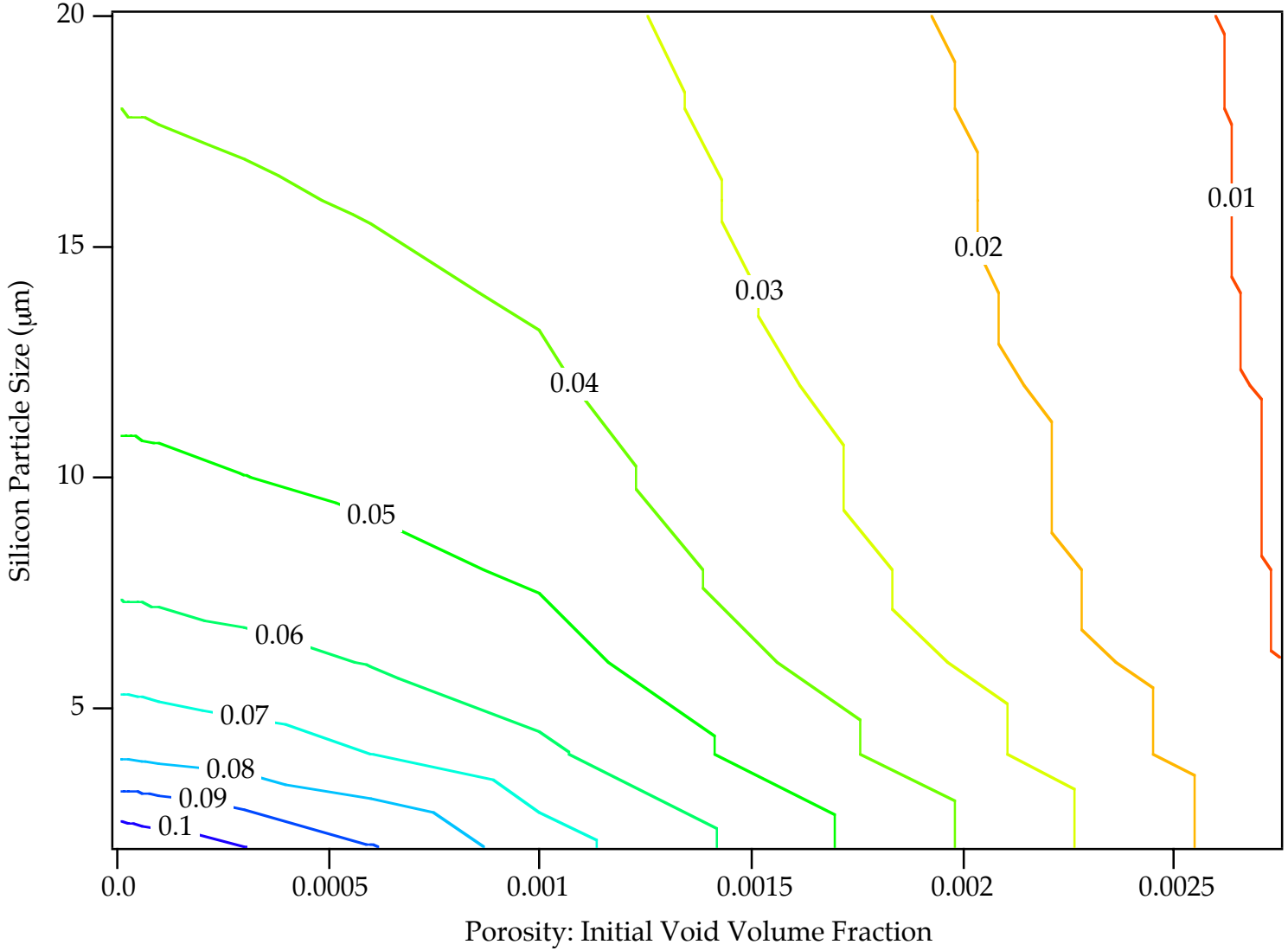

T = 222K
$\dot{\varepsilon}$ = .0002 /sec
DCS = 100 μm

f(Si) = 7%
K_{IC} = 17.3 MPa-$mm^{1/2}$
Plane Strain

Failure Strain - Map34

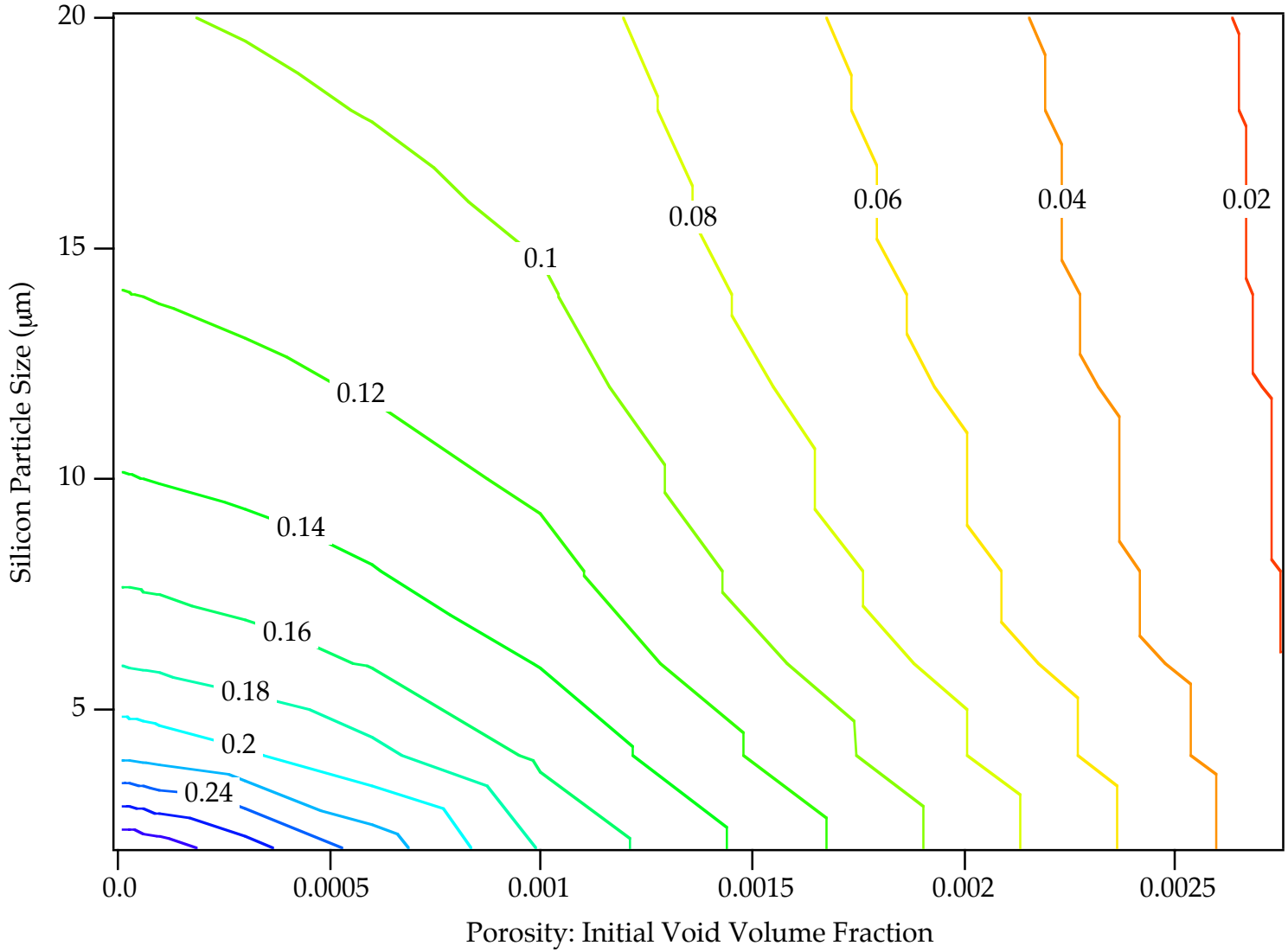

T = 222K
$\dot{\varepsilon}$ = 1000 /sec
DCS = 100 μm

f(Si) = 7%
K_{IC} = 17.3 MPa-mm$^{1/2}$
Uniaxial Tension

Failure Strain - Map35

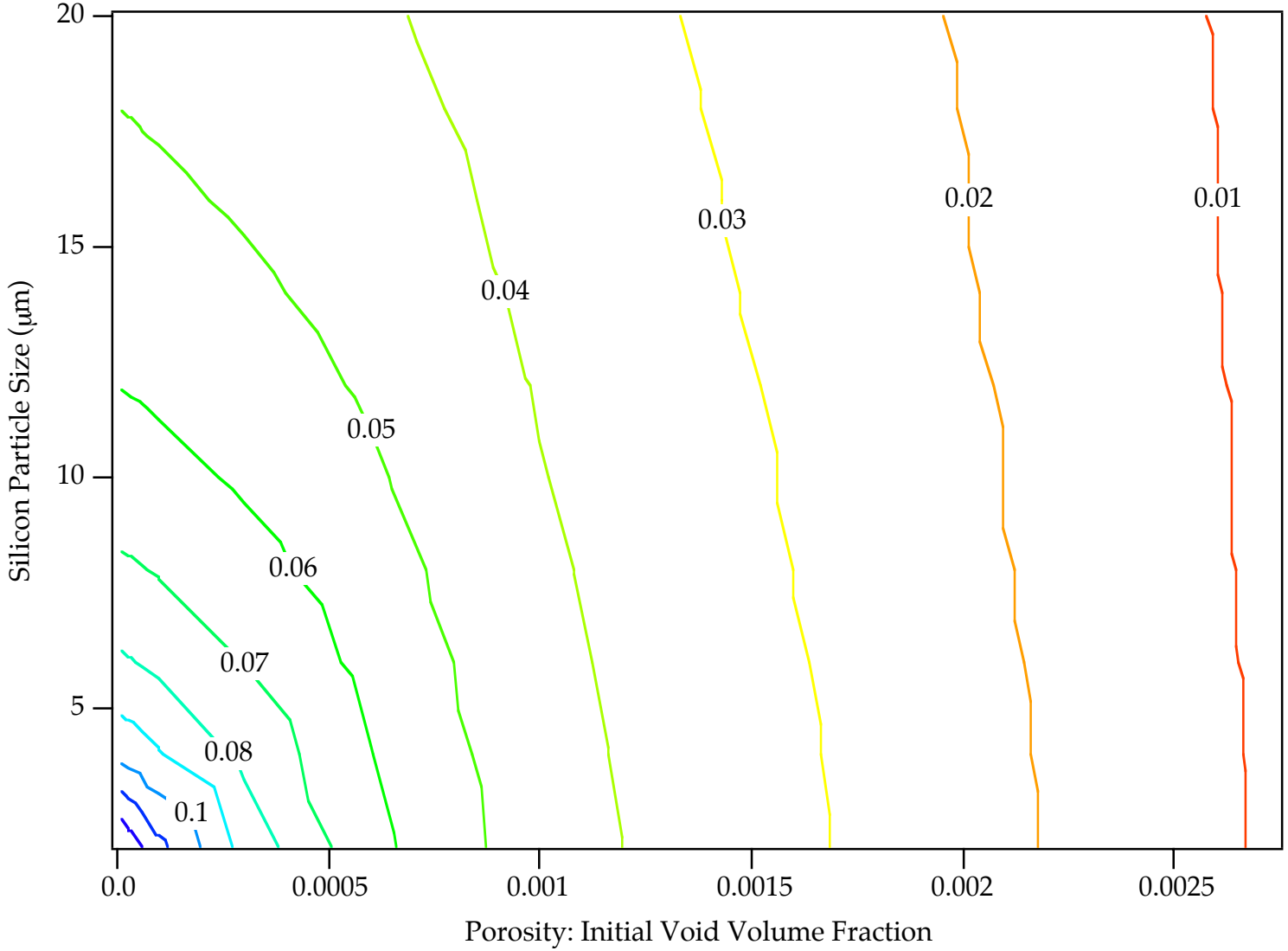

T = 222K
$\dot{\varepsilon}$ = 1000 /sec
DCS = 100 μm

f(Si) = 7%
K_{IC} = 17.3 MPa-$mm^{1/2}$
Biaxial Tension

Failure Strain - Map36

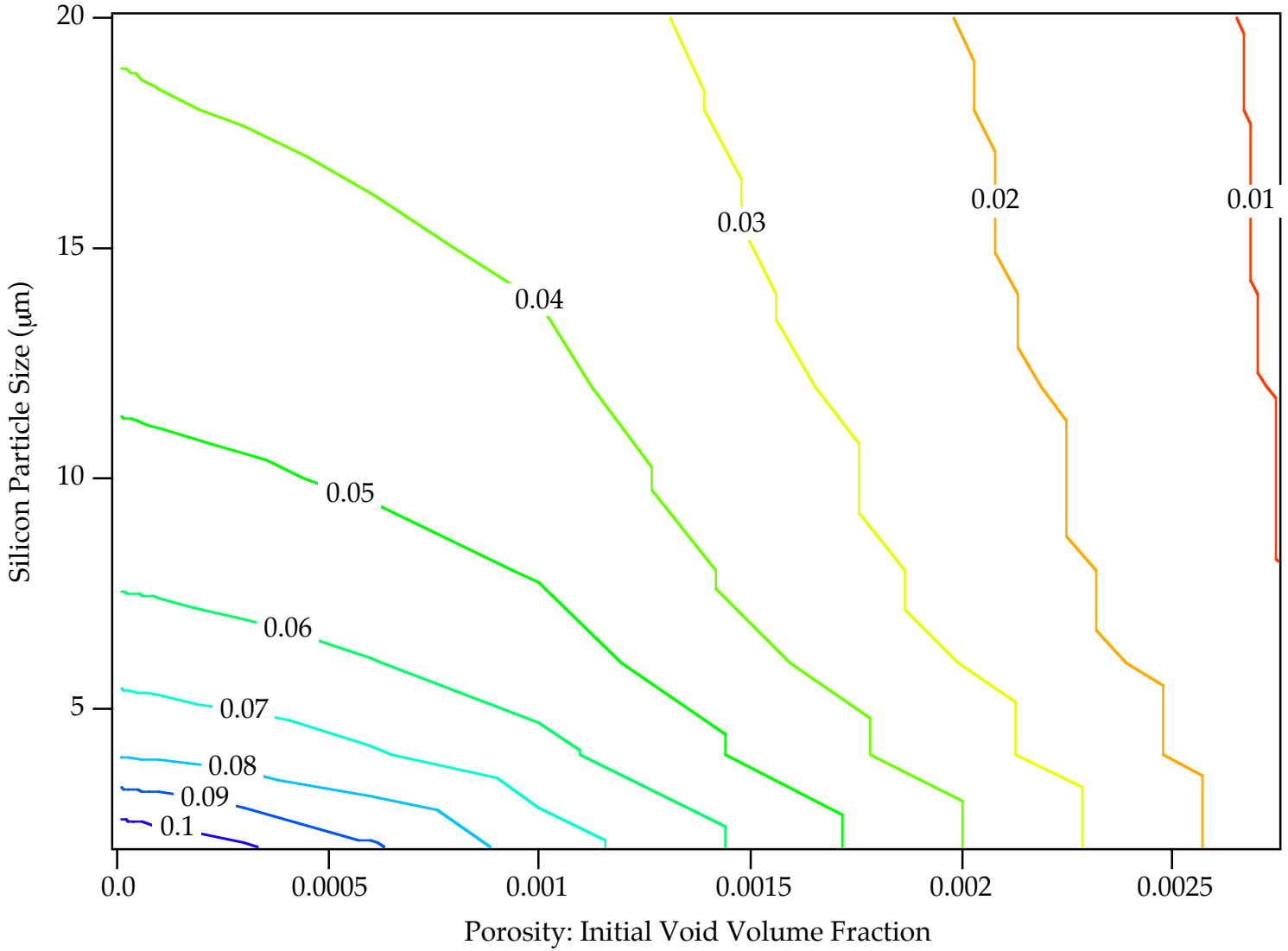

T = 222K
$\dot{\varepsilon}$ = 1000 /sec
DCS = 100 μm

f(Si) = 7%
K_{IC} = 17.3 MPa-$mm^{1/2}$
Plane Strain

Failure Strain - Map37

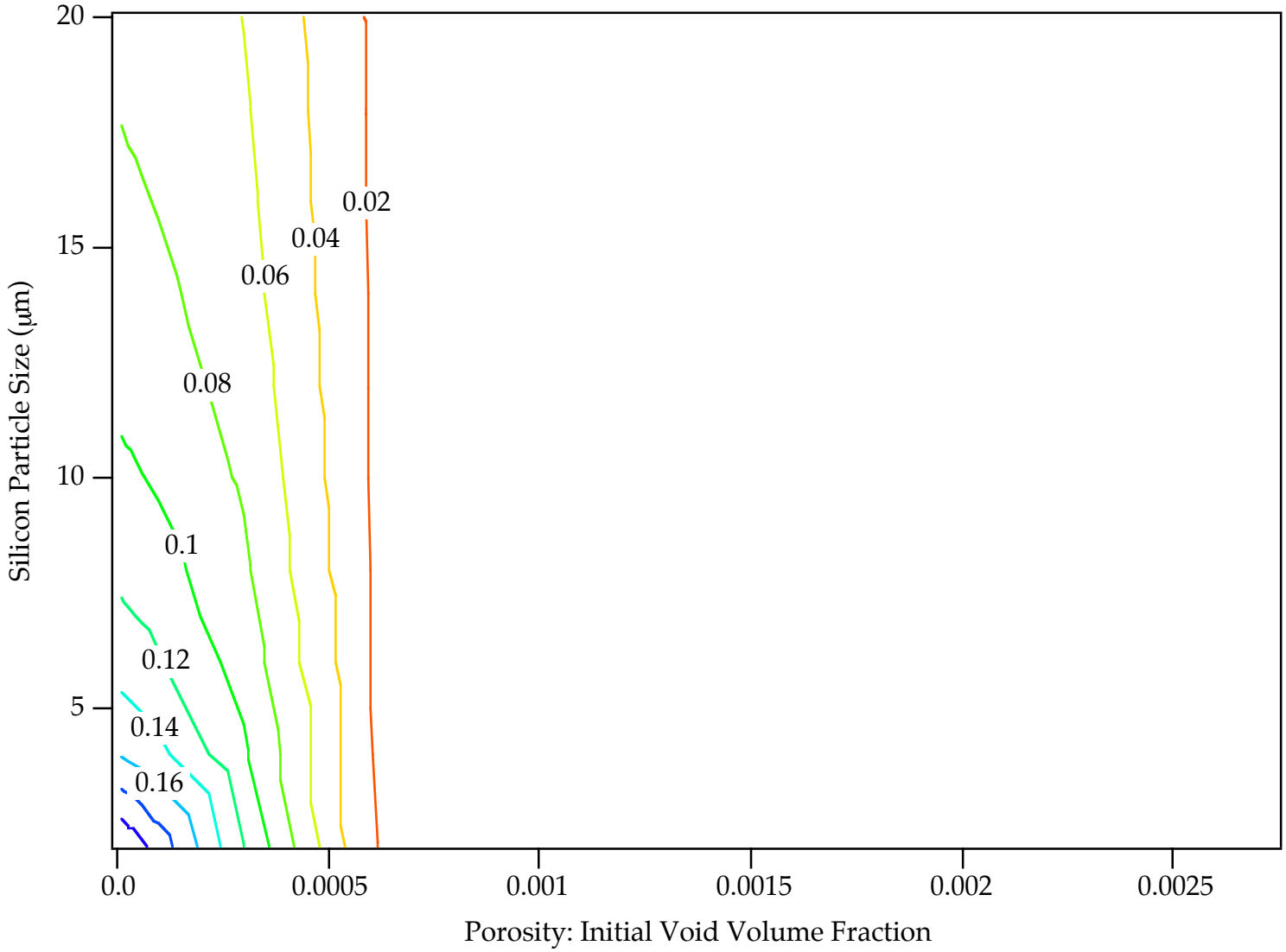

T = 394K
$\dot{\varepsilon}$ = .0002 /sec
DCS = 20 μm

f(Si) = 7%
K_{IC} = 17.3 MPa-$mm^{1/2}$
Uniaxial Tension

Failure Strain - Map38

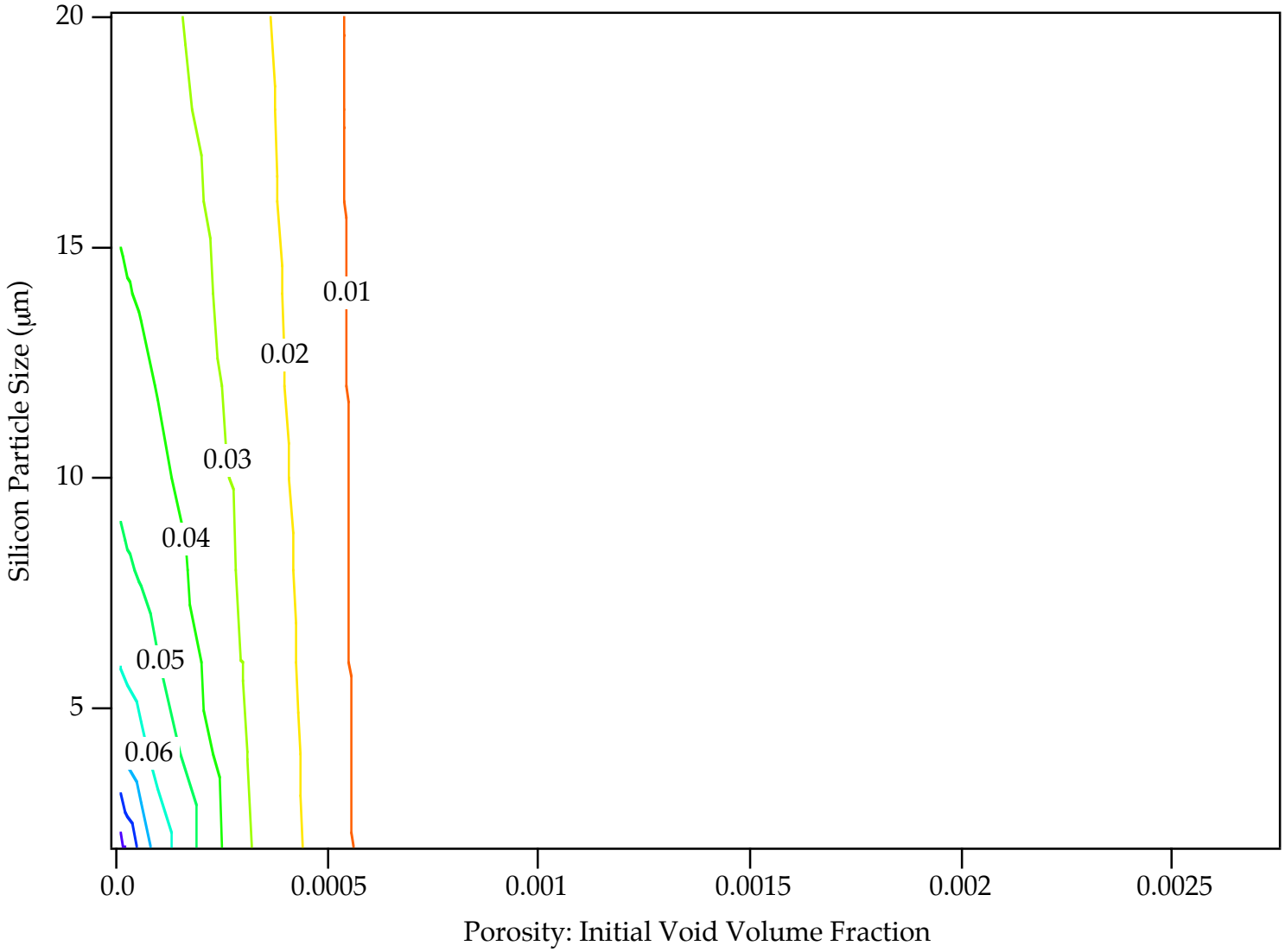

T = 394K
$\dot{\varepsilon}$ = .0002 /sec
DCS = 20 μm

f(Si) = 7%
K_{IC} = 17.3 MPa-$mm^{1/2}$
Biaxial Tension

Failure Strain - Map39

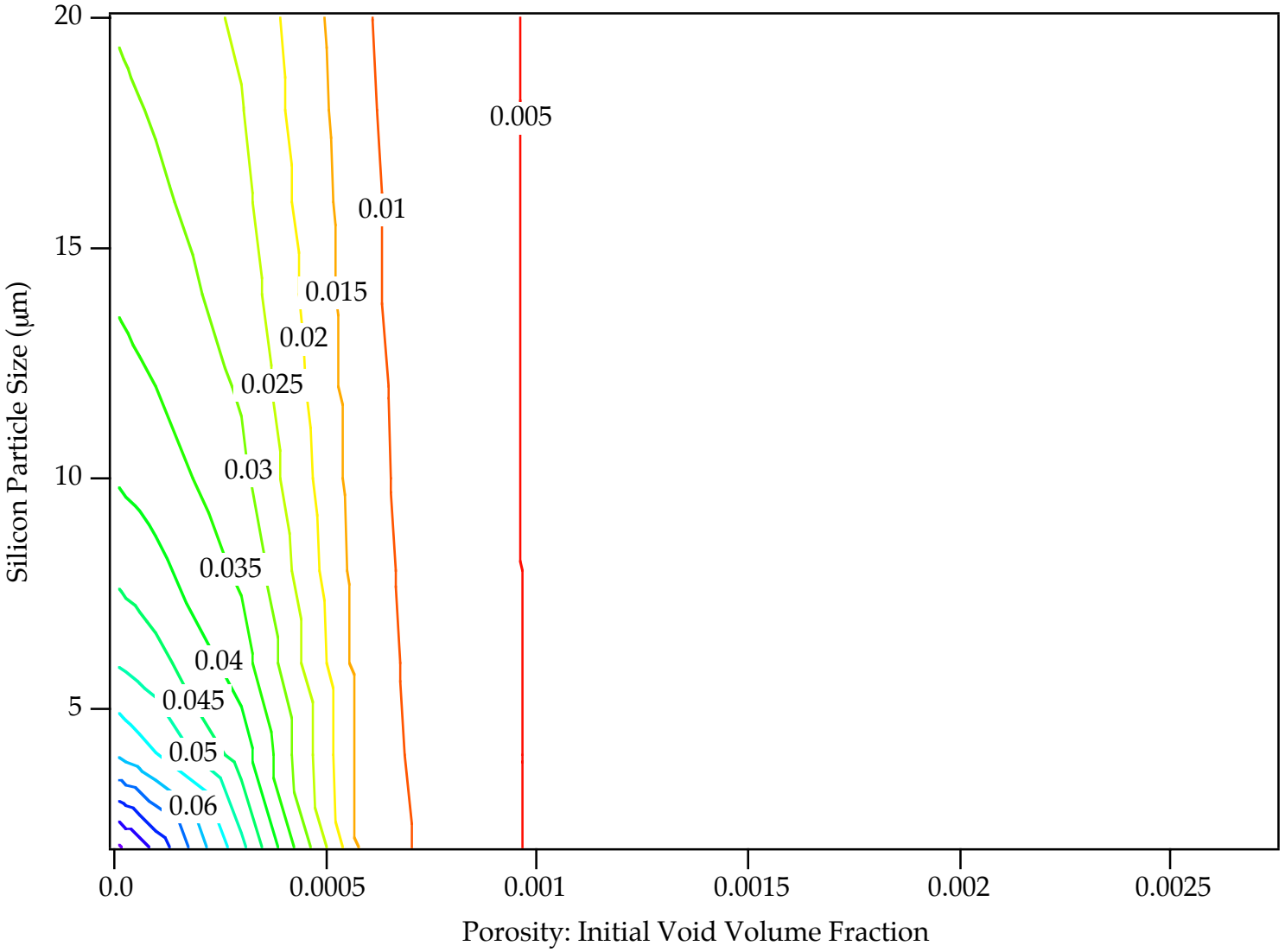

T = 394K
$\dot{\varepsilon}$ = .0002 /sec
DCS = 20 μm

f(Si) = 7%
K_{IC} = 17.3 MPa-mm$^{1/2}$
Plane Strain

Failure Strain - Map40

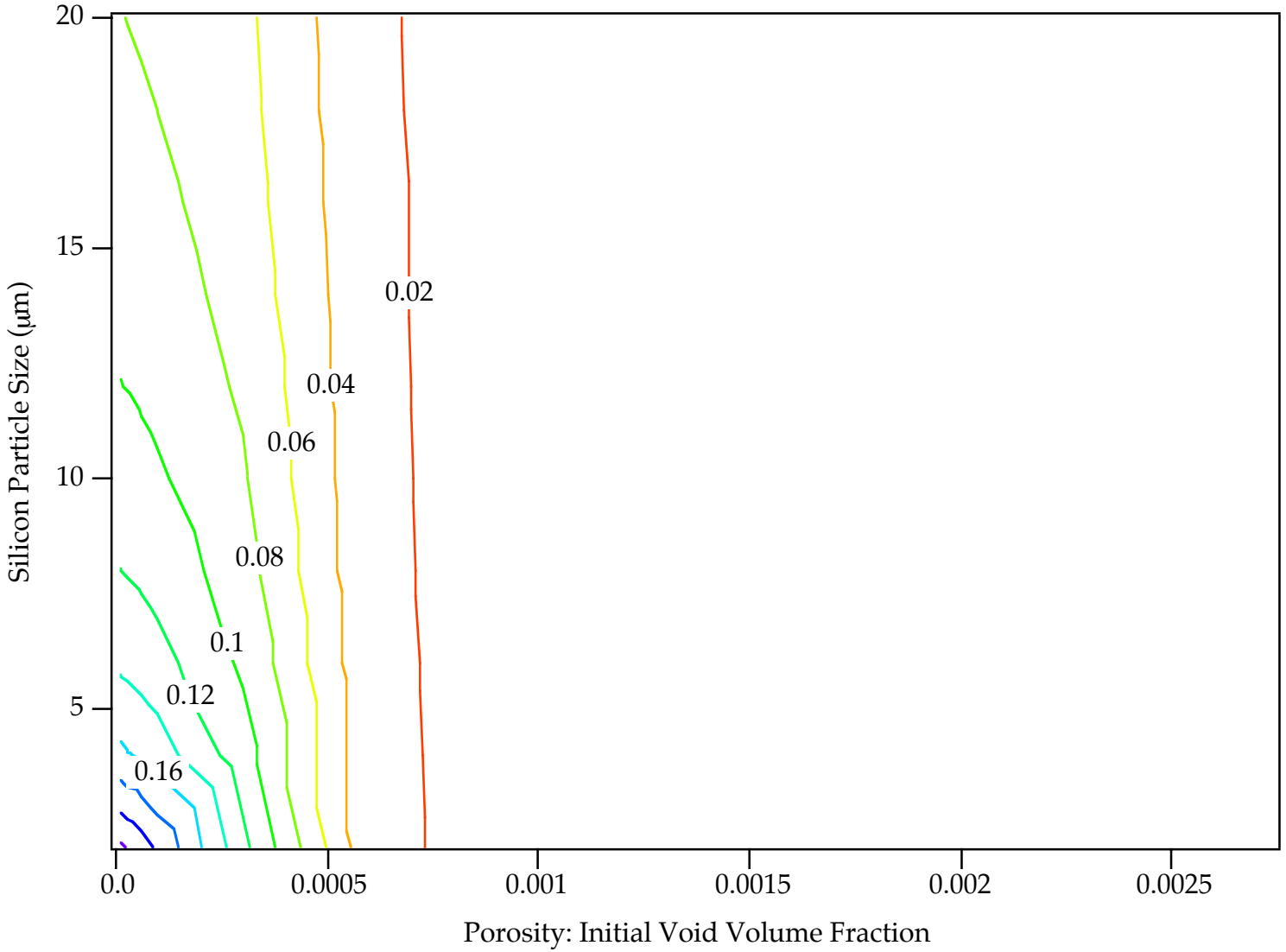

T = 394K
$\dot{\varepsilon}$ = 1000 /sec
DCS = 20 μm

f(Si) = 7%
K_{IC} = 17.3 MPa-mm$^{1/2}$
Uniaxial Tension

Failure Strain - Map41

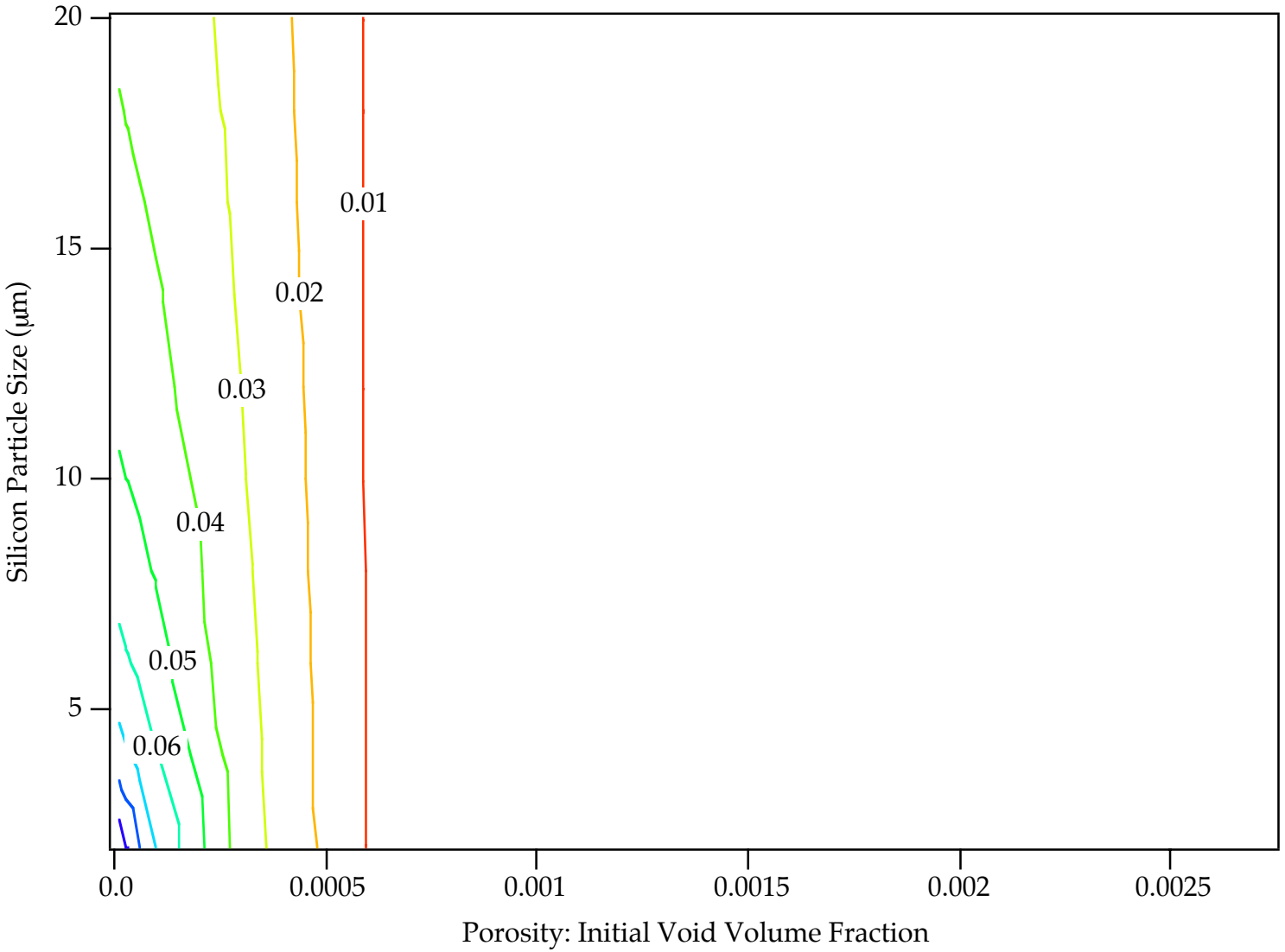

T = 394K
$\dot{\varepsilon}$ = 1000 /sec
DCS = 20 μm

f(Si) = 7%
K_{IC} = 17.3 MPa-mm$^{1/2}$
Biaxial Tension

Failure Strain - Map42

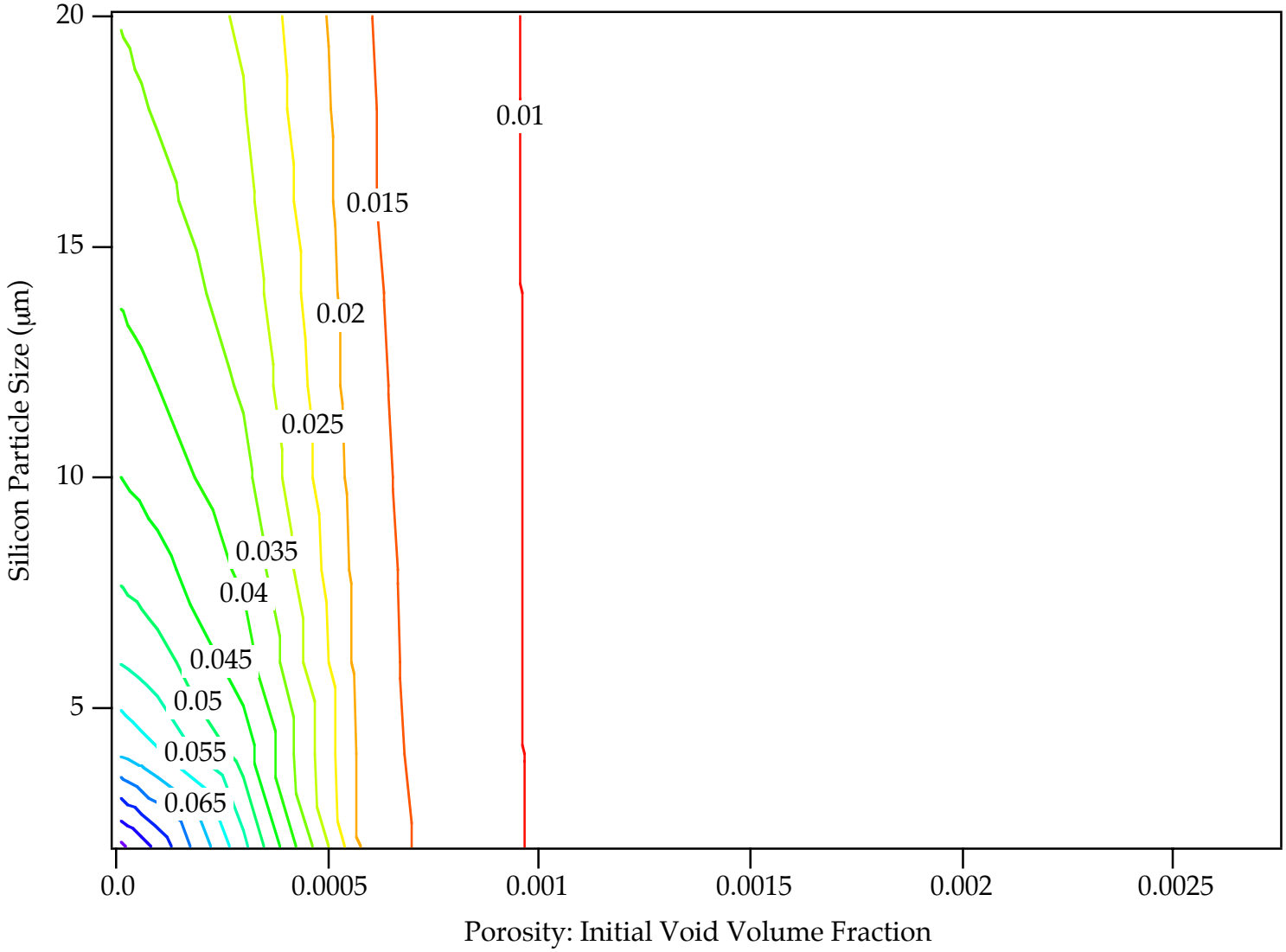

T = 394K
$\dot{\varepsilon}$ = 1000 /sec
DCS = 20 μm

f(Si) = 7%
K_{IC} = 17.3 MPa-mm$^{1/2}$
Plane Strain

Failure Strain - Map43

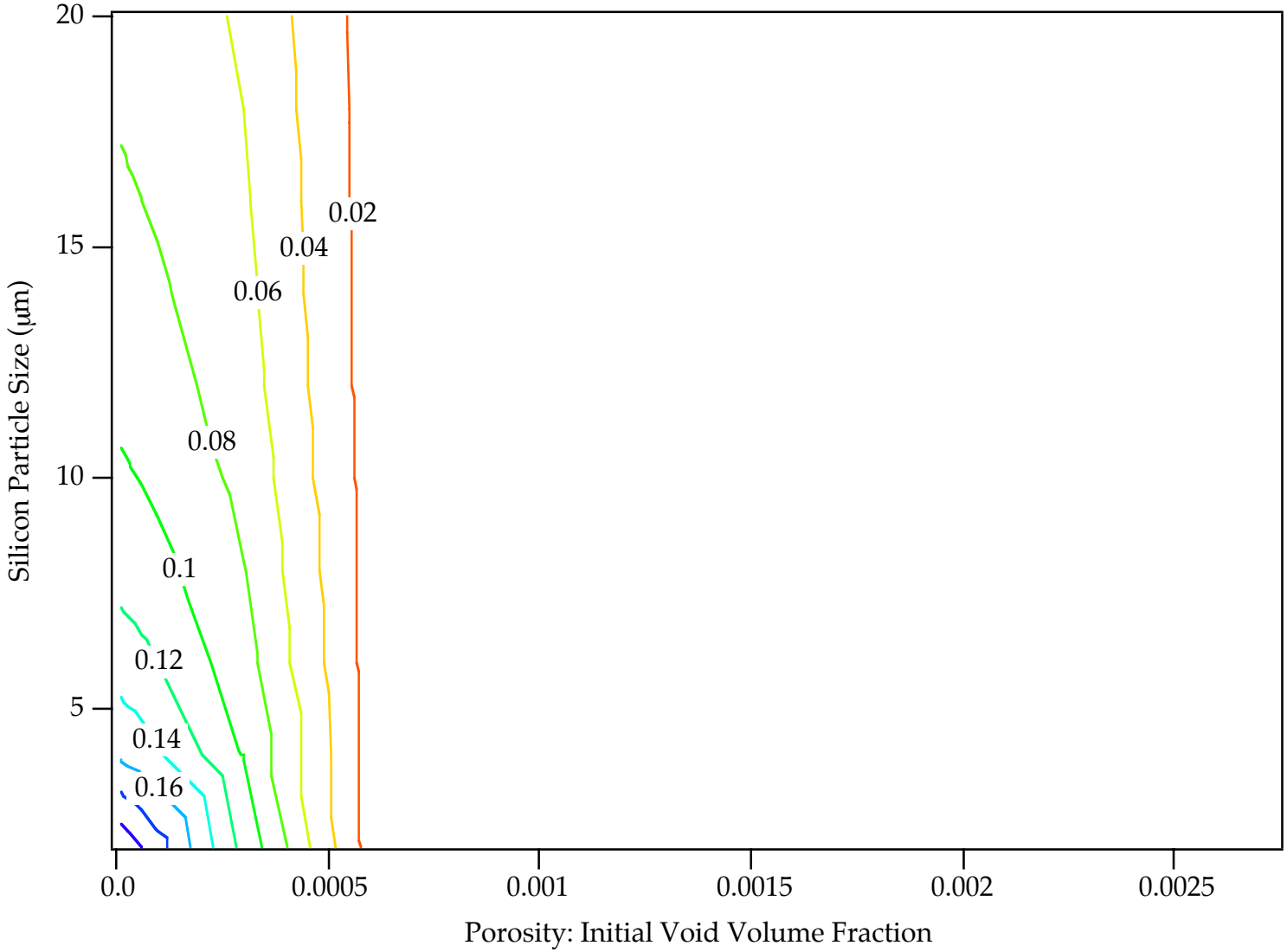

T = 394K
$\dot{\varepsilon}$ = .0002 /sec
DCS = 50 μm

f(Si) = 7%
K_{IC} = 17.3 MPa-mm$^{1/2}$
Uniaxial Tension

Failure Strain - Map44

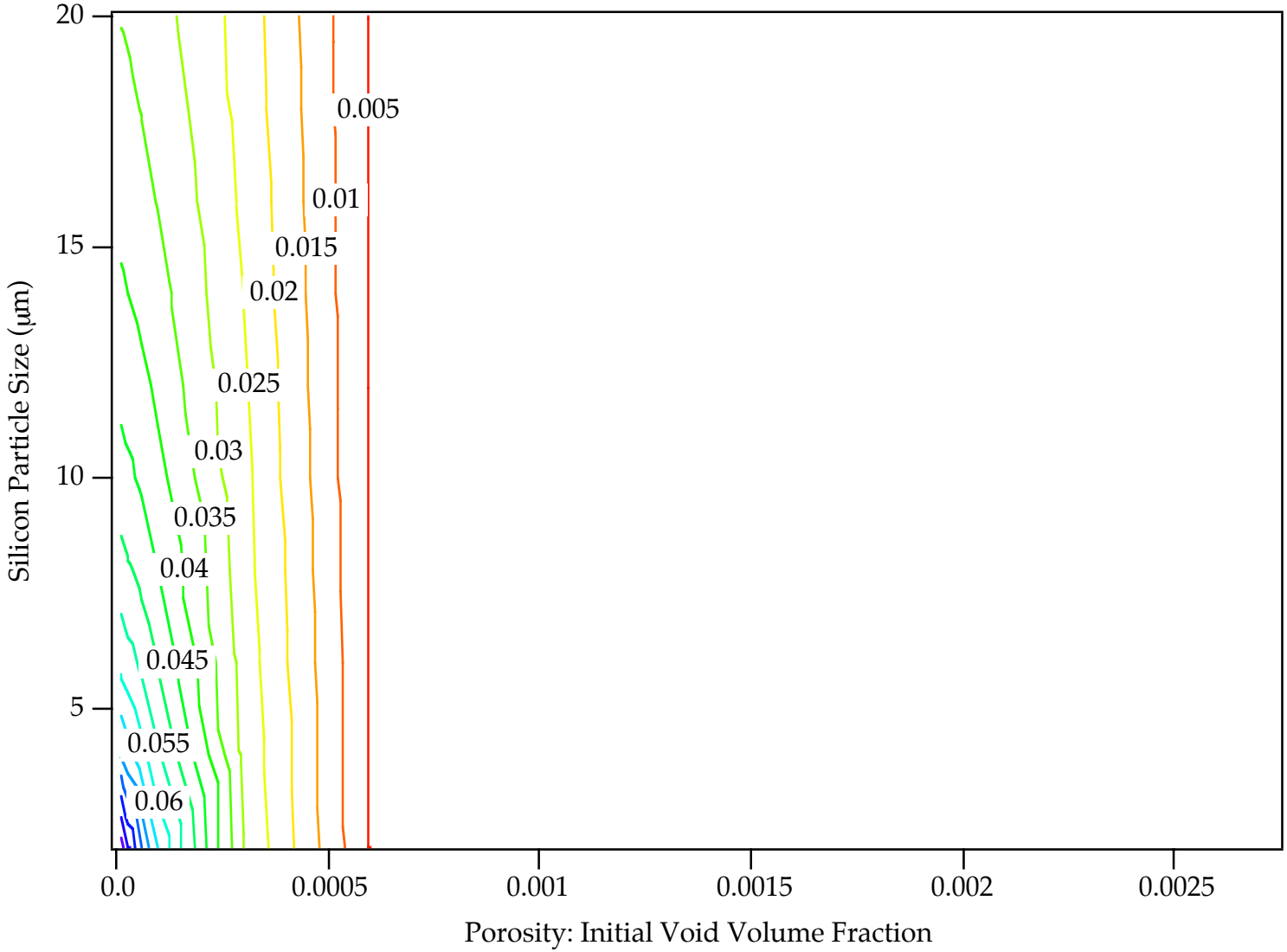

T = 394K
$\dot{\varepsilon}$ = .0002 /sec
DCS = 50 μm

f(Si) = 7%
K_{IC} = 17.3 MPa-mm$^{1/2}$
Biaxial Tension

Failure Strain - Map45

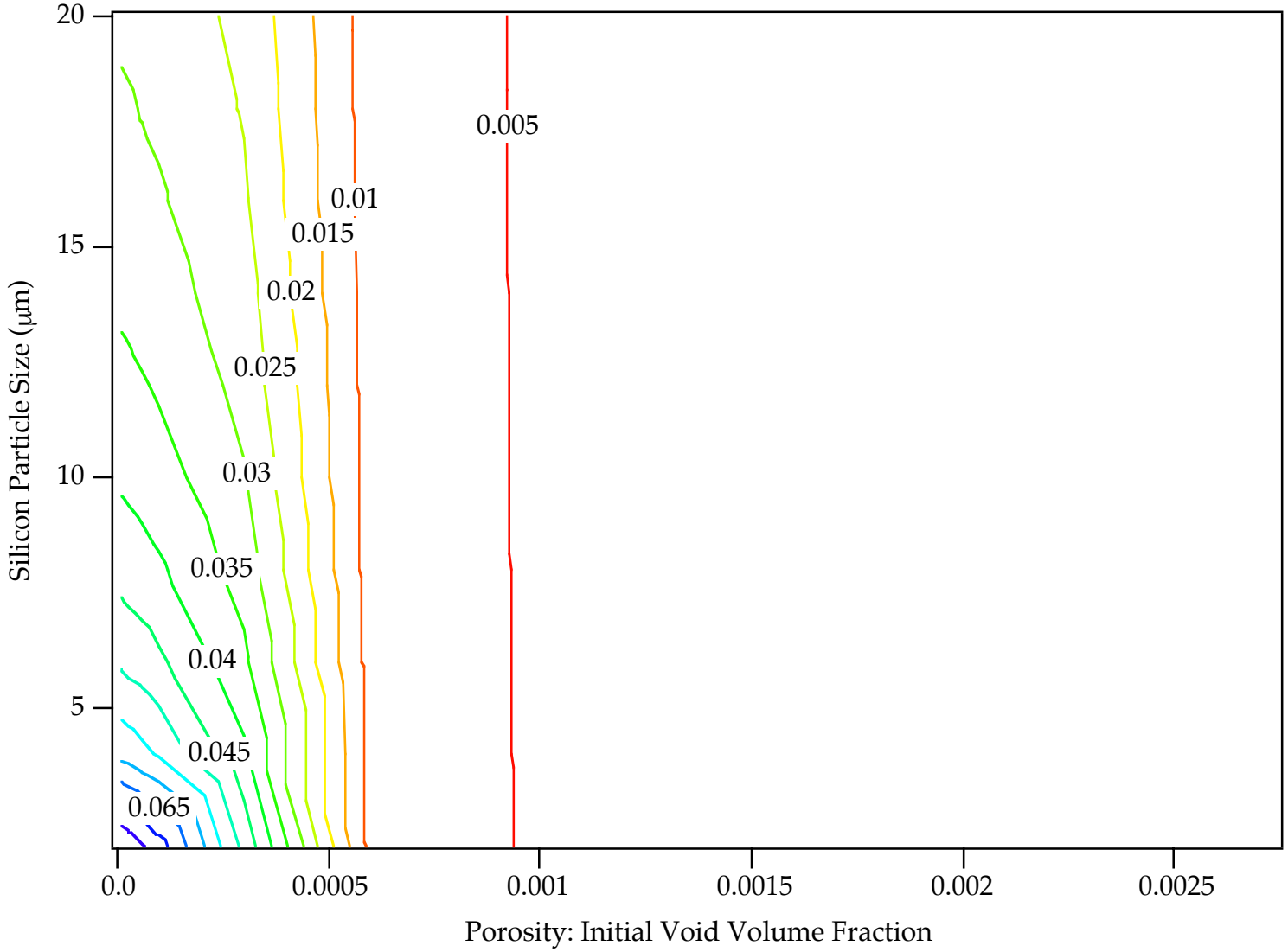

T = 394K
$\dot{\varepsilon}$ = .0002 /sec
DCS = 50 μm

f(Si) = 7%
K_{IC} = 17.3 MPa-$mm^{1/2}$
Plane Strain

Failure Strain - Map46

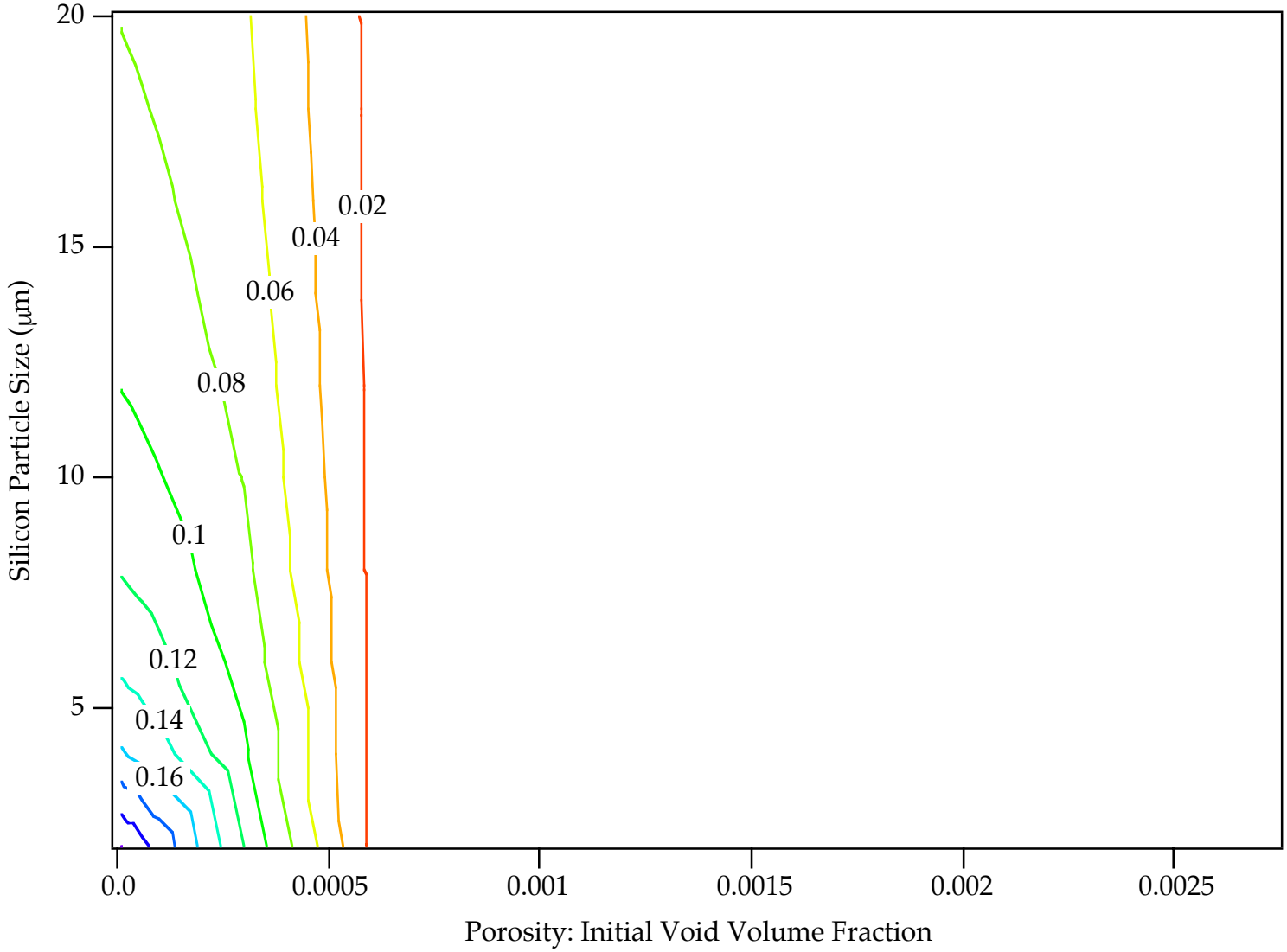

T = 394K
$\dot{\varepsilon}$ = 1000 /sec
DCS = 50 μm

f(Si) = 7%
K_{IC} = 17.3 MPa-mm$^{1/2}$
Uniaxial Tension

Failure Strain - Map47

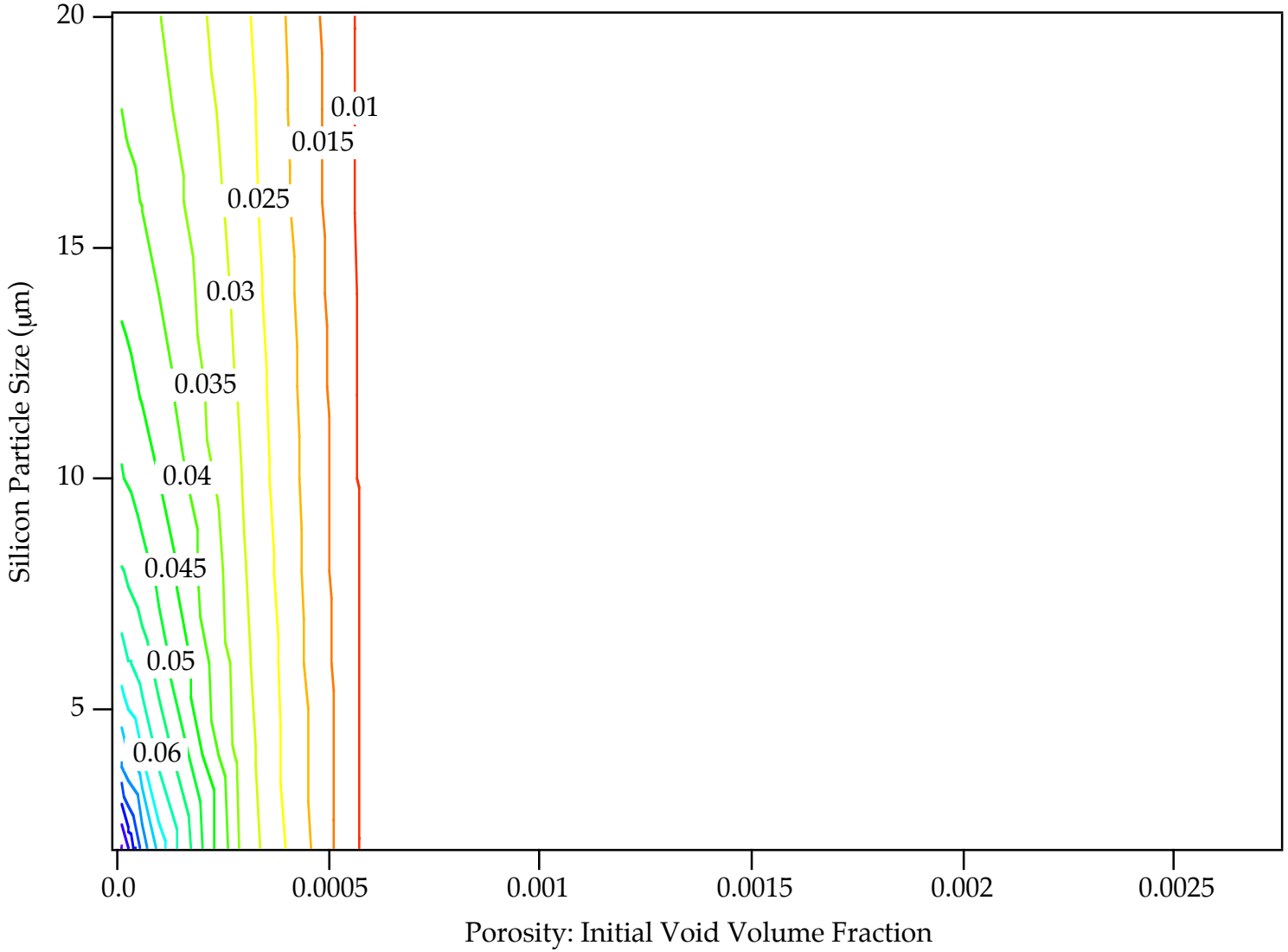

T = 394K
$\dot{\varepsilon}$ = 1000 /sec
DCS = 50 μm

f(Si) = 7%
K_{IC} = 17.3 MPa-mm$^{1/2}$
Biaxial Tension

Failure Strain - Map48

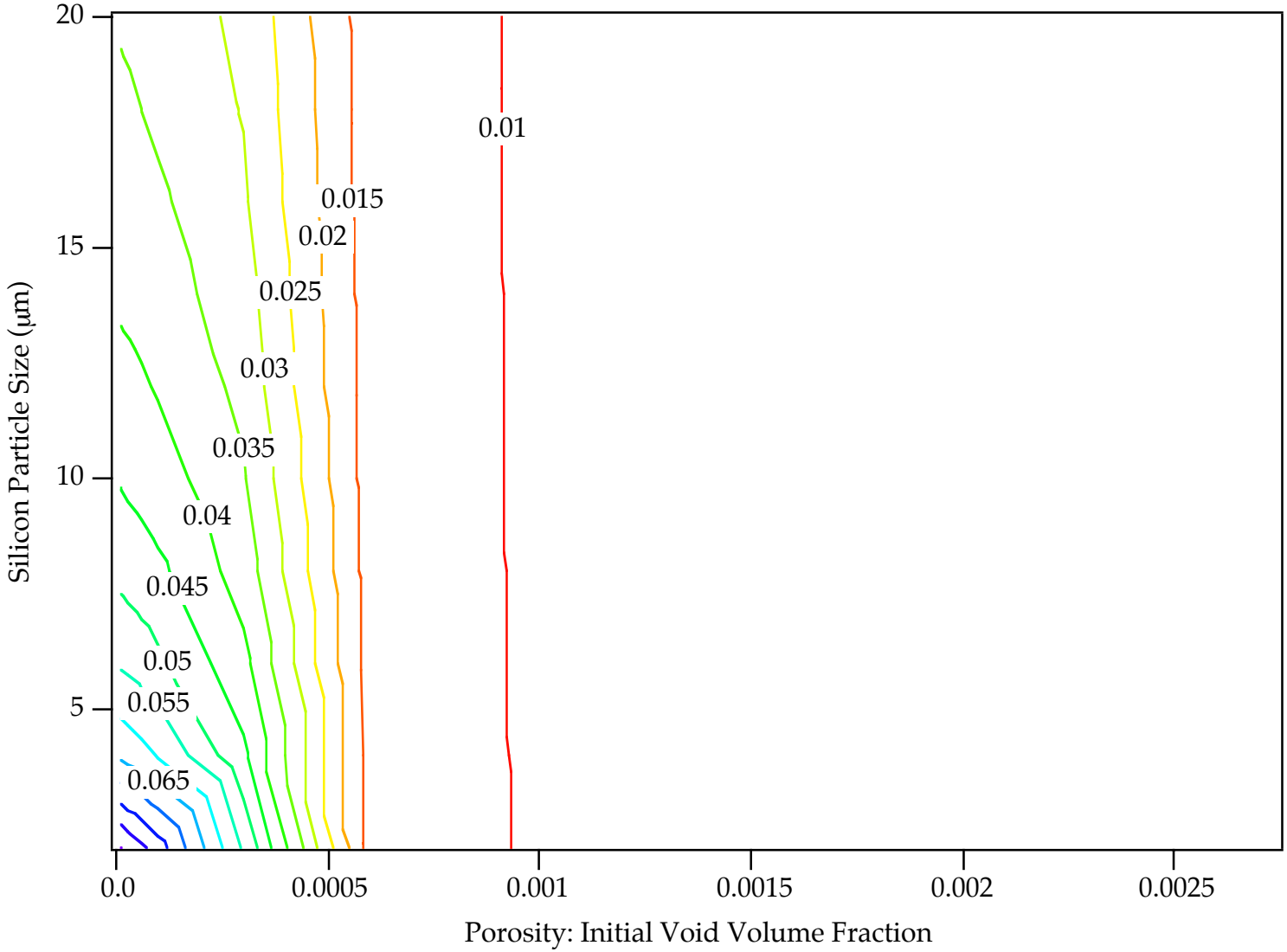

T = 394K
$\dot{\varepsilon}$ = 1000 /sec
DCS = 50 μm

f(Si) = 7%
K_{IC} = 17.3 MPa-mm$^{1/2}$
Plane Strain

Failure Strain - Map49

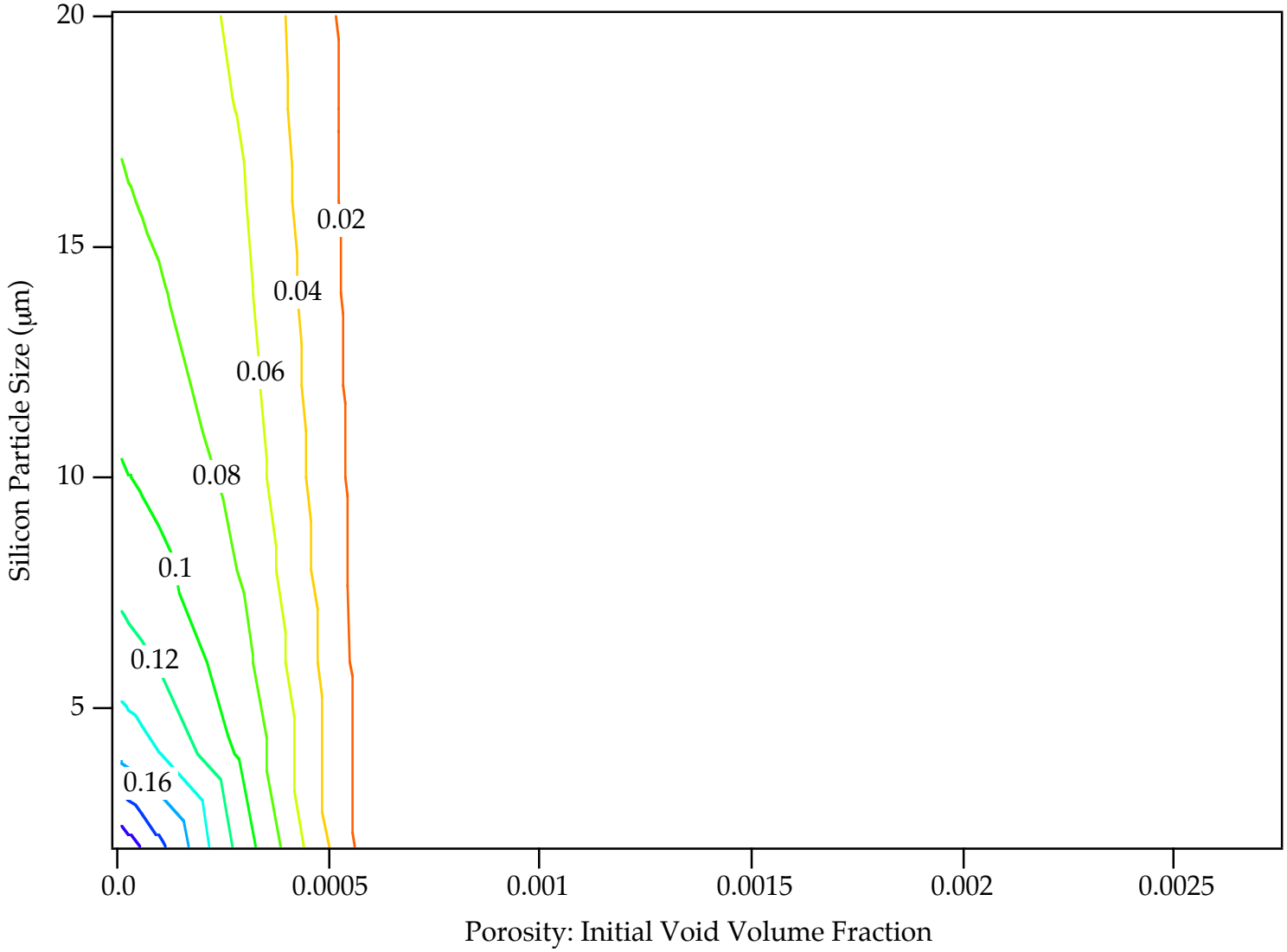

T = 394K
$\dot{\varepsilon}$ = .0002 /sec
DCS = 100 μm

f(Si) = 7%
K_{IC} = 17.3 MPa-mm$^{1/2}$
Uniaxial Tension

Failure Strain - Map50

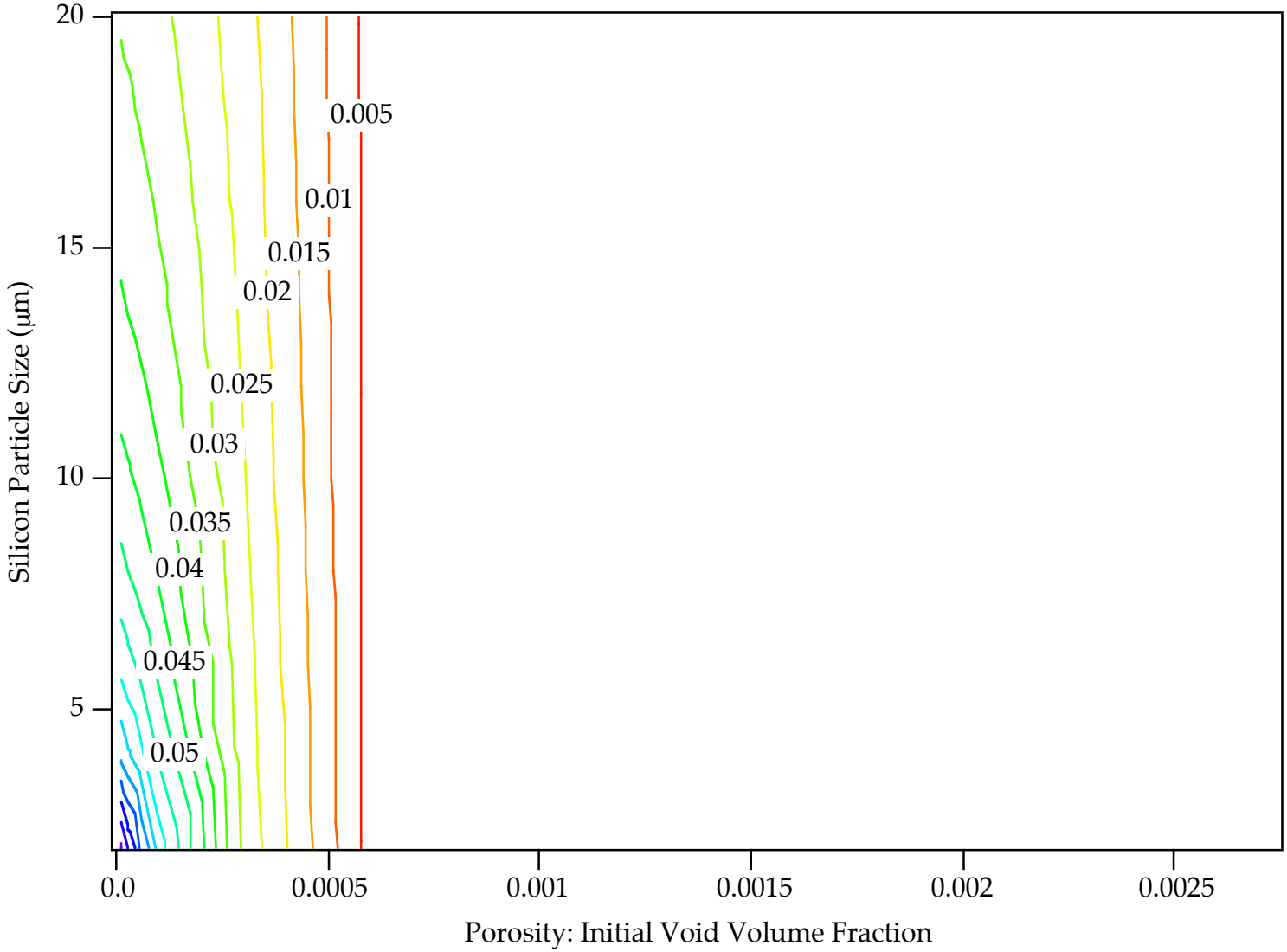

T = 394K
$\dot{\varepsilon}$ = .0002 / sec
DCS = 100 μm

f(Si) = 7%
K_{IC} = 17.3 MPa-mm$^{1/2}$
Biaxial Tension

Failure Strain - Map51

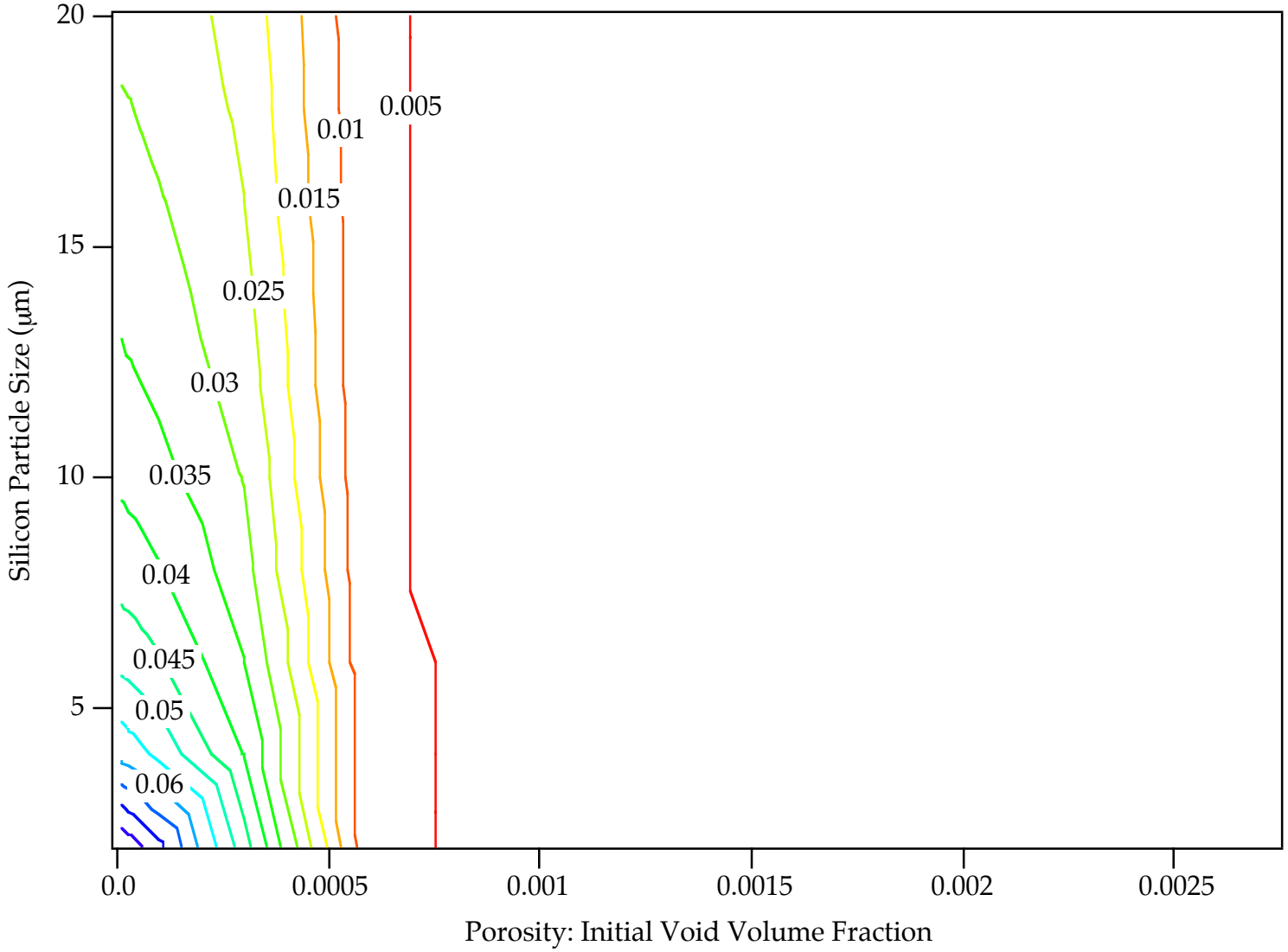

T = 394K
$\dot{\varepsilon}$ = .0002 /sec
DCS = 100 μm

f(Si) = 7%
K_{IC} = 17.3 MPa-$mm^{1/2}$
Plane Strain

Failure Strain - Map52

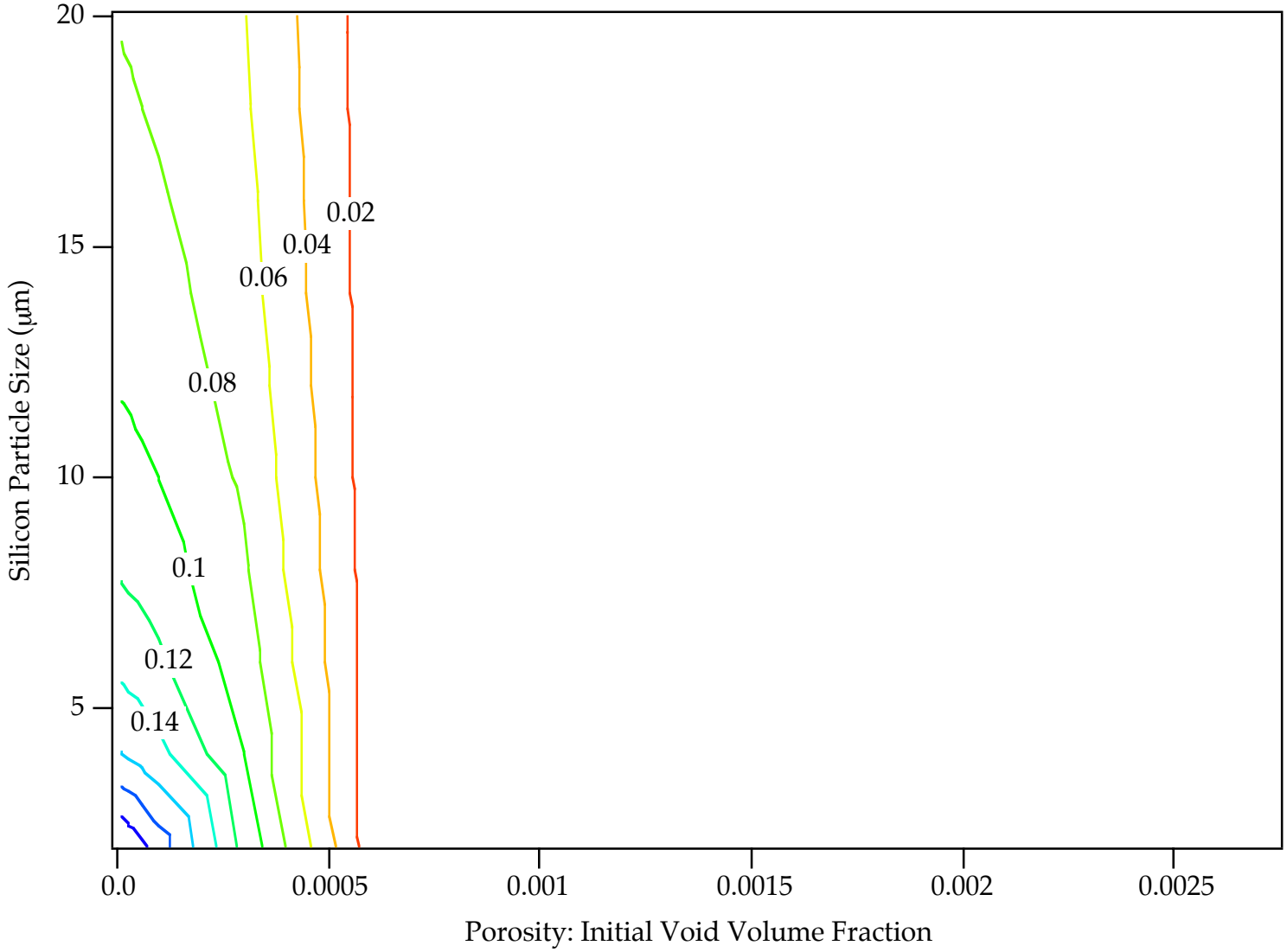

T = 394K
$\dot{\varepsilon}$ = 1000 /sec
DCS = 100 μm

f(Si) = 7%
K_{IC} = 17.3 MPa-$mm^{1/2}$
Uniaxial Tension

Failure Strain - Map53

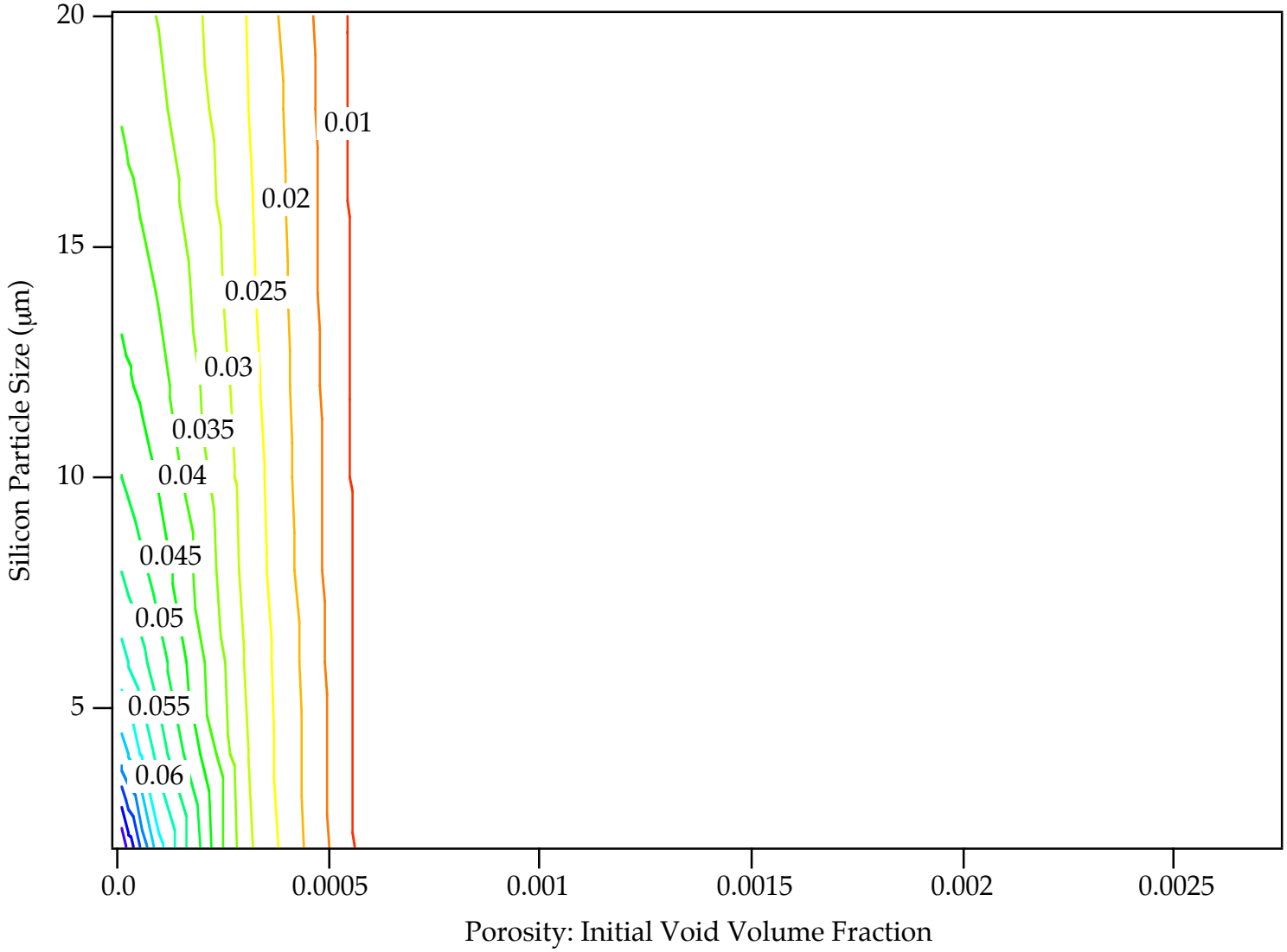

T = 394K
$\dot{\varepsilon}$ = 1000 /sec
DCS = 100 μm

f(Si) = 7%
K_{IC} = 17.3 MPa-$mm^{1/2}$
Biaxial Tension

Failure Strain - Map54

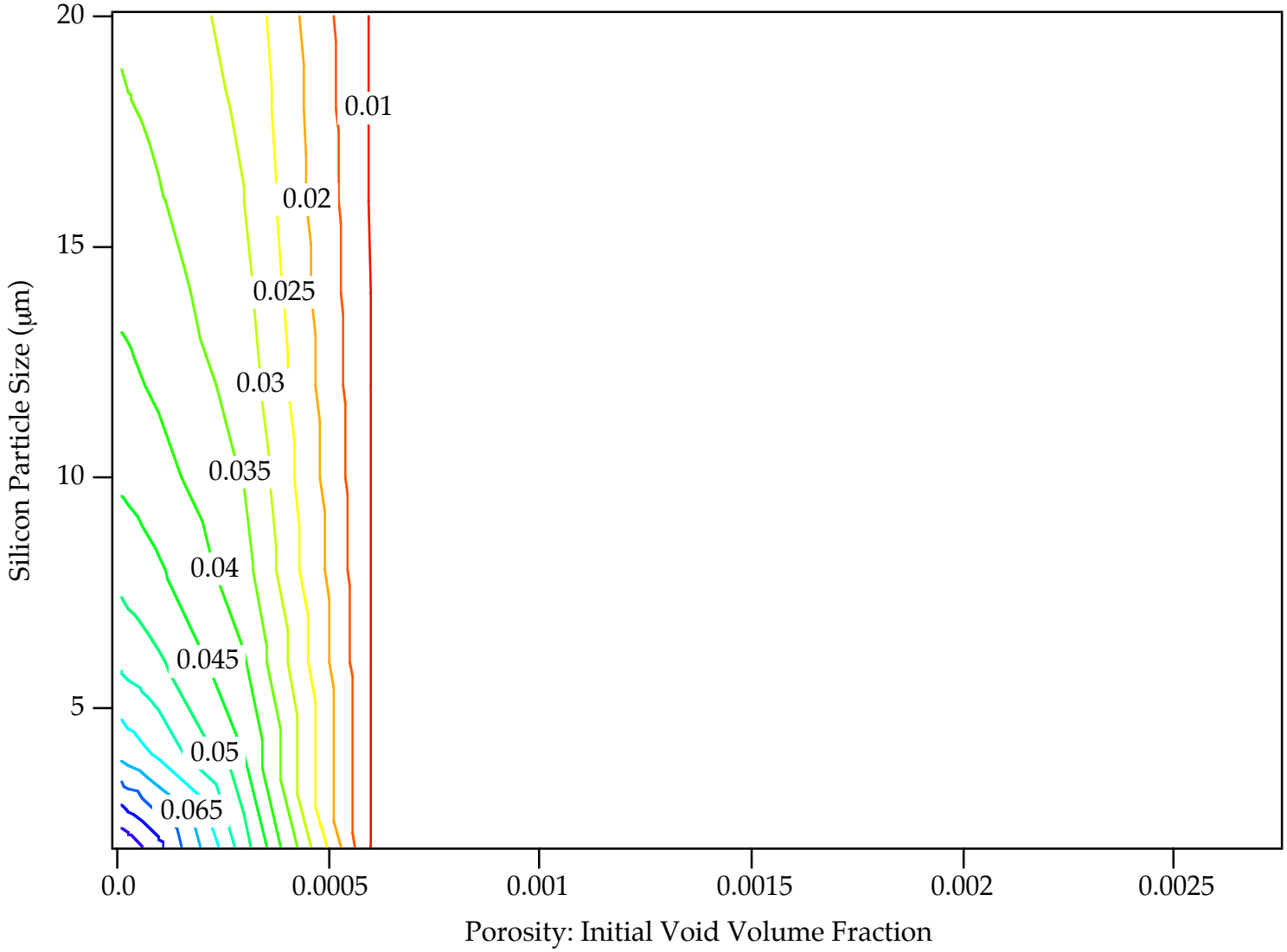

T = 394K
$\dot{\varepsilon}$ = 1000 /sec
DCS = 100 μm

f(Si) = 7%
K_{IC} = 17.3 MPa-$mm^{1/2}$
Plane Strain

DISTRIBUTION

1 Kola Agagu
GM Powertrain Group
General Motors Corporation
Casting Technology Center
Mail Code 486-077-034
77 West Center Street
Saginaw, MI 48605-5073

1 Richard Andriano
Stahl Specialty Co.
111 E. Pacific
P. O. Box 6
Kingsville, MO 64061-0006

1 Diran Apelian
Metal Processing Institute
Worcester Polytechnic Institute
100 Institute Road
Worcester, MA 01609-2280

1 Mike I. Baskes
MST-8, MS G755
Los Alamos National Laboratory
Los Alamos, NM 87545

1 John Bassani
University of Pennsylvania
Dept. of Mechanical Engineering and Applied Mechanics
297 Towne Bldg.
Philadelphia, Pa 19104-6315

1 Armand Beaudoin
Dept. of Mechanical and Industrial Engineering
University of Illinois at Urbana-Champaign
140 Mechanical Engineering Building, MC-244
1206 West Green Street
Urbana, IL 61801

1 Richard Becker
Lawrence Livermore National Laboratory
7000 East Ave
L-228
Livermore, CA 94450

1 Richard Berkmortel
Global Technolgy Centre
Meridian Technologies, Inc.
25 MacNob Avenue
Strathroy, Ontario
Canada N7G 4H6

1 John T. Berry
Mississippi State University
Department of Mechanical Engineering
210 Carpenter Engineering Building
P. O. Box ME
Mississippi State, MS 39762-5925

1 Mary Boyce
Dept. of Mechanical Engineering
Massachusetts Institute of Technology
Cambridge, MA 02139-4307

1 John Brockenbrough
100 Technical Drive
Alcoa Center PA 15069

1 Robert J. Bucci
Engineering Design Center
Aluminum Company of America
Alcoa Technical Center
100 Technical Drive
Alcoa Center, PA 15069-0001

1 James T. Burg
Aluminum Company of America
Alcoa Technical Center
100 Technical Drive
Alcoa Center, Pennsylvania 15069-0001

1 Carloa H. Caceres
Department of Mining, Minerals and Materials Engineering
The University of Queensland
Brisbane Qld 4072
Australia

1 Joseph A. Carpenter, Jr.
Office of Transportation Technologies
U. S. Department of Energy
EE-32, Room 5G-045
1000 Independence Ave., SW
Washington, DC 20585

1 Weinong Wayne Chen
Aerospace & Mechanical Engineering
The University of Arizona
Tucson, AZ 85721

1 Xiaoming Chen
Safety Research and Development Department, FRL
2101 Village Road, P.O. Box 2053
MD 2115, Rm 2626
Dearborn, MI 48124

1 Yang-Tse Cheng
Engineered Surfaces and Tribology
Material and Processes Laboratory
General Motors
Research and Development
Mail Code 480-106-224
30500 Mound Road
P. O. Box 9055
Warren, MI 48090

1 Gerald S. Cole
Manufacturing Systems Department
Ford Research Laboratory
20000 Rotunda Drive
P. O. Box 2053
MD 3135, Rm. 2170, SRL
Dearborn, MI 48121, 2053

1 Bruce M. Cox
Cast Metals Laboratory
DaimerChrysler Corporation
CIMS 481-01-41
800 Chrysler Drive
Auburn Hills, MI 48326-2757

1 Paul Creapeau
General Motors
6595 Joslyn Rd
Pontiac, MI 48340

1 Louis Desrosiers
InTerMag Technologies Inc.
357 rue Franquet Sainte-Foy
Quebec, Canada QCGIP 4N7

1 Sara Dillich
Energy Efficiency and Renewable Energy
Office of Industrial Technologies, EE-20
1000 Independence Avenue SW
Washington DC 20585-0121

1 Ken Dolan
Lawrence Livermore National Laboratory
7000 East Ave
L-333
Livermore, CA 94550

1 Ray Donahue
Mercury Marine
W 6250 Pioneer Rd.
Fond DuLac, WI 54936-1939

1 L. Donay
Alchem Aluminum Inc.
368 West Garfield P.O. Box 139
Coldwater, MI. 49036

1 Mike Evans
Gibbs Did Casting Corporation
369 Community Drive
Henderson, KY 82420

1 Jinghong Fan
Division of Mechanical Engineering,
Alfred University
Saxon Drive
Alfred, NY, 14802

1 Ken Fischer
Consolidated Metco, Inc
13940 N. Rivergate Blvd
Portland, OR 97203

1 Joseph Foster
Wright Laboratory/ Armament Directorate
Eglin AFB, FL 32548

1 George N. Frantziskonis
Department of Civil Engineering & Engineering Mechanics
The University of Arizona
Tucson, AZ 85721-0072

1 Kenneth Gall
University of Colorado
Department of Mechanical Engineering
Campus Box 427
Boulder, CO 80309

1 H. Gao
Dept. of Mechanical Engineering
Stanford University
Stanford, CA 94305

1 Gerald Gegel
740 S. Columbus Ave.
Morton, IL 61550

1 Vincent J. Genise
Product Engineering and Development
Citation
27730 Franklin Road
Southfield, MI 48034

1 Dale A. Gerard
General Motors Corporation
GM Powertrain
Mail Code 480-723-624
30003 Van Dyke
Building 2-7
Warren, MI 48090-9060

1 Bill Gerberich
University of Minnesota
Chemical Engineering and Materials Science
151 Amund H
421 Washington Ave SE
Minneapolis, MN 55455

1 Arun Gokhale
School of Materials Sciences Engineering
Georgia Tech
Atlanta, Ga 30332-0405

1 Nasr M. Ghoniem
Mechanical and Aerospace Engineering Department
46-147G Engr IV
University of California Los Angeles
420 Westwood Plaza
Box 951597
Los Angeles, CA 90095-1597

1 Leo Ghuzhoy
Advance Materials Technology
Caterpillar Inc.
Technical Center – E/854
P. O. Box 1875
Peoria, IL 61656-1875

1 Kasi K. Goundan
GMNA Materials & Fastening Engineering Center
General Motors
Mail Code 480-205-314
30007 Van Dyke
Warren, MI 48090-9065

1 David Hall
Louisiana Tech
Mechanical Engineering Dept
PO Box 10348
Ruston, LA 71272

1 Yanyao Jiang
Department of Mechanical Engineering
College of Engineering/312
University of Nevada
Reno, NV 89557-0154

1 Peggy E. Jones
Advanced Materials Development Center
GM Powertrain
1629 N. Washington
P. O. Box 5073
Saginaw, MI 48605-5073

1 George Johnson
Mechanical Engineering
University of California
Berkeley, CA 94720-1740

1 J.W. Ju
Civil & Environmental Engineering
UCLA
Los Angeles,CA 90024-1593

1 J. G. Kaufman
Daufman Associates, Ltd.
3662 Pevensey Drive
Columbus, OH 43220-4821

1 Akhtar Khan
The University of Maryland Balt. County
ECS 234
Baltimore, MD 21250

1 Chung-Whee Kim
EKK, Inc.
100 North Pond Drive
Suite A
Walled Lake, MI 48390

1 Tom Lacy
Department of Aerospace Engineering
Wichita State University
1845 Fairmount
Wichita, Kansas 67260-0044

1 Joe LaRoche
Alcan Ingot
Division of Alcan Aluminum Corporation
6060 Parkland Boulevard
Cleveland, OH 44124-4185

1 Naiyi, Li
Manufacturing Systems Department
Ford Research Laboratory
22101 Village Road
P. O. Box 2053
MD 3135, Rm. 3011, SRL
Dearborn, MI 48121-2053

1 Hiumin Liu
Product Engineering and Development
Citation Corporation
27730 Franklin Road
Southfield, MI 48034

1 W. K. Liu
Mechanical Engineering Dept.
Northwestern University
Evanston, IL 60208-3109

1 Mike Lovell
University of Pittsburgh
Mechanical Engineering
Pittsburgh, PA

1 D. Scott MacKenzie
Failure Analysis & NDT
The Boeing Company
P. O. Box 516 MC S102-2152
St. Louis, MO 63166-0516

1 Hans U. Mair
Operational Evaluation Division
Institute for Defense Analysis
1801 N. Beauregard Street
Alexandria, VA 22311-1772

1 J. Fred Major
Alcan International Limited
Kingston Research and Development Centre
P. O. Box 8400, 945 Princess Street
Kingston, Ontario K7L 5L9 Canada

1 Antoinette Maniatty
MEAEM
RPI
110 8th St.
Troy, NY 12180-3590

1 Peter Matic
Naval Research Lab
Code 6303
Washington DC 20375-5343

1 Paul J. Maudlin
MST-8, MS G755
Los Alamos National Laboratory
Los Alamos, NM 87545

1 Dave McDowell
GWW School of Mech. Engng.
Georgia Tech
Atlanta, GA 30332-0405

1 John Mckirgan
Code 614, Naval Surface Warfare Center
Carderock Division
9500 MacArthur Blvd
West Bethesda, MD 20817-5700

1 Matt Miller
Sibley School of Mechanical Engineering
194 Rhodes Hall
Cornell University
Ithica, NY 14853

1 Roger Minich
Lawrence Livermore National Laboratory
7000 East Ave
L-097
Livermore, CA 94450

1 Kyran D. Mish
Lawrence Livermore National Laboratory
7000 East Ave
L-151
Livermore, CA 94450

1 Dan Mosher
UTRC MS129-73
411 Silver Lane East
East Hartford, CT 06108

1 Sia Nemat-Nasser
University of California, San Diego
Department of AMES
La Jolla, CA 92093-0416

1 A. Needleman
Brown University
Division of Engineering
Providence, RI 02912-9104

1 Sam Noboulsi
Air Force Institute of Technology
Department of Aeronautics and Astronautics
AFIT/ENY BLDG 640, 2950 P Street
Wright-Patterson AFB, OH 45433-7765

1 Bill Nix
Stanford University
Department of Materials Science & Engineering
Stanford, CA 94305

1 Mike Ortiz
Graduate Aeronautical Laboratories
Mail Code 105-50
California Institute of Technology
Pasadena, CA 91125

1 Mark A. Osborne
Advanced Materials Development Center
GM Powertrain
1629 N. Washington
P. O. Box 5073
Saginaw, MI 48605-5073

5 Richard J. Osborne
GMNA Materials & Fastening Engineering Center
General Motors
Mail Code 480-205-314
30007 Van Dyke
Warren, MI 48090-9065

1 Donald D. Penrod
Manufacturing Services and Development, Inc.
4665 Arlington Drive
Cape Haze, FL 33946

1 David Poirior
Aerospace and Mechanical Engineering
University of Arizona
Tucson, Az 85721

1 Pete Pollack
The Aluminum Association
900 19th. Street N.W.
Washington, D.C. 20006-2168

1 Bob. R. Powell
Research & Development Center
General Motors
Mail Code 480-106-212
30500 Mound Road
P. O. Box 9055
Warren, MI 48090-9055

1 Vincent C. Prantil
Mechanical Engineering Department
Milwaukee School of Engineering
1025 North Broadway
Milwaukee, WI 53202-3109

1 Thomas Prucha
Intermet Corporation
5445 Corporate Drive
Suite 200
Troy, Michigan 48098

1 A. Rajendran
US Army Research Office
4600 South Miami Blvd, PO Box 2211
RTP, NC 27709-2211

1 S. Ramaswamy
General Electric Company
Corporate R&D
Niskayuna, NY 12309

1 K.T. Ramesh
Johns Hopkins University
Department of Materials Science & Engineering
3499 N Charles St.
Baltimore, MD 21218

1 Mark Rashid
Department of Civil and Environmental Engineering
University of California at Davis
Davis, CA 95616-5294

1 Jim Rossi
Westmoreland Mechanical Testing & Research
P.O. Box 388
Youngstown, PA 15696—0388

1 Sunil Saigal
Civil and Environmental Dept.
Carnegie Mellon University
Pittsburgh, PA 15123-3890

1 Mark T. Samonds
UES Software, Inc.
175 Admiral Cochrane Drive, Suite 110
Annapolis, MD 21401

1 Carlos Sanday
Naval Research Lab
Code 6303
Washington DC 20375-5343

1 Gregory Sanders
Entelechy
42325 E. Ann Arbor Road
Suite 220
Plymouth, MI 48170-4356

1 Joseph S. Santner
American Foundry Society
505 State Street
Des Plaines, IL 60016-8399

1 Scott Schoenfeld
Army Research Laboratory
AMSRL-WT-TD
Aberdeen Proving Ground, MD 21005-5066

1 Robert G. Seese
KBAlloys, Inc.
P. O. Box 14927
Reading, PA 19612-4927

1 Vijey Shende
Amcast Automotive
300 Galleria Office Center Suite 208
Southfield, MI 48034

1 Yih-Chyun Sheu
General Motors
Truck Product Center – Central
Mail Code 483-510-2F2, Cube #113E6
2000 Centerpoint Parkway
Pontiac, MI 48341-3147

1 Donald A. Shockey
SRI International
333 Ravenswood Avenue
Menlo Park, CA 94025

1 G. Shulke
Chrysler Corporation
800 Chrysler Dr.
Auburn Hills, MI 48326-2757

1 G. Sigworth
116 Derby Street
Johnstown, Pa. 15905

1 Jerry H. Sokolowski
Mechanical And Material Engineering
University of Windsor
RM 209 Essex Hall, 401 Sunset Avenue
Windsor, Ontario, Canada N9B3P4

1 Al Torok
Kaiser Aluminum
6909 Thornwood St. NW
Canton, Ohio 44718

1 Dan Tortorelli
Dept. of Mechanical and Industrial Engineering
University of Illinois at Urbana-Champaign
140 Mechanical Engineering Building, MC-244
1206 West Green Street
Urbana, IL 61801

1 S. Viswanathan
Oak Ridge National Laboratory
PO BOX 2008, Bldg 4508
Oak Ridge, TN 37831-6983

1 Shaupoh Wang
AEMP Corporation
2404 Dr. F.E. Wright Drive
Jackson, TN 38305

1 Qigui Wang
Advanced Materials Development Center
GM Powertrain
1629 N. Washington
P. O. Box 5073
Saginaw, MI 48605-5073

1 David Weiss
ECK Industries
P.O. Box 967
Manitowoc, WI 54221-0967

1 Hussein Zbib
Washington State University
Dept. of Mechanical and Materials Engineering
Pullman, WA 99164-2920

1 Mohammed Zikry
Dept. of Mechanical and Aerospace Engineering
North Carolina State University
Raleigh, NC 27695-7910

1	MS 0310	P. Yarrington, 9230
1	MS 0316	S.S. Dosanjh, 9233
1	MS 0316	G.S. Heffelfinger, 9209
1	MS0321	W.J. Camp, 9200
1	MS0513	A.D. Romig, 1000
1	MS0820	P.A. Taylor, 9232
1	MS 0826	W.L. Hermina, 9113
1	MS0841	T.C. Bickel, 9100
1	MS 0847	H.S. Morgan, 9123
1	MS 0847	R.A. May, 9126
1	MS 0847	T. Hinnerichs, 9126
1	MS 1111	S.J. Plimpton, 9233
1	MS 1111	H. P. Hjalmarson, 9235
1	MS 1111	M. J. Stevens, 9235
1	MS 1411	J. M. Philips, 1802
1	MS 1411	H.E. Fang, 1834
1	MS 9001	M. E. John, 8000
		Attn: R. C. Wayne, 2200, MS 9005
		J. Vitko, 8100, MS 9004
		W. J. McLean, 8300, MS 9054
		D. R. Henson, 8400, MS 9007
		P. N. Smith, 8500, MS 9002
		K. E. Washington, 8900, MS 9003
1	MS 9221	C. M. Hartwig, 8510
1	MS 9405	R. Stulen, 8700
		Attn: R. Q. Hwang, 8721, MS 9161
		J.M. Hruby, 8702, MS 9401
		K. L. Wilson, 8724, MS 9402

		J. C. F. Wang, 8723, MS 9403
		W. A. Kawahara, 8725, 9042
		J. L. Handrock, 8727, 9042
1	MS 9161	D. L. Medlin, 8721
1	MS 9161	M. Van Schilfgaarde, 8721
1	MS 9405	D. J. Bammann, 8726
1	MS 9161	E. P. Chen, 8726
1	MS 9405	B. Somerday, 8724
1	MS 9405	N. Moody, 8725
1	MS 9405	P.M. Gullett, 8726
1	MS 9405	Y. Hammi, 8726
10	MS 9405	M. F. Horstemeyer, 8726
1	MS 9405	D. A. Hughes, 8726
1	MS 9405	R. E. Jones, 8726
1	MS 9161	P. A. Klein, 8726
1	MS 9161	J. Zimmerman, 8726
1	MS 9405	E. B. Marin, 8726
1	MS 9405	R. A. Regueiro, 8726
1	MS 9042	M. L. Chiesa, 8727
1	MS 9042	J. J. Dike, 8727
1	MS 9012	P. E. Nielan, 8920
1	MS 9054	R. W. Carling, 8360
1	MS 0421	K. W. Mitchiner, 9800
1	MS 0710	B. J. Kelley
1	MS 0188	D. Chavez, LDRD Office, 4001
1	MS 0899	Technical Library, 4916
1	MS 9021	Technical Communications Department, 8511/ Technical Library, MS 0899, 4916
1	MS 9021	Technical Communications Department, 8511 for DOE/OSTI
3	MS 9018	Central Technical Files, 8940-2